

Integrated Optic/Nanofluidic Detection Device with Plasmonic Readout

by

Jonathan S. Varsanik

M.Eng. EECS (2006), B.S. EECS (2005), B.S. Physics (2005)
Massachusetts Institute of Technology

Submitted to the Department of Electrical Engineering and Computer Science in Partial
Fulfillment of the Requirements for the Degree of

Doctor of Philosophy
at the
MASSACHUSETTS INSTITUTE OF TECHNOLOGY
June 2011

© 2011 Jonathan S. Varsanik. All rights reserved

The author hereby grants to MIT and the Charles Stark Draper Laboratory permission to
reproduce and to distribute publicly paper and electronic copies of this thesis document in
whole or in part in any medium known or hereafter created.

Signature of Author: _____

Department of Electrical Engineering
and Computer Science
May 20, 2011

Certified by: _____

Jonathan Bernstein
Draper Laboratory
Laboratory Technical Staff
Thesis Supervisor

Certified by: _____

M. Fatih Yanik
Associate Professor of Electrical Engineering
Thesis Supervisor

Accepted by: _____

Leslie A. Kolodziejcki
Professor of Electrical Engineering
Chair of the Committee on Graduate Students

Integrated Optic/Nanofluidic Detection Device with Plasmonic Readout

by

Jonathan S. Varsanik

Submitted to the Department of Electrical Engineering and Computer Science on May 20, 2011
in Partial Fulfillment of the Requirements for the Degree of Doctor of Philosophy in Electrical
Engineering and Computer Science

ABSTRACT

Integrated lab-on-a-chip devices provide the promise of many benefits in many application areas. A low noise, high resolution, high sensitivity integrated optical microfluidic device would not only improve the capabilities of existing procedures but also enable new applications. This thesis presents an architecture and fabrication process for such a device. Previously, the possibilities for such integrated systems were limited by existing fabrication technologies. An integrated fabrication process including glass nanofluidics, diffused waveguides and metal structures was developed. To enable this process a voltage-assisted polymer bond procedure was developed. This bond process enables high strength, robust, optically clear, low temperature bonding of glass – a capability that was not possible before. Bond strength was compared with a glass-to-glass anodic type bond using various materials and a polymer bond using two polymers: Cytop and PMMA. Bond strength was far superior to standard polymer bonding procedures. Design considerations to minimize background noise are presented, analyzed and implemented. Using Cytop as an index-matched polymer layer reduces scattered light in the device. Plasmonic devices driven via evanescent fields were designed, simulated, fabricated, and tested in isolation as well as in the integrated system. A sample device was made to demonstrate applicability of this process to direct linear analysis of DNA. The device was shown to provide enhanced and confined electromagnetic excitation as well as the capability to excite submicron particles. A demonstrated excitation spot of 200nm is the best we have seen in this type of device. Further work is suggested that can improve this resolution further.

Thesis Supervisor: Jonathan Bernstein,
Title: Laboratory Technical Staff, Charles Stark Draper Laboratory

Thesis Supervisor: M. Fatih Yanik
Title: Associate Professor of Electrical Engineering

Contents

Acknowledgements	7
CHAPTER 1: INTRODUCTION	9
Background	9
General description of device	13
Outline of this thesis	14
Conclusion	17
Works Cited	18
CHAPTER 2: OPTICS.....	21
Integrated Waveguides	22
Reducing Light Scattering.....	30
Conclusion	38
Works Cited	38
CHAPTER 3: FABRICATION	41
Fabrication process overview.....	42
Diffused Waveguides.....	43
E-beam fabrication	55
Hole drilling	59
Coverslip Processing.....	62
Alternative fabrication procedure.....	63
Device filling	64
Conclusion	67
Works Cited	68
CHAPTER 4: WAFER BONDING.....	69
Background	71
Glass-to-glass anodic-type bond	80
Polymer Bonding.....	86
Voltage-assisted polymer bonding.....	91
Conclusions	100
Works Cited	101
CHAPTER 5: PLASMONIC READOUT.....	105
Motivation	106
Plasmons	109
Simulation	113
Plasmonic Testing.....	127
Conclusion	136
Works Cited	137

CHAPTER 6: TARGET APPLICATION – DIRECT LINEAR ANALYSIS	141
Introduction	142
Device Design	150
Testing	156
Conclusion	161
Works Cited	162
CHAPTER 7: CONCLUSION	167
This work	167
Future work	168
Works Cited	170
APPENDIX: FABRICATION PROCEDURES	171
Substrate fabrication process.....	171
Coverslip Fabrication process.....	175

Acknowledgements

This thesis represents the culmination of eleven years at MIT. In those eleven years, I have accomplished and learned much. The most important accomplishment may be meeting the woman who I will soon get to marry. I cannot thank Sarah enough for the support that she has given me during this thesis process. Also, I would like to thank my mom for everything. As always, I cannot come close to describing all that you have done for me. Thank you to my family and friends.

Thank you to my thesis supervisor at Draper, Jonathan Bernstein, whose constant guidance and almost unending supply of knowledge was inspiring and always helpful. Also thank you to Amy Duwel at Draper for her continuing role as a mentor.

For a project of this scale, many people were needed to give assistance in various matters. I would like to point out many of them now.

At Draper, thank you to John Le Blanc for teaching me the art behind working with optics and waveguides. Thank you to the constant help from everyone in the MEMSFab, specifically Bill Teynor, Connie Cardoso, and James Hsiao. Thank you to Gene Cook who has had to share an office with me for the past four years. Thank you to John Mahoney for getting my devices drilled quickly when I needed them.

At MIT, thank you to my MIT thesis supervisor, Professor M. Fatih Yanik for his expertise and help. Also thank you to Professor Michael Watts for being willing to help out on the committee. Thank you to Mark Mondol and the MIT SEBL facility. Thank you to Professors Jongyoon Han and Patrick Doyle for their expertise and advice, as well.

Thank you to the Crozier group at Harvard with whom we collaborated on much of the optics and plasmonics in the early stages of this project. Specifically, Professor Ken Crozier, Paul Steinvurzel, Tian Yang, and Yaping Dan.

Thank you to the Defense Advanced Research Projects Agency for participation in the Center for Microfluidic Integrated Plasmonic Systems, based at Harvard University. The project or effort depicted was or is sponsored by the Defense Advanced Research Projects Agency, the content of the information does not necessarily reflect the position or policy of the Government and no official endorsement should be inferred.

This thesis work was performed at the Charles Stark Draper Laboratory through sponsorship of Internal R&D funds. Publication of this thesis does not constitute approval by Draper of the findings or conclusions contained herein. It is published for the exchange and stimulation of ideas.

Finally, this thesis is dedicated to my father; my inspiration to always be a better person. Thank you.

Chapter 1: Introduction

Integrated opto-fluidic detection has become a useful tool in many biological applications. By integrating optical and fluidic components, devices have become smaller, cheaper, and more robust. By moving from macro-fluidic to microfluidic tools, sample volumes are reduced, saving money and time in reagent use, and enabling higher resolution detection. However, current integrated lab-on-a-chip devices are limited in their applications by existing architectures and fabrication technologies. New architectures can enable completely new applications. In this thesis, an integrated opto-nanofluidic detection architecture and fabrication process developed that will enable new detection applications. This architecture integrates optical waveguiding, nanofluidic channels, and plasmonic resonators to achieve desired device improvements that were not possible before. The components for making these devices are explored, including novel fabrication procedures, and sample devices are fabricated and tested. To enable the new target application, this thesis strives to demonstrate an integrated architecture capable of detecting submicron fluorescent particles. Demonstrating that accomplishment, this architecture and fabrication process is shown to enable many new opportunities in sensitive optical detection.

This chapter outlines the general need shown in literature for the devices that are enabled by this thesis. The general design of the device architecture enabled is described, followed by an outline of the thesis.

Background

Optical microfluidic detection systems are a useful tool in many areas of biology. The ability to achieve high spatial resolution, high sensitivity detection in a flow-through system enables new applications. Much work has been performed to improve the resolution and sensitivity. The general methods to achieve this are reducing the excitation volume and integrating the system components into a lab-on-a-chip-device. Work that has been performed in this area is presented below. Shortcomings from that work and stated desires for further improvement in those areas provide the motivation for this thesis. By integrating optical waveguides, nanofluidics, and plasmonic resonators, we decrease the excitation volume, decrease background noise, and improve sensitivity, enabling new optical detection applications.

A diagram of a typical fluorescence detection system is shown in Figure 1. The sample is suspended in a fluid within the microfluidic channel. Light from some source is focused via external optics to a spot inside the channel. Light emitted from the sample is collected via optics and filtered externally. There are many sources of noise in this system, as both the excitation and signal light must travel through the entire device thickness. Common dimensions for the microfluidic channels are on the order of 100s of microns, and samples are on the order of microns.

The detection of small signals from fluorescent tags, impedance measurements, mass, or other techniques is difficult. Specifically, when looking for such small signals background noise is significant. This noise usually comes from sources such as Raman and Rayleigh scattering from the medium (1) or impurities (2), fluorescence from impurities (2)(3)(4), or the dark current in the detector (2)(3). To enable single molecule detection, it is desired to have: small excitation volume (2)(3), high efficiency collection (2), highly efficient detectors (2), and careful elimination of background fluorescence (2)(3).

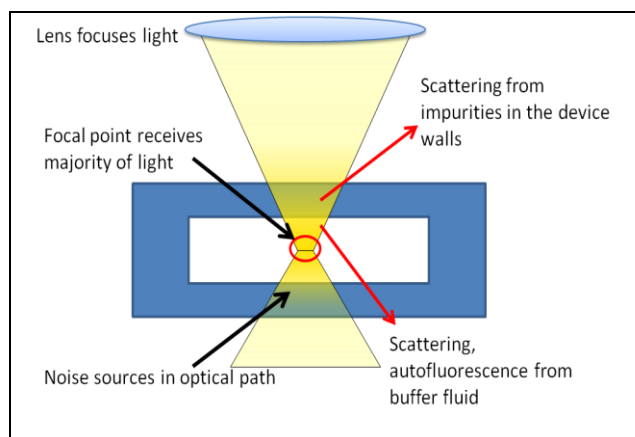


Figure 1: Diagram describing a typical microfluidic fluorescence excitation and detection setup. Excitation light propagating through device walls and large volumes produces noise from scattering and autofluorescence.

High-sensitivity optical detection systems are usually built in glass. This is because glass provides the high optical clarity needed for high-sensitivity detection (5). Furthermore, glass is a common tool because of its biocompatibility, chemical compatibility and strength (6). Finally, because many macro-scale experiments are carried out in glass, it is useful to be able to compare results from glass microfluidics to known data (6).

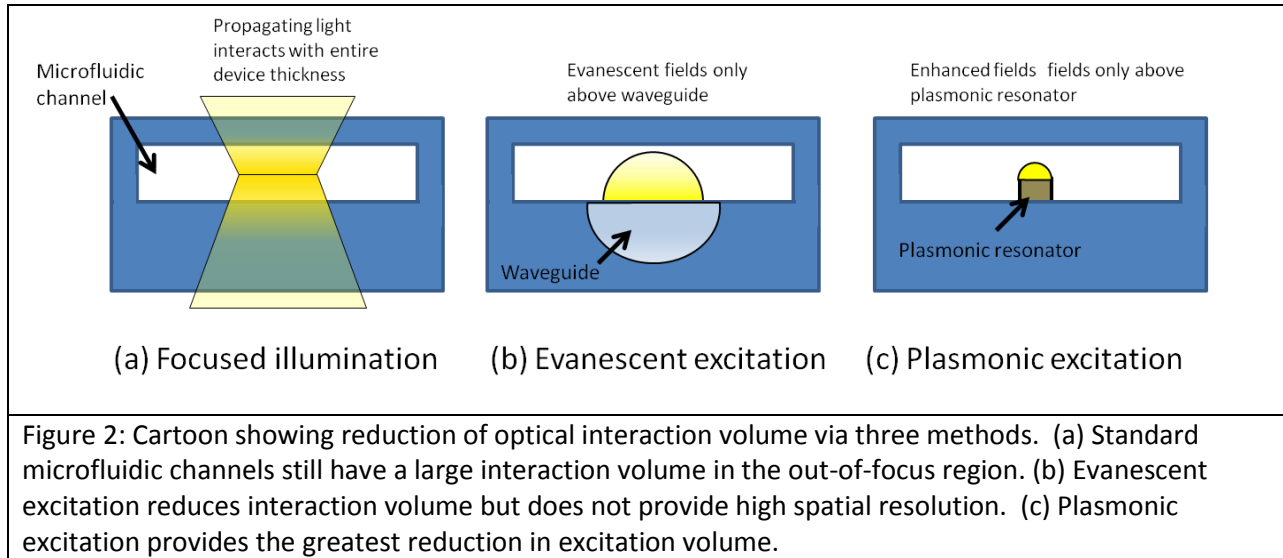
Methods to improve on optical microfluidic detection systems often involve the integration of multiple system components into a lab-on-a-chip

device. Integrating the system components achieves several goals, including making the device simpler and more robust (7)(8). Additionally, an integrated system will decrease cost, and reduce scattering and background noise by eliminating the need for expensive, large optical components that need to be aligned to couple light in and out of the device(9)(10). This reduction in background noise can dramatically increase the sensitivity of the system (7)(11)(12)(13). Work has been done to integrate optics in a high resolution readout by many methods: butting the end of fiber optic cables close to fluidic channels (13) (10) (14), shining light through a narrow slit (14), integrating microlenses into the system (15) (10) (12), or integrating zone plates (17) (18). However, most of this work is done in PDMS, limiting the channel size possible, the tolerable drive pressures, sensitivity, and device lifetime. To achieve a high sensitivity, robust platform, a glass device is desired.

Work has been performed to integrate waveguides and fluidics in glass, but it has been thought that a PDMS layer was needed to encapsulate the microfluidic channels, as the high temperature needed to bond glass would ruin the diffused waveguides (5) (14)(15). A robust low-temperature bond would enable these new devices.

Another generally accepted method to improve the resolution and sensitivity of the device is to reduce the optical excitation volume. By simply having less material excited by the interrogation light, background noise from autofluorescence and scattering from those sources is reduced. Additionally, by

localizing the excitation volume to a sub-micron zone, the spatial resolution of the system is equally improved. Integrated lensing has been one manner to reduce the excitation volume, decreasing a spot size down to 65 μm (16). Integrating waveguides achieved detection of 6 μm particles, but an even smaller spot size was desired (10). Similar work improved the efficiency of flow-separation devices, but still desired a smaller excitation volume and an improved signal to noise ratio (17). A smaller excitation volume would improve resolution and signal to noise ratio (7), decreasing background noise and improving sensitivity (8) (12).



Other novel architectures have attempted to achieve these two goals of improved resolution and sensitivity by increasing the contrast between the excitation signal and the background noise. Integrated optical devices with evanescent detection have become a common design (18)(19). By exciting fluorescent samples with purely evanescent light, the excitation volume is restricted to approximately 100 nanometers above the waveguide, a great reduction from propagating light through the entire device thickness. However, these techniques do not have much signal enhancement, and the spatial resolution is not good, as the minimum width of the excitation volume is limited by the width of the waveguide. The actual dimensions of the waveguide and the extent of the evanescent fields depend on the type of waveguides and materials used, but the logic is generally applicable.

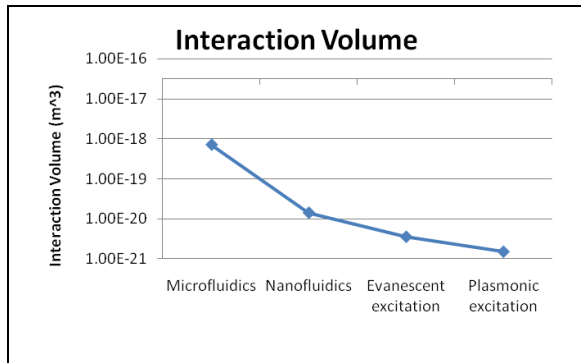


Figure 3: Approximate description of excitation volume reduction from the methods discussed.

Resonant sensors have been explored with ring and dielectric resonators. By having a resonator in an evanescent detection device, the excitation signal is increased, improving the signal-to-noise ratio and sensitivity (20). Most work in integrating plasmonic resonators has been focused on enhancement when next to a gold film (21)(22)(23)(24) (28). This kind of work utilizes the field enhancement, but not the potential for field localization of a plasmon. Other devices utilize plasmonic confinement and enhancement of fields (25)(26)(27) (31) (32) (33) (34). However, the plasmons are usually excited via wide-

field illumination, a large source of noise that we are trying to eliminate. Also, these applications are usually not integrated into a flow system.

In this work, we aim to improve optical microfluidic detection by integrating optical waveguides with nanofluidics and plasmonic readout. As with the work presented above, an integrated system will reduce size and complexity, making the system more robust. Integrated optics will decrease background noise, improving sensitivity. Furthermore, evanescent detection from the integrated diffused waveguides will decrease background noise even further by reducing the excitation volume.

Moving from microfluidic channels to nanofluidics channels will further improve sensitivity and resolution (1)(2)(3). By decreasing the volume of the channels improved sample localization is enforced, improving resolution. Additionally, decreasing the volume decreases the amount of material in the optical path, reducing background noise from scattering and autofluorescence.

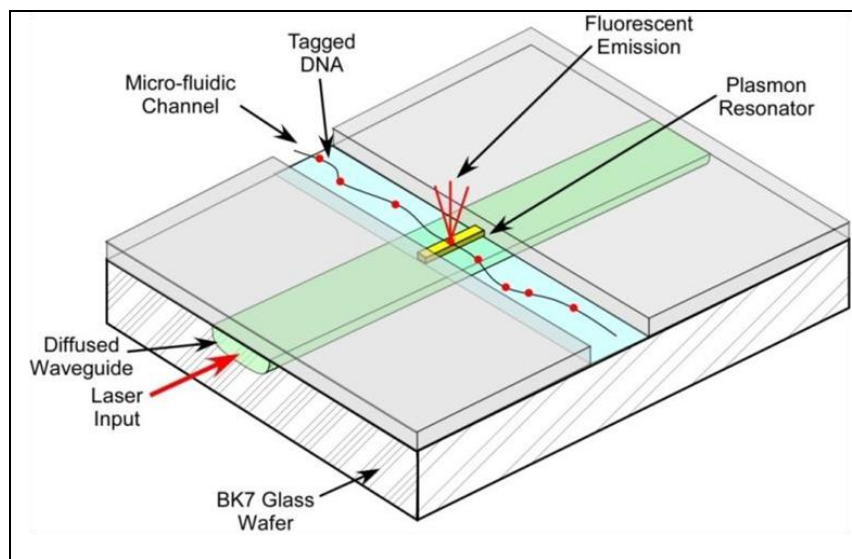


Figure 4: Cartoon of example device, showing operation for Direct Linear Analysis of DNA. This application is explored further in Chapter 7.

A final component to improving optical detection systems is a plasmonic readout. This readout incorporates a localized resonance. This resonance is enhanced and spatially confined to dimensions much smaller than the free space optical wavelength of the signal (36) (35) (33). Therefore, the excitation volume is reduced. This reduction improves sensitivity by reducing background noise from the additional excited volume that is not of interest (2). Furthermore, spatial resolution is also improved by the reduced volume from the plasmonic resonator, as the excitation is highly localized (22) (36).

Figure 2 and Figure 3 demonstrate the benefits of the localized resonance of the plasmonic resonator. The dimensions used to generate Figure 3 came from devices in this work. Representative dimensions are 100 μm x 100 μm for microfluidics, 10 μm x 200 nm for nanofluidics, a 4 μm wide diffused waveguide for the evanescent excitation and 100nm x 100nm for the plasmonic stripe. By moving to the plasmonic stripe we can not only improve our resolution but also reduce the background noise through reduced excitation volume.

By combining the integrated waveguides with nanofluidics and plasmonic readout, we aim to enable a new family of optical fluidic detection systems. These systems have not been possible to produce before now for several reasons. Fabrication methods were not available to integrate all the procedures. Specifically, a bonding method was not available that was compatible with the requirements of the system. In this thesis, we not only develop two bonding methods that enable these devices, but we present an entire fabrication procedure to integrate these previously incompatible capabilities.

General description of device

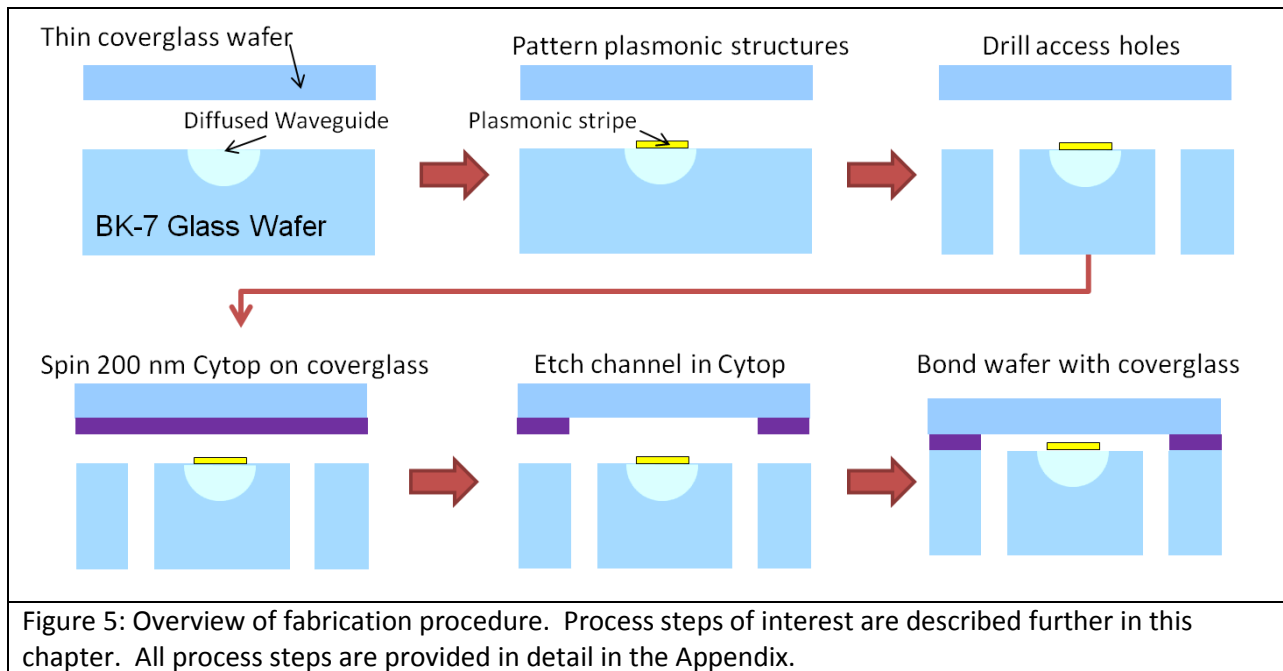
The result of this thesis is an enabling fabrication procedure and family of devices. However, a sample application is explored, as well. A general description of a typical device that is enabled by this process and an overview of the fabrication procedure are provided here, to enable a framework to understand the work in the remainder of the thesis. A cartoon of an example device is shown in Figure 4, above.

The devices in this thesis integrate nanofluidic channels in high-purity optical glass. Additionally, diffused waveguides and evanescently-excited plasmonic resonators are incorporated. The plasmonic resonator is a metallic structure on top of the diffused waveguide that couples to the evanescent light from the waveguide and excites localized resonant fields at its surface. The plasmonic resonator is placed on the waveguide at the point where the waveguide crosses below the microfluidic channel. This places the plasmonic resonator in the microfluidic channel at the region called the interrogation zone.

Laser light is coupled into the diffused waveguide at the edge of the chip and is guided to the interrogation zone. The fluorescent sample (in the cartoon example, this sample is tagged DNA) is introduced in the nanofluidic channel. When the sample crosses the plasmonic resonator at the interrogation zone, the fields from the resonator excite fluorescence in the sample, which can be observed by the detection optics.

This system provides many general advances in optical detection (more specifics are explored in Chapter 6). The integration of optical waveguides confines all propagating light to the waveguide, reducing large amounts of background noise. Excitation via the plasmonic resonator provides confined and enhanced fields, the merits of which were already covered.

The procedure for generating this device is shown in Figure 5, below, and covered in more detail in the Fabrication chapter as well as the Appendix. In general, the device is made by diffusing optical waveguides and patterning plasmonic resonators on one glass substrate, defining channels in a polymer on a different, thin glass substrate, and bonding the two pieces to encapsulate the channels.



Outline of this thesis

This thesis covers the creation of an optical nanofluidic detection device. This work has involved developing new fabrication procedures as well as design considerations to enable integrated device development. Each chapter covers one of the major areas of work, with a final chapter on the application of this architecture to a target device and a conclusion.

Chapter 2: Optics

This chapter covers the work done to minimize optical scattering and noise in the system by integrating an optical waveguide. This work is divided into two large sections. The first portion of work involved the modeling and fabrication of diffused waveguides. The index profile of diffused waveguides is not well defined in the literature. In this chapter, waveguides are modeled, simulated, fabricated, and tested in order to verify the proper shape and index distribution in order to enable accurate simulations in later chapters.

The second portion of work in this chapter involves the design considerations developed for the system in order to minimize scattered light. As a large focus of this thesis is the reduction of background noise, minimizing scattered light is a critical area of interest in producing a high sensitivity device. Various designs for the structure of the system are considered and the one that minimizes the scattered light is chosen. It is shown that a curved waveguide and defining the microfluidic channels in an index-matched polymer layer produces orders of magnitude less scattering when compared to simple evanescent excitation architecture in glass.

Chapter 3: Fabrication

Chapter 3 focuses on the general lessons learned in the fabrication of these devices. While many of the fabrication procedures presented in this chapter are not new, their integration is. Furthermore these steps often include idiosyncrasies that make process repeatability difficult. In this chapter, lessons learned from the integration of many disparate fabrication steps are presented.

The waveguide diffusion process presented many issues in wafer thermal management and diffusion mask chemical interaction considerations. Electron beam fabrication charge dissipation layer and development considerations are presented, as well. Many options for the drilling of access holes were explored and their various merits are presented. Other topics included the considerations for dealing with thin glass samples as well as device filling and fluid management in nanofluidic channels. Additionally, an alternative fabrication procedure is presented. This procedure utilizes an anodic-type bond procedure presented in the bonding chapter and achieves high, robust bond strength, but did not achieve sufficient optical clarity at the bond interface.

Chapter 4: Wafer Bonding

Wafer bonding is a useful tool for many fabrication procedures. In this thesis, it was necessary to implement a low-temperature, high-strength, optically-clean bond. A novel bond procedure that achieves these requirements was developed and evaluated in comparison to other bonding methods.

A background on wafer bonding and general considerations is presented, including bond strength test methods and major factors affecting the strength. Three bond procedures are presented and explored. Glass-to-glass anodic-type bonding is described and shown to achieve high bond strength, but insufficient optical clarity. Polymer bonding is shown to achieve good optical properties, but insufficient bond strength.

A novel bond procedure: voltage-assisted polymer bonding is developed and tested. Voltage-assisted polymer bonding is shown to achieve a low-temperature, high strength bond with polymer. This bond procedure provides improved bond strength over current best practices for polymer bonding, and enables new capabilities in device fabrication.

Chapter 5: Plasmonic Readout

Integrating a plasmonic resonator into the devices is desired to achieve high resolution, field enhancement, and interrogation volume reduction. However, it is necessary to ensure that the plasmonic resonator can operate in this configuration and will achieve the desired effects. This chapter addresses the design and inclusion of a plasmonic readout as well as the tools to achieve those results.

A background on plasmons is presented as well as their applications in biology and how they can be integrated to improve this device. Simulations were performed to design the system for proper behavior of the plasmonic device. The structure of the simulations used is presented as well as their results. Finally, plasmonic resonators were fabricated and tested via two methods: transmission spectral analysis and Near-field Scanning Optical Microscopy (NSOM). These results were compared to simulated results to provide an explanation of the effects observed.

It is shown that a plasmonic stripe can achieve the field enhancement and localization that is desired through evanescent coupling to the diffused waveguides.

Chapter 6: Target Application: Direct Linear Analysis

This chapter describes the application of this system architecture to one motivating application: Direct Linear Analysis of DNA. The motivation for DNA fingerprinting and the benefits of DLA are presented. Furthermore, the benefits to DLA from this device are described. The design, fabrication, and test of sample devices is shown.

It is demonstrated that this architecture is capable of producing an integrated device that can detect submicron particles. Additionally, the excitation volume is determined to be the smallest of any integrated device demonstrated to date. This result demonstrates the usefulness of this architecture and encourages pursuit of further applications.

Chapter 7: Conclusion

The final chapter summarizes the results from this thesis and outlines future work that may be explored.

Appendix

The Appendix includes a detailed fabrication procedure. This procedure is the combination of many potential procedures, but is the one that was used to produce the sample devices.

Conclusion

In conclusion, this thesis strives to present an architecture that will enable new applications in optical detection in fluidics. By developing a fabrication procedure that integrates waveguides, glass nanofluidics, and plasmonic resonators, it is demonstrated that this is possible. While each individual component is not new, their successful combination is. Finally, by demonstrating the ability to observe submicron particles with this integrated device, the usefulness is shown. It is hoped that this work is found to be useful and informative.

Works Cited

1. *Laser-Induced fluorescence of flowing samples as an approach to single-molecule detection in liquids.* **Dovichi, Norman J., et al.** 1984, Analytical chemistry, Vol. 56, pp. 348-354.
2. *Fluorescence Spectroscopy of Single Biomolecules.* **Weiss, Shimon.** 1999, Science, Vol. 283, pp. 1676-1683.
3. *Fluorescence background discrimination by prebleaching.* **Hirschfeld, Tomas.** 1979, The Journal of Histochemistry and Cytochemistry, Vol. 27, pp. 96-101.
4. *Towards a general procedure for sequencing single DNA molecules.* **Stephan, Jens, et al.** 2001, Journal of Biotechnology, Vol. 86, pp. 255-267.
5. *A novel concept of the integrated fluorescence detection system and its application in a lab-on-a-chip microdevice.* **Mazurczyk, Radoslaw, et al.** 2006, Sensors and Actuators B, Vol. 118, pp. 11-19.
6. *Fabrication and mechanical testing of glass chips for high pressure synthetic or analytical chemistry.* **Oosterbroek, R.E., et al.** 2006, Microsystem Technologies, Vol. 12, pp. 450-4.
7. *Rapid fabrication of a microfluidic device with integrated optical waveguides for DNA fragment analysis.* **Bliss, Christopher J., McMullin, James N. and "Rapid, Christopher J.** 2007, Lab on a Chip, Vol. 7, pp. 1280-1287.
8. *Design, simulation and characterisation of integrated optics for a microfabricated flow cytometer.* **Barat, David, et al.** 2010, Optics communications, Vol. 283, pp. 1987-1992.
9. *Integrated optical-fiber capillary electrophoresis microchips with novel spin-on-glass surface modification.* **Lin, Che-Hsin, et al.** 2004, Biosensors and Bioelectronics, Vol. 20, pp. 83-90.
10. *Microfluidic measurement system for fluorescent particles with three-dimensional sheath flow and a self-aligned adjustable microlens.* **Bucheggera, Wolfgang, Rosenauera, Michael and Vellekoopa, Michiel J.** 2009, Proceedings of the Eurosensors XXIII conference. Procedia Chemistry, Vol. 1, pp. 1123-1126.
11. *A SU-8/PDMS hybrid microfluidic device with integrated optical fibers for online monitoring of lactate.* **Wu, Min-Hsen, et al.** 2005, Biomedical Microdevices, Vol. 7, pp. 323-329.
12. **Lee, Luke P., et al.** *Single molecular detection via micro-scales polymeric opto-electro-mechanical systems.* University of California at Berkeley. 2005. AFRL Final Technical Report. DARPA Order No AOJ302/54.

13. *Fabrication of a new micro bio chip and flow cell cytometry system using Bio-MEMS technology.* **Byun, Insoo, Yang, Jooran and Park, Sekwang.** 2008, *Microelectronics Journal*, Vol. 39, pp. 717-722.
14. *Integrated microfluidic-microoptical systems fabricated by dry etching of soda-lime glass.* **Vieillard, Julien, et al.** 2008, *Microelectronic Engineering*, Vol. 85, pp. 465-469.
15. *Application of microfluidic chip with integrated optics for electrophoretic separations of proteins.* **Vieillard, Julien, et al.** 2007, *Journal of Chromatography B*, Vol. 845, pp. 218-225.
16. *Performance of an integrated microoptical system for fluorescence detection in microfluidic systems.* **Roulet, Jean-Cristophe, et al.** 2002, *Analytical Chemistry*, Vol. 74, pp. 3400-3407.
17. *Line laser beam based laser-induced fluorescence detection system for microfluidic chip electrophoresis analysis.* **Xu, Boajian, et al.** 2009, *Sensors and Actuators A*, Vol. 152, pp. 168-175.
18. *Planar-surface-waveguide evanescent-wave chemical sensors.* **Srivastava, Ramakant, Bao, Carmen and Gomez-Reino, Carlos.** 51, *Sensors and Actuators A*, Vol. 1996, pp. 165-171.
19. *Planar waveguides for fluorescence-based biosensing: Optimization and analysis.* **Bernini, Romeo, et al.** 2006, *IEEE Sensors Journal*, Vol. 6, pp. 1218-1226.
20. *Optical slot-waveguide based biochemical sensors.* **Barrios, Carlos Angulo.** 2009, *Sensors*, Vol. 9, pp. 4751-4765.
21. *Surface enhanced spectroscopy.* **Moskovits, Martin.** 1985, *Reviews of Modern Physics*, Vol. 53, pp. 783-826.
22. *Tip enhanced optical spectroscopy.* **Hartschuh, Achim, et al.** 2004, *Philosophical Transactions of the Royal Society of London, A*, Vol. 362, pp. 807-819.
23. *Lifetime of an emitting molecule near a partially reflecting surface.* **Chance, R.R., Prock, A. and Silbey, R.** 1974, *The Journal of Chemical Physics*, Vol. 60, pp. 2744-2748.
24. *A miniaturized germanium-doped silicon dioxide-based surface plasmon resonance waveguide sensor for immunoassay detection.* **Huang, JG, et al.** 2006, *Biosensors and Bioelectronics*, Vol. 22, pp. 519-525.
25. *Enhancement of single-molecule fluorescence using a gold nanoparticle as an optical nanoantenna.* **Kuhn, Sergi, et al.** 2006, *Physical Review Letters*, Vol. 97, p. 017402.
26. *Plasmonic enhancement of Molecular Fluorescence.* **Tam, Felicia, et al.** 2007, *Nano Letters*, Vol. 7, pp. 496-501.
27. *Fiber-optic conical microsensors for surface plasmon resonance using chemically etched single mode fiber.* **Kurihara, Kazuyoshi, et al.** 2004, *Analytica Chimica Acta*, Vol. 523, pp. 165-170.
28. *Integration of polymer waveguides for optical detection in microfabricated chemical analysis systems.* **Morgensen, Klaus B., et al.** 2003, *Applied Optics*, Vol. 42, pp. 4072-4079.

29. *Micro flow cytometers with buried SU-8/SOG optical waveguides.* **Lee, Gwo-Bin, Lin, Che-Hsin and Chang, Guan-Liang.** 2003, *Sensors and Actuators A*, Vol. 103, pp. 165-170.
30. *Fiber-optic conical microsensors for surface plasmon resonance using chemically etched single mode fiber.* **Kurihara, Kazuyoshi, et al.** 2004, *Analytica Chimica Acta*, Vol. 523, pp. 165-170.
31. *Microfluidic systems with on-line UV detection fabricated in photodefinable epoxy.* **Jackman, Rebecca J., et al.** 2001, *Journal of Micromechanics and Microengineering*, Vol. 11, pp. 263-269.
32. *Integrated optical measurement system for fluorescence spectroscopy in microfluidic channels.* **Hubner, Jorg, et al.** 2001, *Review of Scientific Instruments*, Vol. 72, pp. 229-233.
33. *Microfluidic chip: Next-generation platform for systems biology.* **Feng, Ziaojun, et al.** 2009, *Analytica Chimica Acta*, Vol. 650, pp. 83-97.
34. *Fully integrated optical system for lab-on-a-chip applications.* **Balslev, S., et al.** 2004, *Proceedings of the 17th IEEE MEMS (IEEE 2004)*, Vol. 1, pp. 89-92.

Chapter 2: Optics

Detection of fluorescent samples in a fluid is a useful tool in many biological applications (1). By tagging the sample of interest with fluorescent material, it is possible to use an optical filter to remove much of the background noise from the detected signal. However, the applications available to existing devices are limited by their resolution and sensitivity. This thesis is aimed at producing a device that can achieve a much improved resolution and sensitivity – enabling the detection of smaller samples, opening the door to new applications. One important aspect of this improved device is reducing scattering caused by the excitation light by integrating waveguides into the device. This chapter covers the work done in simulation and testing of these integrated waveguides as well as the design considerations that were addressed to minimize scattering. We found that we were able to successfully model the waveguides even though there is disagreement in the literature about the proper index distribution. Additionally, we were able to develop a system design that greatly reduces the scattering in the device, minimizing background noise and therefore improving sensitivity.

Integrated Waveguides.....	22
Motivation for integrated waveguides	22
Index profile background	24
Simulations.....	25
Waveguide modal testing	26
Preferential excitation and end facet imaging.....	27
Fourier analysis	28
Reducing Light Scattering	30
Scattering from the microfluidic channel	30
Evanescent fields	32
Index-matched layer	32
Other solutions	34
Scattered light from fiber optic connection.....	35
Results.....	37
Conclusion.....	38
Works Cited.....	38

Integrated Waveguides

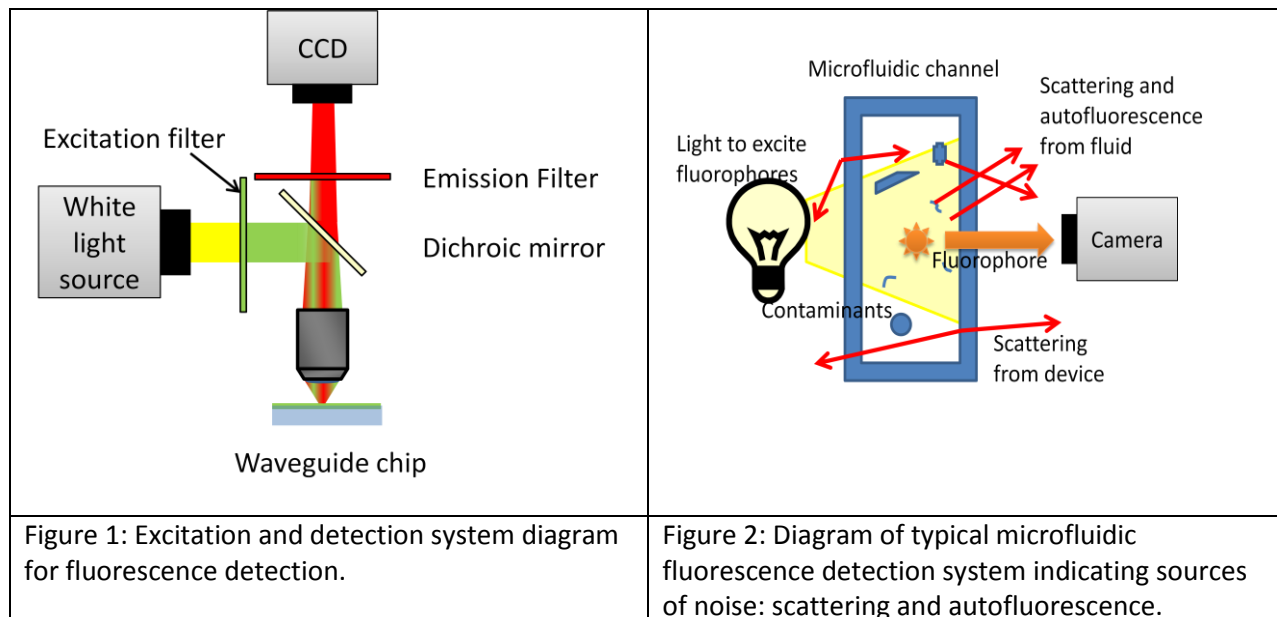
Most fluorescent detection methods have to contend with a lot of background noise as a result of their design. By integrating the waveguides into the device, it is possible to reduce or remove much of this noise, improving sensitivity, enabling the detection of smaller signals. In our system we utilize diffused waveguides to accomplish this integration. However, the diffusion process is not well controlled and it is necessary to perform simulation and tests to ensure that the characteristics of the waveguide are as expected. What follows is the work that was performed in that area.

Motivation for integrated waveguides

In most fluorescent detection methods, an external light is aimed through a fluidic channel in order to excite fluorescence. The size of the illuminated area has a minimum size that is defined by the diffraction limit of the light. The signal that returns to the detection system contains the excited fluorescent signal, but is combined with reflected light from the interfaces in the device, scattered light from impurities in the device or the fluid, Raman scattered light from those sources, autofluorescence, and other background noise. This background light is usually able to be filtered out, but not all. All this background noise is the result of the system design, where in order to illuminate the sample of interest, large amounts of other material are illuminated, as well. A diagram of a typical imaging setup showing routing and filtering of light is shown in Figure 1. A close-up view of the sample area is shown in Figure 2, demonstrating the typical path of light and sources of scattering.

By integrating the waveguides, several benefits are achieved. First, the need for external optics is reduced. This is beneficial because external optics are not only costly, but they also require precise alignment, which may need to be adjusted often. Removing the need for external optics is a great step in improving usability, reliability, and cost.

The second benefit of integrated waveguides is the reduction of noise. Instead of shining light through the entire cross-section of our device, it only illuminates one piece of the device. The sources of noise in old systems were listed before: reflection from interfaces in the surface and scattering and autofluorescence in the detection area – are all removed. There is no propagating light anywhere in the device, except in the waveguide. Therefore, there should be no stray light coming from anywhere. If this is the case, when the fluorophore is excited, that signal should be the only light that exists in the system.



Diffused waveguides in particular provide several advantages when compared to other methods of waveguide creation. Because the waveguides are diffused into the surface of a glass wafer, we are left with a flat substrate. This makes them an ideal choice on which to build fluidic devices. The index changes achievable with ion exchanged waveguides make them relatively easy to integrate with fibers. In order to achieve very low loss fiber to waveguide coupling, the index of refraction profiles must be matched. This can be achieved by using an electric field to migrate the diffused ions beneath the surface of the glass. If one could achieve a circular index profile with a radius and Δn matching a fiber, low loss coupling is achievable. Additionally, they have the advantage of needing minimal capital investment to produce low loss waveguides. Finally, in the asymmetric waveguide structure, the majority of modes have strength maxima near the surface, increasing the strength of fields for coupling to the plasmonic resonators, improving the strength of our excitation (2).

While the diffused waveguides offer many advantages, the diffusion process is not well controlled. In this device, the requirements for the waveguides alone are not very strict. It would be acceptable to merely test the function of the diffused waveguides. Coupling energy efficiently into the plasmonic resonator depends critically on the index and modal behavior of the waveguides. Therefore to properly simulate the behavior of the plasmonic resonators, it is necessary to understand the properties of the waveguides that will be driving them.

To understand the properties of the waveguides, chips were fabricated with diffused waveguides. The modal properties of these waveguides were observed and that information was matched with simulations to determine the diffusion parameters that most closely matched the behavior of the fabricated waveguides. The fabrication process for diffused waveguides and the difficulties that it can present are covered in the Fabrication chapter. In this chapter we cover the testing and simulation of those waveguides.

Index profile background

The images obtained of the modes supported by the fabricated waveguides do not directly tell us the characteristics of the waveguide that we are interested in. To obtain that information, it is necessary to simulate the waveguides based on information in the literature and attempt to match the results with the observed behavior.

There has been much work in defining the index profile resulting from the waveguide diffusion process. However, it is not clear what that profile looks like. In general, it is understood to be described by a combination of functions in the lateral (x) and depth (y) dimensions, as described by:

$$n(x, y) = n_0 + (\Delta n) * g(x)f(y)$$

In the above equation, n_0 is the index of the bulk material and Δn is the maximum index difference. Then, $g(x)$ and $f(y)$ are the equations describing the shape of the diffusion in the lateral and depth dimension. Likely choices for $g(x)$ and $f(y)$ are a Gaussian:

$$g(x) = e^{-\frac{x^2}{h_x^2}}$$

An error function for $g(x)$ only:

$$g(x) = \frac{1}{2} \left\{ \operatorname{erf} \left[\frac{\left(\frac{w}{2} + x\right)}{h_x} \right] + \operatorname{erf} \left[\frac{\left(\frac{w}{2} - x\right)}{h_x} \right] \right\}$$

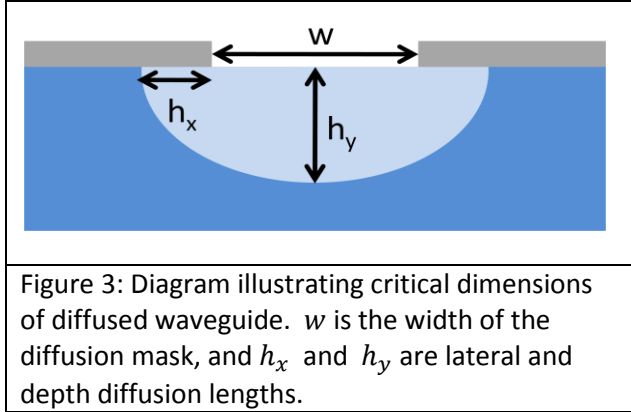
An exponential for $f(y)$ only:

$$f(y) = e^{-\frac{y}{h_y}}$$

Or, for the depth component, a complimentary error function:

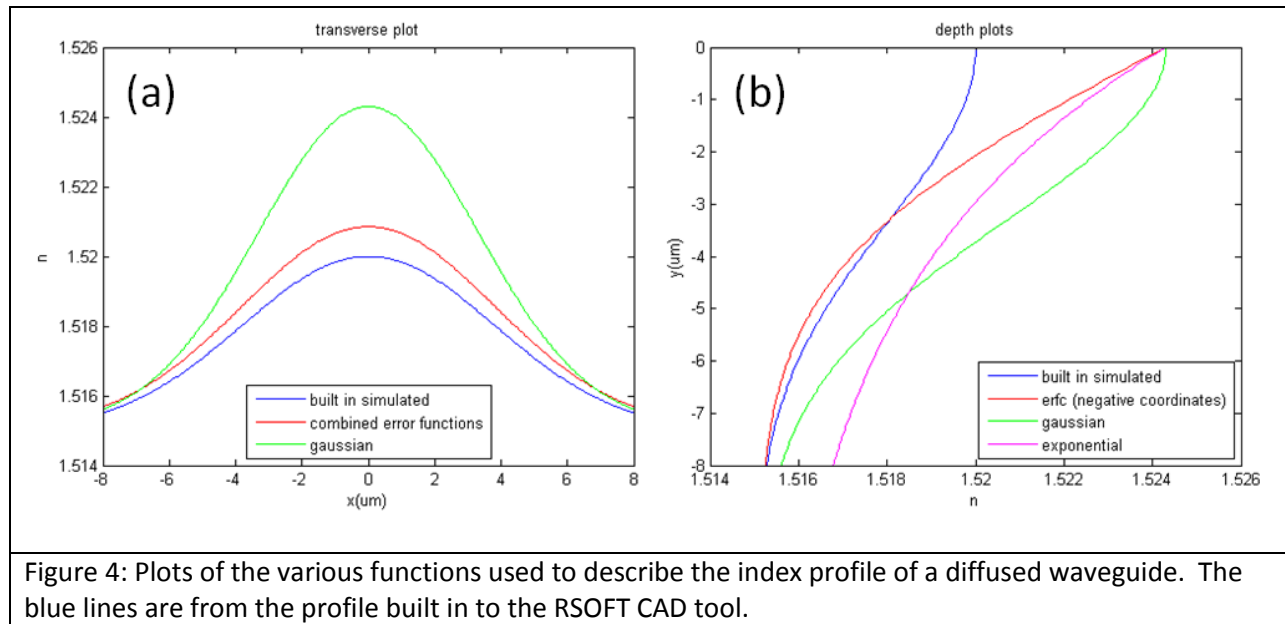
$$f(y) = \operatorname{erfc} \left[\frac{y}{h_y} \right]$$

In the above equations, w is the width of the diffusion mask, and h_x and h_y are lateral and depth diffusion lengths, which are shown in Figure 3, below. The parameters h_x and h_y are determined by the materials used and the specifics of the diffusion process. However, these values are not well defined for each process. Furthermore, the choice of function to describe the waveguide shape is not agreed upon. Plots of these functions and two resulting index distributions are shown in Figure 4, below.



The correct combination of these equations is not agreed upon (3)(4)(5)(6). Additionally, the values for Δn , h_x , and h_y are process-dependent and not well-controlled. Therefore, it is important to verify these properties of the waveguides produced by this process. Potential index distributions are shown in Figure 4, below. These plots vary wildly and affect the expected waveguide modes.

It is important to obtain accurate values of these parameters to ensure that further simulations using these waveguides are accurate. These waveguide properties are critical in the simulations for plasmonic coupling and scattering.



Simulations

Utilizing the functions described above, different combinations were used to produce index distributions that were fed to the simulation software. The simulation software used was the BeamPROP tool from RSoft. BeamPROP is a beam propagation method solver. This means that it solves Maxwell's equations under the slowly varying approximation, in which it is assumed that the simulated structure only changes very slowly in the direction of propagation of the signal. For a waveguide, this assumption is valid.

Upon feeding these various profiles to the simulation software, the simulation was carried out at the wavelengths that were tested and the resulting modes were compared, both in number and shape, to the measured modes. Based on the results, the variables that could be adjusted were: waveguide width, waveguide depth, index difference, and index profile function.

After carrying out this series of simulations, a resulting index profile was found that achieved a very good match. It was found to be a good fit for the work by Weiss and Srivastava (4), with a Gaussian in x and a complimentary error function in y . However, the parameters had to be slightly adjusted, as expected for process variations. Interestingly, the profile for a diffused waveguide that was built in to the BeamPROP software produced very incorrect results. Now, with this resulting information, it is possible to have an accurate model for the excitation of the plasmonic resonator, improving the accuracy of those simulations. The generated index distribution and the RSoft built-in index distribution for diffused waveguides is shown in Figure 5, below

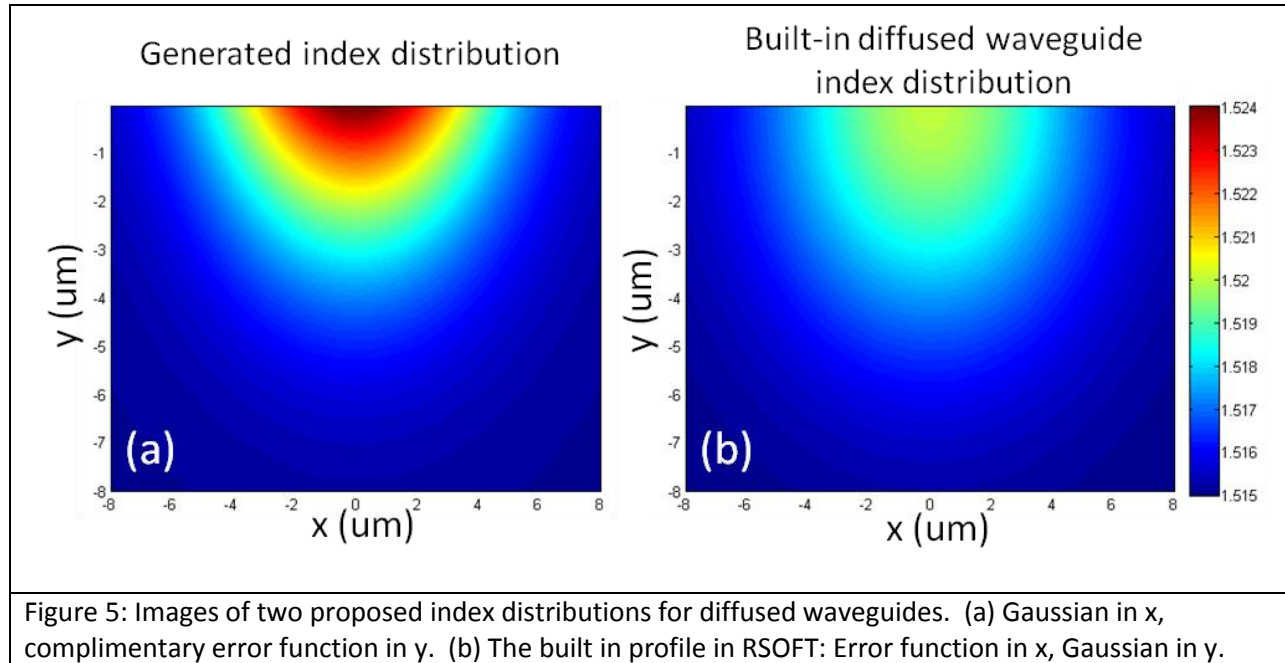


Figure 5: Images of two proposed index distributions for diffused waveguides. (a) Gaussian in x , complimentary error function in y . (b) The built in profile in RSOFT: Error function in x , Gaussian in y .

Waveguide modal testing

Waveguides only support specific electric field distributions called normal modes. The idea of a normal mode can be illustrated most easily in one dimension. If a one dimensional cavity is created with two metal plates, the solutions for any wave between those plates must be zero at the plates. This solution takes the general form:

$$\vec{E} = \hat{k} \sin\left(\frac{m n \pi}{d}\right)$$

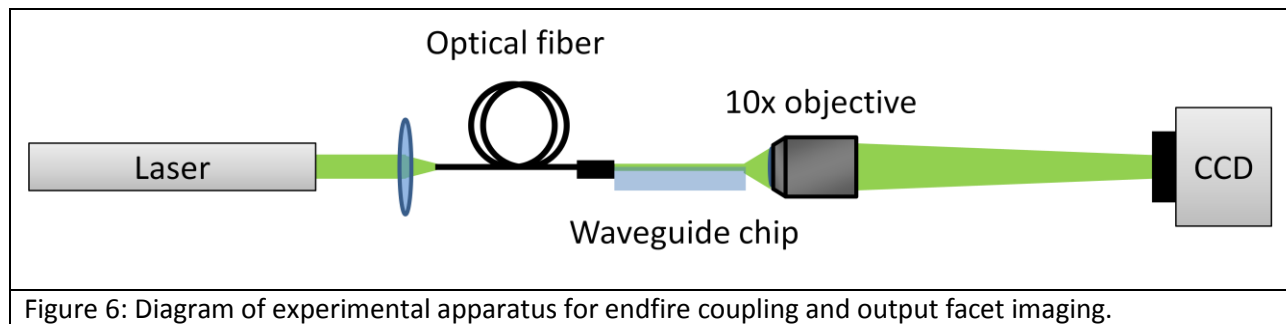
Where \vec{E} is the electric field vector, \hat{k} is the direction of the field, m is the mode number, n is the index of refraction of the material, and d is the separation of the plates.

Moving to two dimensions, there are two mode numbers, and the mode structure becomes more interesting. The number of modes and their separation in frequency is an indication of the waveguide properties. Waveguides with different dimensions, index of refraction, and shape will have different modal behavior. Therefore, it is possible to utilize the modal structure of a waveguide to determine its properties.

There are many methods to determine the modal behavior of a waveguide. By prism coupling light out of the waveguide, it is possible to determine the number and distribution of modes in the waveguide. However, in a diffused waveguide the modes are very closely spaced due to the small difference in refractive index. That close spacing makes it difficult to reliably measure the modes. Therefore another method was used.

Preferential excitation and end facet imaging

In order to determine the modes in the waveguide, light of different wavelengths was introduced into the waveguide. This excitation source was moved with respect to the waveguide. For a given position of the source, different supported modes will be excited. Therefore, by moving the source to positions that isolate a single mode, and repeating this process for each mode that is observed and for each wavelength of interest, it is possible to determine the modes that are supported by that waveguide. Figure 6 is a diagram of the experimental setup used and Figure 7 shows images obtained from the experiment and simulation, demonstrating the different modes that exist in the waveguide.



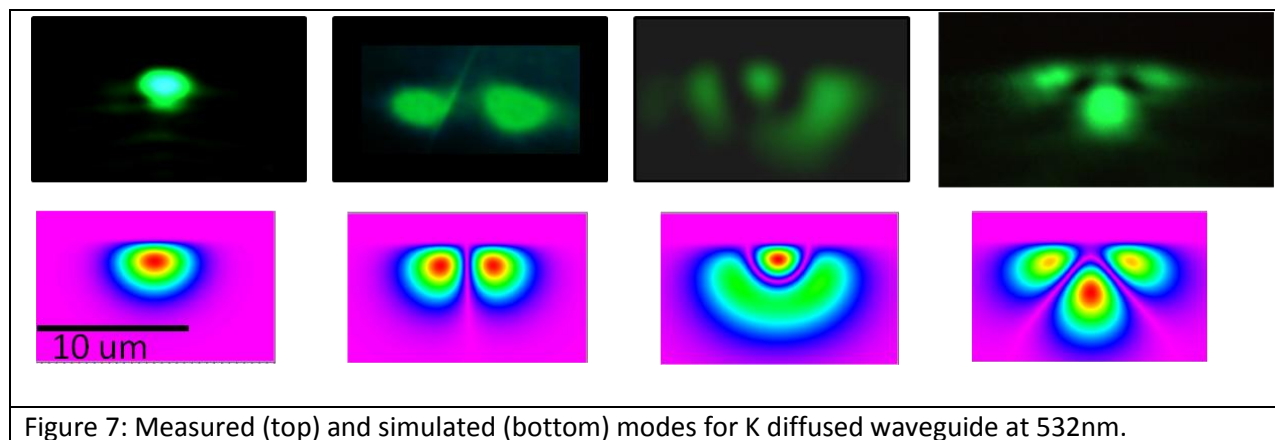


Figure 7: Measured (top) and simulated (bottom) modes for K diffused waveguide at 532nm.

Fourier analysis

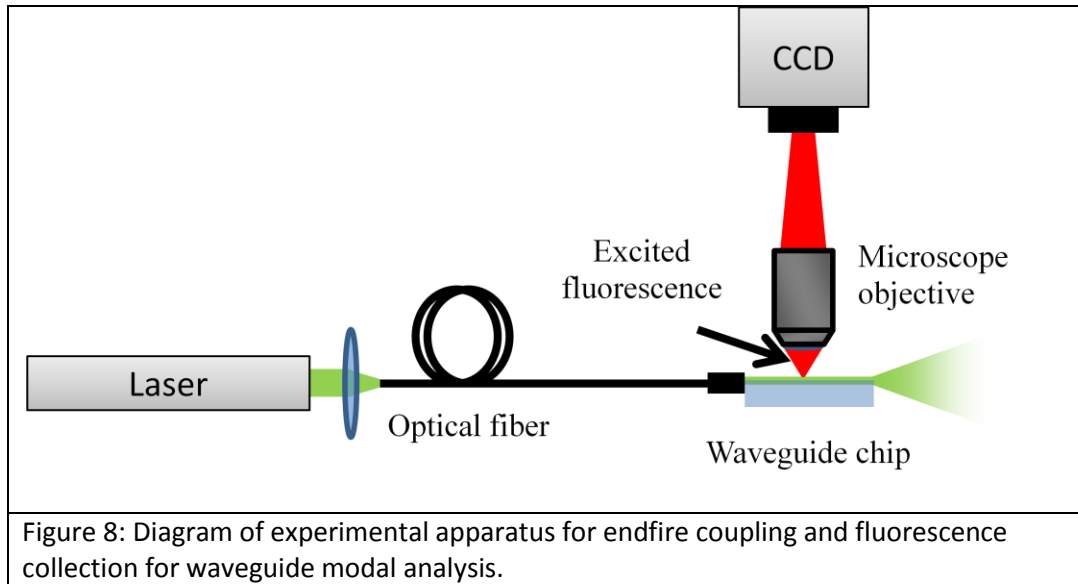
Another method of determining the modal content of a waveguide is through Fourier analysis of the modal beating in the waveguide. Each mode that propagates in a waveguide travels at a different velocity and has a different “effective index.” If there are multiple modes in the waveguide at one time, the modes will interfere constructively at some points and destructively at other points, producing a beating pattern. This pattern will have a sinusoidal pattern produced by modes cycling between the constructive and destructive interference.

The wavelength of a beating pattern produced by two modes is:

$$\lambda_{beat} = \frac{\lambda_0}{n_1 - n_2}$$

In the above equation, λ_{beat} is the characteristic beat wavelength (distance between two subsequent nulls or peaks), λ_0 is the wavelength of the light in free space, and n_1 and n_2 are the effective indices of refraction for the two modes. The beating pattern of a waveguide with multiple modes will be a combination of sinusoids created by the beating between pairs of modes. By performing a Fourier analysis of the beating pattern, it is possible to extract the characteristic lengths of each of these beating patterns, providing a measure of the number of modes in the waveguide and their effective indices.

To visualize and record the beat pattern in the waveguide, a fluorescent film was deposited on the entire surface of a waveguide chip (7) (8)(9). Laser light of various wavelengths of interest was introduced to the waveguide. The fluorophores coating the top of the waveguide fluoresce in response to the beat pattern of the modes in the waveguide. This fluorescence pattern is observed and recorded with a CCD camera. The experimental setup is shown in Figure 8.



Once the beating pattern is recorded, the numerical analysis is performed on it to determine the modal content (10). Using MATLAB, the image of the fluorescence pattern along the waveguide is converted to a one-dimensional series of intensity values. By performing a Fourier analysis on this data and plotting the result, the peaks indicate the beat lengths that are present in that signal. These beat lengths can then be matched with the beat lengths that are present in the simulated waveguides. An image of a waveguide showing the modal beating is shown in Figure 9 and the corresponding intensity values and Fourier analysis is shown in Figure 10. The peaks in Figure 10 align with some of the dotted lined included in that plot, which are locations of beat frequencies expected from the simulated modes of the waveguide. By performing this experiment with different excitation conditions, it should be possible to build a composite plot showing peaks at all expected beat frequencies, matching the modal content of the waveguide.

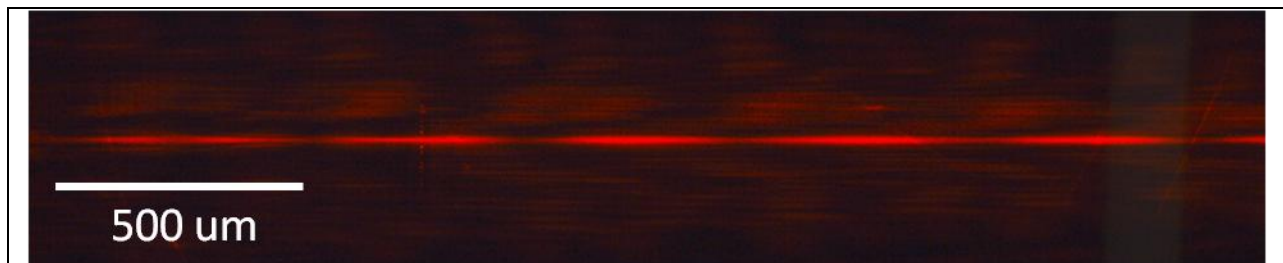
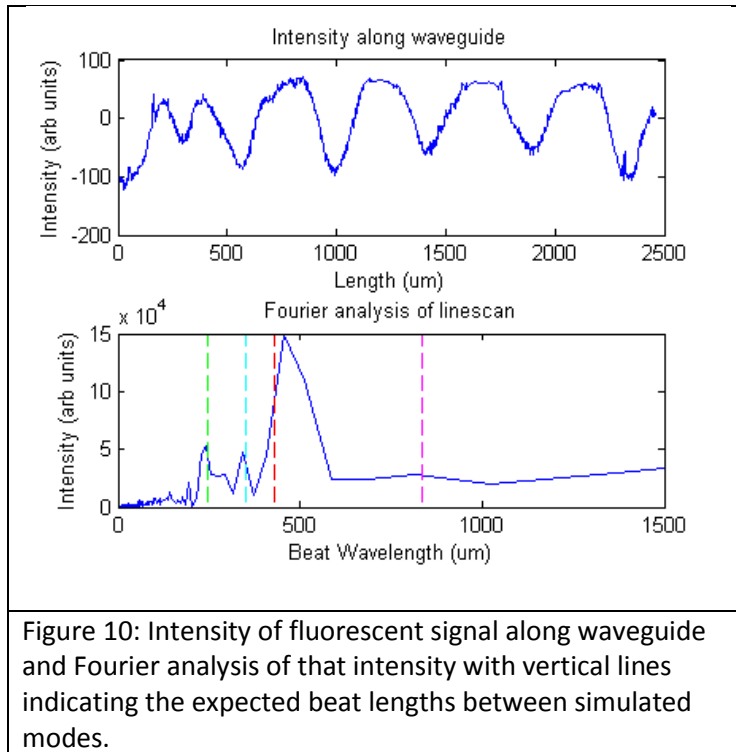


Figure 9: Image of waveguide with a layer of fluorophores on top showing modal beating. The image spans $\sim 2500\mu\text{m}$.

While the beat lengths are unique only for the difference in effective index, not for the absolute index, it is possible that the effective indices in this analysis are incorrect by a constant. However, the maximum index of refraction of the waveguide was confirmed via prism coupling experiment, so by verifying that one parameter of the backing equations and taking all other effective indices in relation to that one, it is possible to be confident in the results of this analysis.



The results indicate that the modal beat lengths present in the detected fluorescent signal occur at lengths that agree with several modes expected from the simulated waveguides. Therefore, it is possible to be confident in the waveguide values that are used in further simulations in this thesis.

Reducing Light Scattering

While integrating the waveguides reduced scattering from many sources, there were still sources of scattered light that needed to be addressed. The two large sources that were addressed were: the microfluidic channel, and the connection point between the incoming optical fiber and the waveguide.

Scattering from the microfluidic channel

The most straightforward design of the system in this thesis would have a microfluidic device etched into the thick substrate wafer. This is the same wafer that contains the waveguides. Therefore, at the interrogation region, where the waveguide and the microfluidic channel cross, the channel would actually be etched into the waveguide. This is quite obviously a situation that would produce scattering. Looking at the modes of the waveguides shown in the previous section, a large change in the index of refraction in the top 200nm of the waveguide would be near some of the most intense fields in the

waveguide mode. This change in index of refraction would cause scattering. Furthermore, the scattering is located immediately adjacent to the detection area, the region where scattering is most detrimental.

This behavior is actually beneficial in some applications. Work in integrated concentration detection devices utilize this exact design to provide integrated illumination for a region of fluid. The light that propagates through the fluid is then sent to a spectrometer, providing a measure of the concentration of the sample of interest (11). But, this behavior is not beneficial for us. The next solution would be then to move the microfluidic channel up out of the waveguide and into the coverslip (the top glass). However, this causes scattering for a similar reason as the channel in the waveguide. The reason why is explained below.

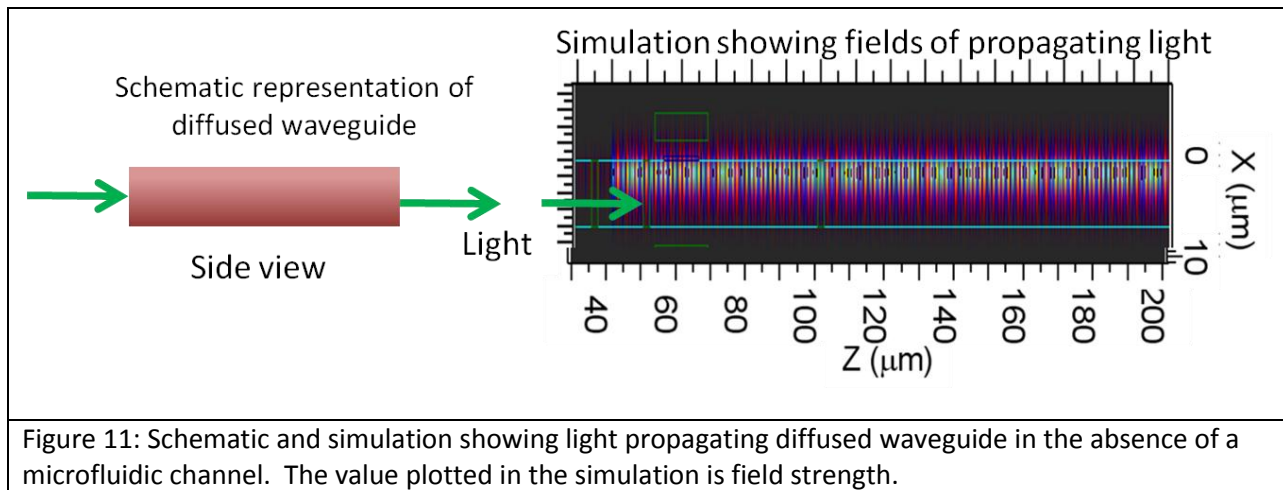


Figure 11: Schematic and simulation showing light propagating in a diffused waveguide in the absence of a microfluidic channel. The value plotted in the simulation is field strength.

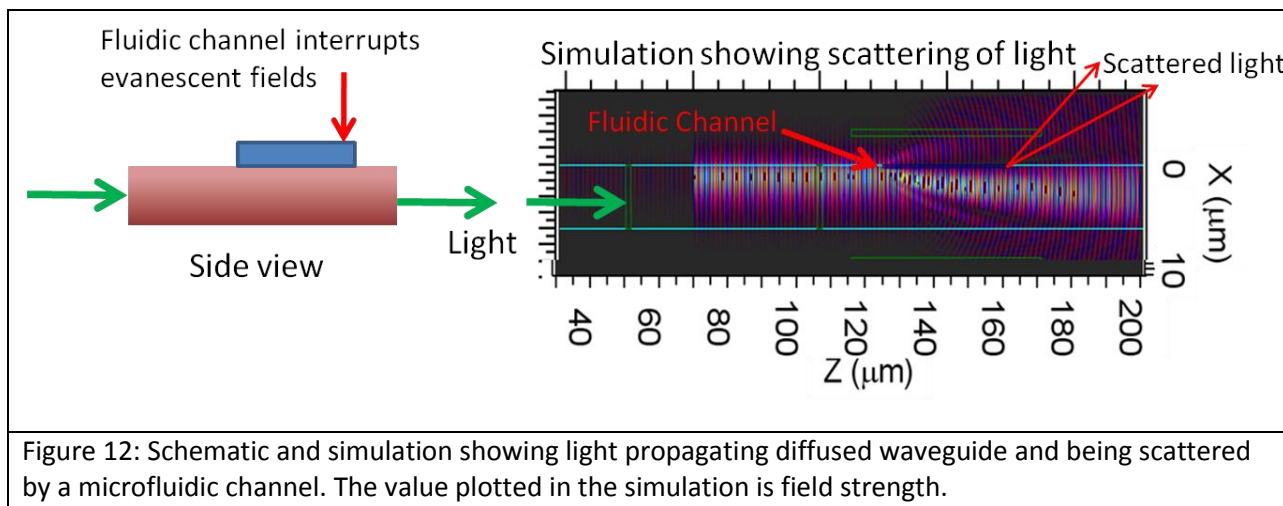


Figure 12: Schematic and simulation showing light propagating in a diffused waveguide and being scattered by a microfluidic channel. The value plotted in the simulation is field strength.

Evanescent fields

While the majority of the energy in a waveguide is contained within the region of higher refractive index, in any dielectric waveguide, some power exists in rapidly decaying fields that extend slightly beyond the waveguide. These fields are called evanescent fields. These evanescent modes are confined modes (they do not radiate energy). Put another way, their wave vector does not match the propagation condition in the medium where they exist. What this ultimately means is that they are confined to the surface of the waveguide, and therefore are not seen.

However, these evanescent fields can be converted into propagating light. If they were to hit something that could alter their wave vector, they could be converted into propagating waves. Put another way, these fields, even though they only exist on the surface, they can be “kicked off” of the surface by a change in material. This is exactly what having a microfluidic channel in the coverglass causes. While the channel is not etched into the channel, it still provides a discontinuity in the index of refraction seen by the evanescent fields, producing scattering of those fields. Another solution is desired to reduce scattering further. Figure 11 and Figure 12 show diagrams and simulations of light travelling in a waveguide and being scattered by a microfluidic channel. The colors in the images on the right side of these figures represent electromagnetic field strength. Scattering can clearly be seen in the right side of Figure 12, as the light no longer propagates only along the waveguide, but scattered to radiating modes above and below the waveguide.

Index-matched layer

As described in the previous sections, scattering is caused by a discontinuity in the index of refraction seen by an electromagnetic field. Therefore, an ideal architecture would provide a uniform index of refraction along the length of propagation of the waveguide. What this necessitates is that the microfluidic channel be embedded in a layer of material that has an index of refraction equal to that of the material in the microfluidic channel (in this case, water, with $n=1.33$). A cross-sectional diagram of this index-matched layer compared to different positions of the channel in a standard glass-to-glass bonded system is shown in Figure 13. In the case of the index-matched layer, there is no index change as a wavefront propagates through the microfluidic channel, resulting in no scattered light.

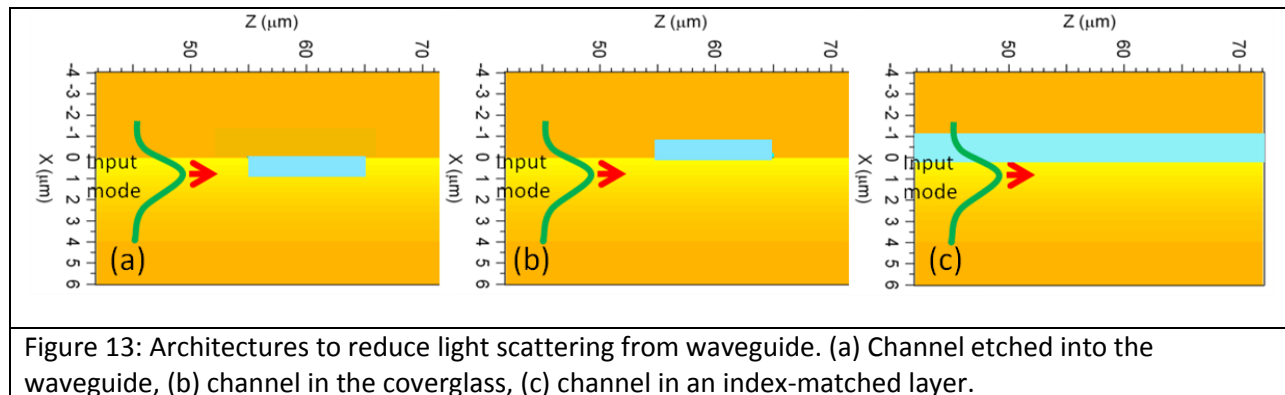


Figure 13: Architectures to reduce light scattering from waveguide. (a) Channel etched into the waveguide, (b) channel in the coverglass, (c) channel in an index-matched layer.

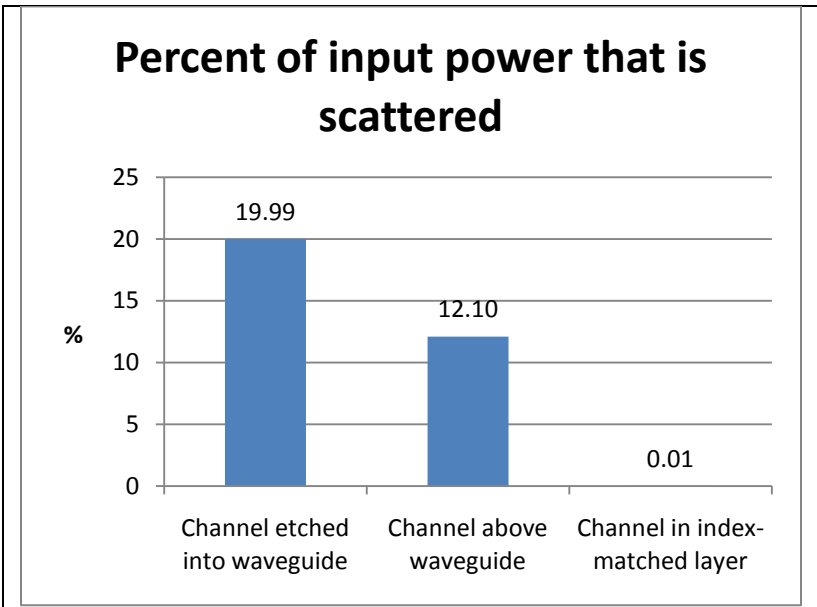


Figure 14: Simulation results showing the scattering resulting from three potential architectures. The results show that an channel in an index-matched layer produces much less scattering than a channel etched into the waveguide or a channel sitting in glass above the waveguide.

Finite-difference time domain (FDTD) simulations were performed to quantify the scattering in these three scenarios. The waveguide model that was developed was used, and a microfluidic channel was inserted in the three proposed configurations. Light that was scattered above and below was measured. The results are shown in Figure 14. This simulation was only performed in 2D, but would likely have similar results in 3D.

A polymer with index of refraction very close to that of water was found. This polymer is CYTOP. CYTOP is a fluoropolymer (like Teflon), and introduced new

challenges in fabrication. These challenges were mostly in bonding, which is where they are addressed in this thesis. The immediate benefits of using the index matched layer are demonstrated by the images of Figure 15. In (a), the channel is clearly visible, indicating that it is empty (filled with air, index of refraction ~ 1). In (b), the channel is filled with water ($n=1.33$, a match to the polymer $n=1.33$). In this case, the refractive index match is observed as the channel is difficult to differentiate from the polymer.

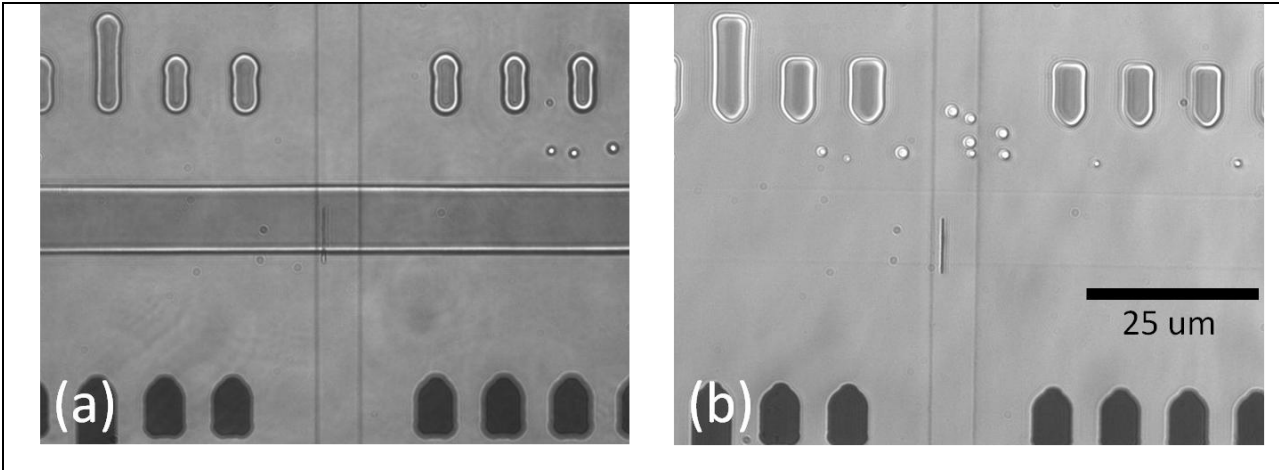


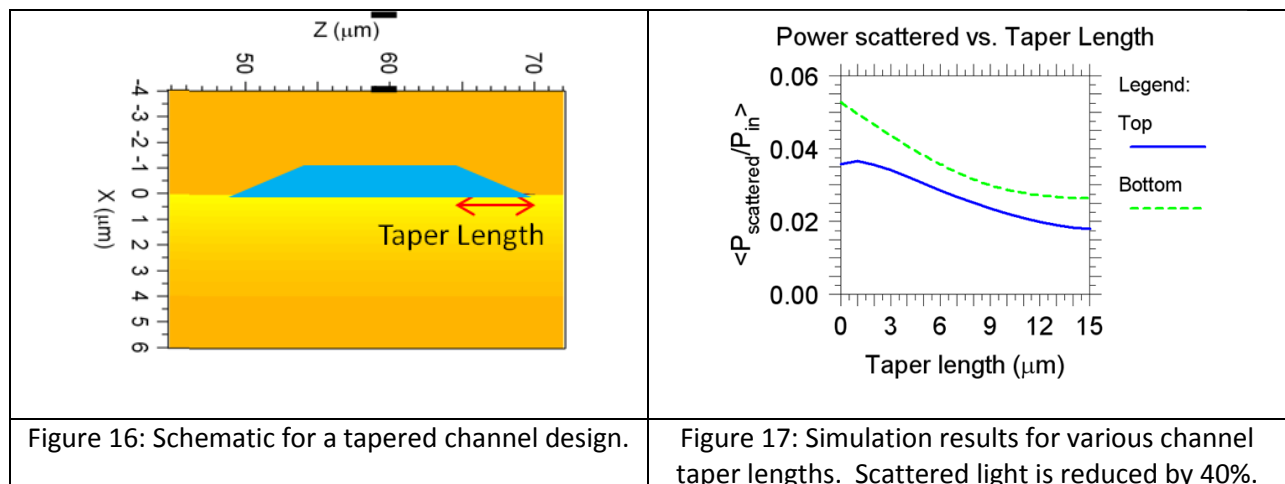
Figure 15: White light images showing a channel defined in the index-matched polymer layer. (a) channel without any fluid, showing the channel clearly. (b) when filled with fluid, the channel is difficult to differentiate from the rest of the region, indicating the good optical match.

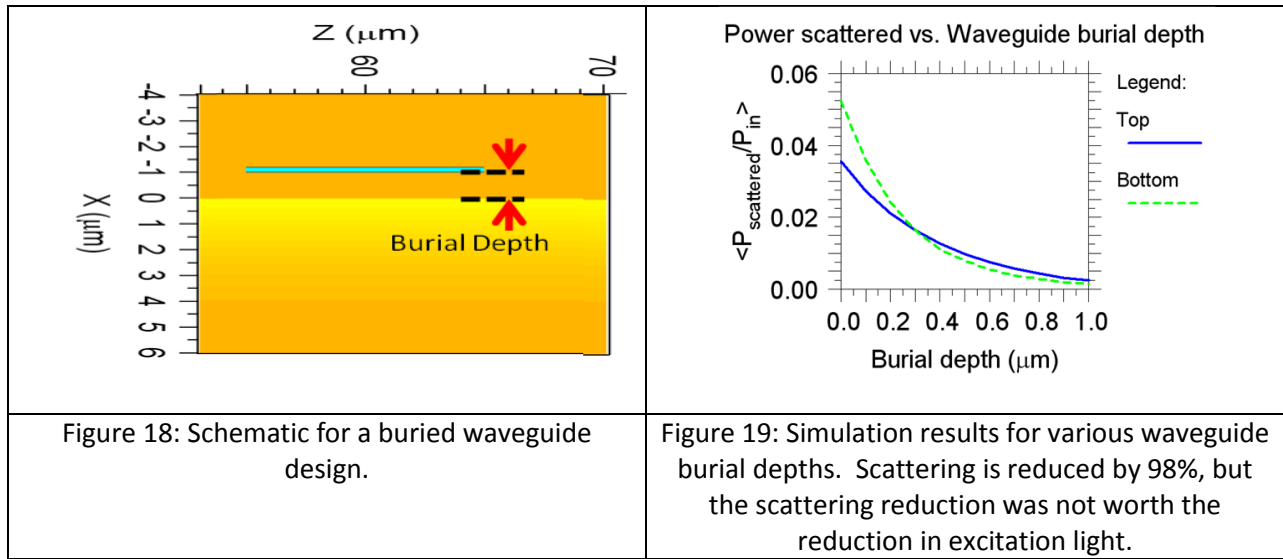
Other solutions

Other solutions were explored to reduce scattering that did not require a polymer layer. Tapering the sidewalls of the microfluidic channel and burying the waveguide.

By tapering the sidewalls of the microfluidic channel, it was hypothesized that scattering would be reduced as the average refractive index of the entire region would transition more slowly from 1.55 (glass) to 1.33 (water). This would be an improvement over the large, immediate index change presented by the microfluidic channel in other architectures. What this architecture would look like and the simulation results are shown in Figure 16 and Figure 17, below. While scattered power is reduced by around 40%, the results are not nearly good enough. Additionally, fabrication of channels with that shape would have been difficult. Processes were explored that would permit this – using grayscale lithography, for example, but it was determined that the small amount of benefit was not worth the effort, and furthermore, the index-matched layer surpassed the performance of this design.

Another potential solution to scattering from the microfluidic channel would be to bury the waveguide. By burying the waveguide, it is further away from the microfluidic channel, resulting in less light being in the region of the channel, and therefore less light scattered. This decrease in scattered light could be dramatic for small burial depths as the evanescent fields decay exponentially away from the waveguide. It was hypothesized that the plasmonic stripe could still couple to sufficient power in the evanescent fields, as it is a strongly resonant phenomenon. Simulations (Figure 18 and Figure 19) confirm that waveguide burial could result in a great reduction of scattering. However, due to the reduction of power available to the plasmonic resonator and the further process development that would occur, this design was not pursued. Furthermore, like all other designs, the performance of a buried waveguide was surpassed by the index-matched polymer layer.





An additional solution that could be comparable to the index-matched polymer layer would be to change the index of refraction of the fluid to more closely match that of glass. This would have a similar effect of reducing the scattering by matching the index at the channel / waveguide interface. However, to increase the index of a fluid to near 1.5, many chemicals would be needed to be added, probably interfering with the sample behavior. This could reduce scattering, but is not worth the cost of completely changing experimental parameters.

Scattered light from fiber optic connection

Another source of scattered light was the connection point between the incoming fiber optic and the device. While diffused waveguides provide a good index match for optical fibers, their shape is not the same, and therefore the match is not perfect. There is some scattered light at the connection that does not get collected by the waveguide. In the simplest design of the system proposed in this thesis, the waveguide is straight. This design has the shortcoming that any light scattered at the interface with the optical fiber is then propagating directly to the detection area, shown in the image of Figure 20 and the diagram of Figure 21.

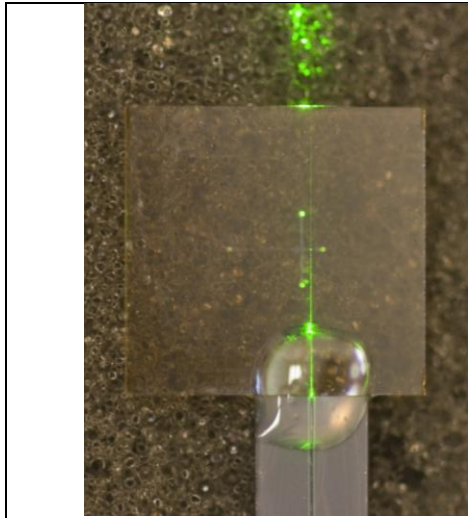


Figure 20: Laser light guided in completed chip with straight waveguide. Light scattered from connection point is visible.

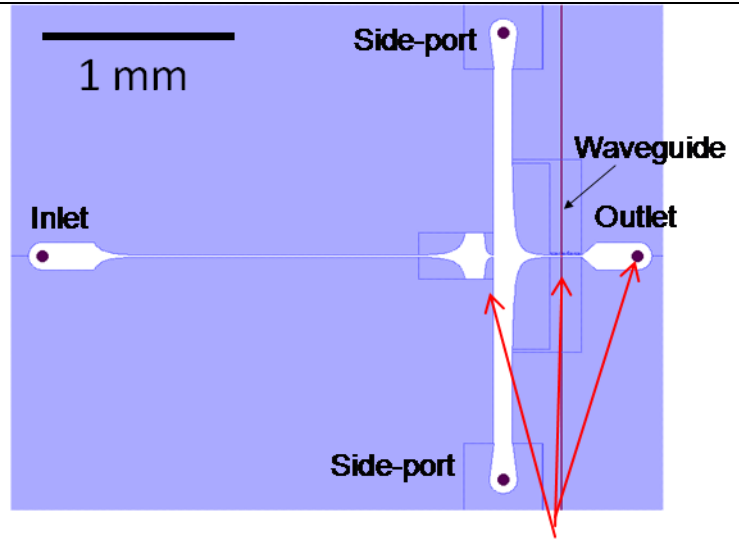


Figure 21: Diagram of straight waveguide design. Light scattered from fiber-waveguide connection scatters into detection zone.

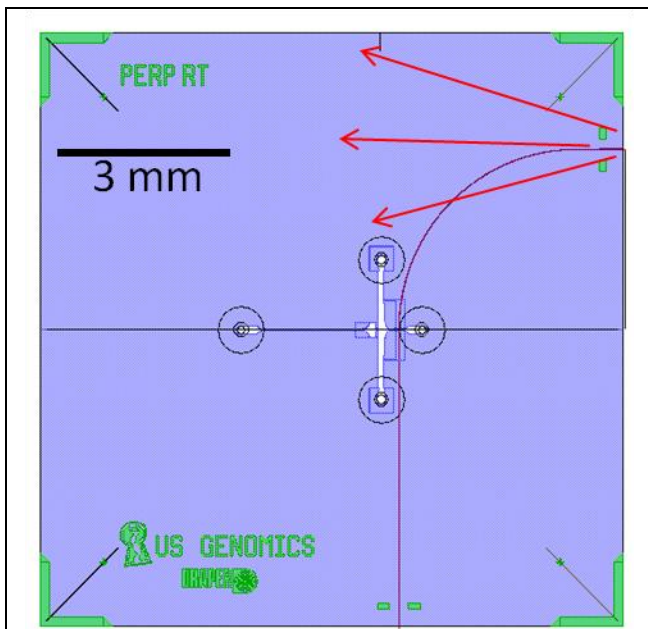
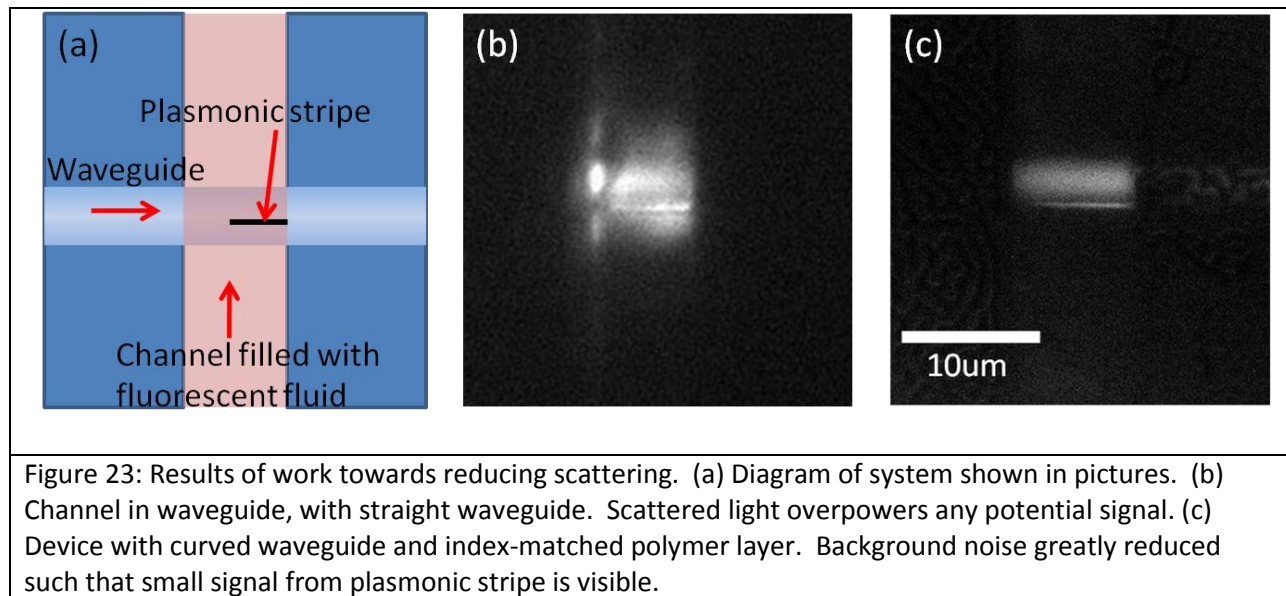


Figure 22: Diagram of curved waveguide design. Light scattered from fiber-waveguide connection avoids detection zone

To make this scattering benign, an improved design was created. In this design, the waveguide makes a 90° turn from the connection point to the detection zone. As a result, any light scattered at the connection will still be scattered forward, but the detection zone is out of the path of this light, as shown in Figure 22. To have a curve in the waveguide, an index difference higher than that achievable with K diffusion was required. Therefore, Ag diffusion was necessitated by the design including a curved waveguide.

Results

With the curved waveguide and index-matched layer, scattering in the interrogation area was greatly reduced, enabling much more precise imaging of samples. A diagram of the interrogation region is shown in Figure 23 (a) . In these experiments the channel is filled with fluorescent fluid, such that anywhere there is light will be observed as a bright spot. That Figure also shows results from a device with the channel etched into the glass substrate. Those results (part (b)) are similar to published results for integrated opto-fluidic detection devices(12)(13)(14). This device demonstrates a large amount of scattered light, which would decrease the ability to localize small discrete particles in that region of interest. In Figure 23 (c) , the device has an index-matched polymer layer and scattered light is reduced to a point where it is much less than other fields of interest. Specifically, in this diagram we are now able to observe fluorescence excited by evanescent fields above the waveguide. This demonstrates that there is very little scattering.



Conclusion

In this chapter, the work done to reduce scattered light was explored in depth. The integrated diffused waveguides were tested and a model of the refractive index profile was produced. This profile fits with the results in some of the literature, but disagrees with other sources. This result enables accurate simulation of the excitation properties for the simulations of plasmonic resonators. Additionally, different device architectures were explored and a design with an index-matched polymer layer and a curved waveguide was chosen as the one to achieve the minimum amount of scattering. Minimal scattering will enable more sensitive detection.

Further work can explore additional designs in scattering reduction, including focal plane masks to reduce the observed area. Additionally, alternative waveguide designs may be explored to achieve multiple excitation points, but will need to be optimized for minimal optical noise, as well.

Works Cited

1. *Integrated optical measurement system for fluorescence spectroscopy in microfluidic channels.* **Hubner, Jorg, et al.** 2001, Review of Scientific Instruments, Vol. 72, pp. 229-233.
2. *Planar-surface-waveguide evanescent-wave chemical sensors.* **Srivastava, Ramakant, Bao, Carmen and Gomez-Reino, Carlos.** 1996, Sensors and Actuators A, Vol. 51, pp. 165-171.
3. *RSoft CAD Environment 7.0.*
4. *Determination of ion-exchanged channel waveguide profile parameters by mode-index measurements.* **Weiss, Martin N. and Srivastava, Ramakant.** 1995, Applied Optics, Vol. 34, pp. 455-458.
5. *Fabrication of planar optical waveguides by K⁺ ion exchange in BK7 glass.* **Gortych, J.E. and Hall, D.G.** 1986, Optics Letters, Vol. 11, pp. 100-102.
6. *Effects of waveguide mode asymmetry on the laser diode-to-diffused waveguide coupling efficiency.* **Hall, D.G.** 1979, Applied Optics Letters, Vol. 18, pp. 3372-3374.
7. *Integrated optical waveguide examination using anti-Stokes fluorescence.* **Ostrowsky, D.B., Roy, A. M. and Sevin, J.** 1974, Applied Physics Letters, Vol. 24, pp. 553-554.
8. *Simple method of measuring propagation properties of integrated optical waveguides: an improvement.* **Okamura, Y., Sato, S. and Yamamoto, S.** 1985, Applied Optics, Vol. 24, pp. 57-60.
9. *Visualization method of modal interference in multipole interference structures.* **Blahut, M., et al.** 2002, Optics Communications, Vol. 214, pp. 47-53.

10. *Apertureless scanning near-field optical microscopy for ion exchange channel waveguide characterization.* **Blaize, S., et al.** 2003, *Journal of Microscopy*, Vol. 209, pp. 155-161.
11. *Microfluidic systems with on-line UV detection fabricated in photodefinable epoxy.* **Jackman, Rebecca J., et al.** 2001, *Journal of Micromechanics and Microengineering*, Vol. 11, pp. 263-269.
12. *Integrated microfluidic-microoptical systems fabricated by dry etching of soda-lime glass.* **Vieillard, Julien, et al.** 2008, *Microelectronic Engineering*, Vol. 85, pp. 465-469.
13. *Application of microfluidic chip with integrated optics for electrophoretic separations of proteins.* **Vieillard, Julien, et al.** 2007, *Journal of Chromatography B*, Vol. 845, pp. 218-225.
14. *A novel concept of the integrated fluorescence detection system and its application in a lab-on-a-chip microdevice.* **Mazurczyk, Radoslaw, et al.** 2006, *Sensors and Actuators B*, Vol. 118, pp. 11-19.

Chapter 3: Fabrication

Many fabrication processes include minor process steps that are required for the process to work, but are not published. Any effort to use a new procedure requires time wasted on trial and error to find these critical steps if they are not already known. While this thesis presents a finalized fabrication procedure, there are many alternative methods that could be used and lessons learned in exploring those options. This chapter provides the experiments and results performed for most of the process steps in this thesis, including the alternative methods that could be used and the results of those choices. The insights here may be helpful to others reading this thesis in creating devices in the future, whether they are making similar devices or just devices that share some similar process steps.

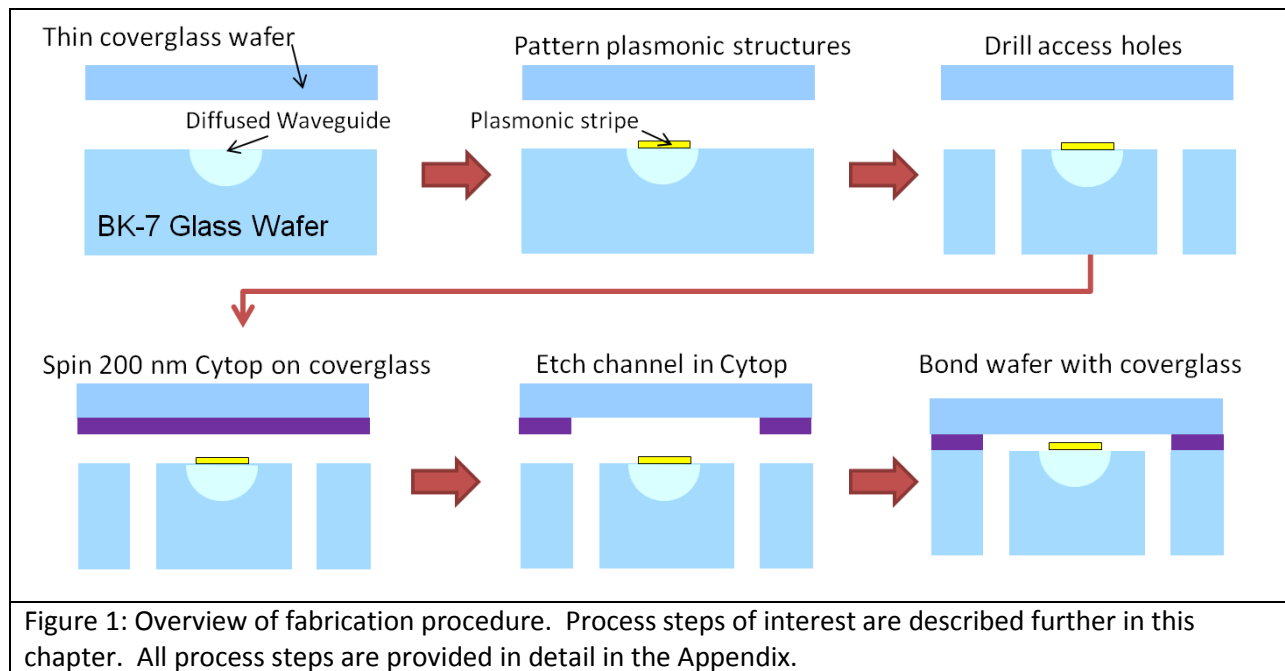
There was much work done for this thesis on wafer bonding; information on that work is presented in a separate chapter. The Appendix holds the detailed fabrication procedure.

FABRICATION PROCESS OVERVIEW	42
DIFFUSED WAVEGUIDES	43
BACKGROUND.....	44
ALIGNMENT MARKS	46
DIFFUSION BATH	47
MASK ISSUES IN $AgNO_3$ BATH	49
WAFER BOAT FOR DIFFUSION.....	53
CONCLUDING ISSUES FOR DIFFUSED WAVEGUIDES	54
E-BEAM FABRICATION	55
CHARGE DISSIPATION LAYER	55
ULTRASONIC DEVELOPING	57
HOLE DRILLING	59
COVERSLIP PROCESSING	62
ALTERNATIVE FABRICATION PROCEDURE	63
DEVICE FILLING	64
CONCLUSION	67
WORKS CITED	68

Fabrication process overview

The fabrication process that is presented in this thesis is the result of many process design choices. Many alternative fabrication procedures are possible, but this procedure provided the optimal tradeoffs in terms of design considerations. Specifically, the desired characteristics were: optical clarity and scattering minimization, low temperature, high bond strength, and process robustness. The procedure utilizes a polymer called Cytop both as a bonding layer and to define the microfluidic channels. The procedure is presented in Figure 1, below. A detailed description is provided in the Appendix.

The microfluidic chips are fabricated on 100 mm wafers of Schott BK-7 glass using mostly processes that are available in a standard MEMS fabrication facility. BK-7 glass was chosen as the substrate due to its high optical purity and strength, and availability of processes to diffuse high quality optical waveguides.



The starting BK-7 wafer (0.5 mm thick x 100 mm diameter) is cleaned with a sulfuric acid/hydrogen peroxide “Piranha” solution. A standard liftoff procedure is used to pattern 200 Å of Ta on the wafer for alignment marks (not shown in above figure of process flow). These marks are used for aligning subsequent photomask steps. Waveguides are next added to the wafer. This process is detailed in the following section on waveguides. After the waveguides are added, the plasmonic resonators are defined. This is accomplished by spinning on 200 nm of PMMA e-beam resist, then coating with

ESPACER 300 (Showa Denko), a conductive polymer, to prevent charging. The PMMA is exposed with an electron beam lithography tool (RAITH 150) at the Massachusetts Institute of Technology SEBL facility. The PMMA is developed in 2:1 MIBK:IPA and rinsed in IPA, after which 10nm of Cr and 100 nm of Au are deposited in an E-beam evaporation tool. After lifting off the Cr/Au, the plasmonic resonators are complete. Figure 2 is a SEM image for a completed plasmonic stripe. The wafers are then sent to have microfluidic access holes drilled in them. This is performed at the Draper machine shop using .75mm diameter diamond tipped drill bits (Tripple Ripple).

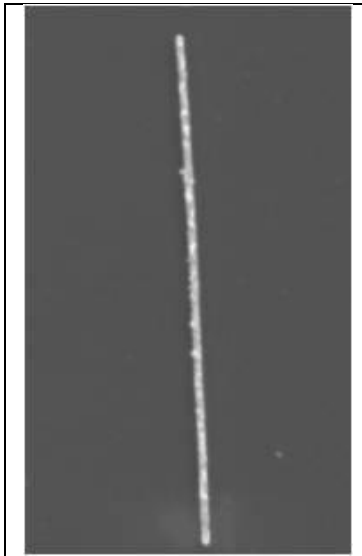


Figure 2: SEM image of plasmonic stripe. This Au stripe is 160nm wide x 100nm tall x 10 um long.

The top portion of the device consists of a thin glass coverslip and a polymer layer that both acts as a bond layer as well as the layer defining the microfluidic channels. The thin coverslip is used instead of a full thickness wafer to enable close proximity for high Numerical Aperture observation optics to the detection area. To fabricate this portion of the device, the polymer, CYTOP, is spun onto a thin BK-7 coverslip. Microfluidic channels are etched into the CYTOP layer using a photoresist mask and an oxygen plasma etch. The coverslip is bonded to the wafer with the waveguides, plasmonic stripes, and access holes with the voltage-assisted bond procedure described in the bonding chapter of this thesis.

After the wafer is bonded to the coverslip, the bonded pair is diced into chips. The sides of the chip that intersect the optical waveguide are optically polished and a fiber optic pigtail is attached with Norland UV curing adhesive. The chips are now ready to test.

The following sections explore some of the interesting experiments and observations from the development of the described fabrication procedure. It is hoped that the results shown can both be useful for the readers' own fabrication work as well as motivation for extending research.

Diffused Waveguides

Diffused waveguides are an established component of many optic devices. The flat surface and deterministic mode structure make them a very good choice for integrated microfluidic devices. However, the fabrication procedure can be difficult as the wafers are submerged in a very hot salt solution for a long period of time. Any incompatible materials will quickly damage the devices. Several experiments were performed to develop the most reliable and compatible waveguide diffusion process. We found that tantalum alignment marks will survive the diffusion process better the chromium. Also,

reusing a chemical bath after a long period of time will damage the wafers. We present our experiments and results in the hope that it will enable diffused waveguides to be easily integrated into more devices.

Background

For optical waveguiding, a high index core needs to be surrounded by a lower index cladding material. There are many technologies and material systems used to fabricate optical waveguides, including glass waveguides made by chemical vapor deposition (CVD), flame hydrolysis deposition (FHD), spin-on glasses, sol gels, ion implantation and ion exchange. In this work, we have chosen ion-exchange waveguides to integrate with our glass microfluidics.

In the ion-exchange process, a glass is immersed in a molten alkali salt bath, allowing ions from the bath to exchange with mobile ions in the glass. Often the glass ion is Na^+ as it not only has a high mobility, but also is found in many common soda lime and borosilicate glasses. When the ions exchange, a change in the glass refractive index can occur by two effects. When a smaller ion replaces a larger ion, the glass matrix can collapse around the smaller ion, with the increased index coming from an increase in density. Secondly, if the ion from the bath has a higher electronic polarizability, such as K^+ or Ag^+ compared to Na^+ , there is an increase in the refractive index. A very high level diagram of this process is shown in Figure 4.

The first ion-exchanged waveguides were reported in 1972 using a $\text{Tl}^+ - \text{Na}^+$ ion exchange (1). Subsequently, ion exchange waveguides have been formed using a wide variety of ions (2) (3). There are also several variations on the ion exchange process, including thermal exchange from a molten salt, field assisted exchange from a molten salt, field assisted burial and thermally annealing (4). For this work, we used both the $\text{K}^+ - \text{Na}^+$ ion exchange system and the $\text{Ag}^+ - \text{Na}^+$ system. The $\text{K}^+ - \text{Na}^+$ ion exchange system is known to produce low loss waveguides with an index change, Δn , comparable to optical fibers. This will be advantageous when trying to couple fibers to the waveguide. The small Δn , however, makes short radius curves subject to bending loss. The $\text{Ag}^+ - \text{Na}^+$ system has a greater Δn value, enabling curved waveguides. However, these waveguides are difficult to fabricate, as they Ag^+ ions tend to cluster, producing Ag depositions on the surface. Also, the Ag clusters throughout the waveguide fluoresce slightly when illuminated with light of wavelengths less than 532nm (5).

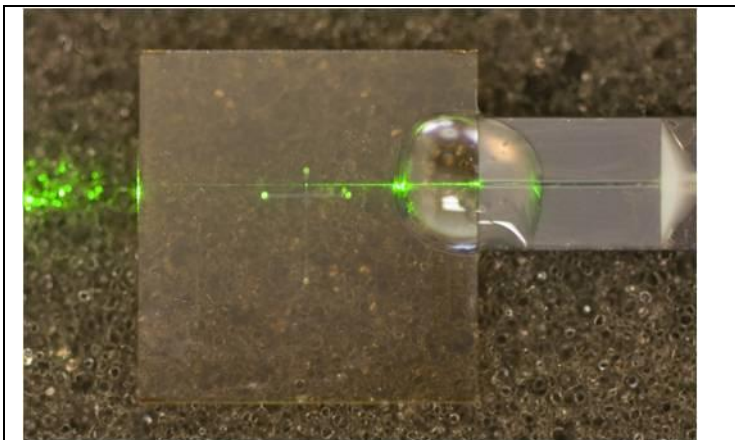
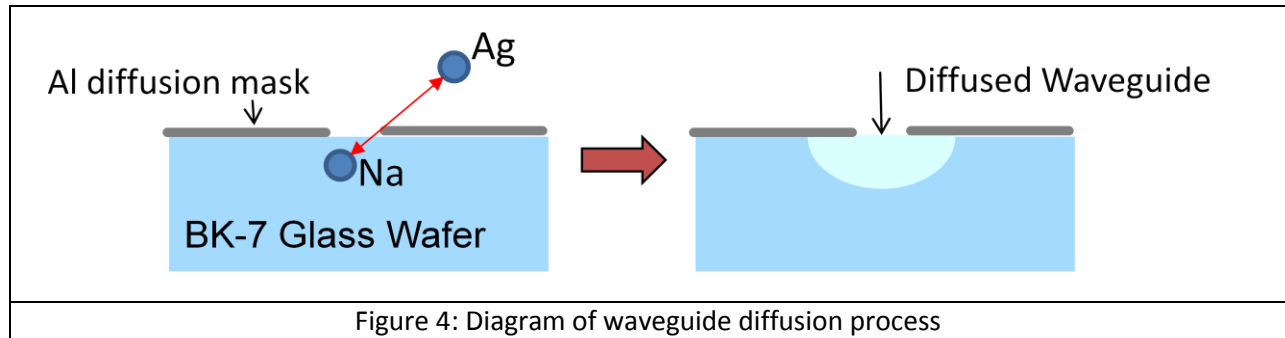


Figure 3: Completed chip with optical fiber attached via v-groove pigtail and optical adhesive. Green laser light is shown being guided to the chip and along the waveguide in the chip to emerge at the other end.



Ion exchanged waveguides were chosen for several reasons. Because the waveguides are diffused into the surface of a glass wafer, we are left with a flat substrate. This makes them an ideal choice on which to build microfluidic devices. The index changes achievable with ion exchanged waveguides make them relatively easy to integrate with fibers. In order to achieve very low loss fiber to waveguide coupling, the diffused ions would be forced below the glass surface, using an electrical field. If one could achieve a circular index profile with a radius and Δn matching a fiber, low loss coupling is achievable. Additionally, they have the advantage of needing minimal capital investment to produce low loss waveguides. Figure 3 shows an image of a completed chip with a fiber optic cable attached, demonstrating waveguiding behavior.

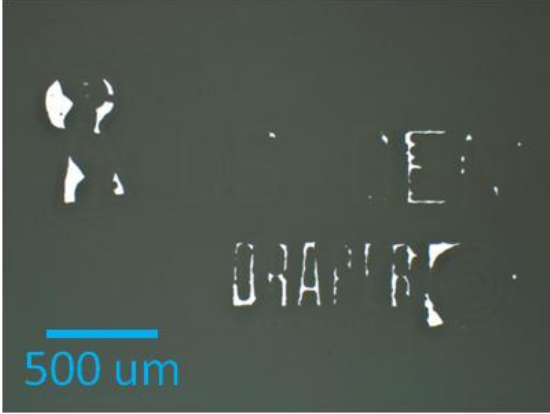

The K^+ - Na^+ and Ag^+ - Na^+ ion exchange in BK7 glass are well-known processes. We deposit and photolithographically pattern a 400\AA Al film on the wafers as a diffusion mask, leaving open the areas to be ion-exchanged. The glass wafer with the aluminum masking layer is submerged in a molten KNO_3 bath at around 355°C for 14 hours. The glass is then cleaned and stripped of the aluminum film. Alternatively, an $AgNO_3 / KNO_3$ salt bath (0.75% $AgNO_3$) at 355°C can be used for diffusion for 1 hour. Because Ag diffuses so readily into the glass, this process takes less time. Also, due to the higher polarizability of the Ag^+ ion, the resulting index difference for the waveguide is higher. This higher index change enables the possibility of curved waveguides. As both types of diffusion were explored, results from experiments done with each are presented here. The K^+ system was originally chosen, for the lack of fluorescence and resistance to further diffusion from high temperatures. However, the Ag^+ process was then used to enable curved waveguides, faster processing, and less wafer bow. The diffusion process for the K^+ diffusion induces stress in the wafer – as indicated by the anisotropy of the resulting index of refraction of the waveguides. This stress can cause wafer bow on the order of several microns (even with a metal protection on the back side of the wafer). Wafer bow is undesirable, as it changes the focal length for subsequent lithographic steps, reducing yield or resolution. Therefore, the Ag^+ diffusion procedure was chosen.

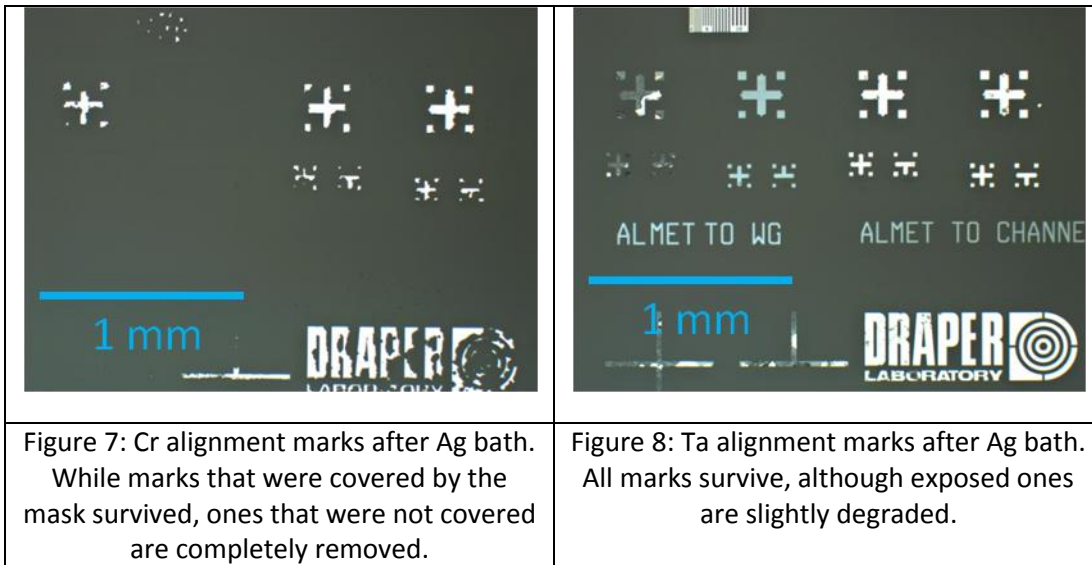
Alignment marks

In most fabrication processes, alignment marks are used to coordinate the location of all process layers. This is especially important in diffused waveguides, as they would be very difficult to locate without any markings. The finished waveguide only differs in index of refraction by less than 1% - very difficult to locate by eye and impossible to locate in an e-beam lithography tool.

Having alignment marks on the wafers before waveguide diffusion is therefore very useful, but can lead to difficulties in diffusion. Photolithography and the associated metal deposition and liftoff may leave trace materials on an otherwise clean wafer surface. Also, the metals used may react chemically with the diffusion bath – even when covered by a diffusion mask. Therefore, it is important to have a very robust metal as your alignment marks – so it can stand up to rigorous cleaning as well as the hazardous diffusion process.

We targeted two common metals that are known for their robust qualities: chromium and tantalum. We performed diffusion experiments using these two materials in a KNO_3 bath and found that tantalum was a much more robust metal through the waveguide diffusion, as shown in Figure 5 through Figure 8. Figure 5 and Figure 7 are images of a wafer with Cr alignment marks after the 14 hour K^+ diffusion bath. These images show that the Cr does not survive the bath very well. On the other hand, Ta shows much better survival, as shown in Figure 6 and Figure 8.

	
<p>Figure 5: Cr design after K^+ waveguide diffusion bath. This design was completely covered by the Al mask during diffusion, but still was degraded.</p>	<p>Figure 6: Ta design after K^+ waveguide diffusion. Much better survival than the Cr marks.</p>



Note that the majority of these features shown are protected by the Al mask when in the diffusion bath. The indication that these metals are still being attacked implies that there is some further chemical reactions occurring in the bath that should be explored further. These issues are addressed later in this chapter.

Diffusion Bath

After choosing the robust tantalum as alignment metal, some wafers still did not survive the diffusion process. The diffusion mask would come out with a milky white film on it, and were difficult to etch. It appeared that the Al mask had grown an oxide. Furthermore, in growing this oxide, Na ions had diffused through the mask into the wafer. Pieces that were covered by the mask were tested and showed waveguiding behavior. The mask had been compromised.

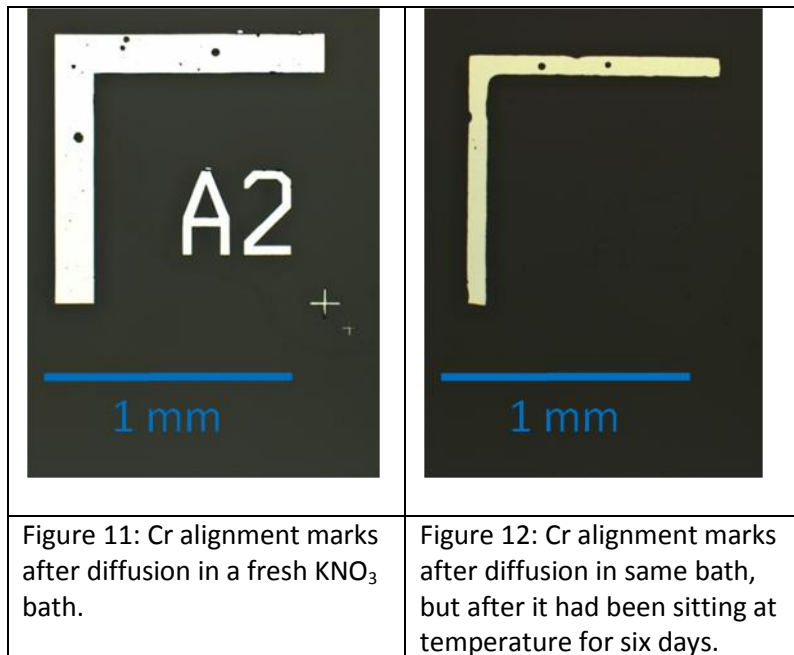
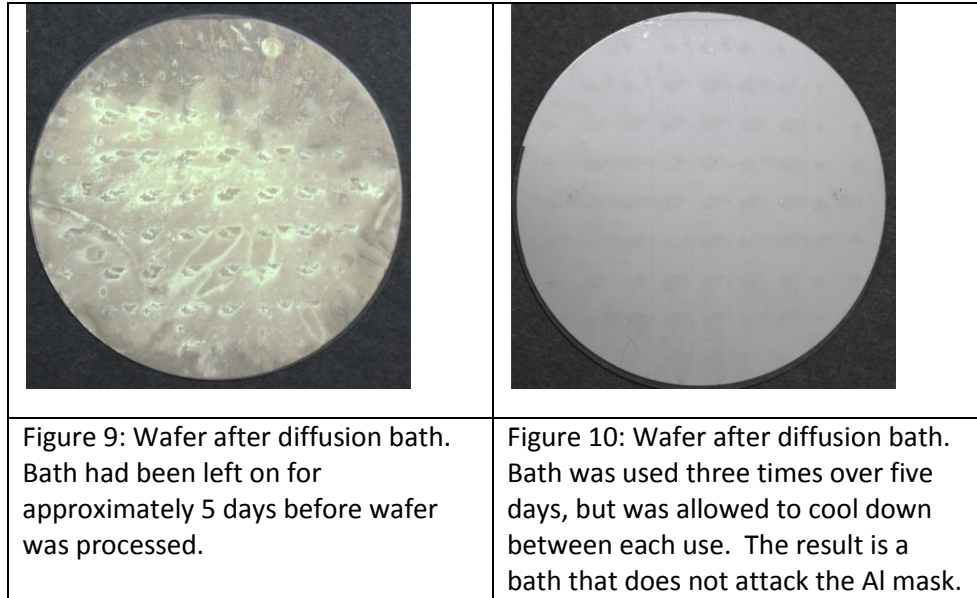
In another experiment, a bath that had successfully diffused wafers without attacking the mask was left at temperature for two days, after which more wafers were placed in the bath. This second batch of wafers, when placed in flowing water to remove salt buildups, had the entire Al mask disappear. The entire mask was compromised. However, other projects in the lab indicated that they had no such issues, even after the baths had been left at temperature for over a week. It appears that there is some difference occurring in our process. In those projects, there was no processing of the wafers before the Al diffusion mask was deposited. So, it appears that our problems may be coming from the earlier processing steps: either the Ta alignment marks are reacting with the Aluminum or the AgNO₃ bath, or there is some thin film of photoresist remaining on the surface of the wafer after liftoff that is compromising the Al mask.

To investigate this phenomenon, wafers were fabricated with different sets of preparation. One wafer had no processing other than depositing an Aluminum layer. Another wafer had the Al layer deposited,

and then lithography performed. A third wafer had all the processing as the other wafers that we had used: Ta alignment marks, Al mask and lithography on that mask.

Experimenting with different diffusion mask metals and cleaning procedures did not solve this

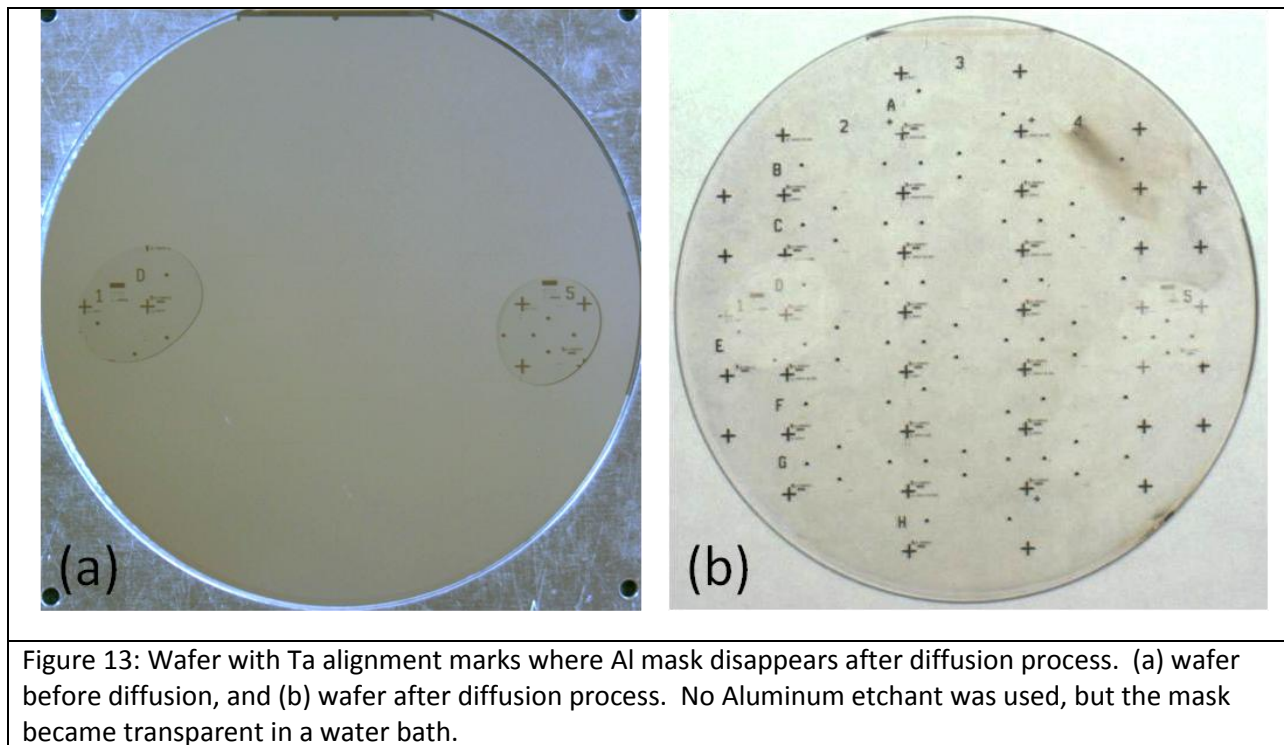
problem. It was found that reusing the diffusion bath was what was causing the detrimental effects. When diffusing multiple batches, common procedure may be to leave the solution at temperature for long periods of time. This is general practice in the field, as the high temperatures of the oven are thought to preclude any moisture forming or chemical composition changes. We found, however, that there is a change when leaving the solution at temperature for a long period of time (even two days make a difference). Wafers that were used for comparison are shown in Figure 9 and Figure 10. From these experiments, we have concluded that if there is to be time between diffusion runs (on the order of days), it was best to let the solution cool down between runs, reducing the time that the solution spends at temperature. This extends the lifetime off the solution.



To determine that it is beneficial to let the solution cool down, we had comparable wafer runs, in either a bath that had been left at temperature for the given amount of time or a solution that had been allowed to cool between each run. The results show that it is much better to let the solution cool down. Close up images of alignment mark feature survival are shown in Figure 11 and Figure 12.

Mask issues in AgNO_3 bath

When using the AgNO_3 bath and Ta alignment marks, initial wafers were very successful in waveguide diffusion. Wafers diffused two days later (with the bath kept at temperature in the interim) however, showed interesting behavior. Upon removal from the diffusion bath, the wafers and the Al diffusion mask appeared normal. However, when placed in a DI water bath to remove residual AgNO_3 from the wafers, the Al mask disappeared! What remained was a brown-tinted film, which could be rubbed off with a sponge, but the Al apparently was completely gone. An example wafer before diffusion and after the DI rinse is shown in Figure 13. This figure shows the almost complete removal of the Al mask without any Al etchant.



Initially, it was assumed that the mask had been compromised and that diffusion had occurred across the entire surface of the wafer, making it unusable. However, prism coupling tests showed that this was not the case. These test results are in Figure 14. These tests indicated that the area under the Al mask during diffusion showed no waveguiding behavior, so the mask was intact during diffusion and prevented ions from diffusing across the entire wafer. So, this was not a problem in our process. However, it was interesting to explore slightly further the cause of the disappearing Al mask.

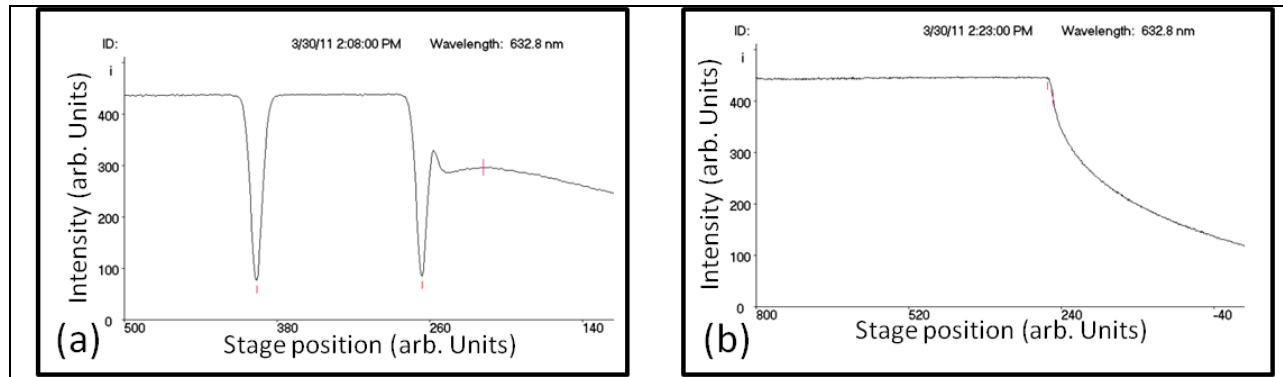


Figure 14: Prism coupling tests of two wafers. (a) Wafer that was diffused with no Al mask shows waveguiding behavior, as indicated by dips in the above plot. Two dips indicate two guided modes. (b) The prism coupling data from the wafer shown above where the Al mask disappeared after diffusion. No waveguiding is shown and the measured index of refraction matches that of pure BK7 glass, so it is concluded that the Al mask was not compromised, even if it suffered some chemical change and became transparent in the water bath.

The first test was to put clean wafers in the diffusion bath to see if the bath itself was attacking the Al mask, or if there was some sort of interaction caused by previous processing steps. These wafers (one with just an Al layer, one with an Al layer that was then patterned and etched) showed no irregular behavior. The mask survived diffusion. So, there must be something caused by the previous processing of the wafers that is resulting in the Al mask disappearing.

Prior to Al deposition for the diffusion mask, there is only one processing step: the creation of the Ta alignment marks. In this process step, there are two potential sources of some sort of interaction with the Al diffusion mask: 1) the spinning and removal of resist or some other processing step may leave a very thin layer of material that interacts with the Al, compromising its integrity, and 2) the metal used for the alignment marks may undergo some chemical or electrochemical reaction with the Al mask.

To test these possibilities, two wafers were prepared as shown in Figure 15. Each wafer would be broken into four pieces for a different test. With 8 pieces we can test three binary steps. Those steps would be: lithography, solvent bath, and metallization. One wafer would have resist spun and photolithography performed on it, the other would not. The wafer with the lithography was broken into pieces: first in half, and then one of the halves was broken into half again. The larger piece was placed in the metal sputtering tool and the bottom half of that piece was covered up – so as to deposit metal only on one half. Then one of the remaining quarters of the first wafers was also placed in the metal sputtering tool. The first half of the first wafer was not broken into half again to see if mere physical proximity or connection had any effect on the Al mask. It was possible that the Al mask would be compromised on the side with metal, but not the one without, or it was possible that it could be compromised on both sides, in either case, when combined with the results from the rest of the pieces; this experimental addition could yield interesting results.

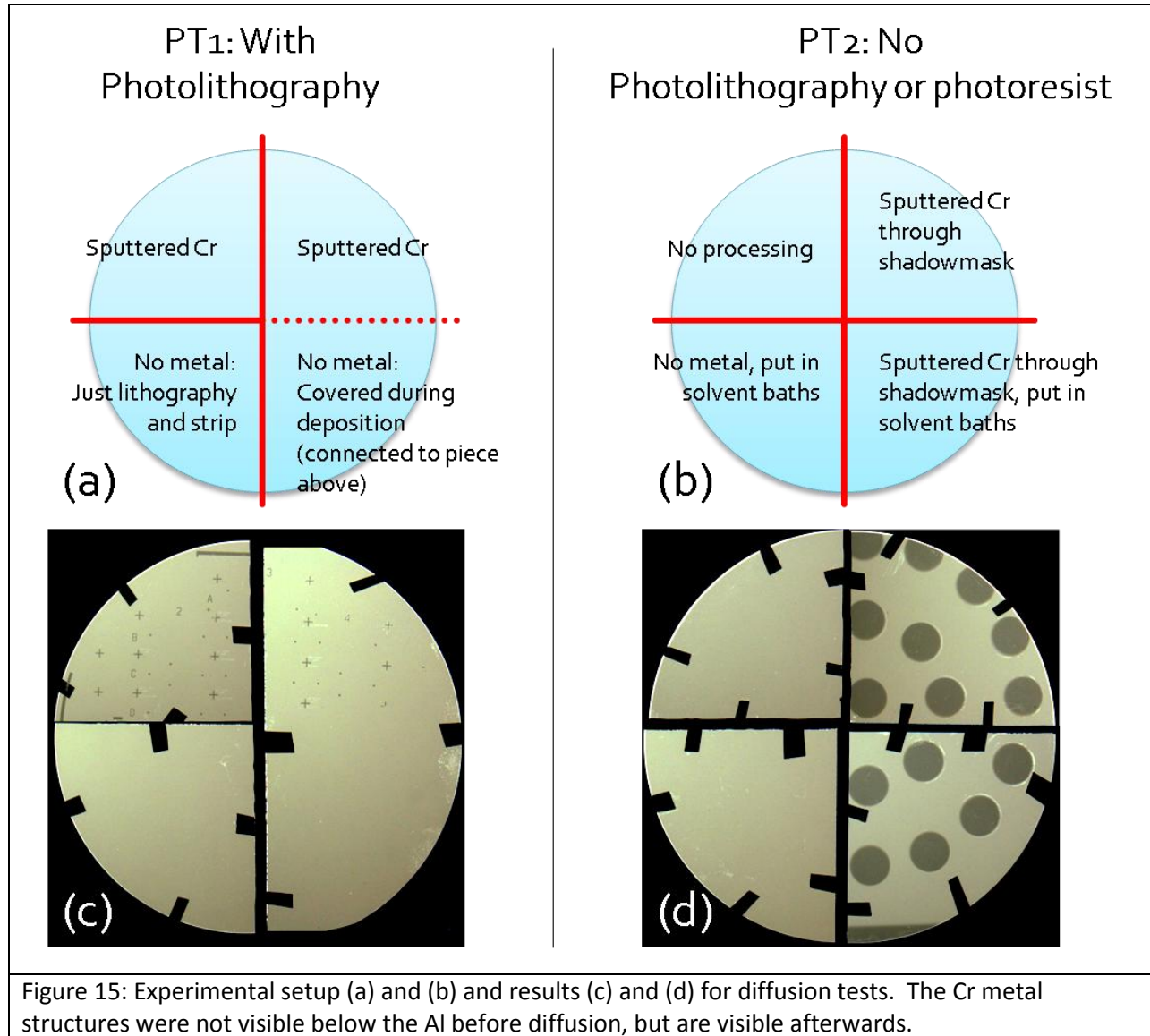


Figure 15: Experimental setup (a) and (b) and results (c) and (d) for diffusion tests. The Cr metal structures were not visible below the Al before diffusion, but are visible afterwards.

The second wafer was broken into quarters. Two of these quarters were placed in the metal sputtering tool with a metal shadow mask over them to produce a pattern of metal without having to deposit photoresist and perform lithography. The described steps would test for two variables: photolithography and metal. However, we wanted a third, as well – If putting in the common solvent baths left a residue that may interfere with the Al mask. This could not be completely independently tested, as any piece that had photolithography performed on it had to be placed in the solvents to strip the photoresist and liftoff the unwanted metal. However, the pieces without photoresist could be tested independently, with one having metal and one without going into the solvent baths (even though they did not need them) and two not. This left one piece with absolutely no processing before the deposition of the Al diffusion mask, and seven other pieces with various combinations of processing. A schematic showing the experimental setup for the wafers that was just described is shown below.

In these experiments, Ta was not available in the sputtering tool at the time the experiments were performed. As such Cr was used as a replacement. While these tests are therefore not exact replicas of

the final process, they still would provide a good answer indicating if the lithography or solvent bath is the cause of the changes in the Al mask.

Images of the resulting pieces (corresponding to the wafers divided as in the diagram next to them) are shown below. While the Al mask did not completely disappear, it did disappear above the Cr alignment marks. It also seems to have disappeared, or at least changed in some manner, also above the metal deposited on the wafers without lithography. The wafers with no metal, even those with lithography, showed no change in their Al mask.

Furthermore, at the edges of the areas where the alignment marks are showing through the Al mask, there is some sort of material debris or deposition. This material took the form of many small tower-like features that were around 5um tall. These towers appeared around the outline of all metal structures, both those that were defined via lithography as well as those that were defined via a shadow mask.

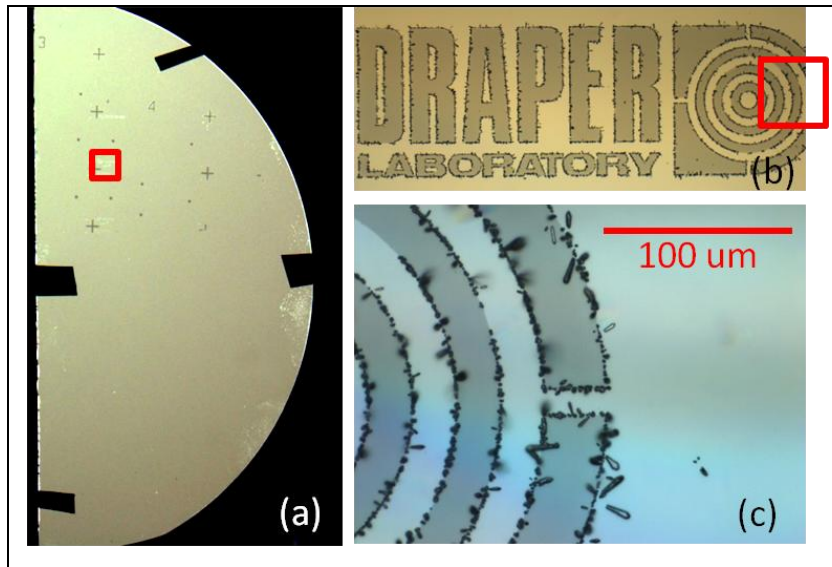


Figure 16: Series of images from diffusion test wafer PT1. (a) Image of the entire wafer piece. (b) enlargement of area boxed on a, showing some debris. (c) Further enlargement of boxed area in b, showing tower shape and size.

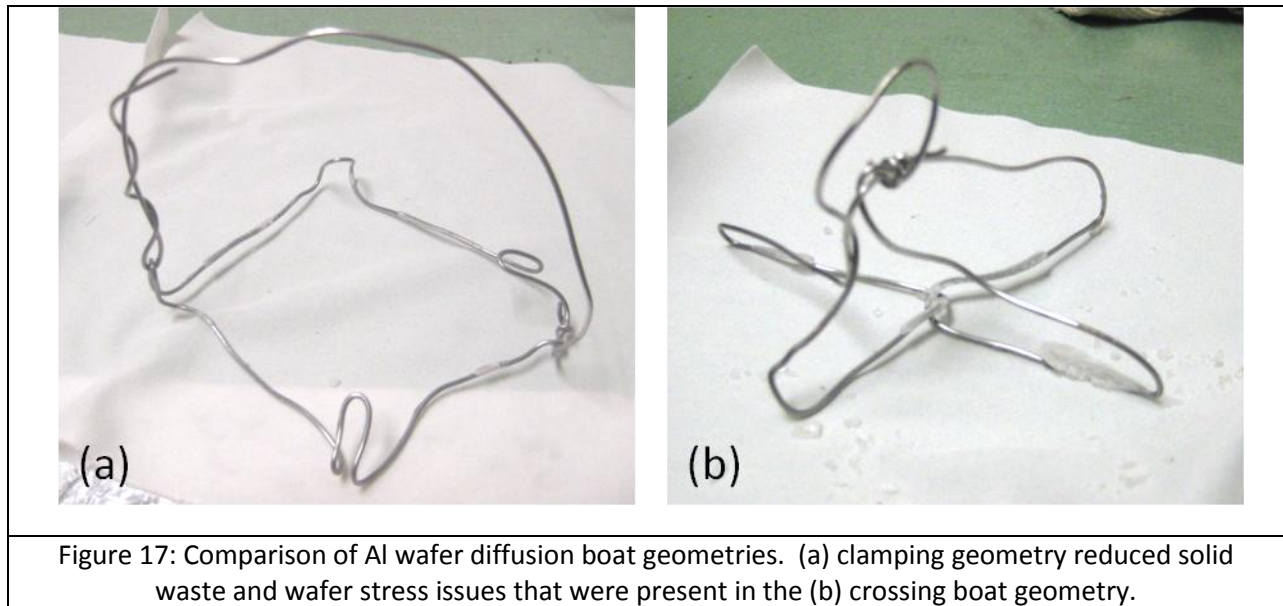
The intriguing results from these experiments are as follows: The Al mask is affected only by the presence of the alignment metal, not the result of other previous process steps. Also, the presence of the debris around the metalized areas is interesting. The images in Figure 16 show these results. Part (a) is from wafer PT1, with alignment metal on the top half and no metal on the bottom. The top half was the only region where the mask showed any degradation. And that degradation was only around the alignment marks. From these results, it appears

that the alignment metal is reacting with the Al mask in some manner. It is hypothesized that the Al mask is being oxidized, hence the transparent appearance. Furthermore, the material around the metal regions is most likely a byproduct of this reaction. The behavior where the entire mask disappears with Ta alignment marks is an interesting phenomena and probably due to the reaction being less limited or self-propagating with the Ta chemistry.

This behavior of the disappearing Al mask is not an issue with the fabrication procedure, as mentioned before, because the mask still functions properly in the diffusion bath and the wafer is only diffused where desired. Nevertheless, this is an interesting avenue for future research.

Wafer boat for diffusion

To enable introduction and removal of wafers from the diffusion bath, they are placed in individual wafer carriers. These wafer carriers are individually made by bending Al wire into an appropriate shape. These boats must have the proper shape to prevent wafer breaking. The clamping geometry was found to be much preferred to the crossing geometry.



Two potential boat geometries are shown above. They can be dubbed the “crossing” or “clamping geometries, as in Figure 17, above. The crossing geometry appeared to be the simplest to create and therefore was utilized at first. However, this geometry leads to a large amount of the diffusion bath solidifying on the boat. These solidified portions also adhere to the wafer sitting in this boat. As the wafer and the boat cool, they decrease in size at different rates, due to a coefficient of thermal expansion mismatch. Since they are coupled due to the solidified bath solution, there is a large amount of stress introduced to the wafer. This leads to wafers breaking, even if cooled down slowly.

Therefore, it was found that the “clamping” boat geometry is much preferred to the crossing geometry. The clamping geometry does not retain nearly as much of the diffusion solution and does not have lines that induce stress crossing through the entire diameter of the wafer. By only contacting the wafer at the corners, there is much less stress that can be imparted to the wafer, leading to less wafer breaking issues.

Concluding issues for diffused waveguides

Diffused waveguides are a good choice for our application. The lack of surface topography is beneficial to future steps for microfluidic encapsulation. Additionally, the index profile of the diffused waveguide produces a field maximum in the fundamental mode near the surface of the waveguide, which produces stronger coupling to a plasmonic resonator that is sitting on the surface of the waveguide. This is in comparison to symmetric waveguides, where the field maximum is generally at the center of the waveguide. Finally, the index profile of a diffused waveguide provides good matching to optical fibers, enabling more efficient coupling to external sources.

While a diffused waveguide architecture had many advantages, the drawback is that the diffusion process is not well controlled. Small changes in the bath over time can produce changes in the waveguide that will alter the modal behavior of the waveguide. This can be a large problem if a design would call for single mode behavior. Additionally, the low index contrast of the diffused waveguide necessitates a larger waveguide than can be achieved with other techniques. Finally, the small index difference also limits the radius of curvature for the waveguide, limiting design to avoid tight turns.

In this application, however, we are not interested in single mode behavior, tight turns, or small waveguides (as the field concentration is achieved with a plasmonic resonator). We do, however want to understand the index profile and the modes of the waveguide, as those parameters may have a strong effect on the behavior of the plasmonic resonator. As such, it was necessary to test the waveguides after fabrication and compare those results to a simulated waveguide to ensure that our model for excitation of the plasmonic resonator is accurate, leading to accurate results in frequencies of operation. This work is covered in the Optics chapter.

In conclusion, through our experiments, we found that:

- Tantalum is more robust to the waveguide diffusion process and it is detrimental to molten salt diffusion bath lifetime to leave it at temperature.
- The alignment metal can react with the Al mask and compromise the mask integrity.
- The “clamping” boat geometry is preferable to prevent wafer breaking.

E-beam fabrication

Ebeam fabrication is a popular fabrication technique for producing nano-scale structures. The process is much the same as standard lithography, but using a directed stream of electrons to expose the resist. By controlling the scan coils of a scanning electron microscope (SEM) to direct the electron beam, it is possible to write patterns with the beam. The resolution of this technique is limited by the ability to focus the beam (which is limited by the amount of current flowing, as electrons repel each other), vibrational noise, and the acceleration voltage that is used.

Two experiments were performed in electron beam writing: effective lifetime of the charge dissipation coating, and evaluation of ultrasonic development techniques.

Charge dissipation layer

When using an insulating sample (like glass and PMMA), charging becomes a significant issue. Electrons that are directed into the sample cannot find a path to ground due to the insulating nature of the sample. As such, they accumulate, charging the sample. When the sample is charged, it will repel or alter the path of the incoming electrons through electrostatic forces, leading to inaccurate beam location. Therefore, it is desired to find a manner to reduce charging of the insulating sample by providing a path to ground for incident electrons.

The method for reducing charging is usually to deposit a thin conductive coating on the top of the sample. This layer needs to be thin enough to not negatively impact the writing process, but conductive enough to provide a path to ground for the electrons once they reach the sample. Common tools are to sputter coat a thin film of Chrome / Gold, or just Chrome. Another option is to utilize spin-on conductive layers. These spin-on layers may be beneficial because they can easily be removed with a solvent, as opposed to requiring some sort of metal etching.

ESPACER (Showa Denko) is one of these types of spin-on conductive layers. It is removed with water. ESPACER has a listed lifetime of three months. To conserve resources, it may be desirable to determine the actual useful lifetime of this product. To accomplish this task, we tested two samples of ESPACER: one that had been expired for five months and another that had been expired for eight months. When putting these samples in a SEM and imaging for an extended period of time, no charging was observed, as seen in Figure 18. Therefore, it is possible to conclude that ESPACER can be used for at least 8 months after its expiration date.

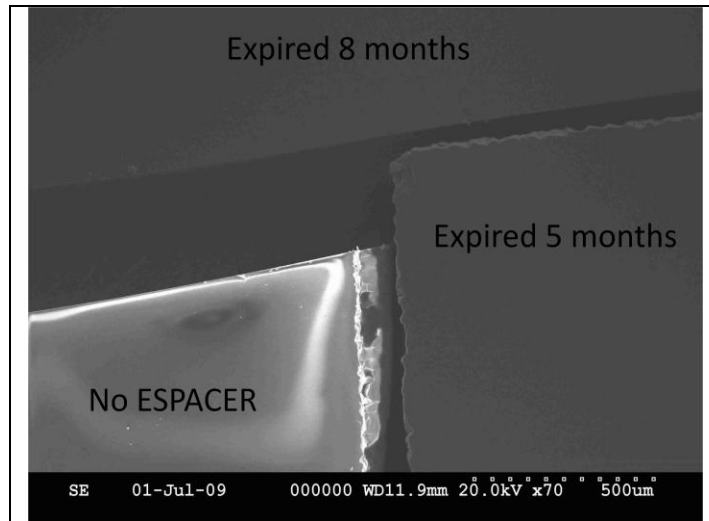


Figure 18: SEM image of three insulating samples with either no ESPACER, or coatings of ESPACER that have been expired. The ESPACER coated samples show no charging after 10 minutes, indicating that expired ESPACER still acts as an effective charge diffusion layer.

Future ebeam writes were performed with this expired ESPACER and the lithography appeared to suffer no ill effects.

Another difficulty in dealing with an insulating wafer coated with ESPACER is achieving a sufficiently accurate level of focus of the SEM tool. It is important to achieve a very tight focus, as this not only ensures that the entirety of beam energy is delivered reliably to the area of interest, but it also ensures the resolution of the written patterns. The beam energy is important when calculating the dose utilized for the resist. If the beam is out of focus, the measured beam current will not all be delivered to the same area, diluting the dose parameters that were calculated. The resolution is important as the entire point

of using e-beam writing is to get very small, well-size-controlled devices.

Focus is typically optimized by focusing on small Au colloid particles that are placed on the sample surface. The difficulty in using ESPACER arises due to the fact that this colloidal solution is suspended in water, which removes the ESPACER coating. As a result, it would be impossible to focus on any area with the gold colloidal solution, as it would charge up, making imaging impossible. To remedy this situation, a different conductive coating was placed on the wafers before the ESPACER. This coating was a sputtered Cr/Au film. The wafer had a shadow mask over it during the sputtering, covering the device area of the wafer, but exposing the remaining external ring. This provided a non-water-soluble coating around the outside area of the wafer, enabling Au colloid to be placed here and used to attain a high quality focus.

This additional coating, however, is not without drawbacks. The coating procedure, or the coating itself, somehow compromised the PMMA layer that it was placed on. The region where the coating was present, the PMMA would not lift off, leaving a Cr/Au layer around the outside of the wafer for the rest of the procedure. This layer did not negatively impact any subsequent process steps, but it is not desirable. Currently, even with up to one hour of ultrasonication in a solvent bath, it has not been possible to remove this material.

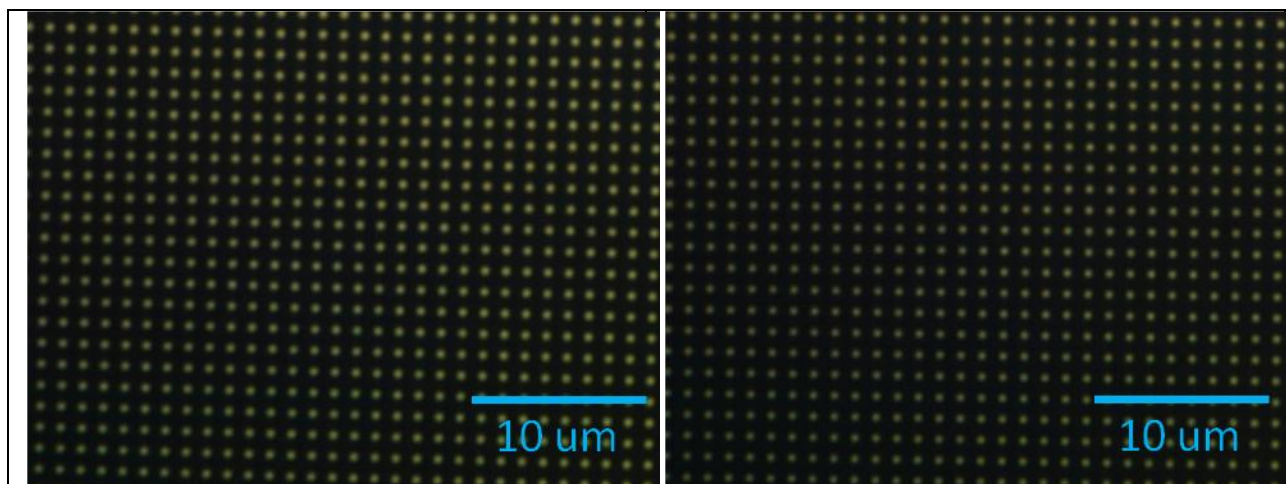


Figure 19: Initial ultrasonic development experiment using DUV lithography. This sample was developed without ultrasonic agitation.

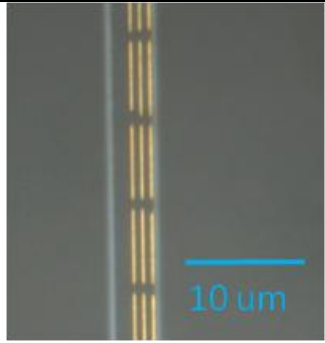
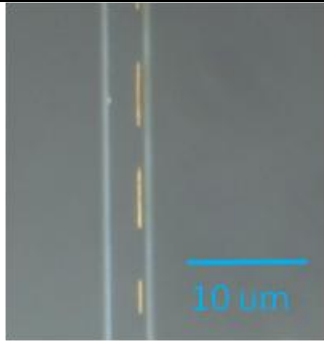
Figure 20: Initial ultrasonic development experiment using DUV lithography. This sample utilized ultrasonic agitation during development. Little difference is seen between the two samples.

Ultrasonic developing

It is common practice to develop ebeam-written PMMA in an MIBK/IPA mixture under ultrasonic agitation. When using this procedure, incredibly low yield was observed. The manner of agitation was explored to determine if manual agitation would achieve a better yield than ultrasonic agitation.

An initial experiment was done with a high resolution photolithographic mask that consisted of 30nm circles. The PMMA was exposed through this mask in a conformable contact deep-UV exposure device. Two separate samples were processed, one with manual agitation during development, one with ultrasonic agitation. The two samples seemed to be identical, shown in Figure 19 and Figure 20. Both produced very high yield. So, it was determined that the experiment should be performed with the ebeam written patterns.

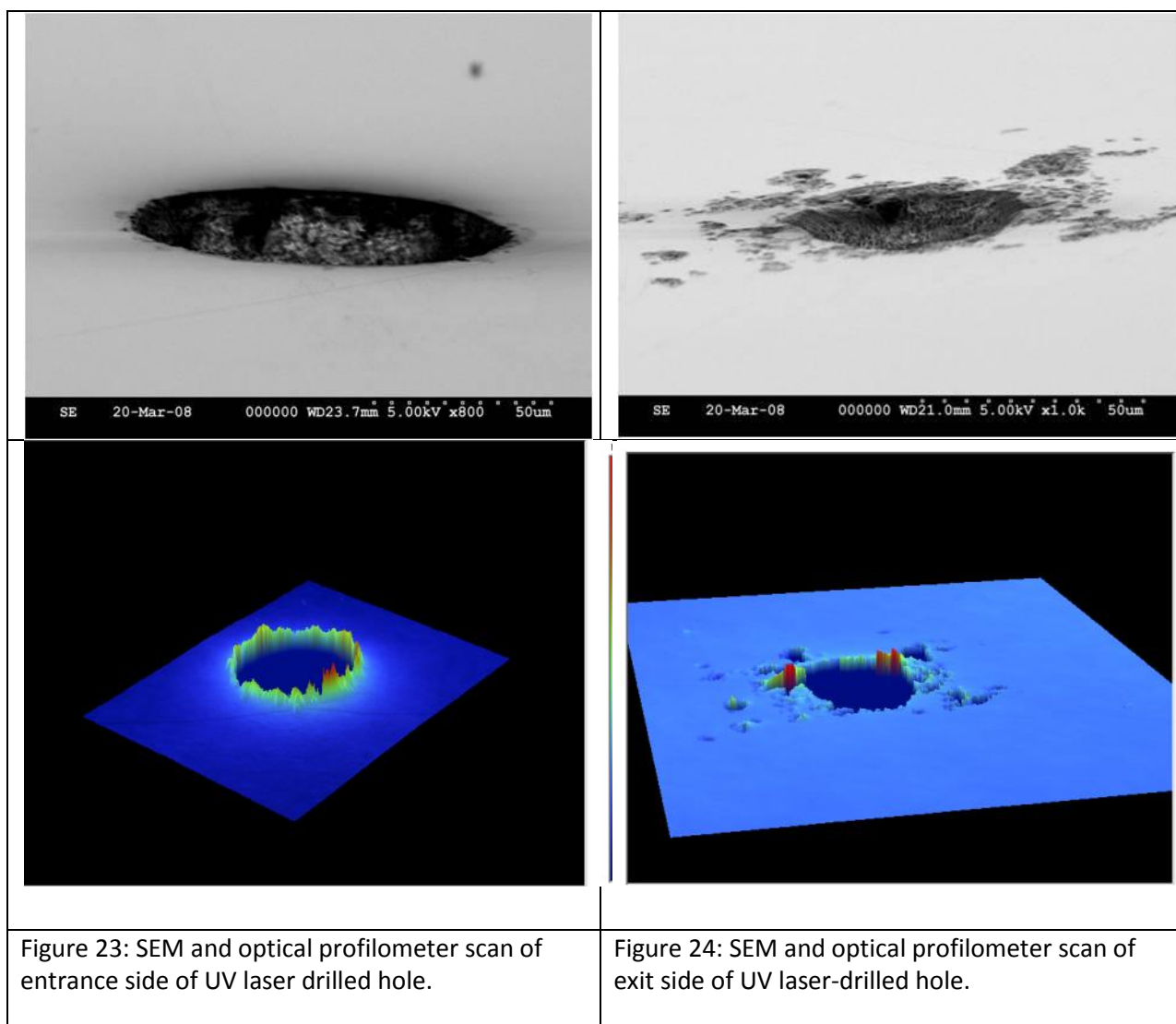
One wafer was written, and then divided into four pieces for experiments in development. Two of the pieces were used for exposure parameter optimization. The other two were used to compare agitation methods. The piece under manual agitation had almost perfect yield through the entire process (Figure 21), while the piece under ultrasonic agitation had no chips with a useful yield. Figure 22 is an image of one of the best regions of the chip developed with ultrasonic agitation. Most had lower device yield. While all patterns were observable after development, after metal deposition and liftoff, patterns that were developed with ultrasonic agitation were either completely missing or missing much of their features.

	
<p>Figure 21: Ebeam development experiment. This sample was developed without ultrasonic agitation. All the chips in this sample had approximately 100% yield for written stripes.</p>	<p>Figure 22: Ebeam development experiment. This sample was developed with ultrasonic agitation. Yield of this chip was at best 33%, and it is the best chip of the sample. Approximately 50% of the chips had around 0% yield.</p>

There are several possibilities why ultrasonic development does not result in viable features. First, it is possible that the exposure parameters that we used are merely optimized for manual agitation, and a higher exposure dose could lead to better features when developed with ultrasound. Another possibility is that the shape of our features, long bars, are not suited well to the ultrasonic development process. The long, narrow stripes may not support the ultrasonic pressure waves entering the developing area, reducing the efficacy of development. The reader is

encouraged to remember that ultrasonic agitation may not be the optimal development method for ebeam-written PMMA patterns, and should explore both development methods for the patterns used.

In summary, two experiments were performed to explore parameters pertaining to ebeam lithography that could be useful to other projects. It was found that ESPACER conductive coating can be used well after its published expiration date. Also, it was found that, for these structures, manual agitation is preferred to ultrasonic agitation during development of ebeam exposed structures. This effect may be design-dependent, and should be explored for each design.



Hole drilling

When producing microfluidic devices, much emphasis is put on how the channels are produced. There is another very important part to fluid handling in microfluidic devices: the access holes. There needs to be a pathway to move fluid in and out of the channels. While producing access holes may be a simple process for the common types of larger microfluidic channels in polymers, producing holes of much smaller dimensions in glass (a much harder material) can prove to be a more difficult project. A survey of several techniques for producing access holes was performed. We noted the size of holes possible with each technique, the amount and size of debris, and other process considerations for each procedure. The procedures explored were UV laser drilling, femtosecond laser drilling, ultrasonic milling, and diamond drilling. Each procedure has beneficial points; it is up to the process developers to determine the best method for their process. Examples of the images taken are shown in the figures

above. Figure 23 and Figure 24 are images of the entrance and exit side of a UV laser drilled hole, and Figure 26 is a SEM image of a fs-drilled hole. For our procedure, we have chosen diamond drilling.

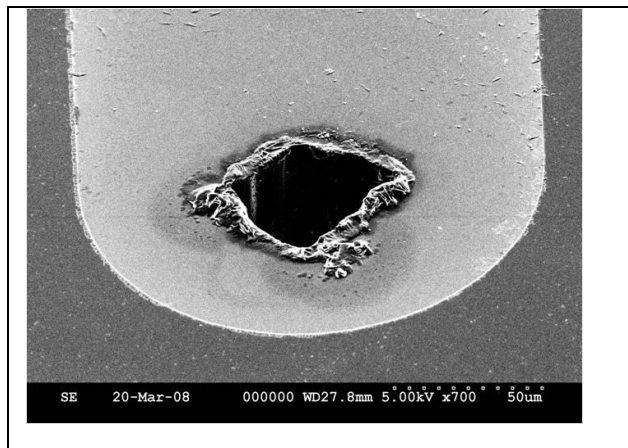


Figure 26: SEM image of femtosecond laser drilled hole at the inlet chamber of an etched microfluidic channel. It can be seen that the hole debris extends above the depth of the microfluidic channel.

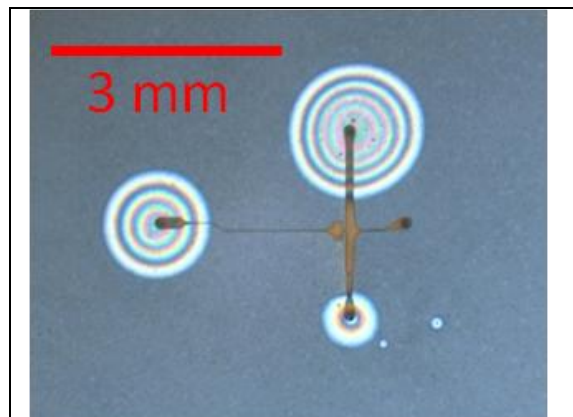


Figure 25: Optical image of a bonded microfluidic device. Debris surrounding the holes prevent complete bonding, compromising the integrity of the device.

When drilling into glass, it is common for some debris to be ejected from the hole on both the entrance as well as the exit side. In general, the entrance side has less debris. Debris is critical, as the vertical extent of the debris must be smaller than the thickness of the polymer bonding layer that is used. If the debris is too high, it will pierce through the entire depth of the polymer, and press against the coverslip, creating voids, as shown in Figure 25. For each drilling procedure the quality of the holes were observed optically. Additionally, an optical profilometer was utilized to obtain quantitative data regarding the dimensions of the holes and the debris surrounding them. A plot of the hole size and debris height is shown in Figure 27, below. Any solution with debris height under 200nm is a usable solution.

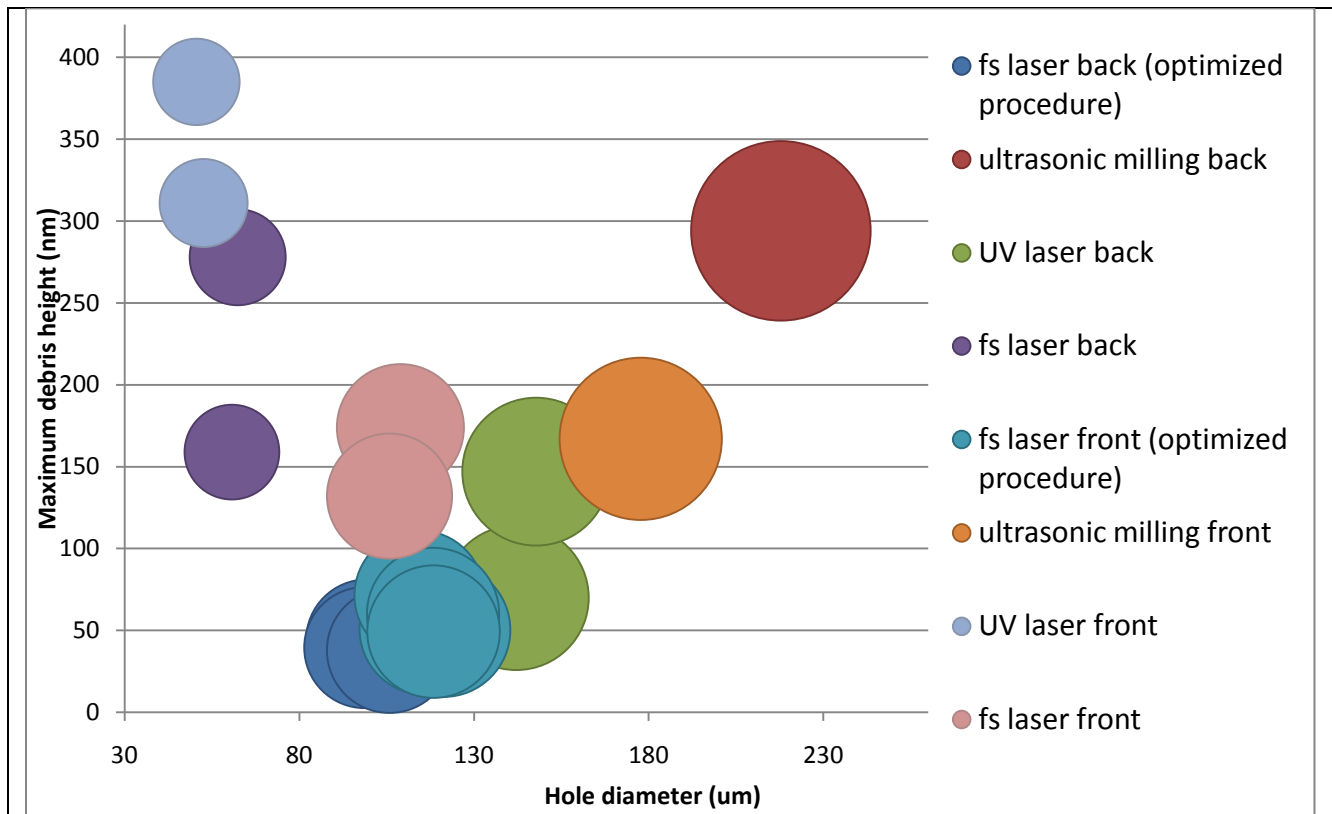


Figure 27: Comparison of hole drilling procedures, including hole diameter and debris height. The size of the circle indicates hole diameter.

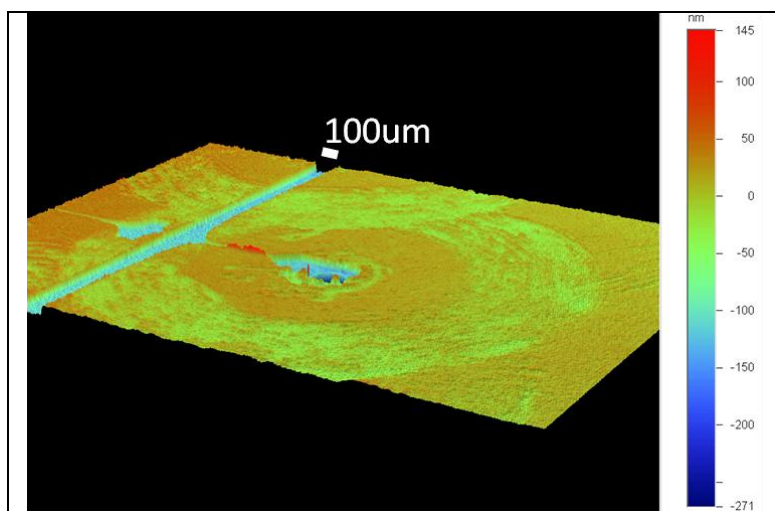


Figure 28: Optical profilometer scan of wafer that was drilled with a fs laser while an amorphous-Si coat was on the surface. Concentric rings of damage are shown.

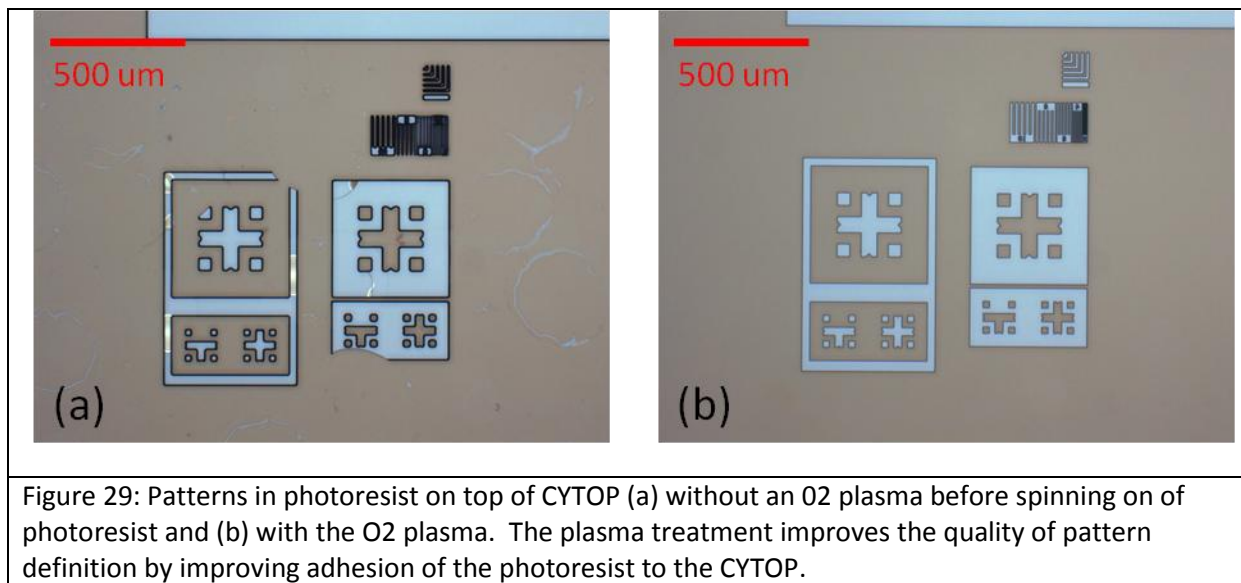
Some results bear recounting. Later in this chapter, an alternative fabrication process is described, utilizing an anodic-type bond with an amorphous Silicon layer as an ion diffusion barrier. In one incarnation of this procedure, the wafer sent out for femtosecond hole drilling had an amorphous silicon layer on it. This produced terrible results. Energy from the laser, most likely reflected from glass interfaces ended up interacting much more strongly with the amorphous silicon than the glass, producing concentric rings of damaged surfaces. An optical profilometer scan of a damaged area

is shown in Figure 28. The depth of this damage is typically around 100nm. Also, for a sense of scale, the wide channel running across the scan is 100um wide.

Coverslip Processing

The top portion of the microfluidic device consists of a thin glass coverslip. This coverslip is very much like a standard wafer, but half the thickness. It is desired to have a thin side of the device in order to allow detection optics to be very close to the detection zone. In our case we utilized a high numerical aperture (NA) lens, which has a very short focal distance, requiring proximity to the area of interest. For process considerations, it was desired to have the polymer that defines the channels on the coverslip. Therefore, it was required to perform some processing on the coverslip.

It was feared that it would be difficult to process this thin glass coverslip, but the pleasant surprise was that the vacuum chucks and other processing tools were gentle enough that it was possible to process the coverslip without the need for a backing wafer.



One process step of note that was developed was the need to perform a short oxygen plasma after spinning on the polymer and before spinning on the photoresist that would be used as an etch mask when determining the microfluidic channels. When lithography and development were performed without a preceding oxygen plasma, the structures were poorly defined. On the other hand, with an oxygen plasma before spinning on the photoresist, the features were well-defined. Examples of this

effect are shown in Figure 29. This is a useful tip for any process that desires to produce an etch mask on top of a polymer.

Alternative fabrication procedure

While one integrated fabrication process was chosen for the end result of this thesis, there are many other combinations of individual steps that could produce a viable, useful device that may be the best device for a different set of design considerations. Here, one different procedure is presented, with its benefits and drawbacks. This procedure produces a much stronger, more robust device, but with slightly worse optical properties and greater light scattering near the detection zone. This could be a useful device where such low noise is not required. The general process flow is demonstrated in Figure 30.

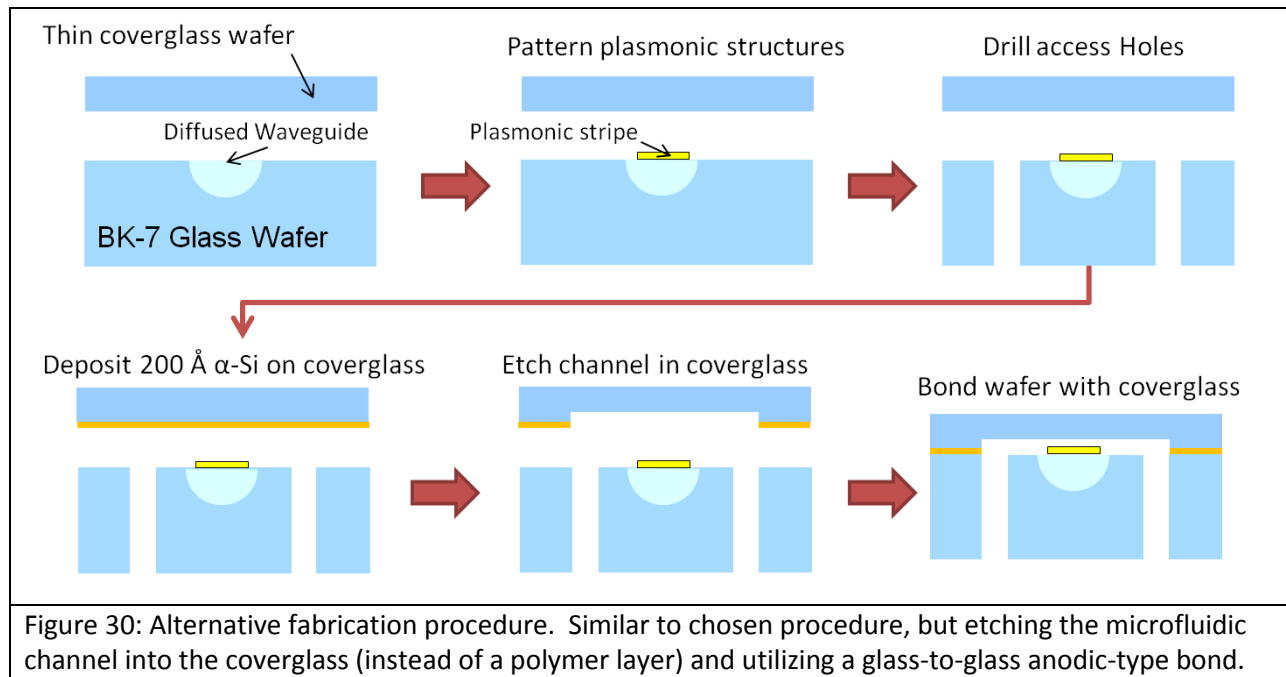


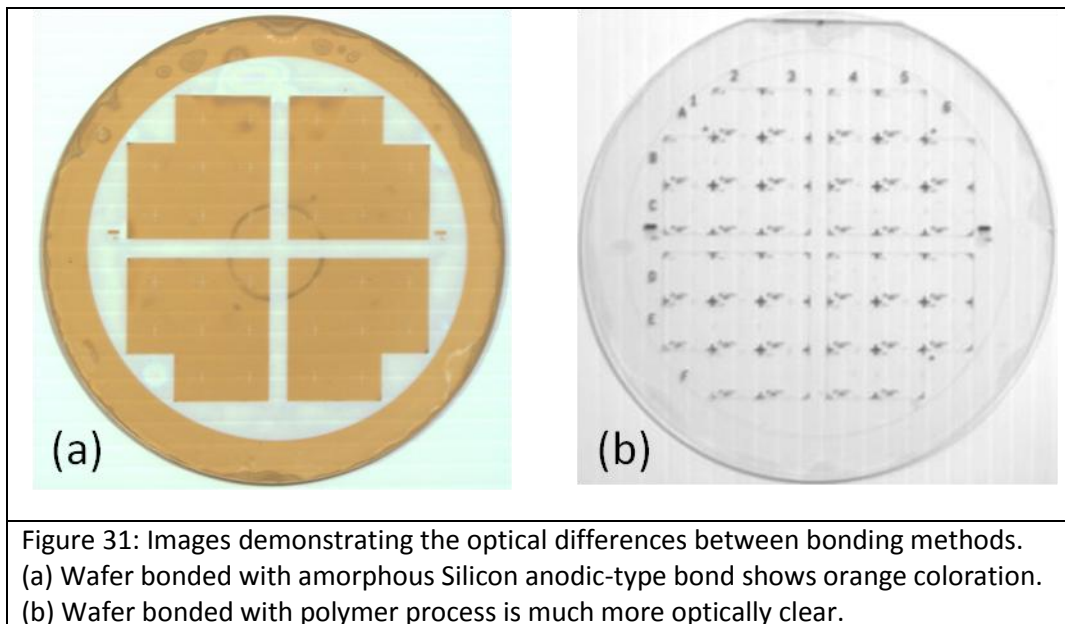
Figure 30: Alternative fabrication procedure. Similar to chosen procedure, but etching the microfluidic channel into the coverglass (instead of a polymer layer) and utilizing a glass-to-glass anodic-type bond.

The main difference in this procedure is that it uses the alternative, anodic-type bond procedure that is described in the bonding chapter of this thesis. Since there is no polymer layer, the microfluidic channels will be etched directly into one of the glass substrates (the coverslip or the wafer). Similarly to the chosen polymer bond procedure, it is desirable to define the microfluidic channels in the coverslip for this device. The other wafer has the waveguides and the holes. If we were to define the channels in that wafer, the channels would etch into the waveguides where the two patterns crossed. This would cause a lot of scattering. The scattering benefit of etching the channels was simulated in an FDTD program (as described in the optics chapter). It is seen that it is desirable to etch the channels into the coverslip.

While we are not etching into the waveguide, there is still a change in the index of refraction above the waveguide due to the presence of the microfluidic channel. This is the source of the scattering that does exist.

This process produces much more robust devices. There is no polymer involved in this procedure, hence very rigorous cleaning can be performed immediately before bonding, leading to better yield. Also, the anodic-type bond leads to stronger bonds. Additionally, because there is no polymer in the channels, there are very few restrictions on the type of fluids that can be processed in devices produced with this process.

While this process produces more robust devices, they are victim to greater scattering at the detection zone. Additionally, the amorphous Silicon leaves a slight yellow impurity at the bond, as indicated by the images comparing an a-Si bond with a polymer bond in Figure 31. So, if more robust devices are required and optical behavior is not as critical, this fabrication procedure is a very attractive alternative.



Device filling

Interfacing nano-channels with the macro-world can be a difficult task. Difficulties include device clogging, locating and connecting to the access holes, and forcing fluid through the channels. Forcing fluid into the channels can be very difficult, as hydraulic effects – the increase in applied force is proportional to the increase in fluid cross-section – are strongly prohibitive. To exert a force in the channel with a syringe of cross section 0.25 in^2 requires approximately $8 \cdot 10^7$ times as much force on the syringe. The relative sizes of the access holes and the fluidic channels are demonstrated in Figure 32. The access holes are also very small when compared to most fluidic tools in the macro-scale.

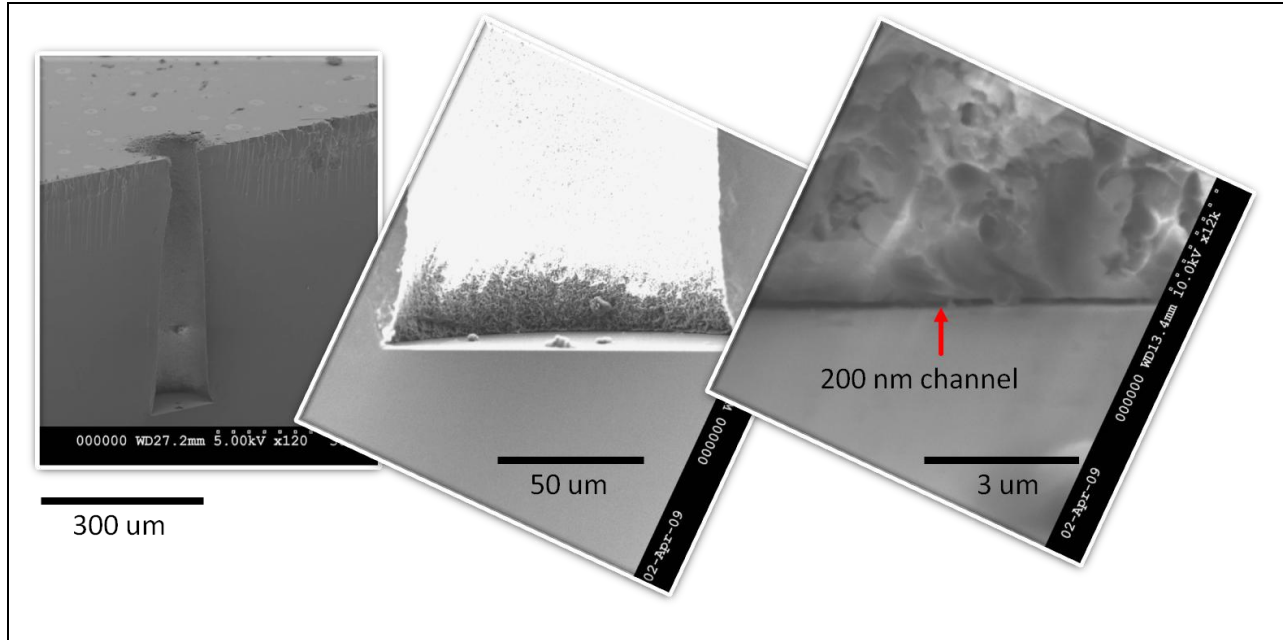


Figure 32: SEM images of laser drilled hole connecting to 200nm channel. These images demonstrate the small aspect ratio of the channels and the vast difference between the volume contained by the holes and that of the channels.

Additional difficulties in filling nanofluidic channels are surface effects. As with much nanotechnology, the surface-to-volume ratio of our channels is very high. Therefore, surface effects dominate fluid filling behavior. We first study what effects the surface properties of our channel will have on fluid behavior. Then, we can explore what requirements that puts on a fluid control system.

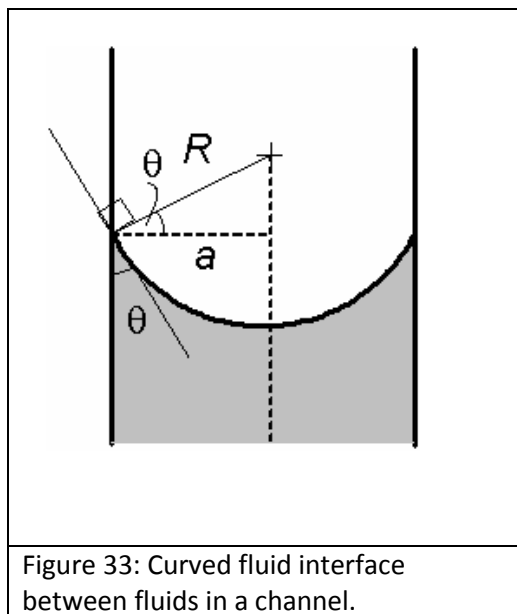


Figure 33: Curved fluid interface between fluids in a channel.

We can use the Young-Laplace equation to identify the pressure differential required to overcome the surface tension effects in a channel:

$$\Delta p = \gamma \left(\frac{1}{R_1} + \frac{1}{R_2} \right)$$

In the above equation, Δp is the pressure differential, γ is the fluid surface tension, and R_1, R_2 are shown in Figure 33. It can be seen that $R = \frac{a}{\cos \theta}$, meaning that values for R can range from a to infinity. The maximum values for Δp occur at $R=a$, so we can plug those values into the equation to generate bounds of our process. As the channels in these devices have an incredibly low aspect ratio, R_2 is

comparatively infinite, and this system operates as a narrow slit, as the $\frac{1}{R_2}$ term is relatively small.

Using the Young-Laplace equation to provide an indication of the pressures needed – depending on the contact angle of the fluid with your channel walls, it could require over 7 atmospheres of pressure to force fluid into the channel. This number was generated by assuming a 0° or 180° contact angle, which results in the strongest pressure differential requirement. Then, depending on your surface properties, the actual pressure needed will be between these numbers. However, these number are only the minimum required to achieve any motion of the fluid, to actually get considerable movement would require even greater pressure. As such, utilizing pressure-backed flow will require not only high pressures, but a system that can withstand them (including the manifold that connects to the device as well as the device itself).

For the device to survive the use of high pressures, the materials it is made of and the bond of the device must be strong enough. Our device is all glass, which is capable of withstanding the high pressures that will be achieved (also due to the small volume in the device). Much work was put into achieving high bond strength and that work is covered in the Bonding chapter. So, if we are able to introduce high pressures into the device, it should be able to handle them.

The other requirement for a high pressure system is a manifold that can introduce the high pressure fluid into the channels. To accomplish this, a manifold was fabricated out of polycarbonate, providing threaded holes to connect to high pressure lines and provide a reduction of size and connection to each port of the device. The manifold is attached to the chips very carefully via UV curing adhesive (Norland 64). This process is difficult, as the holes are very small and possible to clog, but a strong connection is needed to withstand the high pressures that will be introduced. The method of attachment utilizes capillary action to draw the adhesive into a small space between the manifold and the device. An image of a chip attached to a manifold is provided in Figure 34. The attachment process is generally as follows:

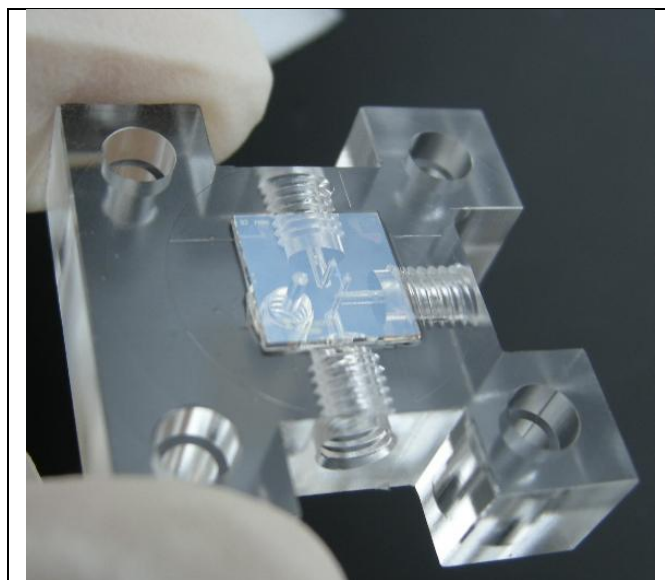


Figure 34: Polycarbonate fluidic manifold attached to chip. (Photo courtesy of US Genomics)

The workstation requirements are: a long working distance microscope, or high magnification camera with video monitor, pressure driven adhesive-dispensing system, and a UV light source. First the manifold was placed on two thin glass coverslips over the holes. It is possible to view the holes through the manifold, as it is very clear. When the manifold is in place, two small drops of adhesive are placed at the corners of the manifold and cured. Then the coverslips are taken away, leaving the manifold aligned

over the holes, but slightly above the surface. Then, to fill in the area between the manifold and the device (without filling in the holes!) small amounts of adhesive are introduced to one side of the gap. The adhesive is wicked into the gap via capillary forces. Adhesive is slowly added, until the entire gap is filled. As the adhesive wicks in, if it is added slowly enough, it will flow around the holes, leaving them unclogged, as there is no capillary force where there are holes. Adhesive is added to only one side of the gap, instead of at multiple places, to prevent the formulation of bubbles or grain boundaries between the multiple propagating fronts.

Once this manifold is attached, fluid is introduced into the device via a very thin syringe, by guiding the syringe through the holes in the manifold and placing a plug of fluid as close as possible to the entrance hole of the device. It is important to get as close as possible as the channel is so small that it takes a long time to flow through a significant volume of fluid, so if there is a significant amount of space between the fluid plug and the device, it may take a long time before that sample will even make it into the device. After the fluid plug is in place, pressurized air lines are connected to the manifold and set to the desired settings.

While this process was worked out and determined to be successful, it was determined that the difficulty of manifold attachment, cost of the manifold, and pressure required was not convenient to use. Therefore, capillary action was the most general method of fluid introduction (requiring some surface modification of the channel or choosing a buffer solution with lower surface tension). To enable this filling, a reservoir of fluid was placed above the inlet and outlet holes to provide the amount of fluid to constantly ensure fluid filling.

Conclusion

This thesis describes a device that contains many components. While many of the individual components and their associated fabrication processes are not novel, their integration is. This chapter presented a few process problems encountered in fabrication and their solutions in hopes that future work in the production of this type of device will be made more effective through the knowledge shared here. Additionally, future avenues of work can explore some of the interesting ideas that were only touched upon here.

Works Cited

1. *Optical waveguide formed by electrically induced migration of ions in glass plates.* **Izawa, T. and Nakagome, H.** 1972, Applied Physics Letters, Vol. 21, pp. 584-586.
2. *Glass waveguides by ion exchange: a review.* **Findakly, T.** 1985, Optical Engineering, Vol. 24, pp. 244-250.
3. *Ion-exchanged glass waveguides: a review.* **Ramaswamy, R. V.** 1988, Journal of Lightwave Technology, Vol. 6, pp. 984-1001.
4. *Recent Advances in ion exchanged glass waveguides and devices.* **Castro, J. and Geraghty, D.** 2006, Phys. Chem. Glasses: Eur. J. Glass Sci. Technol. B, Vol. 47, pp. 110-120.
5. *Fluorescence in ion exchanged BK7 glass slab waveguides and its use for scattering free loss measurements.* **Weisser, Michael, et al.** 1998, Optics Communications, Vol. 153, pp. 27-31.
6. **Tong, Q. and Gosele, U.** *Semiconductor wafer bonding: science and technology.* s.l. : John Wiley, 1998.
7. *A low-temperature bonding technique using spin-on fluorocarbon polymers to assemble microsystems.* **Oh, K. W., et al.** 2002, Journal of Micromechanics and Microengineering, Vol. 12, pp. 187-191.
8. *Fabrication of nanofluidic devices using glass-to-glass anodic bonding.* **Kutchoukov, V., et al.** 2004, Sensors and Actuators A, Vol. 114, pp. 521-527.
9. *Microfabrication design guidelines for glass micro- and nano-fluidic devices.* **Huber, D. and Pennathur, S.** 2008, Lab on a Chip.
10. *A Low Temperature Biochemically Compatible Bonding Technique Using Fluoropolymers for Biochemical Microfluidic Systems.* **Han, A., et al.** 2000. pp. 414-418.
11. *Fabrication of surface plasmon waveguides on thin CYTOP membranes.* **Fong, N., Berini, P. and Tait, R.N.** 2009, J. Vac. Sci. Technol. A, Vol. 27, pp. 614-619.
12. *Glass-to-glass anodic bonding with standard IC technology thin films as intermediate layers.* **Berthold, A., et al.** 2000, Sensors and Actuators A, Vol. 82, pp. 224-228.
13. **Wohltjen, H. and Giuliani, J. F.** *Method for bonding insulator to insulator.* 4452624 US, 1984.

Chapter 4: Wafer Bonding

Wafer bonding is an important component of many fabrication processes. In many applications, it is also necessary to maintain a low processing temperature to protect integrated waveguides, metallic components, nanostructures, or biological surface treatments that are present. Unfortunately, there are no low-temperature bond procedures that achieve sufficient strength for our requirements. Three low-temperature glass-to-glass bond procedures were explored: anodic-type, polymer, and voltage-assisted polymer. In this chapter, the procedures for each of these methods are explored and the process considerations that they present are indicated. Tests to determine bond strength were carried out and the corresponding procedures and results are presented. This work was considered to be of significant depth to warrant a separate chapter; hence it is separate from the previous chapter on fabrication.

It was found that the voltage-assisted polymer bond provides the ideal combination of bond strength and optical behavior for the applications explored in this thesis. Polymer bond (without voltage assistance) was shown to be a good choice to minimize optical noise, but did not achieve a very high bond strength. This procedure may be a beneficial choice for application where an applied voltage may damage the devices being fabricated. Glass-to-glass anodic-type bonding permitted rigorous cleaning and produced very strong bonds, but did not provide sufficient optical behavior. The bond surface was discolored and irregularly patterned, which would cause optical scattering – very undesirable in this application. Voltage-assisted polymer bonding provided a good optical behavior, combining a matched index of refraction with a uniform surface. Additionally, the voltage assistance reduced the size of voids in the bond area as well as improving the bulk bond strength.

These low-temperature bond procedures, especially the novel voltage-assisted polymer bond, enable new applications in integrated opto-fluidics, such as the ones explored in this thesis. Future work should explore the optimal parameters for different polymers and thicknesses of polymer and wafer. Additionally, an interesting avenue for other work would be further exploring the mechanism of bonding.

Background	71
Wafer bonding considerations.....	72
Bond Strength Testing.....	77
Other tests and observations.....	79
Glass-to-glass anodic-type bond	80
Background	80
Previous work and this work.....	81
Experiments and results	83
Summary	85
Polymer Bonding	86
Polymer bonding background.....	86
Process Development	87
Polymer bonding conclusion.....	91
Voltage-assisted polymer bonding	91
Experimental Methods	91
Results and Discussion	94
Conclusions	100
Works Cited.....	101

Background

As new fabrication processes are allowing for more functions to be integrated into microfluidic devices, a low temperature bond procedure for glass offers many advantages and opens up many new applications. Glass is beneficial for microfluidic devices due to its high optical clarity, biocompatibility, chemical resistance, and strength (1). Also, because many macro-scale experiments are carried out in glass, it is useful to be able to compare results from glass microfluidics to known data (1). A low temperature process is beneficial as it allows temperature-sensitive components to be integrated into devices (2) and allows for biological samples to be present in the channels before bonding, making these sorts of devices easier to fabricate. Also, surface modifications (3), diffused waveguides, microstructures, and nanochannels can be damaged by high temperatures. A low temperature bond procedure for glass will open many opportunities for new devices by enabling the inclusion of these technologies. In this work, we specifically focus on biomedical microfluidic applications, but the described process can be useful across a range of applications, as wafer bonding is an important process step for the fabrication of many types of devices, from MEMS to optoelectronics, as well as hermetic sealing or encapsulation of many other types of devices.

There are generally three methods to bond glass: anodic-type bonding, direct bonding, and bonding with an intermediate layer (4). Anodic bonding requires a thin intermediate layer to act as a diffusion barrier, sacrificing optical clarity (5) and requiring high temperature (6). Direct bonding can fall into two types: fusion, and low-temperature. Fusion bonding requires high temperatures to fuse the two pieces of glass together. Low temperature direct bonding requires a very clean and flat surface, limiting process steps available before bonding. Furthermore, low-temperature direct bonding usually cannot achieve a strong bond (7). The third method of glass-to-glass bonding, using an intermediate layer, is generally not as strong as anodic or fusion bonding, and can be limited by the choice of intermediate layer. Surface treatments are available that improve bond strength, but some, such as a solvent-assisted bonding (8)(9), would not be compatible with biological samples. Bond strength can also be increased by increasing the temperature during bonding (9)(10)(11) or simply applying a large amount of force (11)(12), but there is fear of the adhesive clogging whatever channels have been fabricated (11)(13). Low temperature polymer bonds have been demonstrated to be a beneficial process, enabling selective bonding, planarizing a wafer surface, and enabling substrate alignment (14). A low temperature polymer bond process for glass that can achieve high bond strength and maximize yield would be a very attractive alternative to other bonding procedures, while enabling new technologies.

In this chapter, we explore three methods of low-temperature glass-to-glass bonding: low-temperature anodic-type bonding, polymer bonding, and voltage-assisted polymer bonding. First, however, information on general considerations for wafer bonding are covered, as well as the methods by which bond strength can be measured and quantified.

Wafer bonding considerations

In general, all materials can be directly bonded to each other, providing they are clean and flat enough (15). This attraction can primarily occur due to van der Waals forces or Hydrogen bonding. This bonding is not very strong, and is reversible. Water placed near the bond interface can wick in and cause delamination to wafers bonded in this manner. In general, heating a surface will increase the energy of adhesion due to the removal of water at the interface at around 200°C and going up to actually melting and fusing the materials up at their melting temperature. However, we are interested at low-temperature bonding. The three general bonding considerations that are described here are important for all bonding procedures: Cleanliness, flatness, and bubble formation. Cleanliness and flatness are important to ensure intimate contact of the bonded materials and necessary for a strong wafer bond. Bubble formation is a bond failure that can be the result of many different factors, and the considerations for reducing bubble formation is presented, as it is also important in all bonding procedures.

Cleanliness

Cleanliness is perhaps the most important consideration in achieving high bond strength (second to choosing the proper the bond procedure, in general). Due to the importance of wafer cleanliness, it is desirable to clean wafers immediately prior to bonding and that both the cleaning and bond procedures are carried out in a clean environment.

Wafer bonds are weakened by contamination. Generally speaking, there are three kinds of contamination to be considered (15): particle contamination, organic contamination, and ionic contamination. After introducing these three types of contamination and their effects, methods of cleaning will be presented and their benefits.

Particle contamination refers to small pieces of material that physically separate the bonding interfaces. These particles can be from many sources, typically hair, dust, or fibers from clothes or paper. When they are at the surface of a wafer, they prevent intimate contact between the bonding surfaces, and can result in a debonded area much larger than the particle itself. This behavior is shown in Figure 1 below. The best sign of particle contamination is the presence of many isolated, unbounded areas throughout the wafer.

Where particle contamination leads to isolated voids, organic contamination leads to decreased bond strength across the entire wafer. Organic contamination is produced from hydrocarbons in the air or plasticizers from a plastic sample container. These contaminants deposit as single molecules across the surface of the wafer. While they are not large enough to cause voids at the bonded interface due to mechanical separation, they have two detrimental effects. First, these contaminants can serve as nucleation sites for bubbles (a consideration that will be discussed later). The second issue with organic contamination is that they adhere weakly to the substrate. Therefore, when a sample is bonded to the substrate, it is actually bonding to the organic contaminant. Since this contaminant is weakly bonded,

the resulting bond strength is greatly diminished. The indicators of organic contamination are either bubbles at the bonding interface or a generally weak bond.

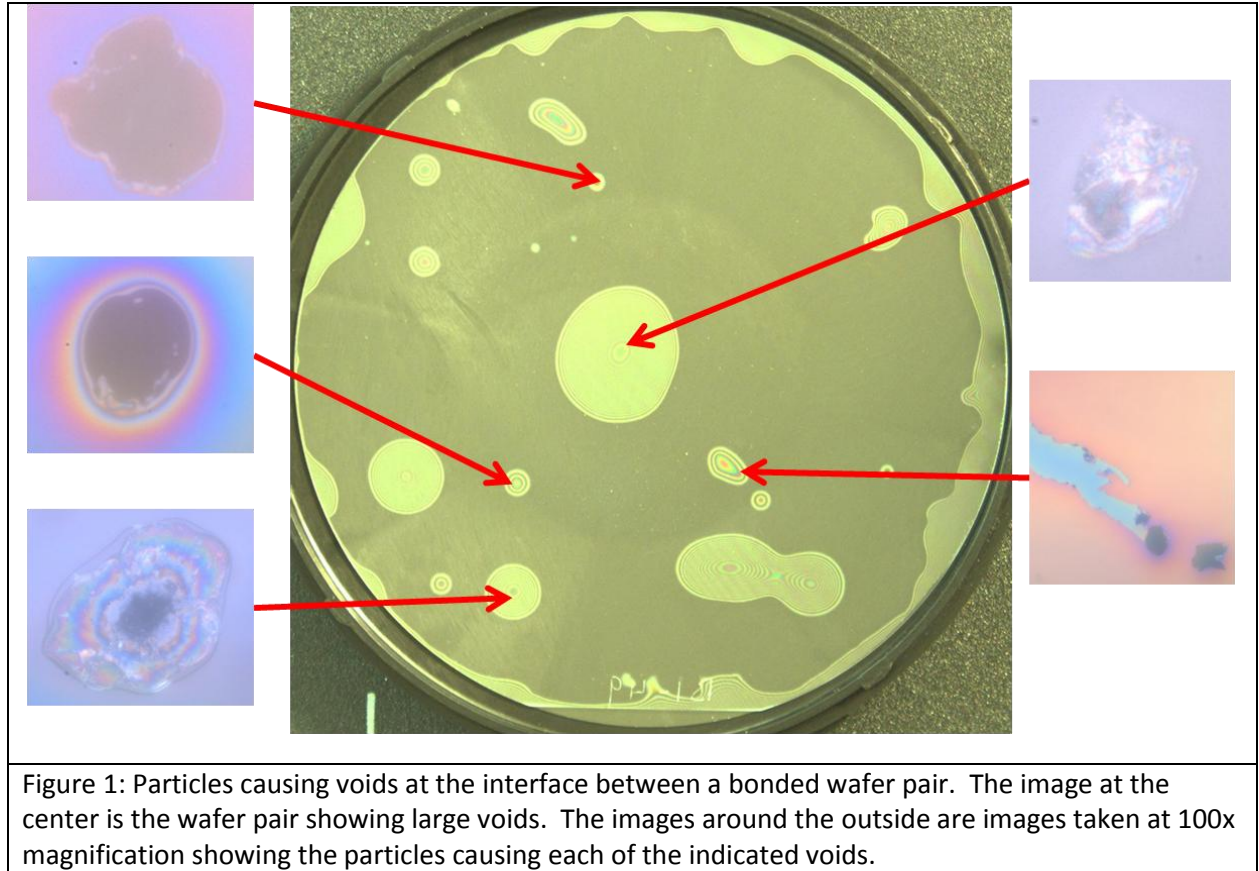


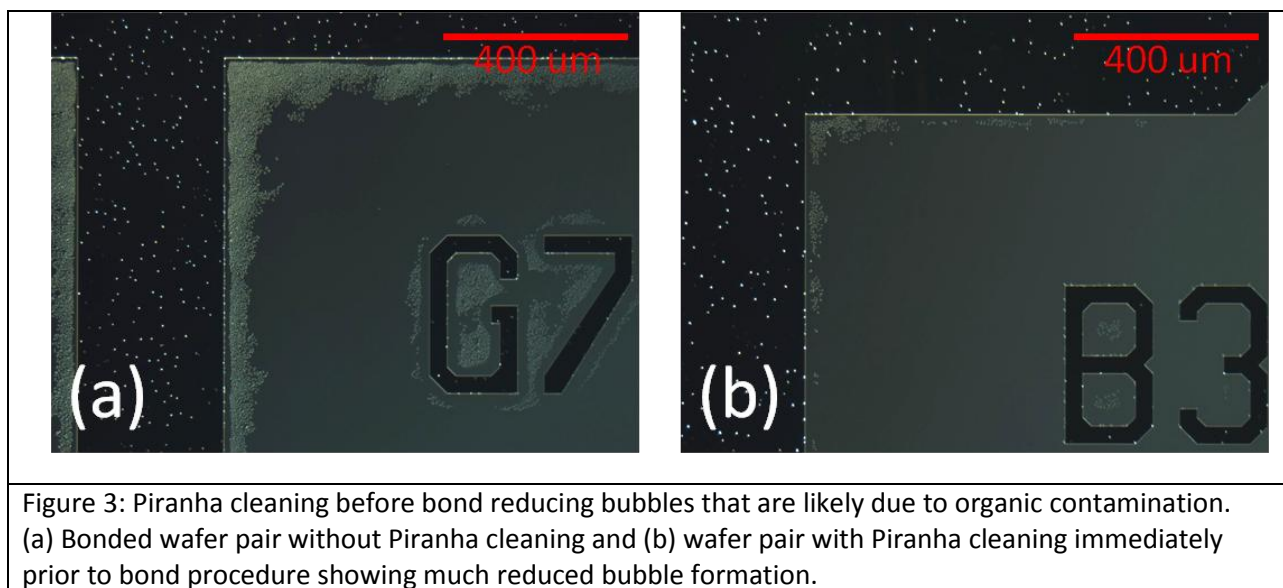
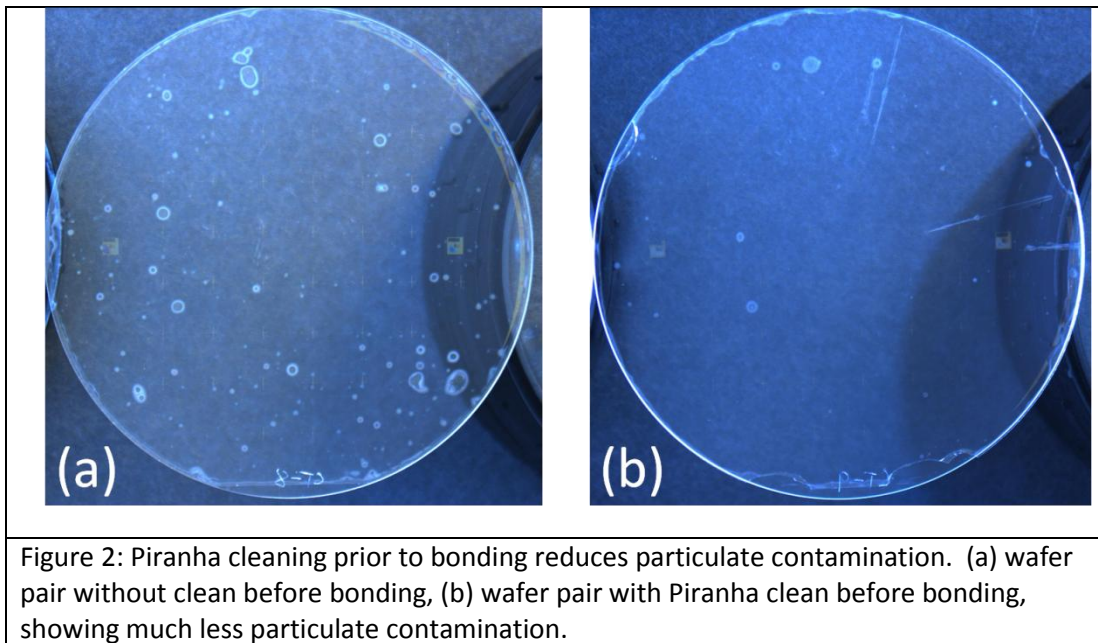
Figure 1: Particles causing voids at the interface between a bonded wafer pair. The image at the center is the wafer pair showing large voids. The images around the outside are images taken at 100x magnification showing the particles causing each of the indicated voids.

The final source of contamination is ionic. This contamination refers to metal ions that have been deposited on the wafer surface from metal tweezers or glass containers. These contaminants have little effect on bond strength, but may interfere with the operation of electrical components that are being fabricated. As this is not the case in our applications, they are not considered much.

In order to remove contamination, we have chosen to utilize a H_2O_2 / H_2SO_4 "Piranha" solution. When mixed in a 1:1 ratio, this solution undergoes an exothermic reaction, producing not only a hot acid solution, but many bubbles. These bubbles are beneficial in producing mechanical agitation, aiding in the removal of particulate contamination. However, Piranha is a very rigorous cleaner and may not be possible for some bonding applications that have delicate materials on their surface. For example, polymer bonding with PMMA cannot utilize a Piranha clean as the solution would remove all the PMMA. For these applications, a more gentle clean is required. We utilized a flowing water bath to clean our PMMA wafers. Additionally, an IPA clean could be used, if desired. Some bonding procedures actually initiate the bond while the wafers are in a flowing water bath, eliminating the potential for any contamination between the cleaning and bonding steps (16). While an interesting solution for low-

temperature bonding, this was not necessary for our application, as the alignment needed between the two wafers would make this difficult without additional process development.

Whatever cleaning method is chosen, it is important to have a clean step immediately prior to bonding. This can be seen from our results in quantitative both bond strength and qualitative evaluation of the amount of bubbles present at a bonded interface. (Both a description of the issue of bubble formation in bonds and the methods of bond strength testing are discussed later in this section.) Comparisons of wafer bonds with and without a clean immediately prior to bonding are shown in Figure 2 and Figure 3.



Flatness

Another critical component to achieving a strong bond is placing the two samples in close contact. While particulate contamination prevented this contact in localized areas, a warped wafer or a rough surface will prevent this intimate contact across large regions of a wafer. There are two methods to prevent non-flat surfaces from causing problems with a bond: achieving a flat surface and providing some sort of conformable material.

The first method to ensuring bond strength is ensuring a smooth, flat surface. Wafers can become warped or bowed due to thermal stress (for example from waveguide diffusion) or stress from a coating. Other sources of surface roughness could be features that were placed on the surface on purpose. To address these issues, it is important to consider the fabrication steps prior to bonding and ensure that they are not causing any undue stress. This should be accompanied with periodic wafer bow and surface roughness measurements. Additionally, in our process, most metal structures are recessed into the wafer surface by etching holes before depositing the metal. This ensures a flat surface for bonding.

However, as hard as one tries, it is likely that the surface of a wafer is not perfectly flat or smooth. To minimize the problems that come from this eventuality, it is useful to have some sort of conformable material in the bond. This can be accomplished in several ways. Two are presented here: conformable surface pressure and conformable polymer.

If one of the samples to be bonded is thin and conformable, it can alleviate problems from an uneven wafer surface. In this situation, however, a conformable force is also required to ensure even force across the entire sample, even when it is uneven. This can be accomplished by utilizing a rubber pad on the device that is used to apply force to the samples while they are being bonded (10).

Another solution to surface unevenness is present in polymer bonding. If the polymer is allowed to heat up slightly, it can flow around any surface features, smoothing them out and ensuring intimate contact with the bonding samples (12)(17). This procedure, however, requires careful choice of temperature, as a temperature that is too high may cause the polymer to flow too much, erasing any features that may have been desired in the polymer(11)(12).

Bubble formation

Bubbles are localized unbonded regions. They are undesirable because they decrease bond strength, cause optical scattering, and compromise fluidic integrity. A compromise of fluidic integrity is shown in Figure 4, where fluorescent fluid escaped into voids around the channel. Bubbles cause scattering due to an interruption of optical uniformity of a material. Light moving along or through the bonded interface will be scattered by these irregularities. Bubbles can either be present at the onset of bonding or can be created during the bonding process. Both types of bubbles are addressed below.

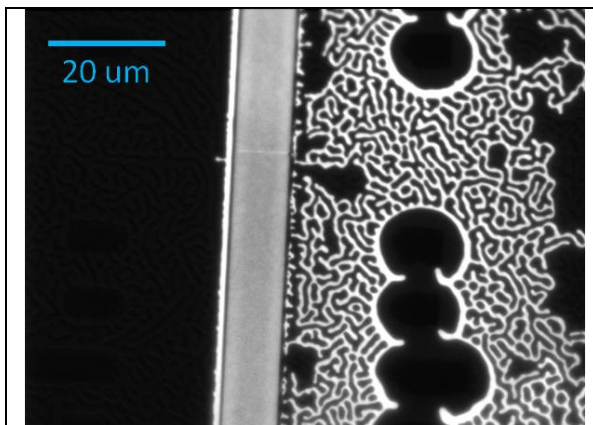


Figure 4: Fluorescence image showing leakage caused by bubbles in the polymer layer. Fluorescent fluid filled the channel (running up-and-down) and then escaped into the network of bubbles adjacent to the channel (on the right), compromising fluidic integrity.

Bubbles that occur before the bond process are present at the bonding interface when the samples are placed into contact. These bubbles can be caused by either particulate contamination, surface topography, or trapped gas. Methods to reduce these bubbles are part of the ones addressed above. A rigorous cleaning procedure can reduce the occurrence of bubbles (voids) due to particulate contamination. Additionally, a flexible sample can minimize the void diameter around the contamination. An unaddressed issue is trapped gas. If, due to slight changes in surface topography or the propagation of the area of contact between the samples, gas may be trapped between the wafers. This can be avoided through changes in the bonding procedure. First, a good procedure is to initiate the

bond at the center of the wafer by applying slight pressure there when the wafers are put into contact. This will cause the bonding area to start in the center and work outwards, pushing gases outwards and not trapping any. Another strategy to reduce trapped gases is to place the samples in a vacuum before placing in contact to bond. Many bonding tools operate in this manner.

The other type of bubble that occurs at a bonded interface is those that occur during the bond procedure. There are many reasons why these bubbles can occur and the procedures for avoiding their appearance depend on the cause. However, a three common causes and solutions will be presented.

One cause of bubbles during bonding is due to hydrocarbons on the surface of one of the wafers. As mentioned above, hydrocarbons deposit in a small layer and do not provide strong adhesion. When heating up during a bond, the thermal energy may exceed the bond surface energy for the hydrocarbon, and it will release from the surface, creating a void. This can happen across the wafer, causing many bubbles. As addressed above, a cleaning procedure including an Oxygen plasma can remove these contaminants.

Another cause of bubbles is outgassing from the samples themselves. This is of concern during polymer bonding. When the polymer is heated up and placed under vacuum, gas or solvents contained in the polymer will nucleate and form bubbles. These bubbles can be avoided by ensuring that there is no residual solvent in the polymer through a hard bake or a pre-bond vacuum exposure. Another method to avoid this cause of bubbles is to bond at higher pressures or lower temperatures.

A final cause of bubbles encountered in this work is due to thermal stress. When heating up a sample, different materials expand different amounts. When placed into contact and cooled, the relaxation to a common size causes stress in the materials. This stress can provide enough force to pull parts of a

material away from the bond interface, causing bubbles. This effect was seen in polymer bonding. Ways to overcome this cause is to bond at low temperature, or work with materials that have similar coefficients of thermal expansion. Additionally, it is hypothesized that if the bond strength is high enough, the interface will be able to withstand the thermal stress without failing.

In summary of this discussion, for a successful bond procedure, wafers should be clean and relatively flat. Additional methods to ensure effective bonding are to apply a conformable force, and design your bond procedure to minimize bubble formation.

Bond Strength Testing

A method to determine bond strength is important when evaluating any bond process. If the device being fabricated will require high pressures, or subsequent process steps will be sufficiently abusive, it is necessary to determine that the bond will be able to survive those conditions.

There are several methods by which the bond strength can be tested. The most popular characterization technique is a tensile pull test (15)(18)(19). In this test, the top and the bottom surfaces of the specimen under test are adhered to the testing setup by some strong adhesive. Then, the specimen is pulled apart normal to the bonded interface until the bond fails (15). While this procedure seems straightforward, it actually does not do an adequate job of testing the bond strength. The test has inaccuracies as most of the applied stress is concentrated around individual defects in the specimen, leading to bond failure being initiated at that point and propagating across the specimen, leading to failure at stresses well below the strength of the entire interface (20). Additionally, any misalignment of the test system will result in bending moments and stresses other than tensile, further contributing to early failure modes of the bond (21). Due to the drawbacks with tensile bond strength testing, other areas were explored.

Other potential tests require specially patterned wafers to cause voids in the bond interface, the size of which is a determinant of bond strength (22)(23). A similar bond test is the “blister test” where a hole to the bond surface is pressurized and the resulting size of the void created is a determinant of the bond strength (24)(25). Another common bond test procedure is the “double-cantilever” or “razor blade” test (15). This is one of the tests that was used and will be described further below. The other bond strength test that was utilized simply applies to polymer adhesion and is described below, as well.

Razor blade bond strength test

To quantify the strength of the bonds, the “razor blade” method was used (26). In the razor blade test, a blade of known thickness is inserted into the bond interface. The distance that the debonded area extends from the blade is an indicator of bond fracture surface energy. The bond fracture energy is determined by the equation:

$$W_{AB} = G_{Ic} = \frac{3h^2 E_1 d_1^3 E_2 d_2^3}{2c^4 (E_1 d_1^3 + E_2 d_2^3)}$$

This equation describes the work of adhesion, W_{AB} , by solving for the critical strain energy release rate, G_{Ic} . The other values involved are indicated in Figure 5, below. E_1 and E_2 are the Young's moduli of the materials of the top and bottom samples. In general, we are using wafers of the same material, but in some tests, the top sample is a thinner sample.

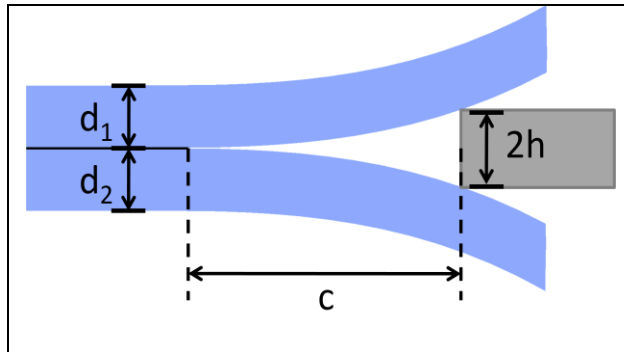


Figure 5: Diagram of the razor blade test. The razor blade, on right, of thickness $2h$ is inserted into the bond interface. The length of the debonded area, c is an indication of bond strength.

This test actually measures the average bond surface energy. The data generated from this test is in units of $\frac{J}{m^2}$, or energy per unit area. This is the energy required to take square meter of this bond and completely separate it; a good measure of bond strength. The number generated from the above equation is considered to be an average as a single razor blade test actually is taking data over an ensemble of small bonding sites.

In the experiments for this chapter, each bonded wafer was diced into 1cm wide strips to most closely approximate ideal dual cantilever geometry to minimize error (27). Taking each strip, a razor blade was forced into the interface and pushed in until the debonding front moved exactly with the movement of the razor blade. This indicates that the bond strength is constant, indicating that the distance observed is a quality value. To record the data, while the razor was inserted into the bond interface, the sample was placed on a holder next to a ruler and a picture was taken. This picture was then used for the actual measurement. The picture was used because it would allow for careful alignment and measurement of the debonded length with the ruler without the possibility of upsetting the bond interface and altering the data. Additionally, this method provided a more robust method of measurement. The pictures were edited digitally to align the sample and the ruler and place them next to each other, ensuring alignment accuracy of $< 1^\circ$. Additionally, the capability to magnify the picture to place lines for measurement enabled more highly accurate data than visual measurement. For each wafer pair, at least three measurements were made on at least four of the diced strips.

Other tests were performed on selected wafer sets. If it was thought that the wafer pair under test would not survive dicing, the test was performed on the wafer pair as a whole, in order to get some

quantitative data, even if the number may be off by 10%. This uncertainty was added into the data. Additionally, after debonding during the razor blade tests, it was recorded which wafer the polymer was attached to – to indicate the location of the weaker bonding surface.

The razor blade test was chosen as it was a repeatable, quantifiable test that could compare across wafer bonding methods and did not require any additional specialized testing equipment.

Scratch and peel polymer adhesion test

The scratch and peel test is a method to determine the quality of adhesion of a polymer to a surface. In this test, the polymer is prepared as normal. Then, a special device is used to create scratches in the polymer. Two sets of scratches are made, crossing each other approximately at right angles. After the scratches are made, a specialized tape is placed on the polymer and peeled off. Observation of the scratch pattern after this procedure indicates the strength of the polymer adhesion to the surface, as demonstrated in Figure 6.

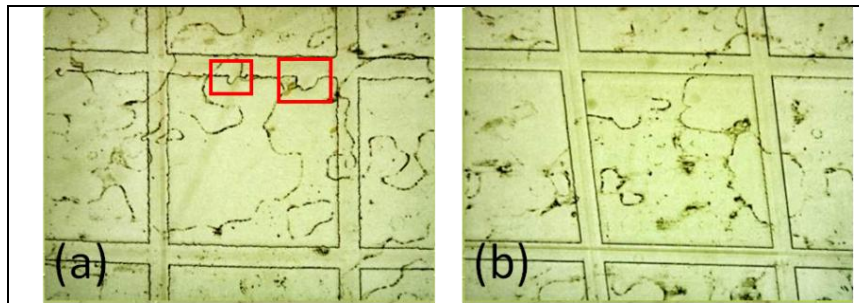


Figure 6: Grid scratch and peel test for polymer adhesion. The grid of scratches and artifacts from the tape are seen on both samples. (a) sample showing slightly poor adhesion, as indicated in the boxed areas, where the tape pulled off some polymer. (b) a strongly adhered polymer – no compromised areas in the test.

The scratch test was a good option to use, as it did not require a bonded wafer, but could provide more immediate information about the polymer adhesion. Utilizing this test, the polymer adhesion strength was maximized in order to ensure that the bonded wafer pairs would be strong enough to survive dicing for the razor blade test. Additionally, understanding the polymer

adhesion informed the identification of failure modes of the polymer bonds.

Other tests and observations

The bonds of some of the wafer pairs failed during dicing after their bond. This bond failure did not completely correlate with bond strength. Also, the uniformity of the bond and the inclusion of voids do not correlate well with bond strength. The results regarding bond survival and uniformity are presented. Additionally, one process run included particles in the resist, creating voids between the wafers after bonding. The size of these voids was measured to determine if voltage can decrease void size.

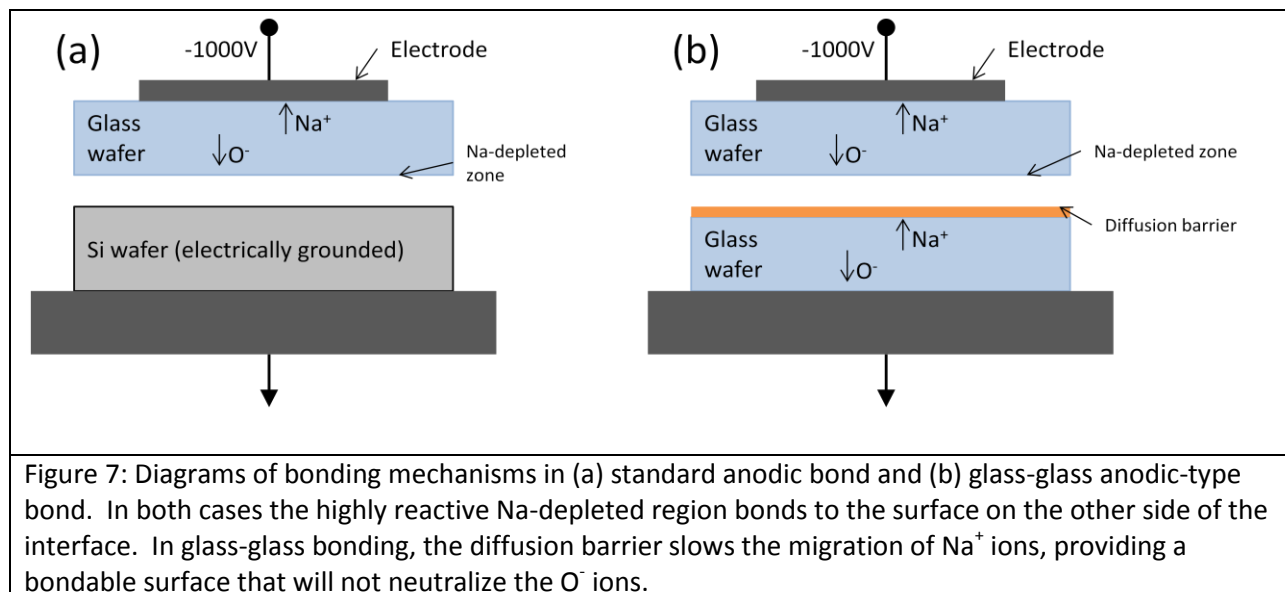
While this information does not provide well-controlled, quantitative data, the results were deemed to be interesting and as such are included in this chapter.

Glass-to-glass anodic-type bond

Anodic bonding is a process for bonding a glass sample to a conducting one (usually Silicon) and is a standard procedure in many fabrication processes. We explored an analogous procedure that utilizes a conducting (or semi-conducting) layer to perform an anodic-type bond between two glass wafers. Previous work in this area did not provide an exploration of different materials or a proper strength test. Different materials and thicknesses were explored and the bond strength was tested with the razor blade method. The results of both the bond strength tests and qualitative uniformity observations are presented. A bond utilizing 200Å of amorphous Silicon (α -Si) was determined to be the optimal process for our interests.

Background

In anodic bonding, a glass wafer and a Silicon wafer are bonded by placing the pair in contact, elevating the temperature of the stacked pair and placing a DC voltage across them. In general (and in this description, for simplicity) the glass wafer is placed on top of the Si wafer and a negative voltage is applied. By elevating the temperature of the wafer pair, the mobility of Sodium (Na) ions in the glass is increased. When the voltage is applied, the Na ions move towards the cathode, leaving a Na-depleted region at the bottom surface of the glass wafer. The Si wafer is comparatively very positively charged and therefore there is a strong electrostatic attraction between the Si wafer and the negatively-charged Na-depleted region of the glass wafer. This electrostatic attraction pulls the wafers into intimate contact. When the Si wafer is in contact with the highly reactive Na-depleted region, irreversible Si-O chemical bonds are formed. The general process is demonstrated in the cartoon of Figure 7 (a).



Glass-to-glass anodic-type bonding follows a procedure similar to standard anodic bonding and the bond is formed through a similar process. The largest difference between the two bond mechanisms is that in

standard, glass-Si anodic bonding, the Silicon wafer functions as the anode, neutralizing ions immediately as they reach it. But in glass-glass anodic bonding, charge transport occurs in both wafers. Glass-glass anodic bonding requires one wafer to have a coating that will act as a diffusion barrier to Sodium atoms during the bond procedure. This layer can be a variety of materials. Materials for the diffusion barrier bonding layer that were explored in this work were: aluminum, titanium, and amorphous silicon (α -Si). This thin layer is deposited on one wafer (usually the bonding surface of the anode wafer). The bond setup for anodic-type bonding is shown in Figure 7 (b).

In glass-glass anodic bonding the two wafers are placed in contact, heated, and then a voltage is placed across them. In the glass, sodium oxide separates into Na and O ions. The ions move in opposite directions due to the applied field; Na towards the cathode, O towards the anode. The following description is based on a wafer stack bond where the cathode is on the top. Na ions in the top wafer travel to the cathode and are neutralized. O ions in the top wafer travel (much more slowly) towards the bonding interface. The combined effect of these groups of ion movement is a negatively charged Na depleted, O-rich layer at the top side of the bond interface.

Similar to the top wafer, in the bottom wafer, the Na ions move towards the cathode. They reach the diffusion layer and their diffusion is slowed. The result is a positive charge on the anode wafer surface, but the surface is not Na-rich. These processes set up the actual bond mechanism. The charged surfaces are attracted to each other by electrostatic forces and are pulled into intimate contact. It is thought by some that this is the only mechanism for bonding (4). However, other work claims there is an additional bond mechanism. O ions on the cathode wafer surface bridge to the Na diffusion barrier layer on the anode wafer and form an irreversible chemical bond.

This process shows the need for the Na diffusion barrier bonding layer. If Na ions from the anode wafer arrive at the bonding interface before O ions from the cathode wafer, the ions will combine and neutralize, forming a weak bond. However, since the Na ions are blocked by the diffusion barrier, the O ions are able bridge the gap and oxidize the layer, creating a strong bond. The glass-glass anodic type bond is desirable due to its strength. Also, because there are no polymers involved, it is possible to put the pieces to be bonded through a rigorous cleaning procedure immediately prior to bonding, further improving bond strength and uniformity.

Previous work and this work

Previous work has explored the effects of temperature or voltage on anodic-type bonding with a single type of diffusion barrier material (4)(5) (6) (28)(29)(30) (31). It was found that higher temperature and higher voltages usually lead to stronger bonds (4). This result makes sense, as both increased temperature and voltage will increase ion drift velocity in the glass wafers. (Increasing temperature increases ion mobility, enabling higher velocity for a given voltage, and increased voltage increases velocity.) An increased ion drift velocity will result in more ions being present at the surface, increasing the surface charge and the resulting electrostatic attraction. Additionally, more ions at the surface can

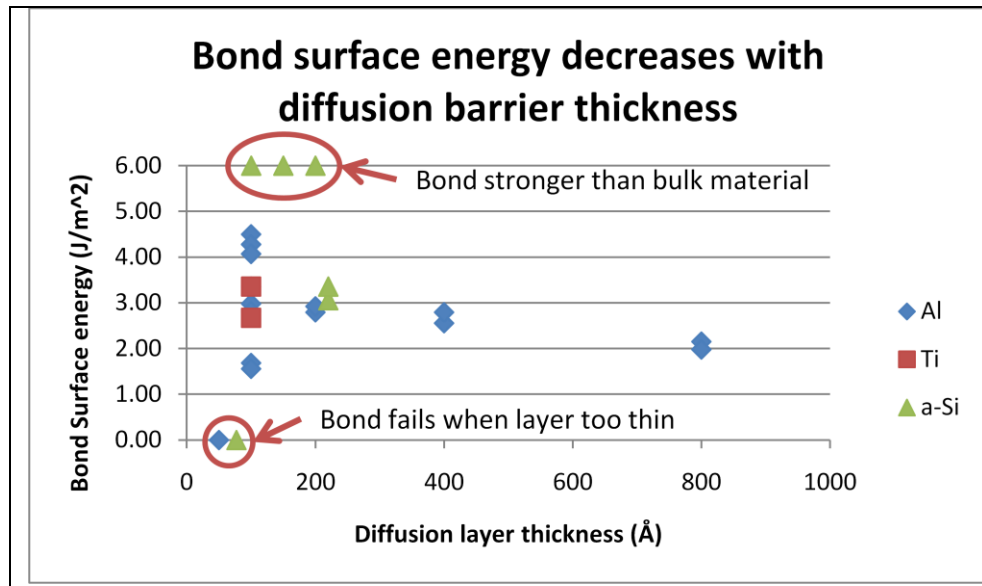


Figure 8: Plot of bond strength as a function of diffusion barrier thickness for glass-glass anodic-type bonds with three different materials as diffusion barrier. Bond strength was measured using the razor blade test and increases with decreasing diffusion barrier thickness, until the diffusion layer is too thin to function.

increase the quantity of chemical bonds that are formed, increasing bond strength. Other work in glass-glass-anodic bonding has explored the effect of bond layer thickness (29). It was found that for an Aluminum bond layer thinner layers provided stronger bonds.

There are several opportunities for exploration in the

work on glass-glass anodic type bonding. First, most existing work focused on only one type of bond material. Because bond test procedures can be variable between performers, this did not allow for direct comparison of different materials. So, in this work, different diffusion barrier materials were explored and the effect that their thickness has on bond strength. Voltage and temperature were not explored, as they were explored elsewhere and we utilized the maximum values that would be allowed by the bond tool (voltage) and the device being bonded (temperature).

The second opportunity to add to the body of knowledge in glass-glass anodic type bonding provided strength data utilizing the double-cantilever bond strength test. The bond interface from a glass-glass anodic-type bond is highly nonuniform and has many localized irregularities, or “speckles” (29). If these locations have any mechanical properties different from the bulk material, they will present points of failure during a bond test. Therefore a tensile strength test, as presented above, will be inaccurate for this type of bond surface. The localized failures will result in not only low numbers, but their randomness will produce great inconsistency in the strength data. Therefore, it was determined that the razor blade test would provide a more robust quantification of the bond surface strength, and that that data could provide useful information for comparison of bond procedures.

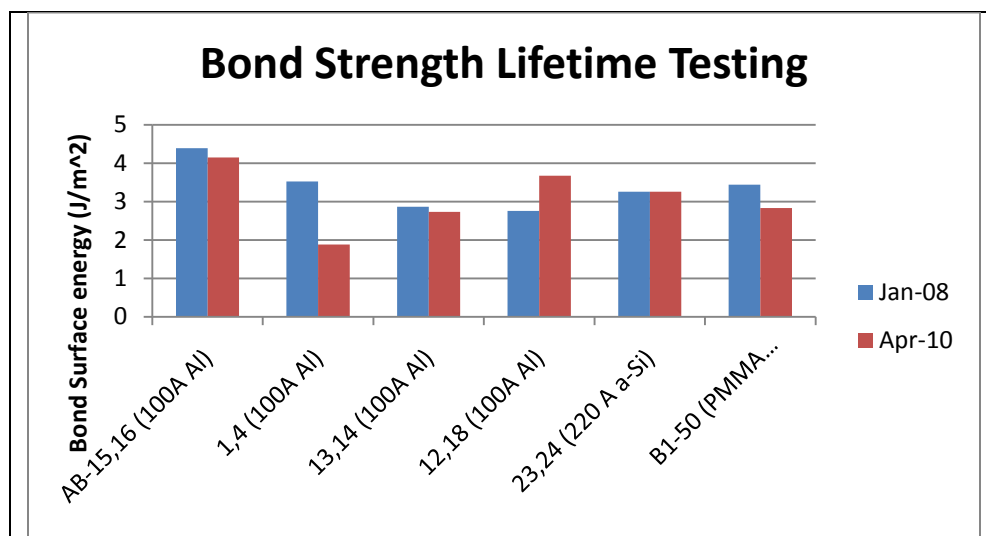


Figure 9: Bond strength lifetime testing. Razor blade tests were performed on the same samples over two years apart. No significant decrease in bond strength was observed.

Experiments and results

To fill in the indicated gap in the field, bonding experiments were performed with various thicknesses of three different diffusion barrier materials. The bond strengths were quantified utilizing a razor blade test.

Wafers were scratched for identification and cleaned in a Piranha solution. The diffusion barrier layer was then deposited on chosen wafers. Wafers were then cleaned again and placed in the bond tool. Wafers were bonded at 335° C, 3×10^{-5} and with an applied voltage of 1000V. The voltage was stepped up to this value in a standard manner and then held for 20 minutes. After being allowed to cool, the bonded wafer pairs were diced into 1 cm wide strips and the razor blade test was performed. Some of the pieces were saved for a later date to do lifetime bond strength testing.

The three materials chosen for the bonding layer were aluminum, titanium, and amorphous silicon (α -Si). Additionally, a the difference between sputtered and evaporated Al was explored, but it was found that there was no difference in bond strength, so results are not presented separately for the different methods of deposition for Al.

Bond strength

Results indicate that the bond strength improves with decreasing diffusion barrier layer thickness, to a point. These results are presented in Figure 8, above. When the diffusion barrier becomes too thin, no bonding occurs. It is assumed that the barrier loses its efficacy at extremely small thicknesses, allowing Na to diffuse through, neutralizing O ions, reducing the charge differential and the resulting electrostatic attraction. Additionally, allowing this recombination prevents the O ions from oxidizing the diffusion barrier layer, which is what produces the strong chemical bonds that give the anodic-type bond its strength.

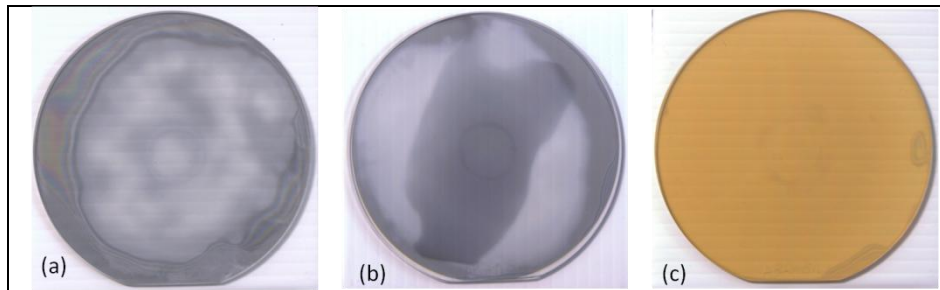


Figure 10: Images of wafers bonded with the three materials of interest. All bonds were performed at 1000V and the materials were 100Å thick. None of the materials became completely transparent – indicating that there will be optical loss. The materials are (a) Aluminum, (b) Titanium, and (c) amorphous silicon.

The use of different metals as a diffusion barrier did not seem to make a large difference in bond strength. The wafers where titanium was used as a bonding layer showed similar strength characteristics as the bonds utilizing aluminum. Amorphous silicon had the best bond strengths. For

several wafer pairs, the bond strength was greater than that of the bulk material. This means that when the razor blade test was attempted, the wafer glass would chip before the bond interface would fail.

A few samples were tested over two years later, as a measure of the lifetime strength of the bonds. Figure 9 presents the data from these experiments. Although some types of bond may decrease in strength over time (15), the data shows that the bond strength did not decrease over that time period for these samples. This indicates that a chemical bond is probably responsible for the anodic-type glass to glass bond. If the bond were simply caused by stored charge, this charge would likely have dissipated over that time period, weakening the bond. The verification of the bond strength over a long period of time indicates that this bond procedure can be considered for devices that require a long lasting bond.

Bond quality

In the context of this thesis, bond strength is not the only figure of merit for a bond. Additionally, it is desired to have a homogeneous, optically clear bond interface. The anodic-type bond falls short of an ideal procedure in this area. The resulting bond is discolored as well as nonuniform. Typical bonded wafer pairs showing this coloration are shown in Figure 10 for the three materials of interest.

Before bonding, the diffusion barrier layer is not transparent. It was hoped that during the bonding process, as the layer became oxidized, it would become transparent. While this occurred somewhat, it was not uniform across the wafer, and did not occur completely. There are several ways that this could be improved: longer bond time, higher voltage, higher temperature, or thinner barrier layer. The longer bond time, higher voltage, and higher temperature would result in more chemical interaction between the oxygen ions and the diffusion barrier, hopefully enabling complete oxidization and therefore clarity. Our experiments in this area were unsuccessful in completely eliminating the discoloration.

Additionally, a thinner layer was explored to improve clarity, but as shown in the bond strength results, it was not possible to maintain a strong bond with below a certain thickness.

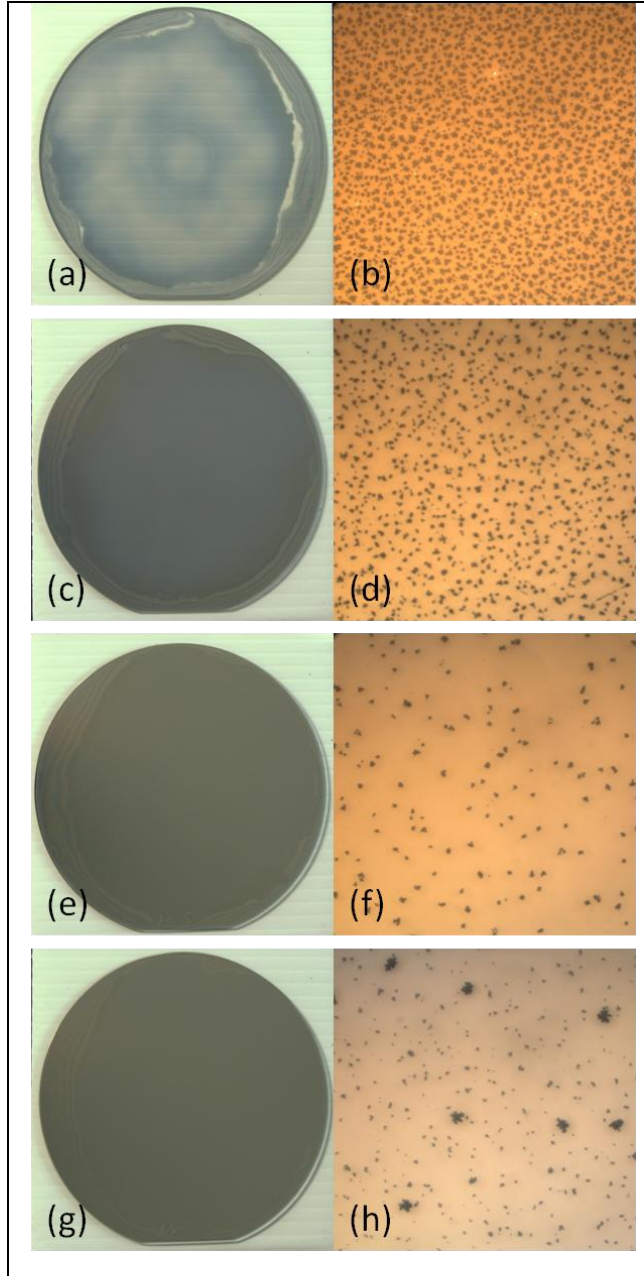


Figure 11: Images of bonded wafer pairs with an aluminum diffusion barrier of various thicknesses - both full wafer images and images under 20x magnification. As the diffusion barrier is thicker, the wafer stack becomes more opaque, but speckle density decreases. This is potentially due to a lack of long-range order in the thicker layers. The images are: (a, b) 100Å, (c, d) 200Å, (e, f) 400Å, and (g, h) 800Å.

Another optical issue with the anodic-type bond is speckling. The bond interface was covered with small irregularities, or speckles. These speckles are noted in the literature and are thought to be points where either the bonding first occurred or where several bond fronts intersected, resulting in a region of altered properties (29). It was determined that the density of speckles is reduced by a thicker diffusion barrier. Images in Figure 11 demonstrate this effect. It is thought that the thicker layer actually has more surface irregularities, and due to these irregularities, there is no long-range contact with the bonding wafers. Therefore, there are not as many bonding fronts in that intersect, reducing the density of speckles(29). It is unclear if this is the case. However, a thicker layer is not desirable due to the decreased bond strength and the reduced transparency. Therefore a thinner layer was considered to be the best choice, even with the increased speckle density.

Summary

An anodic-type glass-glass bond was explored utilizing different materials. A bond strength test that would not be skewed by surface irregularities was utilized to produce reliable, quantities comparisons between materials and thicknesses. Additionally, optical properties of the resulting bonds were evaluated.

It was shown that the strongest bond strength was achieved by utilizing a 100-200Å amorphous Silicon layer as the diffusion barrier. It was not possible to achieve a completely clear bond interface.

Polymer Bonding

Polymer bonding is a common wafer bonding procedure for microfluidic devices. However, little work has been carried out to achieve a glass-glass polymer bond with sub-micron channel depths. This bond procedure was explored and several common methods to improve bond strength were evaluated. It was found that bond quality greatly benefits from adhesion promoters and surface activation. However, surface cleanliness is always of utmost importance. As such, polymer choice determines cleaning procedures that are allowed and ultimate quality of polymer bond, and even so, a stronger bond procedure was desired, leading to the development of a voltage-assisted polymer bond, discussed in the next section.

Polymer bonding background

Polymer bonding can refer to either the bonding of two pieces of a polymer or using a polymer as an intermediate layer to bond two samples of a different material. In this work, we are mostly concerned with the latter: bonding two pieces of glass using a polymer as an intermediate layer. With that stipulation, the bond procedure and many of the procedures to improve the strength of a bonded interface are the same for the two procedures.

In general, to perform a polymer bond, the pieces of interest are placed into contact, heated, and pressed together by a regulated force. An elevated temperature is used for two reasons: first, an elevated temperature enables surface interactions – either chemical bonds (13) (32) or interdiffusion of polymer chains (9). The second reason that an elevated temperature is beneficial is that a heated polymer becomes viscous, and can flow around surface irregularities, ensuring intimate contact with the samples, improving bond quality (12)(17). The temperature that is used must be well-controlled, however; too high of a temperature, and differences in thermal expansion will cause strain, decreasing bond strength (33). Additionally, a high temperature may compromise some features in the polymer (11).

It is difficult to achieve a strong polymer bond due to the low surface energies of typical polymers (9). Bond strength for any bond typically increases with increased hydrophilicity of the bonding surfaces. (34). This is likely due to the wetting capabilities of materials with greater hydrophilicity. However, polymers commonly have atomic components like Nitrogen or Oxygen along with hydrocarbons, which produce a hydrophilic surface, resulting in weak bonds (9).

There are many methods by which the strength of a polymer bond can be increased. Common methods that have been explored include adhesion promoters placed on wafer before the polymer layer, adhesion promoters added to the polymer, and surface treatments. Surface treatments are aimed at increasing the surface energy of the bond interface, improving bond strength. Common surface treatments include: treatment with the polymer monomer (11) solvent treatment (8) (9)(34) and plasma treatment (9) (10)(32). We explored two methods for improving bond strength: an adhesion promoter and plasma surface treatments.

Process Development

It has already been described how a rigorous cleaning procedure is important for a strong bond. It not only removes particulate contamination, reducing voids, it also removes organic contamination, improving bond strength and reducing bubbles. The cleaning procedures that are available depend on the polymer that is being used. PMMA does not stand up to much rigorous cleaning, so it is only cleaned in a water rinse. CYTOP, however, can withstand much more rigorous cleaning. As Figure 2 and Figure 3 earlier in this chapter demonstrated, a Piranha clean before bonding removes organic contamination, which otherwise leads to bubble formation.

To further improve the bond strength, two methods were explored. For both CYTOP and PMMA, an O₂ plasma treatment was explored. For PMMA, an adhesion promoter, MEMO was utilized. The procedures and results are included below.

Plasma treatment

A plasma treatment is a common method to improve bond strength for polymer bonding. In this work, an oxygen plasma was explored. While the exact chemistry modification that occurs during a plasma treatment is not well understood (34), there are a variety of surface modifications that increase the surface hydrophilicity, which, as mentioned above, indicates a higher surface energy and a stronger bond (9)(10) (15) (34). For an O₂ plasma, it is thought that carboxyl groups, along with oxides and aldehydes form, which create the hydrophilic surface (34).

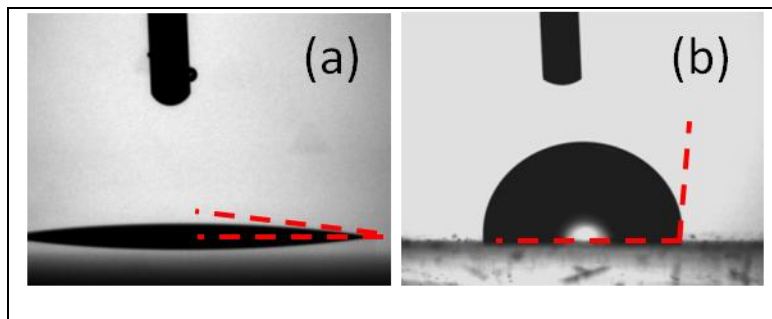


Figure 12: Goniometer images are used to measure the contact angle of a liquid on a surface. The contact angle provides an indication of surface energy, which can be an indication of bond strength. (a) Small contact angle indicates high surface energy of the substrate. (b) Large contact angle indicates low surface energy and a potentially weak bond.

The strength of polymer bonds are strongly influenced by the wetting properties of the polymer. If the polymer completely wets a sample placed in contact with it, it will ensure a complete bond. The wetting capabilities are determined by two things: the viscosity of the polymer and its surface energy(35). Viscosity is determined by the temperature used, and will be addressed later. To test for surface energy, a goniometer is utilized. A goniometer is a tool consisting of a

camera and a mechanism for placing a drop of fluid on a surface. The drop is imaged by the camera at the level of the sample surface and the contact angle of the drop with the surface is measured. This angle is an indication of the surface energy and the hydrophilicity of the surface (35). The smaller the contact angle, the more hydrophilic the surface, and the stronger the bond can be formed by the polymer. Goniometer images in Figure 12 demonstrate typical results for (a) hydrophilic and (b) hydrophobic surfaces.

Other tests that were utilized to analyze the efficacy of plasma treatments were the grid scratch and peel test, as described earlier in this chapter and the razor blade test.

Various lengths of plasma treatment were used and various processing steps afterward were tested. Most tests were performed with PMMA as the polymer. It was determined that a 30 second treatment was sufficient to alter the surface energy of the polymer surface. These results were obtained from goniometer tests shown in Figure 13. This enhanced surface energy effect decreases over time, and would be effectively eliminated if the sample was blown with nitrogen or washed with water after the treatment.

In conclusion of the plasma treatment experiments, a 30 second O₂ plasma treatment immediately prior to bonding is sufficient to improve surface hydrophilicity, surface energy, and subsequent bond strength. An experimenter must be careful to remember to not utilize any air gun to blow off the wafer after the treatment, as doing so will negate the beneficial surface treatment.

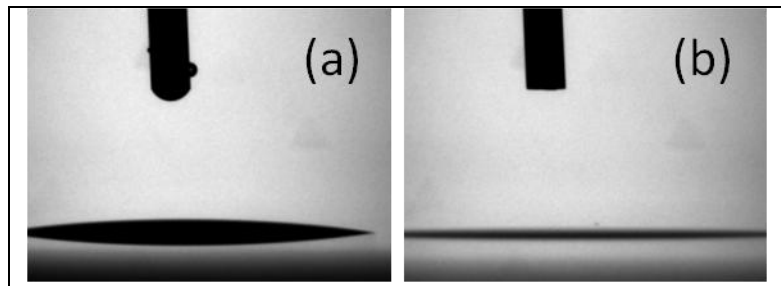


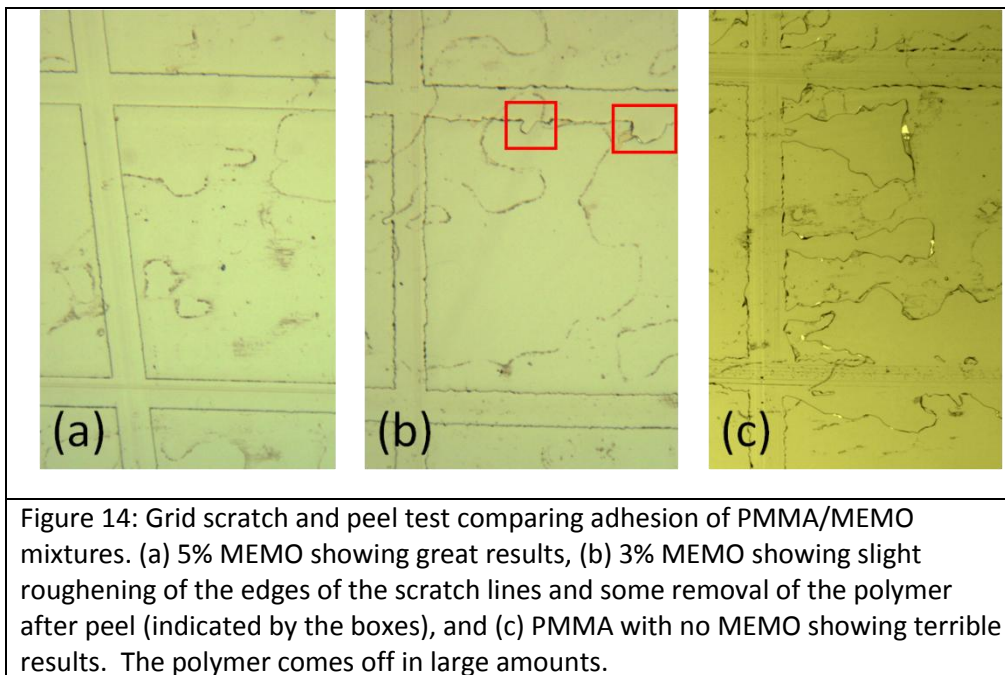
Figure 13: Goniometer images showing effect of plasma treatment on surface energy. (a) PMMA without any plasma treatment shows a small contact angle. (b) After 30 seconds of an Oxygen plasma, the contact angle is reduced, indicating greater surface energy of the treated PMMA, which can result in a stronger bond.

Adhesion Promoter

Polymer adhesion strength is generally influenced by two factors: surface roughness and chemical bonding. Surface roughness increases the surface area of contact between the polymer and the substrate, increasing the bulk adhesion strength. Chemical bonds between the polymer and the substrate can have a much larger effect on bond strength (36). However, many materials are not conducive to forming a strong bond with a polymer. To improve adhesion for these types of materials, a coupling agent or adhesion promoter is used.

When using a glass substrate, a silane coupling agent is a popular way to improve adhesion. Silane coupling agents are molecules that can be added to the polymer before it is spun on to a wafer (36) or can be deposited on the wafer before the polymer, either through spinning (37)(38) or vapor phase deposition (38) (39). Silane coupling agents provide a layer that can interface between siliceous surfaces and organic ones. This behavior is very useful in many types of bonding, as they usually include these two groups(38). Silane coupling agent molecules generally consist of a hydrosylable group, a Si molecule, a linking group, and an organofunctional group. The hydrosylable group hydrolyses with water on the surface and then forms a reactive silane group with the Si molecule. This group actively

binds to the siliceous surface (glass). The result is the organofunctional group is linked strongly to the siliceous surface through the silane and the linking group – presenting a surface that can readily bond with an organic material.



It had previously been shown that adding the silane coupling agent 3-methacryloxypropyltrimethoxysilane (MEMO) to PMMA to form a 5% by weight solution of MEMO improved adhesion by 90% to Si surfaces (36). In this work, this technique was explored in its usefulness for our application. MEMO/PMMA mixtures of 0%, 3%, and 5% MEMO. The mixtures were spun onto glass wafers to achieve a uniform film and then tested using the grid scratch and peel test. The results are shown in Figure 14, above. It was shown that the 5% MEMO solution achieved much better adhesion than the other two. In the work by Kadereit, going above 5% MEMO did not demonstrate any improved adhesion (36). This possibility was not explored in this work because the grid scratch and peel test could not have a better result than the one shown by the 5% solution.

Depositing MEMO on the surface via vapor phase deposition was also tested and compared to PMMA with no adhesion promoter and PMMA with 5% MEMO in solution. These wafers were bonded and tested with the razor blade test. It was shown that the 5%MEMO solution provides the strongest bond. Note that these tests were performed with a voltage-assisted bond, described later in this chapter – so the bond strength numbers are higher than those would be for a standard polymer bond.

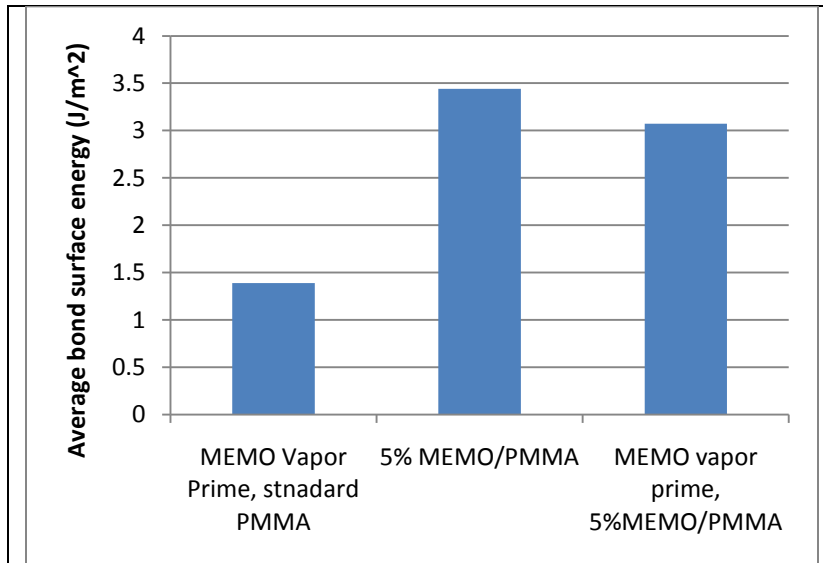


Figure 15: Bond strength for various uses of the adhesion promoter MEMO, as tested by razor blade test. Adding 5%MEMO to the PMMA provides the strongest bond.

Polymer age

It was also found that the PMMA degrades over time, so the published expiration dates should be taken note of, and PMMA should not be used after its expiration date. Tests comparing expired PMMA with new PMMA indicated the expired PMMA has lower adhesion. The grid scratch and peel tests were performed with 5% MEMO solutions. Images from these tests are shown in Figure 16. Additionally, expired PMMA shows altered behavior for electron beam lithography, the data which is not presented in this thesis. It is noted that expiration dates of resists should be observed.

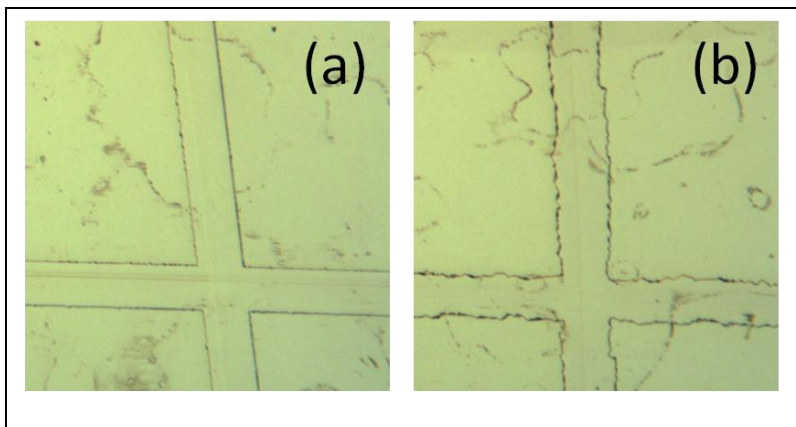


Figure 16: Grid scratch and peel tests comparing new and expired PMMA. Both tests were performed with a 5% MEMO/PMMA mixture. (a) New PMMA shows very good adhesion. (b) Expired PMMA shows decreased adhesion, as indicated by the rough edges of the scratches.

Polymer bonding conclusion

Polymer bonding is a useful tool for producing microfluidic devices. The ability to flow around surface irregularities improves performance when faced with particulate contamination. Additionally, surface treatments with Oxygen plasma and the addition of an adhesion promoter were found to improve bond strength. However, the strength of bonds was not sufficient for our use. A method to improve this bond process was sought out. Specifically, it was thought that a strong, conformable force could improve both bond strength as well as robustness to particulate contamination. These improvements were achieved through voltage-assisted bonding, which is addressed next.

Voltage-assisted polymer bonding

It was determined that a stronger bond was required than those produced using polymer bonding. One suggested manner to improve bond strength not addressed above was to apply a stronger bond force when bonding (12). In addition, this force should be conformable, in order to minimize the effects of particulate contamination. In this section, we explore the benefits of applying a voltage to a polymer bond, both in terms of process improvement, device yield, and bond strength. By applying a voltage, we are able to reduce the size of voids around contaminants and increase bond strength over standard adhesive layer bond procedures.

Experimental Methods

The goal of this section is to determine if applying a voltage across a wafer pair during bonding will improve the bond strength by inducing an electrostatic force between the two glass wafers. A model was constructed to provide insight into the behavior of the materials under test. To support that model, the appropriate material parameters were measured. With the model completed, experiments were performed to determine the effects on bond strength.

Resistance tests

In order to accurately model the electrostatic forces present during bonding, it is necessary to know the electrical properties as a function of temperature for the materials involved. It was deemed necessary to measure these properties.

Fabrication

Glass wafers were cleaned in a 3:1 H₂SO₄ / H₂O₂ “Piranha” solution. A layer of Au (with a layer of Cr for adhesion) was sputtered on the entire wafer. Then thick layers of the polymers were added through repeated spin coating following the parameters in (40)(41). After a hard bake, another layer of Au was deposited through a shadow mask, giving 25 uniform testing spots of ~79mm² area. Wafers for

determining the resistivity of the glass were prepared by simply sputtering a layer of Au on both sides of the wafer after cleaning.

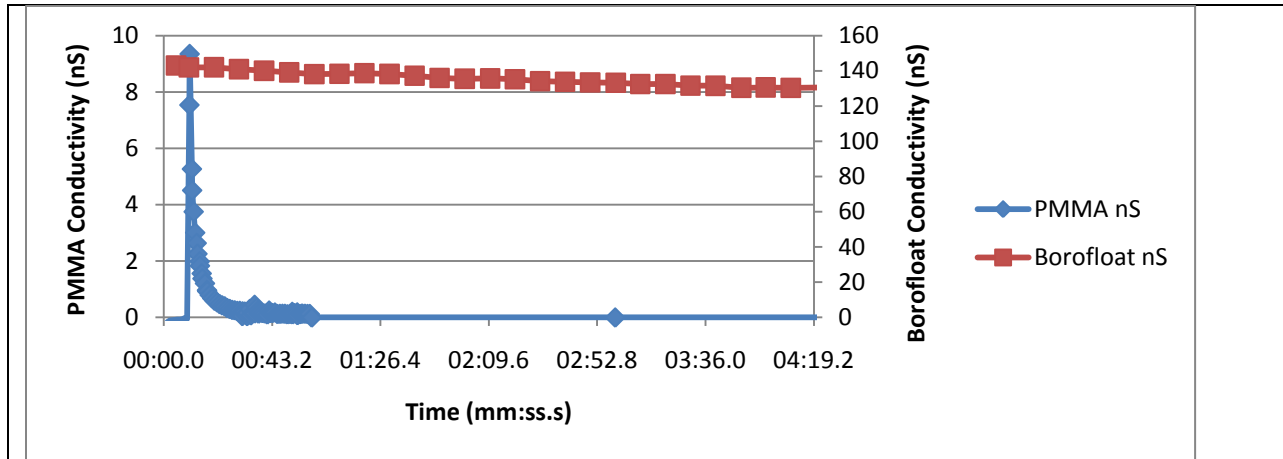


Figure 17: Measured conductivity vs. time for Borofloat and PMMA at a temperature of 160°C. The PMMA quickly polarizes, becoming relatively open.

Testing

The wafers were placed on a hotplate and allowed to sit for 10 minutes to come up to a uniform temperature. A finite element model was created in COMSOL to simulate the temperature gradient across the wafer. This data is shown in Figure 20. Using this model, sitting on a hotplate was determined to provide sufficient temperature uniformity. The difference in temperature between the top and bottom of the wafer was less than 0.5°C, which is below the resolution of our hotplates.

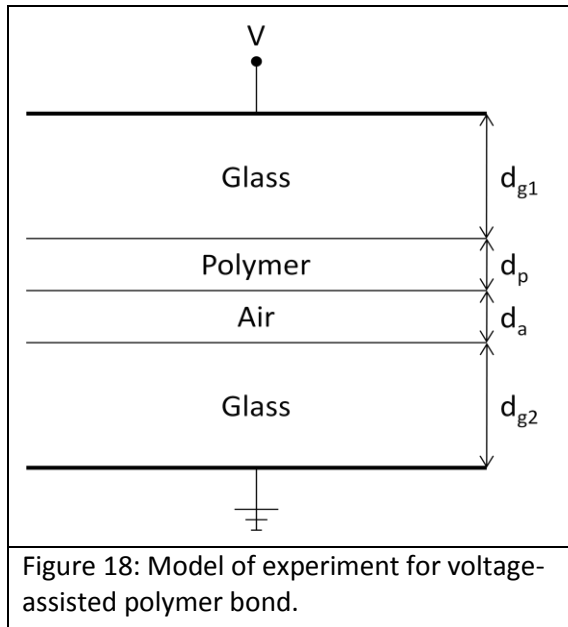
After allowing the sample to arrive at the desired temperature the resistance of the layer was measured with a Fluke 289 multimeter by making soft contact to the gold using a length of Cu tape suspended from a stationary probe tip. An example measurement is shown in Figure 17. Several spots were measured and the measurements were repeated after 5 minutes. The time was required to allow the dissipation of any stored charge from the measurement.

Electrostatic Force Model

It was hypothesized that the voltage would produce an attractive force between the wafers that would cause an improved bond. Additionally, any voids would experience a strong conformal force, reducing their area. This is similar to an anodic bond of glass to metal, where the electrostatic attraction will pull the materials together and an electrostatic potential will persist, holding them together(42). With an experimental model as shown in Figure 18, the force that is produced can be calculated with electrostatics.

For a gap with a voltage across it, the force pulling the outer plates together can be described by the equation:

$$f = \frac{V^2 \epsilon A}{2 d^2}$$



In the above equation, V is the applied voltage, ϵ is the permittivity of the material between the electrodes, A is the area of the wafers, and d is the distance. For different conditions, this equation will describe the force across an air gap, or across the polymer. A diagram of the wafer stack when being bonded is shown in Figure 18. Initially, there is likely a thin layer of air between the wafers (42). When a voltage is applied, the entire voltage drop will be across this air gap. This voltage will induce an attractive force, pulling the two wafers together. Additionally, when there is a particle causing a void between the bonded wafers, the area around this particle is subject to this force as well. From the work by Knetchel (22) the size of the void around the particle will be an indication of bond strength.

When there is no air between the wafers, we assume that the entire voltage drop can be approximated to be across the polymer layer (this can be validated by the resistance tests).

Bonding Experiments

To determine the effect of applying a voltage on bond strength, bonding experiments were performed with two different polymers, CYTOP and PMMA, across a range of voltages. Various parameters were explored, including temperature effects, identification of failure interface, and evaluation of bond strength.

Fabrication

Each wafer pair was prepared and processed individually to ensure all wafer pairs followed the same timeline without any pauses between steps. This was done to avoid any changes to bond strength from accumulated moisture, plasticisers, or polymer aging. All of this work was performed in a cleanroom facility.

To start, the glass wafers were cleaned with a 3:1 H₂SO₄ / H₂O₂ "Piranha" solution. After a cleaning rinse, the polymer was spun on to one of the wafers. Cytop (40) and PMMA (41) were prepared following the procedures described in other literature to achieve a 200nm thick layer. After coating, the wafers were placed in contact on the bond chuck under an air filter and then placed into the EVG-501

bonder. For each experimental run, all bond procedures were identical except for the voltage that was applied during the bond. Bond parameters from (2) were used, heating the wafers up to 160°C, applying 2000N of force to the wafer pair, and applying the voltage for 15 minutes. A run for PMMA was also done at 90°C, to observe behavior below the glass transition temperature of PMMA.

Careful note must be taken of thermal considerations when performing polymer bonding. In initial tests, the wafers were heated before being placed in contact, then the voltage was applied, removed, and the wafers were allowed to cool. Due to differences of thermal expansion rates, this procedure led to misalignment across the wafer. The solution was to place the wafers in contact and apply the voltage before heating. This, however, led to shearing of the polymer. The final solution was twofold: improve adhesion of the polymer and control thermal considerations. To improve adhesion, an adhesion promoter was spun onto the thick glass waver immediately before bonding (after the rigorous clean, and in place of an oxygen plasma treatment. The coverslip still went through the oxygen plasma. To control thermal considerations, the bond recipe was written to closely control the rates of heating and cooling of the top and bottom portions of the bond tool. It was discovered that before this adjustment, the top and bottom were heating and cooling at vastly different rates, leading to polymer shearing. But controlling these rates, a uniform heating and cooling was established, and the thermal stress was minimized. This led to a bond that was well-aligned, with vertical sidewalls, and few defects due to thermal stress.

Testing

To quantify the strength of the bonds, the “razor blade” method was used (26). In the razor blade test, a blade of known thickness is inserted into the bond interface. The distance that the debonded area extends from the blade is an indicator of bond fracture surface energy. Each bonded wafer was diced into 1cm wide strips to most closely approximate ideal dual cantilever geometry to minimize error (27). For each wafer pair, at least three measurements were made on at least four of the diced strips. Other tests were performed on selected wafer sets. One process run included particles in the resist, creating voids between the wafers after bonding. The size of these voids was measured to determine if voltage can decrease void size. Additionally, after debonding, it was recorded which wafer the polymer was attached to – to indicate the location of the weaker bonding surface.

Results and Discussion

The results show that the bond strength is improved by applying a voltage, but the direct relationship and cause is an avenue of future work.

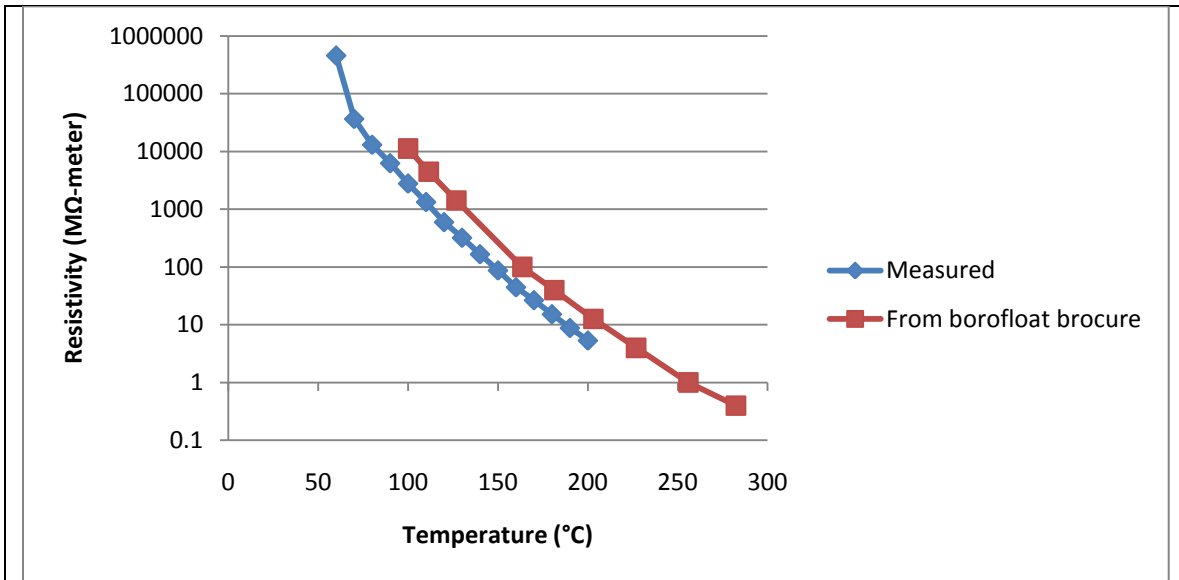


Figure 19: Measured resistivity values for Borofloat and values from Borofloat datasheet (43).

Resistivity

The resistivity data for Borofloat glass is shown in Figure 19. The data for the polymers is not shown in this plot, as the quantitative resistance data from those tests is inconclusive. As shown in Figure 17, the measured resistance of the polymer layers changes quickly over time. The initial spike in the conductivity can be interpreted as several things. This could be the bulk resistance of the polymer, which then becomes polarized, increasing the resistance (42). Another interpretation is that the bulk resistance is still very high, and the measured spike is due to stored charge or a spike simply due to the contact method or a measurement transient. As these results are not well-explained, the quantitative resistance data was deemed not reliable. However

However, regardless of mechanism, the polymer quickly reaches a high-resistance state. Therefore, the equation used in the electrostatic force model is a valid approximation.

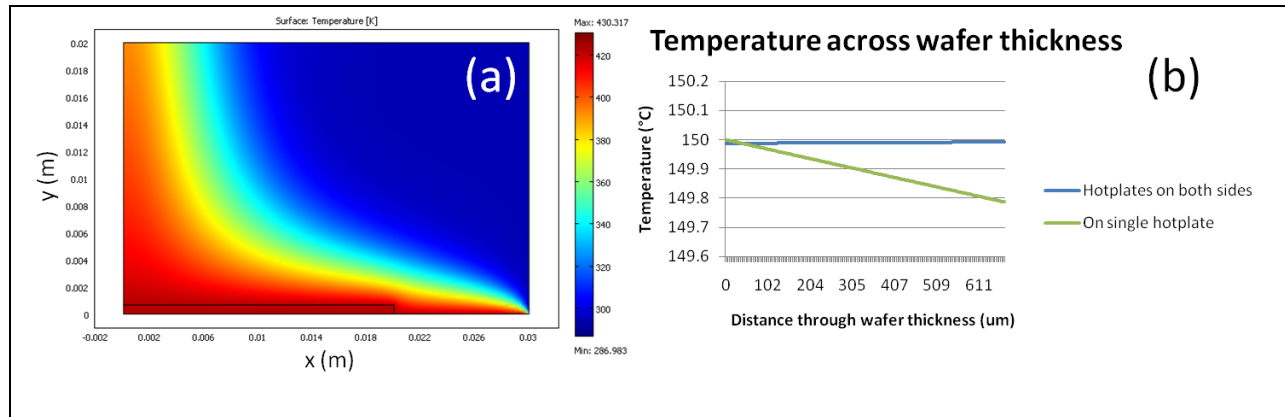


Figure 20: Simulations to evaluate temperature gradient across wafer on hotplate. (a) heat-map of temperature for radial slice of wafer showing cooling properties of air flow. (b) plot of temperature across the wafer. A wafer sitting on a hotplate shows a variation of 0.2° C across the wafer.

An additional note to consider is the temperature distribution across the wafer thickness during these experiments. The experiments were performed on a hotplate in a fume hood, so there is cooling air flow across the top of the wafer, cooling it somewhat. COMSOL simulations of the temperature across the thickness of the wafer indicate that when sitting on a hotplate, the temperature at the top surface of the wafer can vary around 0.2° C from the temperature of the hotplate, as shown in Figure 20. Experiments were performed with another hotplate on the top surface of the wafer, ensuring uniform temperature, but it was determined that this level of temperature control was not necessary. Instead, the temperature gradient of 0.1% was tolerated.

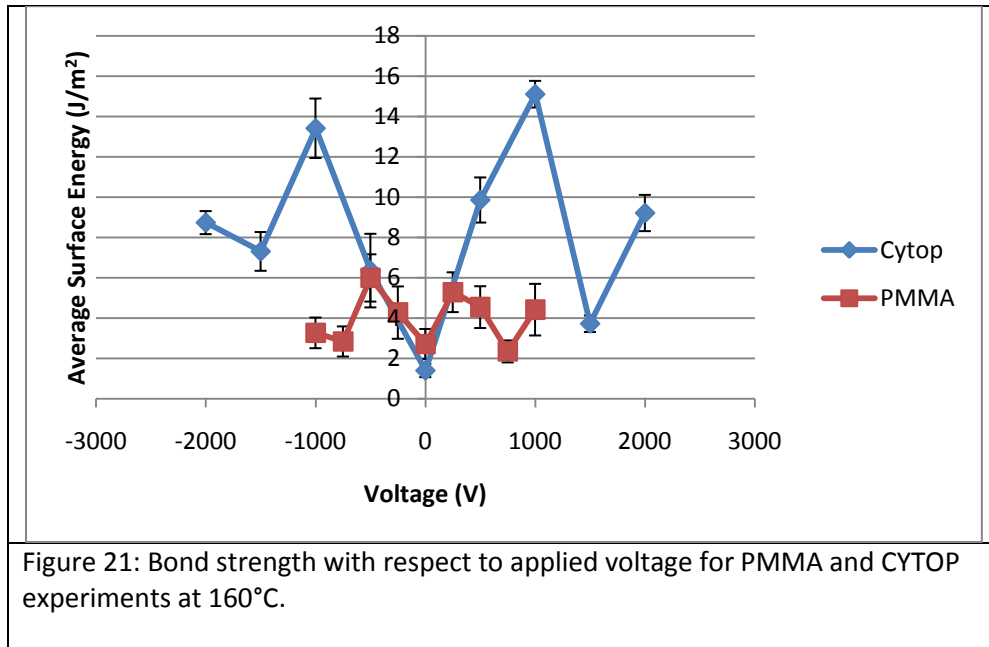
Bonding Experiments

The various experiment runs provided information on the voltage effect on bond strength, the voltage effect on uniformity and void size, the temperature effect on bond strength and uniformity, and the identification of which interface was the source of bond failure.

Voltage effect on bond strength

The results from the bonding experiments are shown in Figure 21. Applying a voltage does, in general, lead to an improved bond. However, the bond strength does not follow directly with applied voltage.

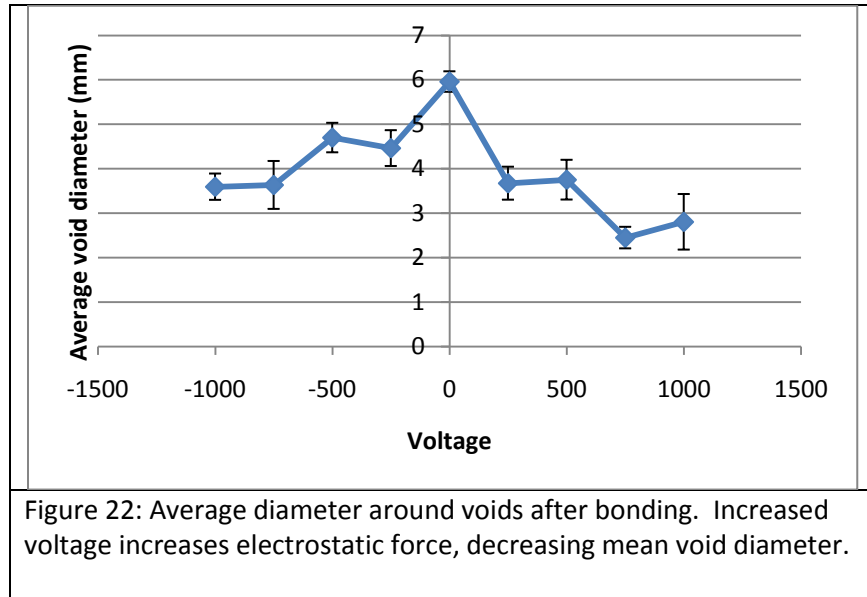
The improved bond strength due to an applied voltage fits with other types of bond optimization results (11) (13). The applied electrostatic pressure enhances the intimate contact of each surface (4) (13). Also, bonding is sensitive to surface roughness and a high applied force can cause the polymer to flow over surface irregularities (12).



However, a higher applied voltage does not always result in a stronger bond. This agrees with the results of (22)(29). Those authors do not explore the reasons behind the decreased bond strength at higher voltages, and while these results were for an anodic bond, the mechanism may be similar and bears exploration. There are two potential reasons for the decreased bond strength at higher voltages. First, we expect that some electrochemical reaction is occurring at the interface of the glass and the polymer. While this reaction may lead to the increased bond strength at moderate voltages, the excessive voltages may lead to overproduction, weakening the bond strength. Another possible cause of decreased bond strength at higher temperatures is an increase in the size of the charge depletion layer in the glass. At higher voltages, the Na⁺ ions evacuate a larger region in the glass, effectively increasing the size of the nonconduction region in the glass, increasing the distance across which the voltage drop occurs. Because the attractive force between the polymer and the glass is inversely proportional to the distance squared, this increase in distance may have a large effect on the bond strength.

Voltage effect on void size

The void size measurements are shown in Figure 22. This data presents a strong argument for the usefulness of voltage-assisted polymer bonding in improving yield. Void diameter decreases with voltage, as expected from the electrostatic force applied across the air gap. While the size of the particles was not controlled, we are assuming that the sizes are distributed similarly across wafers. This is a valid assumption, as all wafers were coated with resist from the same closed dispensing apparatus, which was not opened in between coatings.



Temperature

Experiments were also performed with PMMA at two different temperatures. While the experiments at 90°C produced higher bond strength, the experiments at 160°C were much more uniform, had fewer voids and more pieces survived dicing. This fits with the results of (33) where a higher temperature produced a more uniform bond (as explained earlier), but differences in thermal expansion caused strain at the boundary, decreasing bond strength.

Identifying stronger interface

Figure 23 shows the recorded data of the location of the polymer on the wafers after debonding. The polymer was spun onto the top substrate, so with increasing positive voltage, we see that the force across the gap between the polymer and the bottom wafer must be much greater than that to the top wafer, as the polymer preferentially adheres to the bottom wafer with increasing voltage. The polymer is always on the top wafer for a negative applied voltage, indicating that it preferentially bonds to the negative surface.

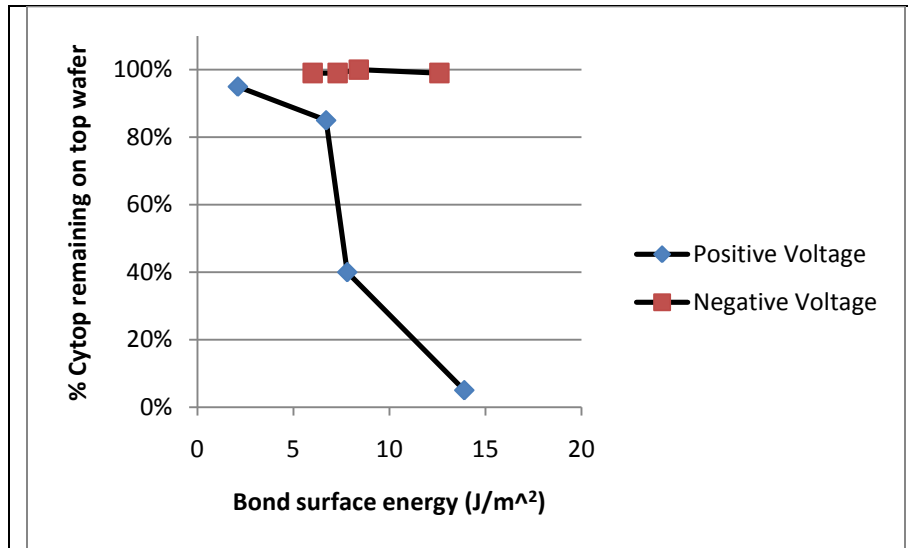


Figure 23: Location of polymer with respect to bond strength. May support theories for electrochemical interaction or charge movement.

Because the charge carriers in glass are positive, the voltage drop within the glass is always far greater near the positive electrode than the negative(44). This could explain the preferential adhesion of the polymer towards the negative electrode. A larger voltage drop would indicate a larger potential near that surface, producing a higher electric field at that interface.

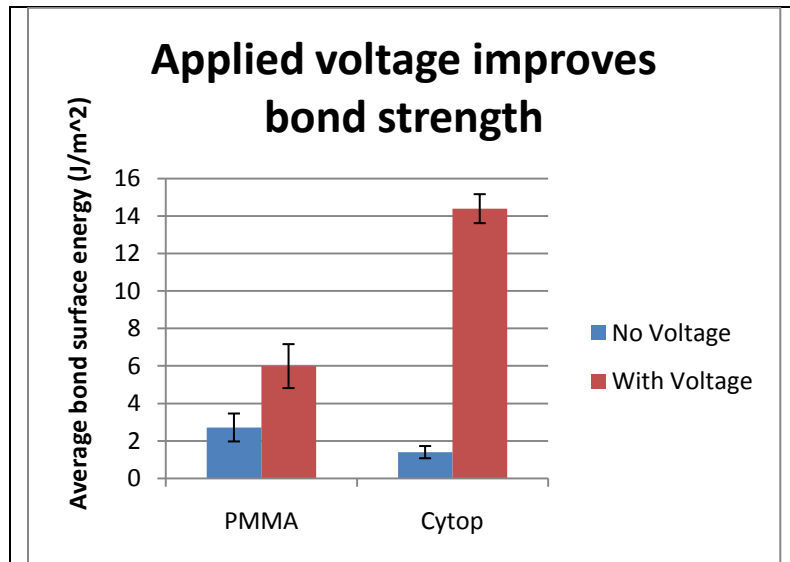


Figure 24: Comparing the bond surface energy of polymer bonds with and without voltage. The "with voltage" data is an arithmetic mean across the many different magnitudes used. Therefore, the standard deviation is large, but the mean value indicates strongly the benefit of applied voltage. Also, the "no voltage" data was produced using an adhesion promoter and plasma surface activation – standard methods to maximize bond strength.

Voltage assisted Conclusion

A method for low-temperature bonding of glass wafers was explored. This method achieves high strength, uniformity, and yield. Improvement upon the bond strength from best-known procedures is demonstrated in the strength plots of Figure 24. This bond procedure can likely be used for polymer bond of any material with a high resistivity. By applying a voltage to a polymer bond, bond strength is improved and debonded area around particles is decreased. These improvements are most likely to a conformal electrostatic force. While applying a voltage during polymer bonding is definitely beneficial, a greater voltage does not always create a stronger bond. Further work is suggested to explore the mechanism of bonding and

explain the deviation from the direct force model. Further work is also required to optimize the voltage and temperature for each polymer that is desired.

Conclusions

A low temperature, high strength method for glass-glass bonding will be useful in many areas of fabrication. In this chapter, several methods were explored. Anodic-type glass-glass bonding was found to achieve very high strength bonds, but did not fit process considerations for optical clarity. The process of voltage-assisted polymer bonding was developed, and was found to provide high quality bonds. It was found that the void size decreased linearly with applied voltage, while the bond strength did not increase in the same manner. However, applying any voltage to a polymer bond was found to increase the bond strength. Further work can explore the mechanism of the bond strength as well as the optimal parameters for various polymers and thicknesses.

Works Cited

1. *Fabrication and mechanical testing of glass chips for high pressure synthetic or analytical chemistry.* **Oosterbroek, R.E., et al.** 2006, *Microsystem Technologies*, Vol. 12, pp. 450-4.
2. *A low temperature biochemically compatible bonding technique using fluoropolymers for biochemical microfluidic systems.* **Han, A., et al.** 2000. pp. 414-418.
3. *A fast prototyping process for fabrication of microfluidic systems on soda-lime glass.* **Lin, Che-Hsin, et al.** 2001, *Journal of Micromechanics and Microengineering*, Vol. 11, pp. 726-732.
4. *Glass-to-glass anodic bonding process and electrostatic force.* **Wei, J, et al.** 2004, *Thin Solid Films*, Vols. 462-463, pp. 487-491.
5. *Glass-to-glass anodic bonding with standard IC technology thin films as intermediate layers.* **Berthold, A., et al.** 2000, *Sensors and Actuators A*, Vol. 82, pp. 224-228.
6. *Fabrication of nanofluidic devices using glass-to-glass anodic bonding.* **Kutchoukov, V., et al.** 2004, *Sensors and Actuators A*, Vol. 114, pp. 521-527.
7. *Fabrication and characterization of 20 nm planar nanofluidic channels by glass-glass and glass-silicon bonding.* **Mao, Pan and Han, Jongyoon.** 2005, *Lab on a Chip*, Vol. 5, pp. 837-44.
8. *Applying Tauchi methods for solvent-assisted PMMA bonding technique for static and dynamic u-TAS devices.* **Hsu, Yi-Chu and Chen, Tang-Yuan.** 2007, *Biomed Microdevices*, Vol. 9, pp. 513-22.
9. *Low temperature bonding of PMMA and COC microfluidic substrates using UV/ozone surface treatment.* **Tsao, C.W., et al.** 2007, *Lab on a Chip*, Vol. 7, pp. 499-505.
10. *New results on plasma activated bonding of imprinted polymer features for bio MEMS applications.* **Kettner, P., et al.** 2006, *Journal of Physics: Conference Series*, Vol. 34, pp. 65-71. International MEMS Conference 2006.
11. *Study of PMMA thermal bonding.* **Zhu, Xuelin, et al.** 2007, *Microsystem Technologies*, Vol. 13, pp. 403-7.
12. *PMMA to SU-8 bonding for polymer based lab-on-a-chip systems with integrated optics.* **Bilenberg, B., et al.** 2004, *Journal of Micromechanics and Microengineering*, Vol. 14, pp. 814-8.
13. *Low-temperature direct bonding of poly(methyl methacrylate) for polymer microchips.* **Shinohara, Hideotoshi, Mizuno, Jun and Shoji, Shuichi.** 2007, *IEEJ Trans: Transactions on Electrical and Electronic Engineering*, Vol. 2, pp. 301-6.

14. *Silicon wafer-to-wafer bonding at $T < 200^{\circ}\text{C}$ with polymethylmethacrylate.* **Eaton, William P., Risbud, Subhash H. and Smith, Rosemary L.** 1994, Applied Physics Letters, Vol. 65, pp. 439-441.
15. *Wafer direct bonding: tailoring adhesion between brittle materials.* **Plößl, Andreas and Kräuter, Gertrud.** 1999, Materials Science and Engineering, Vol. R25, pp. 1-88.
16. *Bonding of glass-based microfluidic chips at low-or room-temperature in routine laboratory.* **Chen, Lingxin, et al.** 2006, Sensors and Actuators B, Vol. 119, pp. 335-44.
17. *PMMA to SU-8 bonding for polymer based lab-on-a-chip systems with integrated optics.* **Bilenberg, B., et al.** 2003.
18. *Silicon Wafer Bonding Mechanism for Silicon-on-Insulator Structures.* **Abe, Takao, et al.** 1990, Japanese Journal of Applied Physics, Vol. 29, pp. L2311-L2314.
19. *Tensile strength characterization of low-temperature fusion-bonded silicon wafers.* **Muller, B and Stoffel, A.** 1991, Journal of Micromechanics and Microengineering, Vol. 1, pp. 161-166.
20. *Interface Strength Characterization of Bonded Wafers.* **Petzold, M., et al.** [ed.] C.E. Hunt, et al. 1995. pp. 380-389.
21. *A Kinetics Study of the Bond Strength of Direct Bonded Wafers.* **Farrens, S.N., et al.** 1994, Journal of the Electrochemical Society, Vol. 141, pp. 3225-3230.
22. *A test structure for characterization of the interface energy of anodically bonded silicon-glass wafers.* **Knechtel, R., Knaup, M. and Bagdahn, J.** 2006, Microsystem Technologies, Vol. 12, pp. 462-7.
23. *A test structure for bond strength measurement and process diagnostics.* **Horning, R.D., Burns, D.W. and Akinwande, A.I.** [ed.] U. Gosele, et al. 1992. pp. 386-393.
24. **Tong, Q.Y. and Gosele, U.** *Semiconductor Wafer Bonding.* s.l. : Wiley and Son, 1999.
25. *Accurate characterization of wafer bond toughness with the double cantilever specimen.* **Turner, Kevin T. and Spearing, S. Mark.** 2008, Journal of Applied Physics, Vol. 103, p. 013514.
26. *Bonding of silicon wafers for silicon-on-insulator.* **Maszara, W.P., et al.** 1988, Journal of Applied Physics, Vol. 64, pp. 4943-50.
27. *Characterization of directly bonded silicon wafers by means of the double cantilever crack opening method.* **Bagdahn, J., et al.** 1998. Vols. PV97-36, pp. 291-8.
28. **Berthold, Axel.** *Low-temperature wafer-to-wafer bonding for microchemical systems.* Delft University of Technology. 2001.
29. *Anodic bonding of glass to aluminum.* **Schjolbert-Henriksen, K., et al.** 2006, Microsystem Technologies, Vol. 14, pp. 441-9.

30. **Wohltjen, H. and Giuliani, J. F.** *Method for bonding insulator to insulator.* 4452624 US, 1984.
31. *Anodic bonding using the low expansion glass ceramic Zerodur.* **Elp, J. Van, Giesen, P.T.mM. and der, J.J. van.** 2005, Journal of Vacuum Science and Technology B, Vol. 21, pp. 96-8.
32. *Fabrication of a microchannel device by hot embossing and direct bonding of Poly(methyl methacrylate).* **Shinohara, H., Mizuno, J. and Shoji, S.** 2007, Japanese Journal of Applied Physics, Vol. 46, pp. 3661-4.
33. *Integration of electrodes in Si channels using low temperature polymethylmethacrylate bonding.* **Dukkipati, V.R. and Pang, S.W.** 2007, J. vac. Sci Technol. B, Vol. 25, p. 368.
34. *Fabrication and characterization of poly(methyl methacrylate) microfluidic devices bonded using surface modifications and solvents.* **Brown, Laurie, et al.** 2006, Lab on a Chip, Vol. 6, pp. 66-73.
35. *Adhesive bonding in microelectronics and photonics.* **Yacobi, B. G., et al.** 2002, Journal of Applied Physics, Vol. 91, pp. 6227-6262.
36. *Studies of the adhesion properties of LIGA microstructures by X-ray spectroscopy and mechanical measurements.* **Kadereit, D., et al.** 1996, Microsystem Technologies, Vol. 2, pp. 71-74.
37. *Adhesion promotion between poly(methylmethacrylate) and metallic surfaces for LiGA evaluated by shear stress measurements.* **Khan, C. G. and Das, S.S.** 1998, Journal of Vacuum Science and Technology B, Vol. 16, pp. 3543-3546.
38. **Gelest, Inc.** Silane coupling agents. 2006.
39. *Growth behavior and surface topography of different silane coupling agents adsorbed on the silicon dioxide substrate (0001) for vapor phase deposition.* **Cai, Chujiang, et al.** 2007, Journal of Material Science, Vol. 42, pp. 6108-6116.
40. *Cytop Data Sheet.* s.l. : AGC Chemicals, Asahi Glass Co., Ltd.
41. *PMMA Data Sheet.* s.l. : Microchem, 2001.
42. *Direct-current polarization during field-assisted glass-metal sealing.* **Wallis, G.** 1970, Journal of the American Ceramic Society, Vol. 53, pp. 563-567.
43. *Schott Borofloat 33 - technical specifications.*
44. *Space charge and electrode polarization in glass, II.* **Sutton, Paul M.** 1964, Journal of the American Ceramic Society, Vol. 47, pp. 219-230.
45. **Wu, Souheng.** *Polymer interface and adhesion.* s.l. : CRC Press, 1982.
46. *Accurate characterization of wafer bond toughness with the double cantilever specimen.* **Turner, Kevin T. and Spearing, S. Mark.** 2008, Journal of Applied Physics, Vol. 103, p. 013514.

47. *Glass Transition Temperature for PMMA from Molecular Dynamics Simulations.* **Tsige, Mesfin and Taylor, P.L.** 2001. p. 40112.

48. *Double-cantilever cleavage mode of crack propagation.* **Gillis, Peter P. and Gilman, J.J.** 1964, Journal of Applied Physics, Vol. 35, pp. 647-58.

Chapter 5: Plasmonic readout

Microfluidic devices for optical detection currently provide a useful tool in many biological applications. However, the ultimate resolution and sensitivity of these tools are often limited by their architecture. In this thesis, work has been presented to improve upon the state of microfluidic optical sensors through avenues including: integrated optics to reduce background noise and simplify design, and nanofluidics to reduce sample volume, improving sensitivity. Another method to improve the resolution and sensitivity of an optical detection device is to reduce volume of material that interacts with the excitation light. In this chapter, the work to integrate a plasmonic readout into the opto-nanofluidic device is presented. This readout mechanism not only achieves benefits due to a reduced excitation volume, but it also achieves a resonant field enhancement. A background on volume reducing methods is provided as well as a primer on plasmonics. Simulations were performed to maximize coupling at the proper wavelengths and fabrication and test efforts are presented. It is found that it is possible to integrate the plasmonic stripe into these devices and it performs to provide a localized excitation source. A gold stripe of 120nm wide and 80 nm tall provides the best coupling to red light. Most of the work in this chapter is based on work done in collaboration with the Crozier group at Harvard University. Future work can further optimize the structures to achieve improved bandwidth, higher field enhancement, or higher field localization. Tests of the integrated system, showing the capabilities of the plasmonic readout to excite fluorescent tags in a flowing system, are provided in Chapter 6.

Motivation	106
Plasmons.....	109
Evanescent coupling	110
Plasmons in Biology	111
Plasmonic readout overview	112
Simulation.....	113
FDTD Background.....	113
Dispersion relation and absorption with periodic boundary conditions	115
Dispersion relation and absorption with reduced area	120
Metal Properties	124
Plasmonic Testing.....	127
Transmission spectrum	127
NSOM Measurements.....	132
Conclusion.....	136
Works Cited.....	137

Motivation

To enable new biological sensing modalities, this thesis strives to present a method to produce a high resolution, high sensitivity optical microfluidic detection device. One general way to achieve both high resolution and high sensitivity is by reducing the optical excitation volume (1). As an additional method to improve sensitivity, a resonant field enhancement would ensure that the fluorescent signal was well above the noise floor. In this chapter we explore the use of a plasmonic resonator to achieve both these goals of reduced excitation volume and enhanced electromagnetic fields.

High resolution is achieved with reduced excitation volume when the excitation volume is smaller than the resolution of your detection optics, providing higher accuracy of localization of the detected signal. Conventional optics are limited by a phenomena called the diffraction limit, which dictates that, due to the wavelike properties of light, any beam cannot be focused to a spot smaller than approximately 0.6 times the free-space wavelength of the light. At optical wavelength, this limits us to a maximum achievable resolution of $\sim 300\text{nm}$, which provides resolving power to the order of 1000 base pair, which is much too coarse to achieve strong fingerprinting results.

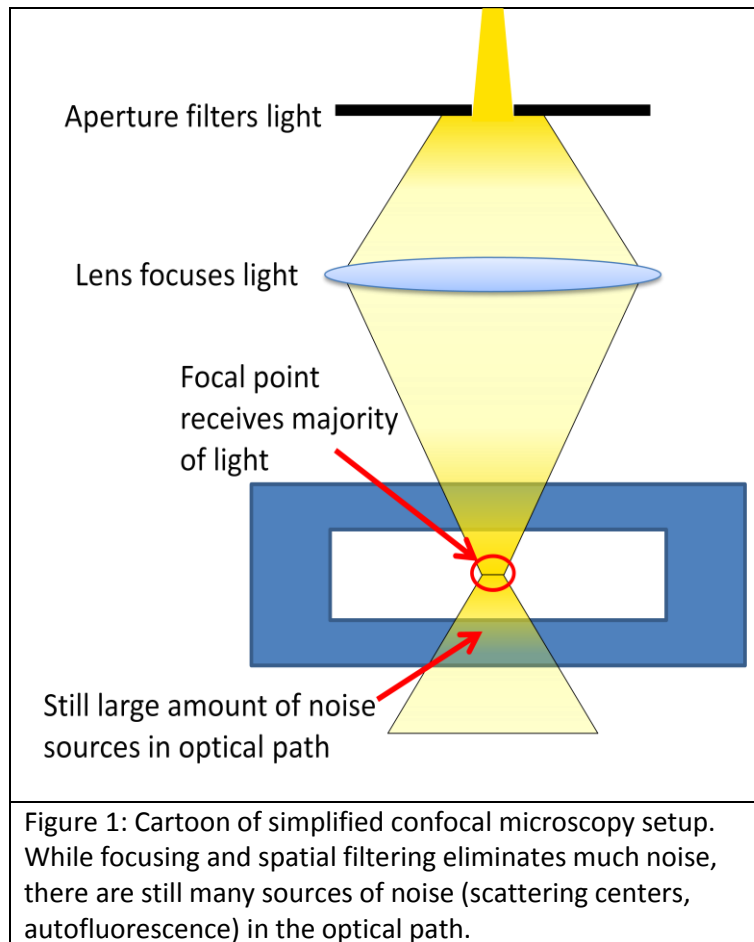
Several groups have done explored methods to achieve high resolution readout. Work has been done in structured illumination (2), and shining illuminating light through a slit (3) to achieve a high resolution readout. However, these techniques did not improve the sensitivity, as light would still illuminate the entire channel and decreasing the excitation light also decreased the signal.

Sensitivity is improved using a reduced excitation volume because less material is exposed to excitation, there is less autofluorescence, and therefore less background noise. It has been shown that in microfluidic applications aimed at single-molecule detection, most of the noise comes from Raman scattering of the water containing the sample (4). Additional sources are impurities in the excited material (either the water or the walls of the microfluidic channel (5)). Common methods to improve sensitivity usually involve simply integrating more of the system onto the chip, eliminating extraneous background noise.

Additional methods to improve sensitivity common rely on two-photon excitation methods (6). Two-photon excitation is a common tool used in live tissue imaging, due to its ability to do high-depth imaging in three dimensions due to the effective penetration of IR light through tissue. In two-photon excitation, the sample, which includes fluorescent particles, is illuminated with red-shifted light. This light is lower energy, so any single photon will not excite fluorescence. A fluorophore will only be excited when excited by two photons at the same time. Since the probability of two photons hitting the same molecule is extremely low, there is little light generated. However at the focal point of excitation, this probability is greatly increased, so the sample in the small volume in focus is much more likely to generate light than the rest of the sample. Therefore there is very little light from the rest of the sample, reducing the background noise. Two-photon imaging, however, has some drawbacks. It still requires an expensive confocal microscope setup. Additionally, a high photon flux is required, because

the probability of two photons hitting the same molecule is so low, necessitating a high power illumination source, usually a femtosecond laser. These requirements make the device large and costly.

Another method to achieve high sensitivity is time-gated detection, also known as fluorescence lifetime imaging (when utilized in conjunction with a microscopy setup). In time gated detection, the unique fluorescent lifetime of the sample of interest is utilized to ignore signals from other sources. Fluorescent materials all have a characteristic (but not necessarily unique) fluorescence lifetime. This is the amount of time that the molecule stays in an excited state, which therefore determines the time delay between absorbing an excitation photon and emitting the fluorescence photon when the molecule decays to the relaxed state. In time-gated detection, the time delay for the fluorescent sample is known and only signals that arrive around that time period are noted, and all other signals are ignored. This method is useful as it ignores reflected and scattered light, only allowing fluorescence light with the same lifetime. Time-gated detection can be used in conjunction with confocal microscopy or two-photon imaging to improve the sensitivity of those techniques. However, it requires sensitive timing equipment (lifetimes are typically in the nanosecond range), as well as a large optical setup.



Most systems utilize confocal microscopy to read out optical tags. A cartoon describing the typical operation of this type of system is shown in Figure 1. Although a confocal system eliminates a large amount of extraneous autofluorescence by reducing the excitation volume via focusing, the light is still travelling through the entire thickness of the sample. Even if it is out of focus, this light can cause scattered light and autofluorescence. Additionally, a confocal system is still limited by the diffraction limit.

As mentioned above, one way to achieve both high resolution and high sensitivity in a microfluidic optical detection system is to reduce the excitation volume. There has been some work in reducing the excitation volume for optical microfluidic devices. The standard method of achieving a small excitation volume is to utilize

confocal microscopy for detection (5). In this type of system, the illuminating light is focused down to a

spot that is coincident with the focal point of the imaging portion of the system. This type of setup eliminates out-of-focus illumination, improving sensitivity and enabling three-dimensional imaging. This technique achieves that diffraction limited resolution and high sensitivity through a reduction of the highly excited volume.

However, the benefits of a confocal microscope are limited: the spot size is limited by the diffraction limit. Also, the principle of using propagating illumination to excite a sample leads to extraneous excitation. Light must travel through the material that comprises the walls of the microfluidic channel and through the entire height of the channel and back again in order to excite a fluorescent sample. Even if this light is out of focus, it can produce background noise. By utilizing some sort of resonator on an integrated diffused waveguide, we are able to circumvent this drawback, as excitation light does not need to travel that long distance, potentially exciting autofluorescence from the materials or impurities.

An additional goal that will enable high sensitivity optical detection is increasing the intensity of the exciting electromagnetic fields (4) (7). In order to increase the exciting fields without increasing the background noise, a resonant phenomena or structure must be employed. This has been explored by several groups. The most popular method of resonant excitation for optical detection is utilizing a ring resonator. A ring resonator is an optical waveguide that is bent into a circle. Light propagating in this ring will interfere with itself as it goes around the circle, and only signals that have a wavelength that will fit an integer number of times around the circle will be allowed. All other signals will not constructively interfere and will die out. This resonant phenomenon is dependent on the size of the ring and the optical properties of the waveguide and the surrounding material. Any shift in either of those properties will result in a corresponding shift in the resonant wavelength of the resonator. In this manner, when a biological sample attaches to a functionalized surface of a ring resonator, the resonant frequency will shift, and this attachment can be detected. There is not actually much work done in detecting fluorescent signals from samples that attach to resonators. However, there is much work done with utilizing fluorescence from plasmonic resonators, and we will explore that phenomenon soon.

In this chapter we explored a method to achieve both reduced excitation volume as well as enhanced fields: utilizing a plasmonic resonator. A background on plasmons and their current use in biology and optical sensing is presented. Then, the work done in this thesis is shown.

Plasmons

A plasmon is a collective oscillation of electrons in a metal. To better understand what this means, consider a thought experiment using the free-electron model of a metal atom. Electrons are orbiting around a heavy nucleus of opposite charge. If all the electrons in a piece of metal were simultaneously pulled to one side (the nuclei staying in the same place), and then released, the electrons would oscillate back and forth about the positively charged, stationary nucleus. This resonant phenomenon is due to the mass of the electrons and the restoring force between them and the nucleus; producing the textbook example of a simple harmonic oscillator. The quantization of a group of these oscillators is called a plasmon. The resonant frequency of this oscillation is in the optical regime, encouraging the use of plasmonic resonators in optical detection tools.

The plasmonic effect has been used for centuries to utilize the wavelength-specific interaction with light that the phenomenon presents. A popular example of historical use of plasmons is in glass pottery and windows. The common example of the Lycurgus cup (Byzantine empire, 4th century, A.D.) demonstrates interesting optical behavior of having a striking red color when viewed in transmitted light, but green in reflection. This behavior is due to the presence of Au nanoparticles that have a strong plasmonic absorption in the green part of the visible spectrum embedded throughout the glass (8). After these uninformed uses of metal nanoparticles, Mie (9) investigated the electromagnetic properties of small particles and Ritchie investigated the same for surfaces (10). Further exploration of the actual plasmonic behavior in these areas was performed later by Kreibig and Vollmer and Bohren and Huffman (11) (12) on metal particles and Raether (13) for films and rough surfaces.

There are several benefits of using plasmonic resonances as a readout tool. Primarily, by having a quality factor greater than unity, the resonant system produces electromagnetic field strengths that are higher than those of the driving light. This is standard behavior for a resonant system. A second benefit of utilizing plasmons is that they occur at optical frequencies, enabling integration with the common optical tags, filters, and methods currently used in biology. A third benefit of a plasmonic resonance is the small dimensions possible for structures that can support these oscillations.

While the oscillation of an electron about the nucleus as described in the thought experiment above can be arbitrarily small (neglecting quantum mechanical effects), the plasmon modes supported by a structure are determined by shape and material parameters. To understand this effect, consider a plasmon on the surface of a continuous metal film.

The plasmon can be represented (in one dimension) as an electromagnetic plane wave (the standard approximation for most waves), which can be described by the simple equation:

$$\vec{E} = \vec{E}_0 e^{j(\omega t - \vec{k}\vec{r})}$$

In this equation, E_0 is the intensity of the field, ω is the angular frequency and k is the wavevector. The wavevector is an important tool in electromagnetic that many not in the field may not know. To understand what the wavevector means, it is useful to look at the equation above and compare the wavevector with the angular frequency, which most people are familiar with. Simply put, where ω is

the change in the phase with respect to time, k represents the change in the phase with respect to space. So, the wavevector is the component that describes how the wave looks in space.

The wavevector is inversely proportional to the spatial wavelength of the wave. Therefore, with a high value of k , the spatial wavelength will be small. The spatial wavelength corresponds to the dimensions of structures that will support a specific wave. For a given frequency, a Plasmon has a higher k value than light in a dielectric medium. Therefore, a plasmon at optical frequencies can exist on structures smaller than free-space optical wavelengths.

To further decrease the dimensions of the excited fields, plasmonic structures can also be shaped to induce “hot spots” at sharp corners or very small gaps (14). By utilizing this effect, it is possible to obtain highly enhanced fields in dimensions that are much smaller than achievable with standard optical focusing techniques (2) (15) (16) (14) (17).

Considering these beneficial aspects of a plasmonic resonance (resonant phenomena in the optical range, but with sub-optical oscillation dimensions), it presents a perfect contender for an application to provide reduced excitation volume and enhanced excitation fields in an optical microfluidic detector. Additionally, the enhancement benefit from a resonant phenomenon could provide improved sensitivity through stronger excitation fields in a small volume (18) (19).

Evanescent coupling

Many designs that utilize the plasmonic effect take on unintuitive design choices. These choices are necessitated by the difficulty of actually coupling light to a plasmonic resonance. To understand this difficulty, a short background on electromagnetic waves must be presented.

The relationship between ω and k is called the dispersion relation, and is a common tool in electromagnetic wave analysis. For modes to couple to each other they must have a point where the plots of their dispersion relation cross (where they have equivalent values of ω and k). The dispersion relation for a surface plasmon (parallel to a surface in the x direction) is described by the equation:

$$k_x = \frac{\omega}{c} \left(\frac{\epsilon_1 \epsilon_2}{\epsilon_1 + \epsilon_2} \right)^{\frac{1}{2}}$$

In the above equation, c is the speed of light in a vacuum, and ϵ_1 and ϵ_2 are the electric permittivity of the two materials that form the surface that the plasmon exists on at frequency ω . For given, linear values of ϵ_1 and ϵ_2 , the surface plasmon dispersion relation will never cross the dispersion relation (light lines) for those materials. Therefore, it is not possible to directly couple into a surface plasmon.

Therefore, it is necessary to excite a plasmon in some manner where the energy or momentum of the excitation light is shifted in order to be able to couple to the plasmon. This can be achieved in several ways. First, surface roughness can provide the desired momentum shift to enabling coupling to plasmons. However, this can also create unwanted scattered light.

Another general method for coupling to a plasmon involves using evanescent fields and an intermediate material. If the plasmon dispersion relation is based on values ϵ_1 and ϵ_2 from two materials, but the light is actually coming in through a different material (e.g. a prism) with permittivity of ϵ_3 , it is possible, through choice of material, for the dispersion relation lines to cross. Commonly, light is reflected off of a material below the interface of interest, and the evanescent fields reach to the interface where the surface plasmon is desired. The evanescent fields have propagation constants based on the incident light and material, but can then be used to excite the plasmon on the second interface. In this manner, it is possible to couple to plasmons via evanescent fields.

Plasmons in Biology

The plasmonic effect has been used in biological applications for some time, even before it was known. It was first utilized by the discovery of Surface Enhanced Raman Spectroscopy (SERS). SERS is a variant of Raman Spectroscopy, a spectroscopic technique for identifying materials of interest. In Raman spectroscopy, a sample is illuminated with laser light. The light interacts with the molecules in the sample, exciting molecular vibrations, phonons or other phenomena, subsequently extracting energy from the light, resulting in a frequency shift for each mode that is excited. This collection of frequency-shifted signals provides an identifying spectrum.

In SERS, it was discovered that the Raman signal of molecules on rough metal surfaces produced an enhanced Raman signal. This enhancement was as much as 10^{10} to 10^{11} (18) (20), and it turns out that the majority of that enhancement was due to the plasmonic effect (21) (22). An additional benefit of SERS is that the plasmonic fields are confined to an area very close to the surface, reducing background noise, enabling sensitive detection modalities (19).

Another application of plasmonics in biology is in Surface Plasmon Resonance (SPR) sensors. These devices are similar to the SERS ones, where a metal film is functionalized and samples of interest adhere to the surface. The device is interrogated with a collimated laser from the bottom side (where the sample adheres to the top). This laser is oriented at the proper angle to excite a surface plasmon on the top surface of the metallic surface. Like in the ring resonator sensors, the resonance is highly dependent on the proper combination of incidence angle, frequency of light, and index of refraction of the surrounding material. When samples adhere to the surface, the index of refraction changes, altering this balance. This change can be detected through an intensity change in the reflection of the laser (23).

Additional applications of plasmons in an integrated biological system involve using plasmonic fields to trap particles (24) (25) (26) (27). While those applications take advantage of the resonant behavior of plasmons and the opportunity for spatial confinement in one dimension, this work aims to take further

advantage of the properties of a plasmonic resonator to improve the resolution of a flow-based fluorescence detection system.

Plasmonic readout overview

For a high resolution, low noise optical biosensor, it is desired to have a reduced excitation volume that has much higher field intensities than the area around it. This requirement provides the high degree of localization required for high resolution detection, as well as the suppression of background noise that enables low-noise conditions. The aim of this chapter is to present work towards producing a device that achieves these goals using a plasmonic resonator.

The design of a device with plasmonic readout is described in the Introduction chapter of this thesis. Basically, a plasmonic resonator sits on top of a diffused waveguide at the intersection with a microfluidic channel. Evanescent fields from the waveguide drive the plasmonic resonance, producing confined and enhanced fields above the plasmonic resonator. These fields excite optically tagged samples as they pass over the plasmonic resonator while flowing through the microfluidic channel. This optical signal can be detected with an integrated photodetector, but in research efforts, it has been detected using a standard inverted microscope.

The shape of this plasmonic resonator has been chosen to be a rectangular bar, approximately 120nm wide, 80nm tall, and 10um long (to stretch across the microfluidic channel) (28). This simple shape was chosen after previous work considered arrays of posts or dots (29) (30). However, the bar was determined to provide sufficient field enhancement while providing significant simplification in design, simulation, fabrication, and analysis. Most of the optimization work has been altering the dimensions and metal of this bar. Further work can focus on different shapes for alternative effects.

The characteristics that make the plasmonic effect so sensitive in an SPR sensor make this device difficult to design. The highly nonlinear dependence on frequency, refractive index and (in this case) shape of the metallic structures, dictate careful design and simulation to ensure that the plasmonic resonance occurs at the proper frequencies of light. While the resonance can generally provide some enhancement across a broad band of frequencies, to ensure optimal operation, the resonance should be driven efficiently, necessitating proper design. In the rest of this chapter, that work is presented. It consists of simulating plasmonic structures of various metals and shapes and extracting their coupling and enhancement efficiency. Some tests were performed on fabricated devices, and those results were used to validate the simulations. Unfortunately, much of the tests were inconclusive due to difficulties in experimental setup and tool availability, but the simulation results match with literature values, so the simulations are considered accurate.

Simulation

To test many design variations without the need for lengthy fabrication runs, simulation tools are invaluable. In this thesis much use was made of Finite Difference Time Domain (FDTD) simulation tools. These tools were used to simulate the plasmonic components; including their coupling to waveguide modes, their field enhancement and confinement, and their spectral behavior. Through the use of FDTD simulations, it was possible to determine the proper size, shape, and metal for a plasmonic resonator to operate at desired frequencies. This section covers that work. We present a method for determining that information and provide the results for our specific application. Much of this work was performed based upon the help of the Crozier group at Harvard University. Specifically, the wave-vector isolation technique to generate dispersion relations was based on their work (29). Also, the absorption tests performed were based on their work and using their equipment (31) (30).

The goal of this simulation work was to verify that a plasmonic readout could provide a field enhancement and localization that would benefit an optical microfluidic device. The ideal information to make that determination would be a plot of the field intensity above the plasmonic stripe with respect to wavelength of input light. It may seem that this simulation could have been carried out directly, by simply simulating a plasmonic stripe on a waveguide in water. The greatest barrier to simulating the structure exactly is the difference in scale between the diffused waveguide and the plasmonic stripe. The simulation would have to extend several microns in order to provide enough space for the waveguide to confine the light. While this is not a difficulty in itself, the critical dimensions of plasmonic stripe are only tens of nanometers, necessitating a very small grid size. These two constraints would produce a simulation that required inaccessible amounts of processing power and memory.

Therefore, two methods were used to reduce the simulation domain. The first was to perform the simulation on a plain glass substrate and take advantage of periodic boundary conditions to enable many simulations, from which the desired information can be gathered. The modal behavior of the waveguide is introduced later in data processing. The second method to reduce the simulation domain was to increase the index of refraction of the waveguide with respect to the surrounding glass, to enable the shrinking of its dimensions while retaining the same modal properties. These two methods are explored below. After that, the work done to improve on the model used to simulate metal's electromagnetic properties is presented.

FDTD Background

FDTD simulation tools are programs that enable the computation of the behavior of light waves in arbitrary geometries. Essentially, these programs solve Maxwell's equations on a spatial grid, and iterate to determine the behavior of a system from a given starting point to an end time.

The input parameter for a FDTD solver is a spatial lattice indicating the permittivity and permeability for every point in the spatial domain of the simulation. The permeability and permittivity can be constant or a function of frequency. An additional input for a FDTD solver is the initial electromagnetic conditions, usually the excitation wave. Starting with the initial electromagnetic conditions, the FDTD solver numerically solves Maxwell's differential equations to determine the changes in E and H in all directions for that step in time. Maxwell's equations relate the change in time for a field at a point to the changes in space about that point, so this sort of numerical solving is possible without differential solvers. After the entire domain is solved for, the process iterates, and the domain is solved again using the new fields as the starting conditions. The electric and magnetic field values are usually computed on a Yee lattice (32). In a Yee lattice the E and M components are offset spatially in all directions by one half of a spatial grid step. In this manner, second order accuracy is enabled in the derivatives. For this thesis, the RSoft Photonics Suite, specifically their FullWAVE FDTD solver, was used. A typical simulation is shown in Figure 2. Section (a) of that figure shows the index file used for the simulations. Section (b) of that figure shows the fields for a resonant mode of an Au stripe when illuminated along the waveguide at a specific frequency.

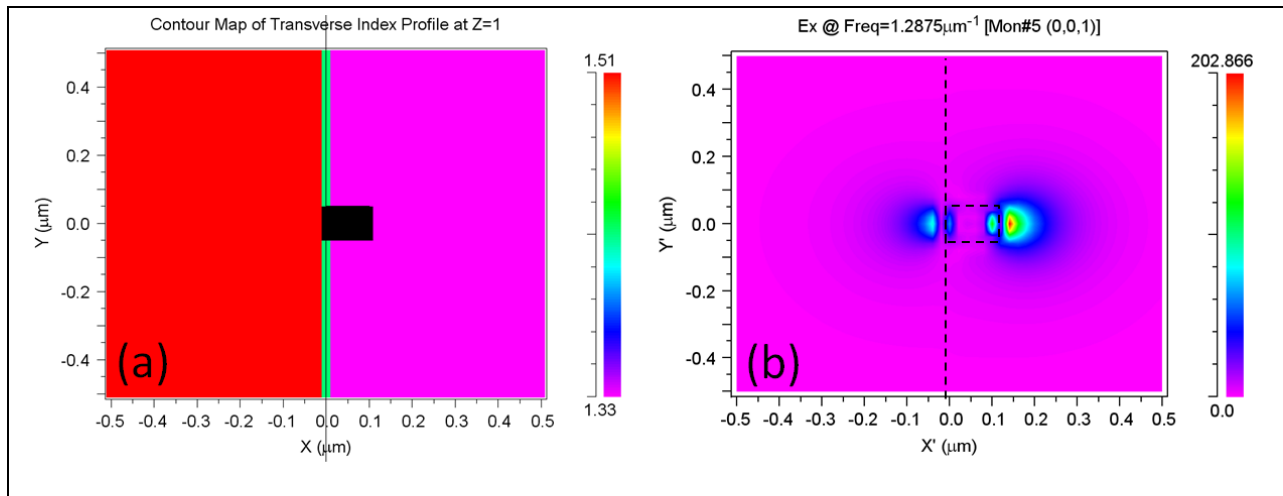


Figure 2: FDTD simulation setup and results. (a) Index distribution file for simulations. The left side shows the glass, with index around 1.5, the right side shows the water, with index around 1.33. The black box in the middle is the metal stripe with a frequency dependent index. (b) Simulation results for index file in (a). The structure outlines are shown in dotted lines. Resonant field enhancement is shown at both the metal-glass and metal-water interfaces. Results show resonant field enhancement of 200 times at around 700nm wavelength at the metal-water interface.

In the ideal form, the FDTD technique is not based on any assumptions or approximations (except for spatial discretization), so it can provide accurate results for complex phenomena. In practice, however, due to processing constraints, it is necessary to make approximations in order to have a problem that is solvable in a reasonable time period. The most direct approximations are increasing the spatial and temporal grid. This is possible up to the point where the results become affected. To know the proper size of these grids, test simulations are run with a very fine grid. The grid spacing is slowly increased

until the results change. At this point the grid is too large. In this manner, the grid size can be optimized for the tradeoff between simulation time and accuracy of results.

Another common method to reduce simulation expense is to utilize symmetry conditions in the structure. Many structures are symmetric in some dimension, enabling analysis to only be performed on a unique portion of the domain, and the results be interpreted via symmetry conditions across the rest of the domain. In the next section, some work was done using periodic boundary conditions to reduce the simulation area. It should be noted that for both methods, initial simulations were performed for continuous metal films. These simulations were performed, as the behavior of metal films is well-studied, and this provided a reliable method to validate the simulation procedure. The experiments with alternative geometries were performed only after the data from these simulation procedures were shown to match analytical and reported data from metal films.

Dispersion relation and absorption with periodic boundary conditions

The plasmonic structure being considered is a bar of regular cross-section. Therefore, it is periodic along its length and the computational domain can be reduced by taking advantage of this periodic characteristic. A periodic boundary condition is created in an FDTD tool by setting the values for E and H to be equal at opposite boundaries. This simulates the behavior of having infinitely repeating, exact copies of the structure being simulated. A phase shift can be enforced; simulating a delay between elements or angled propagation, but the structure is always representing an infinite array. This work was based on the procedures utilized by the Crozier group at Harvard (29).

The goal of these simulations was to produce a plot of the dispersion relation of the plasmon resonance on the top surface of the gold stripe. The top surface is the interface between the gold and the water in the microfluidic channel. The other surface is the interface between the gold and the glass of the waveguide. Using this dispersion relation, it is possible to extract a plot of field intensity with respect to wavelength. The reason that the dispersion relation is needed as an intermediate step is due to the different possible values of wavevector for the incident light. Light coming through the waveguide will not only have a frequency defined by the laser that is used, but it will also have a wavevector that is defined by the modes that are excited. The combination of these two parameters define the excitation phenomena. And by producing the dispersion relation, we are able to extract the values of these parameters for the plasmon mode, which we can then convert into an intensity plot with respect to frequency. Because the plasmonic stripe does not change at all along its length, the simulation domain along that dimension can be made very small – down to a single element in the spatial grid, saving computational resources.

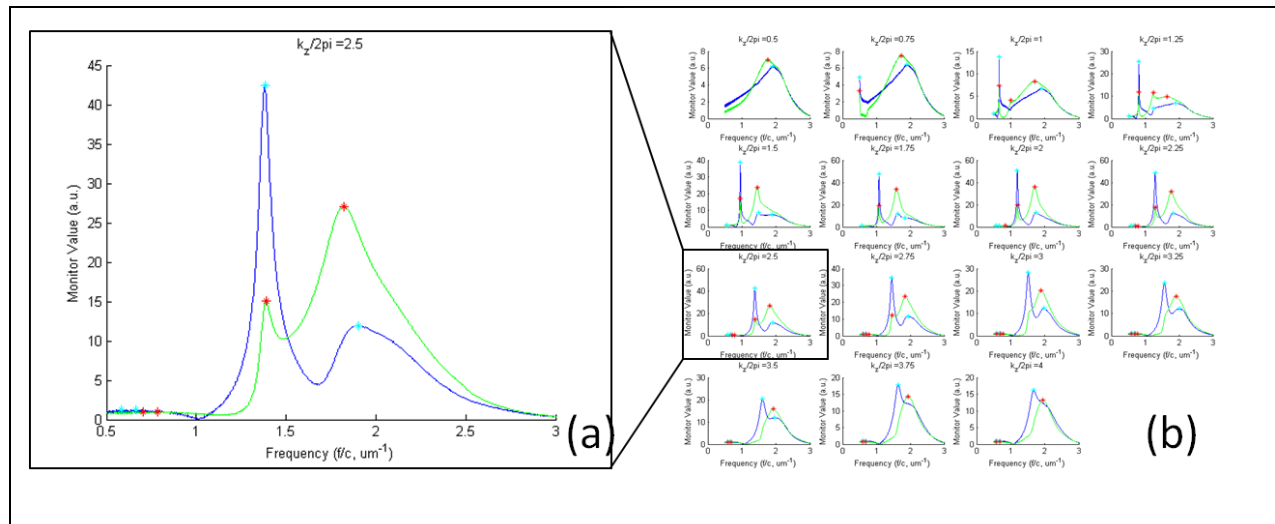


Figure 3: Spectra of field strength at material boundaries from simulations with periodic boundary conditions, enforcing wavevector values. (a) Spectrum from one simulation, showing peaks at the glass-metal interface (blue) and water-metal interface (green). (b) Many simulations were performed for different values of wavevector. Extracting the peaks generated the dispersion relation for the various modes present in the system.

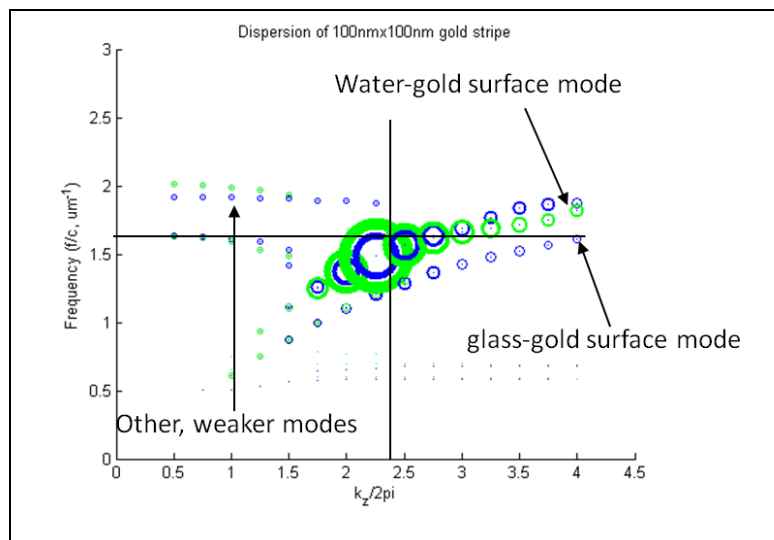


Figure 4: Plot of extracted dispersion relation from top four peaks of each simulation, showing multiple modes. Circle size is an indication of field strength, showing that there are two strong plasmonic modes. Green circles are values measured at the water-gold interface and blue are those measured at the glass-gold interface.

The spatial structure simulated in these tests is shown in Figure 2 above. Again, all that is required is the permittivity and permeability for each spot in the spatial grid, and the initial electromagnetic conditions. The figure above shows the plot of the index of refraction (which is equal to $\sqrt{\mu_r \epsilon_r}$). The gold stripe (with a frequency-dependent index of refraction) is sitting on the top surface of the waveguide (simulated here only as glass with uniform index of 1.5241). That value, 1.5241 is the refractive index at the middle of the diffused waveguides that were fabricated. It is possible to make this approximation as we have a reduced simulation domain and are not relying on waveguiding

phenomena in this simulation. The modal behavior is enforced through our restriction of the wavevector, and the index of refraction is a close approximation for the values at any mode. Around the stripe and above the glass is water, with index 1.33.

The values that are measured are the field strength immediately above and below the plasmonic stripe. This will be a measurement of the plasmonic field strength for the mode at the metal-water interface and metal-glass interface, respectively.

To produce the dispersion diagrams, the defined spatial grid is excited with a pulsed excitation. The signal is allowed to propagate and decay. Then a Fourier analysis is performed on the recorded signal. This produces a plot of field strength with respect to frequency. This, however, is for only one value of wavevector. To produce a full dispersion diagram, we need to also scan the values of k . The periodic boundary conditions are defined with a specific phase delay. By varying this phase delay, it is possible to enforce various values of k . Remember that k is the change in phase with respect to position. Therefore, if there is a defined phase delay between the two periodic boundaries (which are separated by a chose distance) this enforces a specific value of k . In this manner, by scanning k and producing a spectrum for each value of k , all the data to produce a dispersion diagram is generated. This data is shown in Figure 3, above. The plots on the right are for various values of k . One example plot is pulled out to show in greater detail, so the peaks can be observed.

The next step to generating the dispersion diagram is extracting the values from the actual plasmonic modes. These are embodied in the data as peaks in the field spectrum. There may be multiple peaks in this spectrum, indicating multiple plasmonic modes on the surface. Recording the intensity of the peak, and what wavelength it appears at, the information for one data point in the dispersion relation is obtained. Following the same procedure, the peaks of the spectral data generated for each wavevector value (each separate simulation) are obtained, and the entire dispersion relation is generated. The modes with the highest peaks are taken as the dominant mode, and are usually the only ones that is plotted. However, in other work, it may be useful to know the behavior of other modes, so this information was recorded. The plot in Figure 4, above, shows this data. The green circles represent values measured at the water-gold interface and the blue represent those measured at the glass-gold interface. The size of the circles represents the strength of the fields. From this plot, one major mode is observed at each interface.

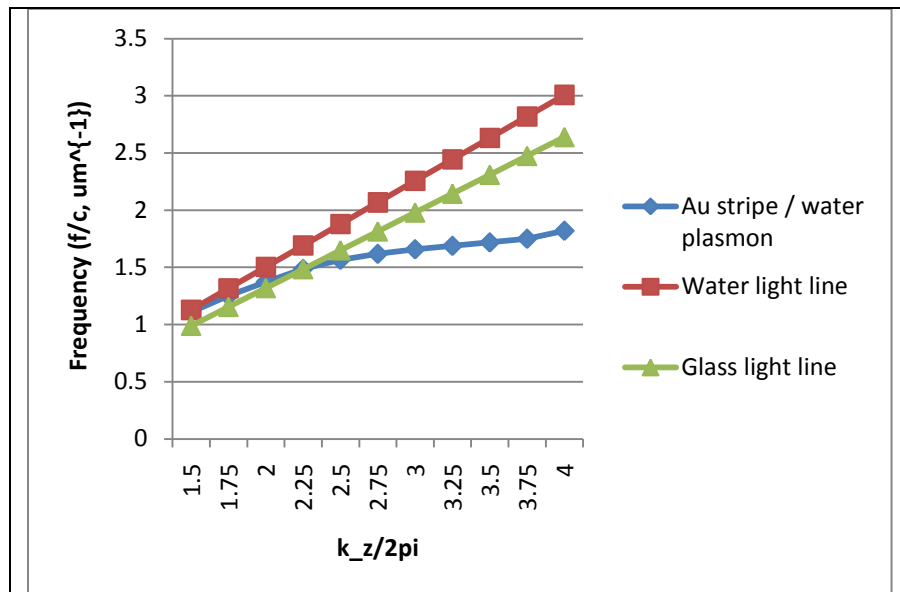


Figure 5: Extracted dispersion relation for water-metal plasmonic mode. Also, the light line for BK7 glass is plotted. The intersection of these two plots shows the criterion for coupling between the modes.

Taking this data from Figure 4, the dispersion relation for the major water-gold mode is shown in Figure 5. The light lines for the two materials of interest, glass and water are included, showing how the dispersion relation for the metal-water mode does cross the glass light line, indicating that light from the waveguide can excite this mode.

While the dispersion relation provides useful information, a plot of the field intensity with respect to the wavelength of light in

the waveguide would be the most directly applicable method to present information. It is possible to generate this plot from the same data that was gathered for the dispersion relation, with one additional piece that was obtained in an earlier chapter.

The desired plot would indicate the field intensity above the plasmonic stripe for a given wavelength of light in the waveguide. To produce this plot, information from the simulations of the waveguide is used. From these simulations, we extract the wavevector for the dominant mode at each wavelength along the spectrum. Then, the field intensity value for each wavelength is extracted from the plot that was generated from the simulation with the corresponding wavevector. In this manner, the wavevector from the waveguide simulations is used to choose the proper simulation from which to extract the field intensity at that wavelength. Plotting these field intensity values with respect to wavelength produces the field intensity spectrum above the metal for excitation from the waveguide. Results from this procedure for 100 nm x 100 nm stripes of three metals are shown in Figure 6.

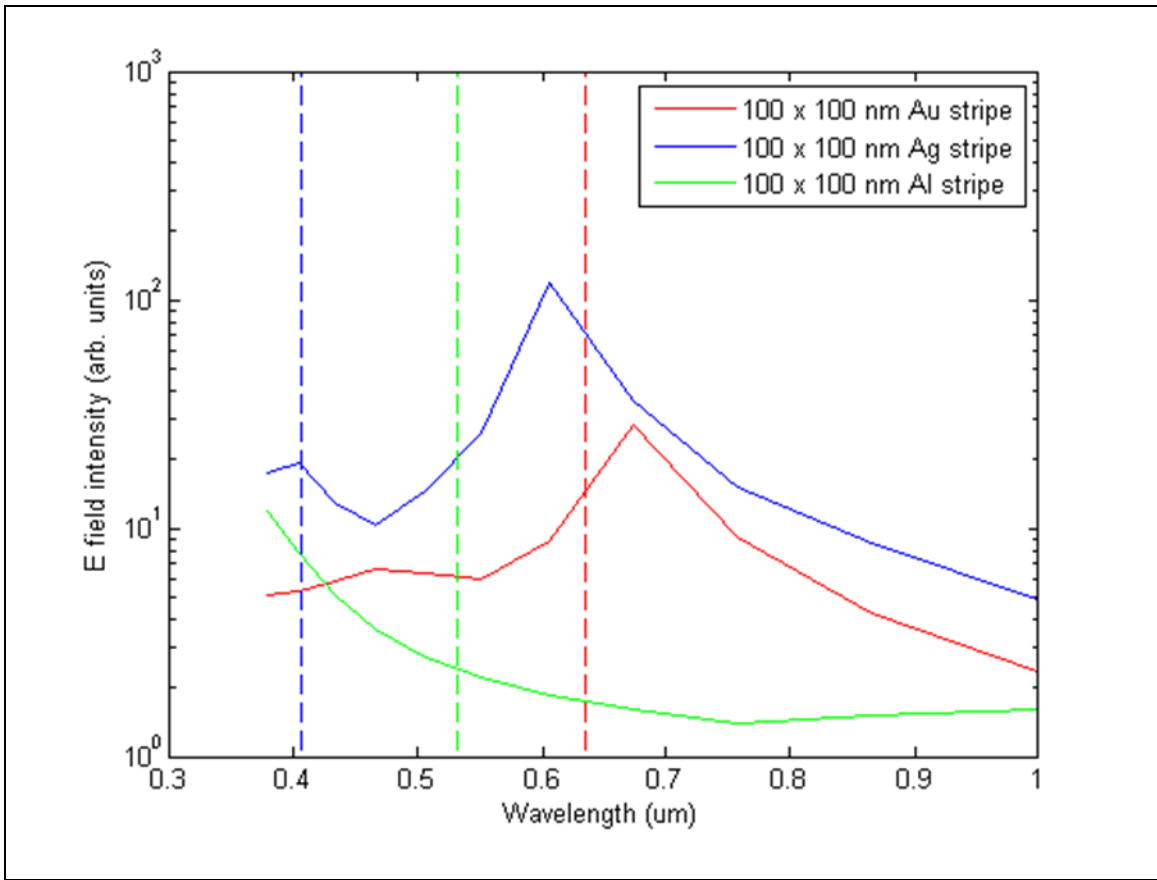


Figure 6: Field intensity spectra of the desired plasmon mode for three candidate metals. The simulations modeled 100nm x 100nm cross-sectional stripes on BK-7 glass in water. The three vertical lines are three wavelengths of interest, 405 nm, 532 nm and 633 nm. The wavelengths are common colors used for fluorescent tagging by US Genomics. (Refer to Chapter 6 for information on US Genomics)

This simulation procedure can be carried out for different metals, dimensions of plasmonic stripe, and polarizations, in order to optimize the coupling to the evanescent fields at the wavelengths of interest. Some of this work was performed in order to determine qualitative adjustments available. Further optimization work on plasmonic stripes had been performed via prism coupling in air (28), so it was determined that it was not necessary to explore this area further. For this work, we had achieved the goal of demonstrating plasmonic enhancement and field confinement, and the optimization can be explored in future work. Simulations demonstrating the ability to alter the spectrum via several methods are shown in Figure 7. The methods demonstrated are (a) material, (b) polarization, (c) dimensions, and (d) structure.

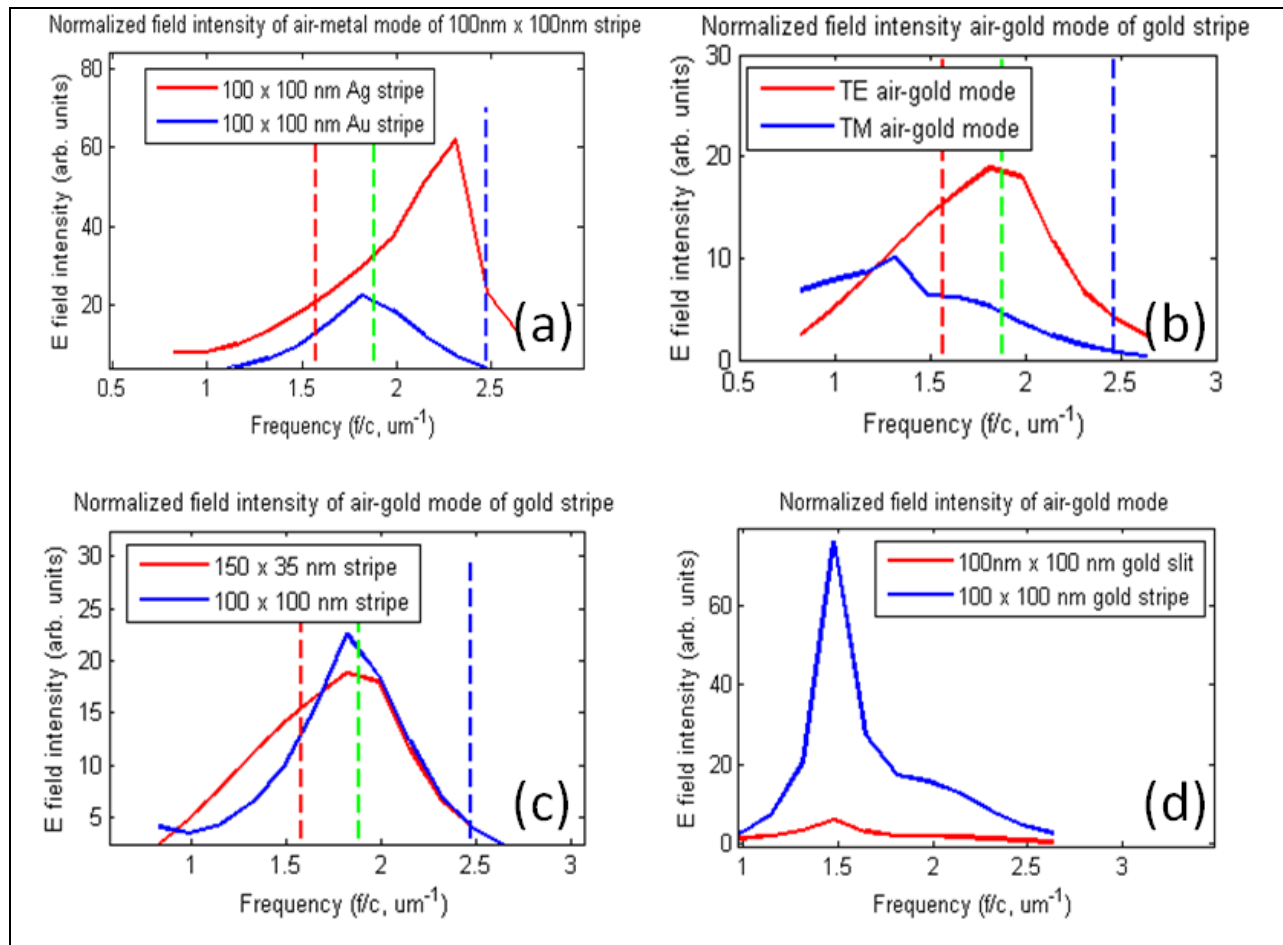


Figure 7: Four simulations comparing various adjustments for plasmonic stripes. (a) Au and Ag stripes in air (as opposed to water), (b) Difference between resonant properties of TE vs TM modes. (c) Shape effects – 100nm x 100nm stripe compared to 135nm x 35nm – resonant frequency does not change, spectrum just broadens a little. (d) Stripe compared to same sized nanoslit – resonant frequency is same for nanoslit, resonance is broadened.

Dispersion relation and absorption with reduced area

While the periodic boundary condition method provided useful results for the dispersion and absorption curves, it did not provide an analysis of the coupling length from the waveguide to the resonator or analysis of the effects of a finite length resonator. As mentioned above, the greatest barrier to simulating the structure exactly is the difference in scale between the diffused waveguide and the plasmonic stripe. By utilizing some common properties of dielectric waveguides, an equivalent waveguide with similar modal behavior can be simulated in place of the larger one, decreasing the required simulation domain, and enabling simulation of the structure directly.

In order to actually simulate these structures in the RSOFT package, MATLAB scripts were written to produce accurate representations of the devices of interest. The plasmonic stripe had to be generated

by a script based on AFM scans of fabricated structures, in order to ensure the proper shape. The waveguides had to be generated via script as well to enable the simulation procedures that were desired. First, however, it is important to understand how it was possible to shrink the size of the waveguides while still achieving accurate simulations.

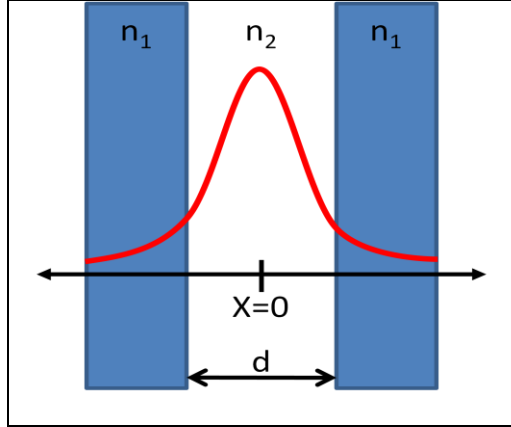


Figure 8: Diagram of standard slab waveguide. A region of refractive index n_2 and thickness d is between two semi-infinite regions with lower index of refraction, n_1 . A typical field profile is shown. Increasing n_2 and decreasing d can retain the field profile while reducing dimensions of the structure.

For general, one dimensional dielectric slab waveguides, like the one demonstrated in Figure 8, the modes are defined by equations taking the forms:

$$E(x) = \begin{cases} A \sin(hx) + B \cos(hx), & |x| < \frac{d}{2} \\ C e^{-q|x|}, & |x| > \frac{d}{2} \end{cases}$$

The specific values of h and q are not important in this analysis, but the observation that if they are kept equal while changing the dimensions of the waveguide, the actual fields will not be affected. This is the plan. The parameters are generally proportional to the relationship:

$$h, q \propto d^2(n_1^2 - n_2^2)$$

Therefore, if it is desired to decrease d (the dimension of the waveguide), h and q can be held constant by adjusting n_1 and n_2 correspondingly.

$$d^2(n_1^2 - n_2^2) = d'^2(n_1'^2 - n_2'^2)$$

In order to reduce d by some amount, r , without changing n_1 .

$$d' = \frac{d}{r}, \quad n_1' = n_1$$

$$d^2(n_1^2 - n_2^2) = \frac{d^2}{r^2}(n_1'^2 - n_2'^2)$$

And solving for n_2' :

$$n_2' = \sqrt{r^2 n_2^2 - (r^2 - 1)n_1^2}$$

Using this equation, it is possible to obtain a new value for refractive index that should produce a waveguide of reduced dimensions, but equivalent modal behavior. However, this solution is for a one dimensional slab waveguide, and we are using a diffused waveguide, so it may not be accurate. To account for this inaccuracy, the resulting waveguides were simulated using a BPM tool (as described in the optics chapter) to further adjust and verify similar effective index and modal behavior. In this manner, it was possible to decrease the size of the simulation domain to make more straightforward simulations possible.

Using this reduced dimension, a profile for the diffused waveguide was produced using the index distribution results from the optics chapter (Figure 9) and our simulations here to ensure the proper waveguide behavior while achieving a reduced waveguide dimension. This way, we can produce a 3 dimensional area that we can simulate in its entirety, in order to quantify plasmonic coupling lengths and finite length behavior.

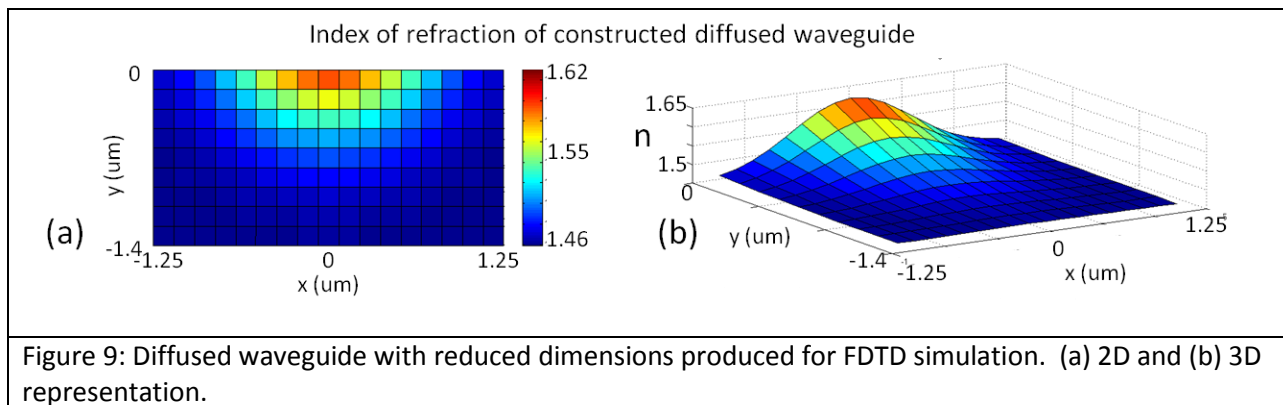


Figure 9: Diffused waveguide with reduced dimensions produced for FDTD simulation. (a) 2D and (b) 3D representation.

It is shown that the evanescent fields will couple to the plasmonic modes in only a few microns length, which is an acceptable result. The majority of the DNA in the devices being produced will be flowing near the middle of the channel due to hydrodynamic focusing from the side ports. Therefore, the plasmonic modes will be able to have sufficient excitation in the region where the samples cross the plasmonic resonator.

Another benefit of enabling the direct 3D simulation of the plasmonic structure is the ability to directly replicate tests that were performed. Three tests were performed to measure the plasmonic behavior of our system: transmission spectra measurements, Near-field Scanning Optical Microscopy (NSOM), and fluorescence tests. For the first two tests, it was necessary to simulate the structure in this manner in order to produce results that could compare to the tests performed.

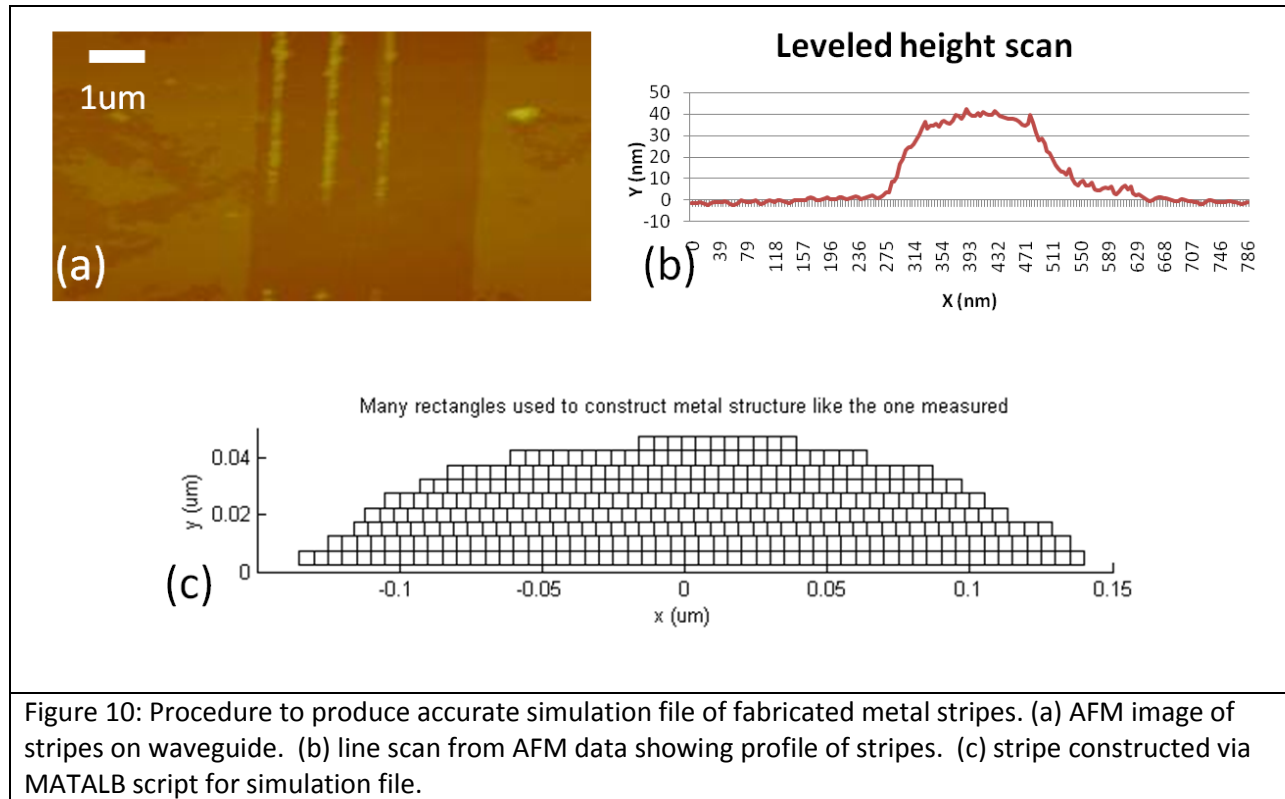
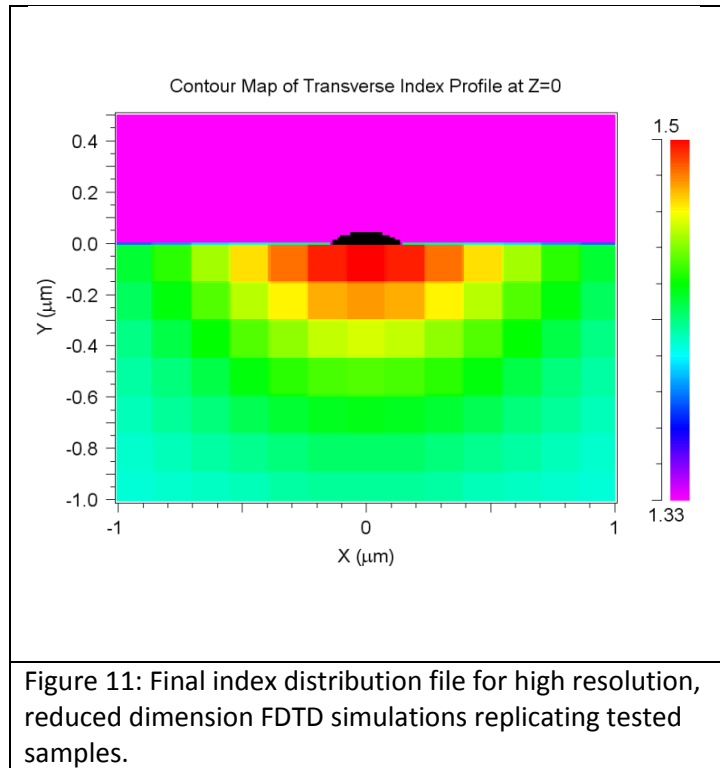


Figure 10: Procedure to produce accurate simulation file of fabricated metal stripes. (a) AFM image of stripes on waveguide. (b) line scan from AFM data showing profile of stripes. (c) stripe constructed via MATLAB script for simulation file.

Similar to the work done to verify the proper shape of the diffused waveguides in the optics chapter, it is important for the simulated metal structures to have the same shape of those that are fabricated in order to achieve accurate simulations. Fabricating perfectly rectangular structures with nanometer dimensions is very difficult. Surface roughness of the metal and degradation from cleaning procedures can cause irregularities and general smoothing of the devices. Therefore, test samples were fabricated and tested in manners described later in this chapter. These samples were also measured with an atomic force microscope (AFM) to determine the actual shape. The AFM images of the fabricated stripes are shown above. As can be seen, the structures are far from a square cross section. Therefore, a MATLAB script was written to produce an index distribution file for the RSOF simulation tool that matched the shape of the fabricated stripe. The AFM data and a generated stripe profile are shown in Figure 10.

Additionally, as mentioned in the optics chapter, the built-in diffused waveguides of the RSOF simulation tool was found to not be accurate for our measured waveguides. Furthermore, even if they were accurate to our fabricated waveguides, diffused channels are not permitted in RSOF simulations that allow for nonlinear frequency responses. Therefore, it was necessary to write another MATLAB script that would produce the proper diffused waveguide profile as a collection of rectangular dielectric waveguides. Rectangular waveguides are permitted to be used in nonlinear simulations using the FULLWave tool.



Utilizing MATLAB scripts to produce RSOFT files that accurately replicate both the shape of the plasmonic stripe and the index distribution of the diffused waveguide, it is possible to produce a simulation file that can accurately simulate the tested devices. A sample of the resulting index file is shown by Figure 11. The tests and results of both simulation and tests will be shown later. One final component to the simulation tools is ensuring an accurate representation of the frequency-dependent behavior of the metallic structures.

Metal Properties

The values describing metallic properties used in many simulations in the literature (33) (34) are admittedly not accurate in the lower-wavelength part optical regime (33) (34) (35). Some work was performed to improve the material model that was used in order to achieve more accurate results.

The FDTD simulations described in this chapter are based entirely on a spatial grid with each point representing the refractive index values at that point. While this is simple enough, the interesting behavior that we are interested in relates to the changing of the index of refraction (or more specifically, the permittivity) with respect to frequency. The simulation tools allow for this behavior in two ways: a lookup table, and an equation.

Metallic values for permittivity are well studied (33) (36) (37). Therefore, the most straightforward method to simulate nonlinear material frequency responses would be to have a lookup table, indicating the proper permittivity for the wavelength that is being utilized in that simulation. However, this method would not allow multi-spectral simulations, and may miss frequency-conversion phenomena. Specifically, describing a material in this manner would disallow pulsed excitation and Fourier analysis, as the lookup table cannot account for the multiple frequencies being present at once. On the other hand, materials can be described with an equation – a method which will allow for these types of analyses.

The common equation that is used to describe the optical behavior of metals is a Lorentz-Drude model. Using this model, the complex dielectric function is described by a combination of a Drude model for the intraband, or free electron, behavior, and a Lorentz description of the interband behavior. The combined equation for the permittivity is (33):

$$\hat{\epsilon}_r(\omega) = \hat{\epsilon}_r^{(f)}(\omega) + \hat{\epsilon}_r^{(b)}(\omega)$$

In this equation, $\hat{\epsilon}_r(\omega)$ is the complex relative permittivity, $\hat{\epsilon}_r^{(f)}(\omega)$ represents the free-electron, or Drude component, and $\hat{\epsilon}_r^{(b)}(\omega)$ represents the Lorentz component. The Drude contribution is:

$$\hat{\epsilon}_r^{(f)}(\omega) = 1 - \frac{\Omega_p^2}{\omega(\omega - i\Gamma_0)}$$

Where the plasma frequency associated with intraband transitions is represented by $\Omega_p = \omega_p\sqrt{f_0}$, where ω_p is the plasma frequency and f_0 is the oscillator strength for that oscillator. In addition, Γ_0 is the damping constant.

The Lorentz portion of the equation represents the semi quantum sum of k oscillators:

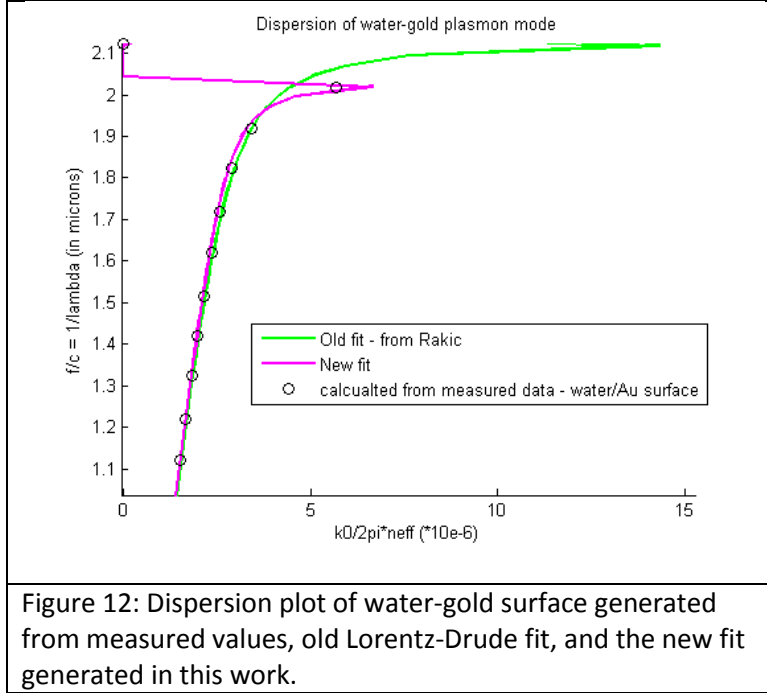
$$\hat{\epsilon}_r^{(b)}(\omega) = \sum_{j=1}^k \frac{f_j \omega_p^2}{(\omega_j^2 - \omega^2) + i\omega\Gamma_j}$$

The notation is similar to the that used in the Drude portion, but in relation to k oscillators, each oscillator, j , with frequency ω_j , strength f_j , and lifetime $\frac{1}{\Gamma_j}$.

This type of model has been used to fit the permittivity of metals for wavelengths down to 500nm (33) (34). However, it is not accurate below there. Furthermore, due to the nonlinear relation between the permittivity and the dispersion relation, these small changes can cause large inconsistencies in simulated results.

Therefore, to produce accurate simulations of the plasmonic behavior, an optimization of the parameters were fit for this model was performed. As opposed to the work by Vial (34), the fitting that was performed was of the dispersion relation of plasmonic modes resulting from that dielectric behavior, as opposed to fitting the permittivity values themselves.

Because most of the measurements of metal properties were performed on uniform films of metal, the equation for the surface plasmon on a smooth metal sheet, as presented earlier in this chapter, was used. Then, using measured values of the permittivity at wavelengths of interest (36) (37), a curve was created that the Lorentz-Drude model would be fit to. The fit was performed via a least-squares optimization routine written in MATLAB. The resulting plots are shown in Figure 12.



The values were calculated using a format for the Lorentz-Drude model that is used by the RSoft software. This model is:

$$\varepsilon(\omega) = \varepsilon_{\infty} + \sum_{j=1}^k \frac{A_j \omega_p^2}{-\omega^2 - 2i\omega\delta_j + \omega_j^2}$$

And is represented generally by:

$$\varepsilon(\omega) = \varepsilon_{\infty} + \sum_{j=1}^k \frac{\Delta\varepsilon_j}{-a_j\omega^2 - b_ji\omega + c_j}$$

So the conversion between the LD model and the RSoft model can be accomplished by:

$$\begin{aligned} \Delta\varepsilon_j &= A_j \omega_p^2 \\ a_j &= 1 \\ b_j &= 2\delta_j \\ c_j &= \omega_j^2 \end{aligned}$$

The values for the new, improved fit are shown in the table below. While the fit is slightly better for the dispersion relation in the optical regime, it is worse outside of the optical regime. Therefore, care should be used when using these values, as they are preferentially fitted to the measured values only for these wavelengths of interest. However, it should be noted that outside of the wavelengths of interest, these fitting parameters are much worse than the values generated by Rakic (33).

$\epsilon_\infty = 1.191202$					
Resonance number	1	2	3	4	5
$\Delta\epsilon_j$	2640.211978	-39.108148	22.777305	167.813519	1909.977711
b_j	0.339837	1.505620	2.293626	2.404078	7.887062
c_j	0.001996	5.767599	17.621173	217.483773	378.716256

Table 1: New Lorentz-Drude fit parameters for dispersion relation simulations in RSoft at optical wavelengths.

Using this method to fit the dielectric function of the metal to the proper plasmonic response in the frequencies of interest, we are able to generate a more accurate metal model for our plasmonic simulations.

Plasmonic Testing

After the simulations were performed, several tests were carried out on fabricated structures to determine the behavior of the fabricated plasmonic devices. While the results for the behavior of the entire system are presented in later chapters, this section covers the test performed to directly evaluate the plasmonic behavior. Most of the tests were inconclusive due to inability to directly reproduce simulation conditions, equipment limits, and equipment sensitivity. However, the results provide qualitative matches to simulated data, and the simulations are consistent with literature, so the work is considered sufficient for indications for the behavior of the completed devices. Further work can build upon this framework to further optimize the plasmonic readout.

Three tests were performed: transmission spectra, NSOM, and fluorescence tests. The results of each of these were matched to simulations.

Transmission spectrum

The plasmonic modes of a resonator sitting on top of a waveguide selectively extract energy from specific wavelengths present in the waveguide. Therefore, if white light is introduced into the

waveguide, the signal emerging from the other end will take on a characteristic spectrum that will indicate the wavelengths of light that are coupled to the plasmonic resonator. This test was performed and compared to simulations.

Other work (28) has performed prism coupling to the plasmonic resonators to obtain similar data, but it was desired to utilize waveguide excitation. Utilizing the waveguides provides a more direct analog to the completed device architecture and incorporates the modal and spectral behavior of the waveguides, which have the potential to change the test results.

In the final device design, the single, small plasmonic resonator would not extract a large portion of the light present in the waveguide. Therefore, performing the tests with these devices would not produce a discernable signal. Therefore, test devices were made with many more plasmonic resonators along the waveguide. Instead of one resonator, there were 1500 groups of three resonators along the waveguide. In this manner, the absorption should be increased by around 4500 times, increasing the signal that we are looking for by that same amount. However, since we are now putting resonators close to each other, there may be interaction between the resonators. In order to ensure that this interaction does not color the test data, samples were produced with different spacing distances. Images in Figure 13 show typical samples of Au stripes with 1 μ m (a) and 3 μ m (b) spacing between stripes. The edges of the Ag diffused waveguide can be observed in those images, as well. The bright white features in Figure 13 are fiduciary marks made of the Ta alignment metal.

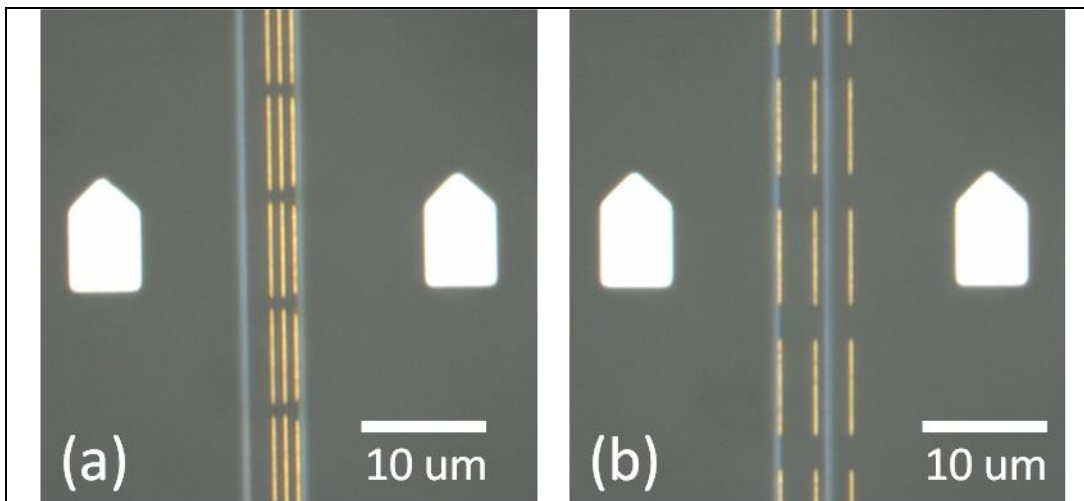


Figure 13: Fabricated metal stripes on waveguides for transmission spectrum measurements. Several spacing values were used, ranging from (a) 1 μ m to (b) 3 μ m.

The tests were performed at the Crozier group lab space at Harvard University, due to the high power white light source (Oriel 66004 Xe arc lamp, driven with Oriel Arc Lamp Supply) and high sensitivity spectrometer (Princeton Instruments Acton PS series with SPEC-10 LN Camera) available at that

laboratory. The experimental setup is shown in Figure 14, below. The white light is focused into an optical fiber, which is connected to a v-groove block for connecting to the chip. The use of the v-groove block is expanded upon below. Once the light is in the waveguide in the chip, it propagates along the chip and certain spectral components are absorbed by the plasmonic resonators. The light coming out the end of the waveguide is collected via a 10x objective, put through a spatial filter to cut out all light that was not from the waveguide, and then focused into another optical fiber, which is connected to a spectrometer.

Tests were performed on waveguide chips with and without plasmonic resonators. The chips without resonators were utilized to provide a control spectrum, which evaluates the spectrum of the light source, the optics, and the waveguide itself. Using this baseline, the differences produced by the plasmonic resonators can be observed by normalization. One additional note: as the plasmonic behavior that we are looking for would occur in a microfluidic channel that is filled with water, the tests should be performed with water on the surface of the chips in order to be an accurate test. Therefore, a drop of water was placed on the surface of the chips immediately before each experimental run. The water was held in place by surface tension.

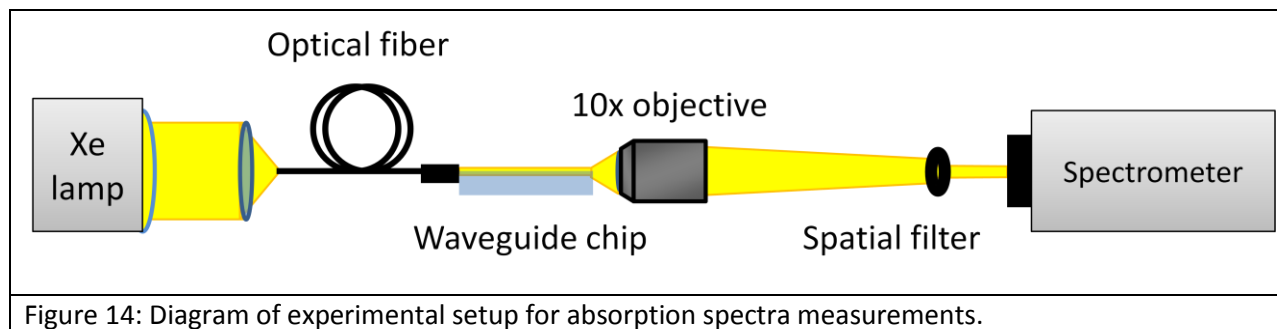
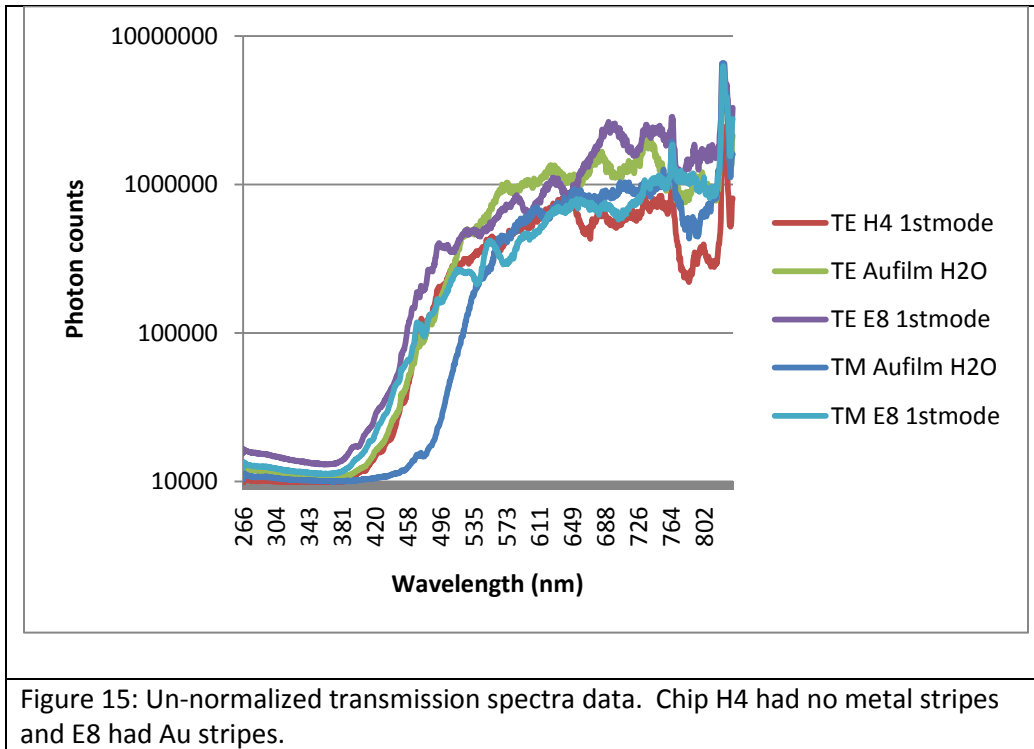


Figure 14: Diagram of experimental setup for absorption spectra measurements.

The v-groove block is a block with a groove that holds the optical fiber in it and provides a manner to connect the fiber to chips. The fiber is cleaved and the end of the fiber and the v-groove block are polished, presenting a completely flat and level surface for the block and the fiber. Using this v-groove block to hold the fiber, the fiber is aligned to the waveguide in the chip by shining light through it and observing the output end of the waveguide. When the maximum amount of light is observed being guided in the waveguide, the fiber and the v-groove block are attached to the chip with UV adhesive (Norland). The v-groove block provides a strong, solid base to hold the fiber and glue it, providing structural stability for the small fiber, ensuring it stays affixed in place.



The resulting spectra are shown in Figure 15, above. Slight differences can be seen, but without normalization, not much data can be understood. The normalized data is shown below, and compared to simulated values.

Simulations were also performed to obtain similar data. The simulation setup with a waveguide of reduced dimensions was utilized. First, the BPM tool, BEAMProp was utilized to determine the shape of modes in the waveguide. Then, this modal shape was used as the excitation (or “launch”) field in subsequent simulations. A detector was placed at the end of the simulation region (5 μm away). This detector would record the electric field components, power, and overlap integral with the launch field. It is the propagating power that we are interested in, as that is what was measured by the experiments performed. Similar to the normalization procedure for the experiments, a simulation with just the waveguide was performed and one with plasmonic stripes on the waveguide. The stripes were of a similar shape and spacing to those that were fabricated, in order to most closely model the experiment.

Simulations were performed with a continuous wave excitation and the final, steady-state intensity value was recorded at the monitor. The simulations were repeated at different wavelengths in order to produce a spectrum. This data was normalized with the corresponding simulation data from the bare waveguide simulations.

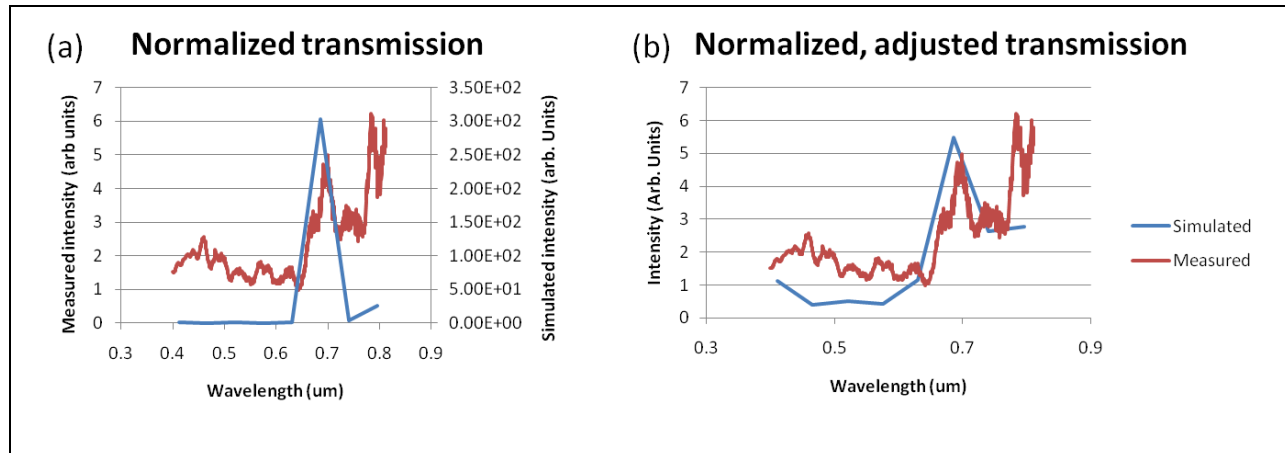


Figure 16: Simulated and measured normalized transmission spectra for Au stripes in water. (a) Normalized transmission, not adjusting for noise in detector or different base levels. The simulated data is on the right scale – much larger normalized intensity. (b) Spectra when a small amount of noise is added to the simulated data. With this adjustment, simulated and measured values match more closely.

The normalized data from the transmission simulations and experiments is shown in Figure 16, above. In the first plot, the simulation data was simply plotted without any adjustment. While the peak that emerges in the simulated data is aligned with the peak from the measured data, the scale is dramatically different. It was considered that the total power level was not normalized, as the tests were performed on different chips, each which may have had a slightly different efficiency of coupling from the v-groove to the waveguide. Additionally, there may have been some noise in the signal. A baseline of noise added to each signal could dramatically alter the data.

Adding a small constant to both signals to simulate a constant background noise in the simulation brings the normalized simulated data into scale with the measured data. This constant noise is considered valid, as noise in the detector, or stray light from the system are likely to exist in the measured data, but not the simulated. Additionally, the finite size of the detection region in the simulation could have missed the outer edges, decreasing the overall signal strength. For these reasons, adding the constant noise floor is justified. The noise was 23% of the baseline signal. Adding that noise floor shows that the simulated values match the measured data at one peak, indicating simulated plasmonic absorption. The peak that exists at longer wavelengths does not seem to be captured by the simulation could be due to interaction between plasmonic stripes, which was not simulated.

The behavior shown in these plots is interesting, as it is not the expected plasmonic behavior. The typical plot of transmission from a plasmonic setup like this would show broadband transmission, and then a localized dip in transmission as the plasmonic mode coupled light out of the waveguide. This work instead shows the opposite; a baseline of transmission with a localized peak. The interpretation of this is broadband coupling of the plasmonic stripe to the waveguide, with a localized frequency where the plasmonic resonance is quenched, and most of the light is transmitted. This behavior could be possible due to the irregular nature of the shape of the fabricated plasmonic stripe. The curved profile could lend itself to broadband plasmonic coupling. In order to verify this behavior, it was desired to use

Near-field Scanning Optical Microscopy (NSOM) and simulations to observe the fields around the plasmonic stripe in order to determine if this broadband coupling is taking place. This is explored in the next section.

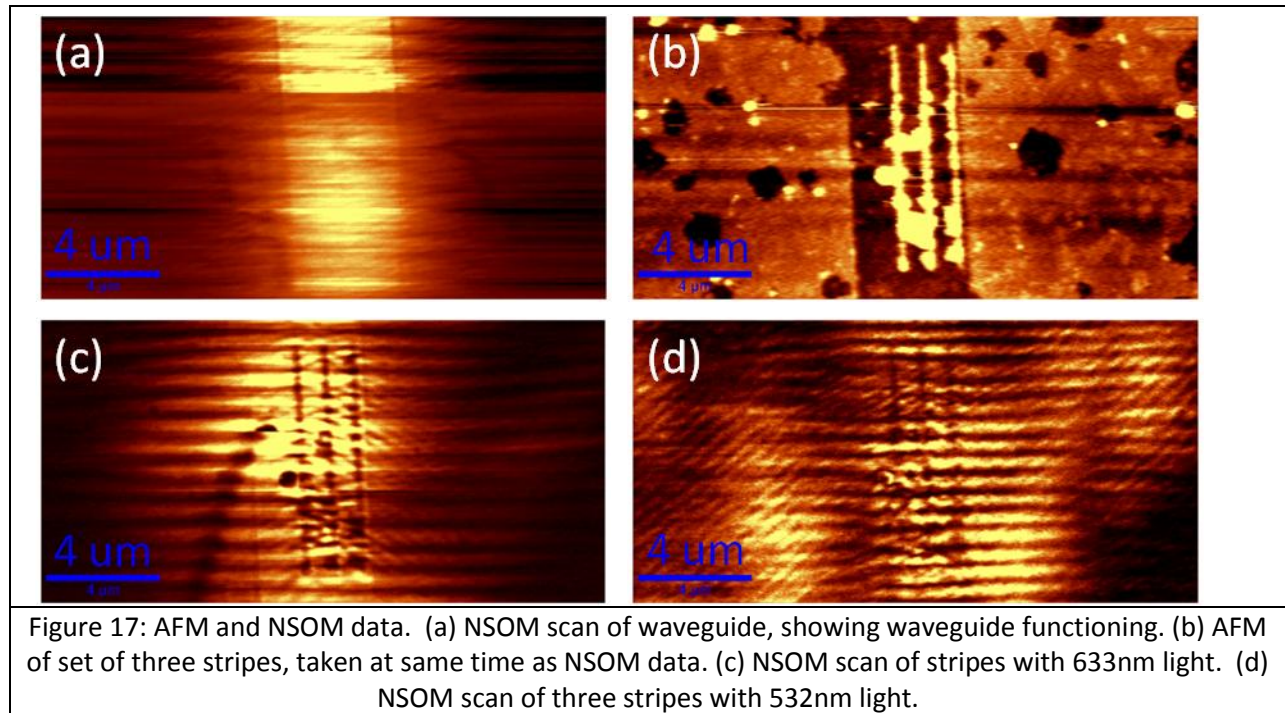
NSOM Measurements

Near-field Scanning Optical Microscopy (NSOM) is a microscopy technique for viewing electromagnetic fields below the diffraction limit of light. Additionally, NSOM enables the visualization of evanescent and near-field fields, which can enable the visualization of plasmonic modes. Utilizing an NSOM in the Harvard University Center for Nanoscale Systems and comparing those results to simulations performed, a theory for the behavior of the fabricated plasmonic stripes is explored. A qualitative match between NSOM measurements and simulation data provides a qualitative explanation of the behavior of the plasmonic stripe. Further work in the sensitivity of NSOM and the enabling of underwater NSOM will enable future explorations to produce a more refined model of behavior.

An NSOM tool is very similar to an Atomic Force Microscope (AFM), but with additional optical detection capabilities. In the NSOM, a very small tip scans across the surface of the area that is being imaged. At each point in the scan, the tip probes down to the surface and determines the height value at that point, generating a profile of the sample. This is general AFM operation. In an NSOM, the sample has some near-field electromagnetic fields that are of interest. As the tip comes close to the surface of the sample, these fields are scattered (much like evanescent fields were scattered in the optics Chapter of this thesis). This scattered light is collected by some optics near the tip and sent to a photodetector, recording the intensity of scattered light. The intensity of scattered light is an indication of the intensity of near-field waves. By plotting the intensity at each point probed in the 2D grid, a plot of the electromagnetic fields in that region is produced.

NSOM measurements are prone to many structures artifacts in their measurements, leading to the potential for spurious results. The potential sources of artifacts are propagating light noise and signal beating from the optical detection setup. Both of these artifacts are seen in our measurements, making analysis difficult. Regardless, some generalized results were able to be obtained when used in conjunction with simulations.

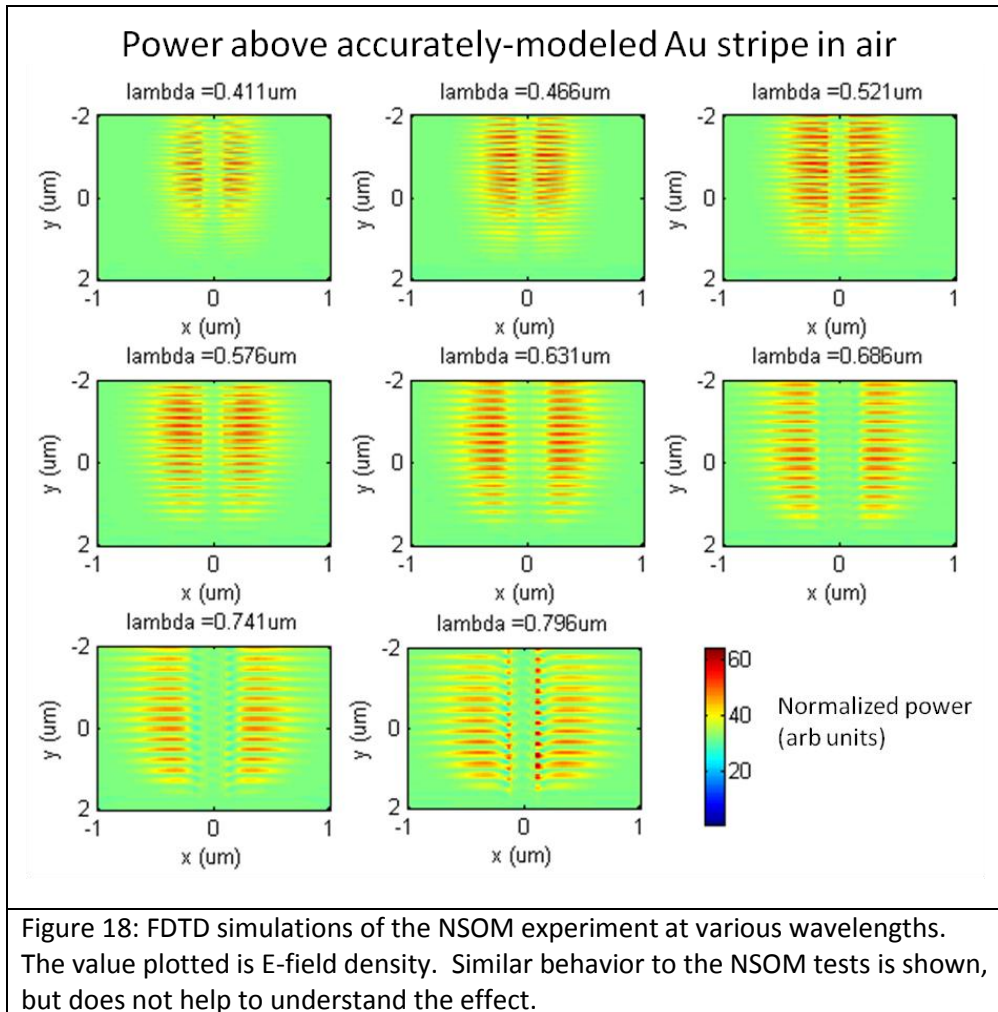
NSOM measurements were taken on the samples that were used for the absorption plot tests, done in the previous section. As opposed to those tests, which were performed with the plasmonic stripes immersed in water, NSOM must be performed in air. This is to enable proper vibrational operation of the AFM tip. Operating in water would damp the oscillation. Some work is being done in underwater AFM, but we did not have access to this type of tool at the time. The NSOM plots that were generated are shown below.



In Figure 17, (a) is an NSOM scan of the bare waveguide when excited with 633nm light. This scan shows the light is confined to the waveguide and provides an indication of the fields that will excite the plasmonic stripes. The distribution of these fields closely matches that of a pure fundamental mode in the waveguide. Part (b) of the figure shows the AFM scan of a set of three metal stripes. This AFM scan is taken at the same time as the NSOM data, so it is possible to directly compare topography and the NSOM data. The AFM scan shows that the stripes are very dirty. This is due to the NSOM tool being in an unclean environment for an extended period of time, leading to contaminants settling on the surface over the time that the chip was being used.

Sections (c) and (d) are NSOM scans of the same area shown in (b). Section (c) was taken with 633nm light passing into the system, and (d) was taken with 532nm light. These tests also proved to be inconclusive. While there were enhanced fields, there were also quenched fields, and there were beating patterns in the data which was difficult to account for. The beat length for the 633 nm light was around 700nm, a length that is not explicable by any combination of beating between modes. Copropagating modes would have a much longer beat length, and counterpropagating modes would have beat lengths much shorter than this. It is possible that this periodic pattern is an artifact from the NSOM tool, as suggested in (38), but the design of the tool that was used would not cause the periodic signals described in that source.

The NSOM data did show the metal stripes, but it appears that the fields are quenched, not enhanced, at their surface. This is a similar behavior to that seen in the absorption tests. However, with only two wavelengths of light as data points, it is difficult to draw conclusions from this data. In order to flush out the behavior of the stripes, simulations were performed.



Simulations were performed similar to those for the transmission spectra experiments, but designed to replicate the NSOM tests. The large differences are that the stripes in the NSOM are in air, where in the transmission spectra tests they were immersed in water. Furthermore, different types of data are generated to compare to the experiments. In the transmission spectrum tests, average intensity values were taken. In these tests, 2D plots of field intensity are produced to provide an indication of the specific behavior of the plasmonic modes – separating different surface modes with waveguide behavior and edge modes.

The simulation data that is analogous to the NSOM data is shown in Figure 18, above. It appears to show similar behavior as the NSOM experiments. A quenching at the stripes at 633 and 532nm wavelengths and the periodic beating behavior from the propagating light. However, this does not provide much additional insight. Crosssection plots of the plasmonic resonator and the waveguide were generated as well in order to obtain that insight.

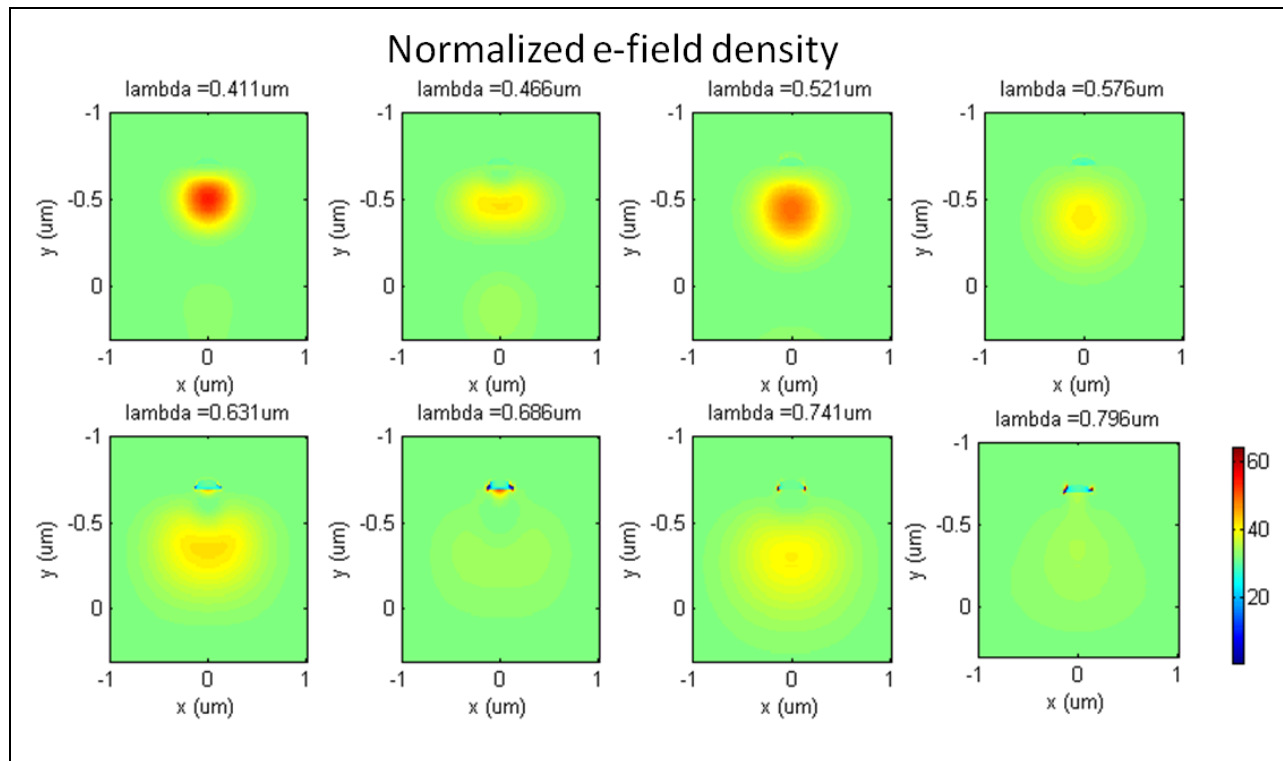


Figure 19: Simulations replicating the NSOM experiments, but showing the cross-section. With this information, the behavior is explained. Broadband corner modes and a glass-metal mode were not observable by NSOM or other simulation, but can be seen here, explaining the results seen in the experiments for both transmission spectrum and NSOM.

The cross-section plots in Figure 19 show the difference in behavior between the modes at the top of the plasmonic stripe and those at the bottom. Additionally they show very nicely how the stripe couples light out of the waveguide, decreasing the intensity of the fields in that area of the plots.

These cross-section plots provide a useful conclusion to the behavior seen in both the NSOM as well as the transmission spectrum measurements. The oddly shaped stripes quench fields up to 600nm (in air). At longer wavelengths, broadband edge states couple light out of the waveguide. A strong gold-glass mode on the bottom of the plasmonic stripe couples light out of the waveguide most effectively at 686nm, while above that, around 750, no resonances appear, leading to increased fields in the waveguide. This simulated behavior matches closely with the observed results from both the transmission spectrum and the NSOM experiments.

Conclusion

In this chapter, work was performed to integrate and understand the operation of a plasmonic readout in an integrated opto-nanofluidic device. Simulations were performed with Finite Difference Time Domain (FDTD) software to both optimize the structure of the plasmonic readout and understand the plasmonic behavior behind experimental results. Experiments were performed to test the plasmonic behavior. A new fit of a Lorentz-Drude model for the optical response of metals was generated. Transmission spectra were generated to observe plasmon stripe coupling to the waveguide. Additionally, Near-field Scanning Optical Microscopy (NSOM) tests were performed to characterize excitation topography from the plasmonic stripe.

All of the experiments performed demonstrated field enhancement and localization. The sensitivity of testing methods is not great enough to resolve the fine plasmonic behaviors that we are interested in. However, the results obtained did provide ample coherent explanation of plasmonic behavior to demonstrate field localization and enhancement.

Further work in this area can explore new plasmonic structures, including structures to incorporate Fano resonances to eliminate any scattering from evanescent fields or transformation optics to enable more broadband operation (39). Additionally, further optimization of the plasmonic readout could enable higher field enhancement or operation at multiple wavelengths.

Works Cited

1. *Fluorescence background discrimination by prebleaching.* **Hirschfeld, Tomas.** 1979, The Journal of Histochemistry and Cytochemistry, Vol. 27, pp. 96-101.
2. *Optical antennas integrated with concentric ring gratings: electric field enhancement and directional radiation.* **Wang, Dongxing, Yang, Tian and Crozier, Kenneth B.** 2011, Optics Express, Vol. 19, p. 2148.
3. *Line laser beam based laser-induced fluorescence detection system for microfluidic chip electrophoresis analysis.* **Xu, Boajian, et al.** 2009, Sensors and Actuators A, Vol. 152, pp. 168-175.
4. *Laser-Induced fluorescence of flowing samples as an approach to single-molecule detection in liquids.* **Dovich, Norman J., et al.** 1984, Analytical chemistry, Vol. 56, pp. 348-354.
5. *Fluorescence Spectroscopy of Single Biomolecules.* **Weiss, Shimon.** 1999, Science, Vol. 283, pp. 1676-1683.
6. *Two-photon absorption fluorescence imaging to characterize microfluidic device performance.* **Gibson, Emily A., et al.** 2006. p. paper CMH4.
7. *Efficient coupling of photons to a single molecule and the observation of its resonance fluorescence.* **Wrigge, G., et al.** 2008, Nature Physics, Vol. 4, pp. 60-66.
8. *Plasmonics: Localization and guiding of electromagnetic energy in metal/dielectric structures.* **Maier, Stefan A. and Atwater, Harry A.** 2005, Journal of Applied Physics, Vol. 98, pp. 011101-1 to 011101-10.
9. *Beiträge zur Optik trüber Medien, speziell kolloidaler Metallösungen.* **Mie, Gustav.** 1908, Ann. Phys., Vol. 330, pp. 337-445.
10. *Plasma Losses by Fast Electrons in Thin Films.* **Ritchie, R. H.** 1957, Physical Review, Vol. 106, p. 874.
11. **Kreibig, Uwe and Vollmer, Michael.** *Optical Properties of Metal Clusters.* [ed.] J. Peter Toennies. s.l. : Springer-Verlag, 1995.
12. **Bohren, Craig F. and Huffman, Donald R.** *Absorption and scattering of light by small particles.* s.l. : Jon Wiley and sons, 1998.
13. **Raether, Heinz.** *Surface Plasmons on Smooth and rough surfaces and on gratings.* s.l. : Springer-verlag, 1988.
14. *Optical antennas: resonators for local field enhancement.* **Crozier, K.B., et al.** 2003, Journal of Applied Physics, Vol. 94, pp. 4632-42.
15. *Plasmonic Laser Antenna.* **Cubukcu, Ertugrul, et al.** 2006, Applied Physics Letters, Vol. 89, p. 093120.
16. *Field Enhancement and Gap-Dependent Resonance in a System of Two Opposing Tip-to-Tip Au Nanotriangles.* **Sundaramurthy, A., et al.** 2005, Physical Review B, Vol. 72, p. 165409.

17. *Non-regularly shaped plasmon resonant nanoparticle as localized light source for near-field microscopy.* **Kottmann, J. P., et al.** 2002, *Journal of Microscopy*, Vol. 202, pp. 60-65.
18. *Single-Molecule Surface-Enhanced Raman Spectroscopy of Nonresonant Molecules.* **Blackie, Evan J., Le, Eric C. and Etchegoin, Pablo G.** 2009, *Journal of the American Chemical Society*, Vol. 131, pp. 14466-14472.
19. *Probing Single Molecules and Single Nanoparticles by Surface-Enhanced Raman Scattering.* **Nie, Shuming and Emory, Steven R.** 1997, *Science*, Vol. 21, p. 1102.
20. *Surface Enhanced Raman Scattering Enhancement Factors: A Comprehensive Study.* **Blackie, Evan J., et al.** 2007, *Journal of Physical Chemistry C*, Vol. 111, pp. 13794-13803.
21. *Tip enhanced optical spectroscopy.* **Hartschuh, Achim, et al.** 2004, *Philosophical Transactions of the Royal Society of London, A*, Vol. 362, pp. 807-819.
22. *Separation of Electromagnetic and Chemical Contributions to Surface-Enhanced Raman Spectra on Nanoengineered Plasmonic Substrates.* **Saikin, Semion K., et al.** 2010, *Journal of Physical Chemistry Letters*, Vol. 1, p. 2740.
23. *A miniaturized germanium-doped silicon dioxide-based surface plasmon resonance waveguide sensor for immunoassay detection.* **Huang, JG, et al.** 2006, *Biosensors and Bioelectronics*, Vol. 22, pp. 519-525.
24. *Trapping and Sensing 10 nm Metal Nanoparticles Using Plasmonic Dipole Antennas.* **Zhang, Weihua, et al.** 2010, *Nano Letters*, Vol. 10, pp. 1006-1011.
25. *Nano-optical Trapping of Rayleigh Particles and Escherichia coli Bacteria with Resonant Optical Antennas.* **Righini, M., et al.** 2009, *Nano Letters*, Vol. 9, pp. 3387-3391.
26. *Propulsion of Gold Nanoparticles with Surface Plasmon Polaritons: Evidence of Enhanced Optical Force from Near-Field Coupling between Gold Particle and Gold Film.* **Wang, Kai, Schonbrun, Ethan and Crozier, Kenneth B.** 2009, *Nano Letters*, Vol. 9, pp. 2623-2329.
27. *Integration of plasmonic trapping in a microfluidic environment.* **Huang, Lina, Maerkl, Sebastian J. and Martin, Olivier J.** 2009, *Optics Express*, Vol. 17, pp. 6018-6024.
28. *Experimental characterization of dispersion in plasmonic nanostripes for integrated DNA sensing.* **Steinvurzel, Paul, Yang, Tian and Crozier, Kenneth B.** 2010. *Proceedings of the SPIE - The International Society for Optical Engineering*. Vol. 7604, p. 760417.
29. *Dispersion and extinction of surface plasmons in an array of gold nanoparticle chains: influence of the air/glass interface.* **Yang, Tian and Crozier, Kenneth B.** 2009, *Optics Express*, Vol. 34, p. 244.
30. *Experimental measurement of the dispersion relations of the surface plasmon modes of metal nanoparticle chains.* **Crozier, K.B., et al.** 2007, *Optics Express*, Vol. 15, pp. 17482-17493.

31. *Experimental observation of narrow surface plasmon resonances in gold nanoparticle arrays.* **Chu, Yizhuo, et al.** 2008, Applied Physics Letters, Vol. 93, p. 181108.
32. *Numerical solution of initial boundary value problems involving Maxwell's equations in isotropic media.* **Yee, K.S.** 1996. Vols. AP-14, pp. 302-307.
33. *Optical properties of metallic films for vertical-cavity optoelectronic devices.* **Rakic, Aleksandar D., et al.** 1998, Applied Optics, Vol. 37, pp. 5271-5283.
34. *Improved analytical fit of gold dispersion: Application to the modeling of extinction spectra with a finite-difference time-domain method.* **Vial, Alexandre, et al.** 2005, Physical Review B, Vol. 71, p. 085416.
35. **Novotny, Lukas and Hecht, Bert.** *Principles of nano-optics.* s.l. : Cambridge University Press, 2006. p. 382.
36. **Weber, Marvin J.** *Handbook of optical materials.* s.l. : CRC Press, 2003.
37. *Optical constants of noble metals.* **Johnson, P.B. and Christy, R.W.** 1972, Physical Review B, Vol. 6, pp. 4370-4379.
38. *Probing photonic and optoelectronic structures by apertureless scanning near-field optical microscopy.* **Bachelot, R., et al.** 2004, Microscopy Research and Technique, Vol. 62, pp. 441-451.
39. **Maier, Stefan A.** Plasmonics: Plasmonic nanostructures concentrate light. *Plasmonics: Plasmonic nanostructures concentrate light.* 2011.
40. *Rapid DNA mapping by fluorescent single molecule detection.* **Xiao, Ming, et al.** 2007, Nucleic Acids Research, Vol. 35, p. e16.
41. *Determination of ion-exchanged channel waveguide profile parameters by mode-index measurements.* **Weiss, Martin N. and Srivastava, Ramakant.** 1995, Applied Optics, Vol. 34, pp. 455-458.
42. **Raether, H.** *Surface plasmons on smooth and rough surfaces and on gratings.* s.l. : Springer-Verlag, 1988.
43. *Integrated optical waveguide examination using anti-Stokes fluorescence.* **Ostrowsky, D.B., Roy, A. M. and Sevin, J.** 1974, Applied Physics Letters, Vol. 24, pp. 553-554.
44. *Surface-plasmon fluorescence spectroscopy.* **Neumann, T., et al.** 2002, Advanced Functional Materials, Vol. 12, pp. 575-586.
45. *Mode dispersion in diffused channel waveguides by the effective index method.* **Hocker, G.B. and Burns, W.K.** 1977, Applied Optics, Vol. 16, pp. 113-118.
46. *Effects of waveguide mode asymmetry on the laser diode-to-diffused waveguide coupling efficiency.* **Hall, D.G.** 1979, Applied Optics Letters, Vol. 18, pp. 3372-3374.

47. *Fabrication of planar optical waveguides by K⁺ ion exchange in BK7 glass.* **Gortych, J.E. and Hall, D.G.** 1986, *Optics Letters*, Vol. 11, pp. 100-102.
48. *Rapid quantitative analysis using a single molecule counting approach.* **D'Antoni, Christina M.** 2006, *Analytical Biochemistry*, Vol. 352, pp. 97-109.
49. *Apertureless scanning near-field optical microscopy for ion exchange channel waveguide characterization.* **Blaize, S., et al.** 2003, *Journal of Microscopy*, Vol. 209, pp. 155-161.
50. *Molecular probes - the handbook.* **Molecular probes - the handbook.** 2010.
51. *Optical trapping of dielectric nanoparticles in resonant cavities.* **Hu, Juejun, et al.** 2010, *Physical Review A*, Vol. 82, p. 053819.
52. *Theory of Nanometric Optical Tweezers.* **Novotny, Lukas, Bian, Randy X. and Xie, X. Sunney.** 1997, *Physical Review Letters*, Vol. 79, pp. 645-648.
53. *Controlling the near-field oscillations of loaded plasmonic nanoantennas.* **Schnell, M., et al.** 2009, *Nature Photonics*, Vol. 3, p. 287.
54. *A microfluidic fluorescence measurement system using an astigmatic diffractive microlens array.* **Schonbrun, Ethan, Steinvurzel, Paul E. and Crozier, Kenneth B.** 2011, *Optics Express*, Vol. 19, p. 1385.
55. *High-throughput fluorescence detection using an integrated zone plate array.* **Schonbrun, Ethan, et al.** 2010, *Lab on a Chip*, Vol. 10, p. 852.
56. *Asymmetric cancer-cell filopodium growth induced by electric fields in a microfluidic culture chip.* **Wang, Chun-Chieh, et al.** 2011, *Lab on a Chip*, Vol. 11, pp. 695-699.

Chapter 6: Target application – Direct Linear Analysis

In this chapter, the architecture developed in this thesis is applied to demonstrate its capability to enable new integrated microfluidic systems. Specifically, an application to enable Direct Linear Analysis (DLA) for DNA fingerprinting is explored. Current applications for DNA fingerprinting are limited by their design, and we show how this device can enable new procedures. In this chapter, background on DNA fingerprinting and DLA is presented. The design of a DLA device is produced, and its fabrication and testing is performed. The fabricated device was able to detect sub-micron fluorescent particles – demonstrating the capability to expand into many other submicron optical detection applications. This result can enable on-chip DLA as well as other procedures not possible until now. Future work can build upon this to fingerprint a full strand of DNA in a DLA process. Also future work can utilize this new architecture for another application.

Introduction	142
DNA Fingerprinting	142
Single molecule DNA analysis	145
Direct Linear Analysis.....	147
Device Design	150
DNA Location	151
DNA Stretching.....	154
Testing	156
Conclusion.....	161
Works Cited.....	162

Introduction

DNA fingerprinting, the procedure of retrieving uniquely identifying information from a sample of DNA without fully sequencing it, is a useful tool in many areas. While the most well-known application of DNA fingerprinting is the identification of biological material from a crime scene (1)(2)(3), a robust DNA fingerprinting process has applications that reach beyond criminology and a controlled lab environment. DNA fingerprinting can also be used to also detect and identify diseases(4)(5)(6), biological warfare agents (1)(7), strains of virus (8)(9)(10)(11)(12), and strains of plants (2)(13).

The most common method of DNA fingerprinting is performed using Pulsed Field Gel Electrophoresis (PFGE) of restriction enzyme-digested DNA segments. In this process, DNA is broken into many segments of varying sizes (digested by a restriction enzyme) and the fragments are placed in a gel medium within an electric field. The charged DNA segments migrate through the gel due to the electric field, with the smaller segments moving more quickly. After time, due to this size-dependent difference in speed, the segments separate into discrete groups based on their mass. The location of these segments in the gel after a given time is an indicator of the distribution of restriction sites in the original DNA sample, and is an identifying characteristic for individuals (2)(8)(14)(15).

This process is material- (16) (10) and time-consuming (16) (10) (17) (18)(19). Also, it requires sample preparation, purification, and amplification, steps which require more time and consumables, as well as a trained operator (16) (10)(18). Many new techniques have been explored that improve upon PFGE. Specifically, single-molecule methods, in which analysis is performed on an individual strand of sample DNA, can achieve greater information output without costly processing steps. One exciting single-molecule fingerprinting method is direct linear analysis (DLA). I propose to develop a nanofluidic device with integrated waveguiding optics and metallic nanostructures that can be used to interrogate fluorescent tags. This integrated micro- opto- fluidic device can be used as an improved implementation of DLA as well as for other potential applications.

DNA Fingerprinting

DNA fingerprinting is a useful method of extracting identifying information from biological material. It can be used to identify people by comparing test results to a database (8) (15), and can determine sex, population of origin, and other phenotypic features (2). DNA fingerprinting methods can be used to determine the species of a sample, or to identify a member of that species, as when pieces of hair found at a crime scene were discovered to be a rare breed of cat, and then used to locate that cat's owner (2).

Because DNA fingerprinting can identify species, it can identify viruses, making it a useful tool for biological threat detection (1). Biological threat detection is an important application area where speed is important, as a disease can spread while undetectable by other means, creating the potential for biological warfare agents to kill more people than a nuclear or chemical attack (7). In epidemiology it is important to identify specific virus strains, and DNA fingerprinting is a useful tool for this as well, as it achieves the required identification without the cost and time to sequence the entire sample (8) (9)(11).

The basic theory behind DNA fingerprinting has not changed in the 25 years since it was first developed. Each person's DNA contains similar sequences, but these sequences appear at different places for different people. When comparing the locations of these sequences, it is possible to identify the person from their DNA. The first work done in DNA fingerprinting was by Alec Jeffreys in 1984, where he looked at the different locations of highly variable loci known as *minisatellites* (15).

In Jeffreys' work, DNA was digested by restriction enzymes, cutting it up into many pieces. These segments were observed via Southern blot, in which they are separated via electrophoresis, then transferred to a membrane and eventually stained with a fluorescent probe. This probe only attached to segments that contained a specific sequence, producing the characteristic striped "barcode" image of the DNA fingerprint (3). A typical example of this image is shown in Figure 1.

Much work has been done since then in improving both the biological techniques used for DNA fingerprinting as well as the interpretation of the results. Amplification by Polymerase Chain Reaction (PCR) has made it possible to work with smaller starting amounts of genetic material (2). Short Tandem Repeat (STR) and Single Nucleotide Polymorphism (SNP) analysis has allowed for higher accuracy, repeatability, and robustness to sample degradation (1)(2).

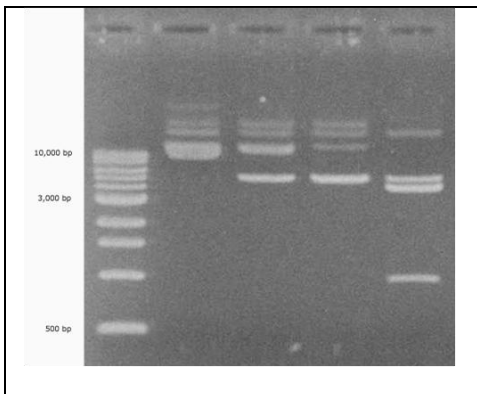


Figure 1: Typical DNA fingerprint output from PCR and gel electrophoresis method. Each horizontal bar is a group of DNA fragments. The separation of these bars is indicative of the size of the fragments. This spacing is the information used to identify DNA sources.

Readout techniques like PFGE and capillary gel electrophoresis have improved the ability to read the output of DNA fingerprinting processes (13) (20)(21)(22), but these techniques still have much room for improvement. Contamination of the sample, leading to mixtures of genetic material, can occur during or in between the process steps, leading to confusing results (1)(2). Even with a pure sample, fragments with different sequences may end up being the same size or a similar size, and these techniques will not be able to resolve them (12)(17). This degeneracy of having the same size but different sequence is not as catastrophic to DNA fingerprinting via restriction enzyme digestion as it may first seem. Actually, in capillary electrophoresis, two samples of the same size but with different sequences move at different speeds 56% of the time (17). So, while it is possible to differentiate two fragments with the same size, this effect still decreases the accuracy of a single run of these electrophoretic methods.

History of improvements in DNA fingerprinting

While Jeffreys and colleagues looked at a single blot for several minisatellites, DNA fingerprinting soon moved to focus on the use of a specific cloned minisatellite in a given test, revealing only one, highly variable change in sequence location. These specific tags were called single-locus probes (SLPs). In this process, the DNA is digested into many fragments as before. Then, several different Southern blots can

be performed, each with a different SLP to produce a fingerprint for each individual SLP that is easier to interpret, but has a high enough accuracy (2).

Polymerase chain reaction (PCR) was invented in 1983 and applied to DNA fingerprinting later, due to slow adoption of new techniques demanded by the forensic lab accreditation process(2), reducing the amount of genetic material required to perform an analysis. PCR uses DNA polymerase to make copies of desired fragments of DNA. By performing PCR on extracted DNA segments, many copies are made, enabling analysis when starting with much smaller amounts of DNA. However, in PCR only a handful of SNPs can be targeted due to the limitations placed on the enzymes available for this process (2), and it is difficult to interpret the results of a mixture of genetic material (1) (2).

Short tandem repeats (STRs) are DNA sequences that repeat a shorter sequence multiple times. These sequences show little change between PCR runs, and therefore increased the resolving capability of PCR based DNA fingerprinting methods (2), and making the idea of DNA databases possible. However, STR analysis requires long segments of DNA, so any degraded sample is difficult to analyze with this technique.

A method that can analyze shorter fragments of DNA is single nucleotide polymorphism (SNP) typing. A SNP is when two sequences of DNA match with the exception of a single base pair. SNP has been shown to be useful in testing degraded DNA, such as that from the World Trade Center disaster (2). However, this shorter length also indicates that more samples are needed to perform a statistically significant fingerprint (2), as well as leading to difficulties in understanding the output from mixtures (1). However, STR typing remains the preferred method for forensic applications (1).

Along with the advances in tagging methodologies, the manner of reading out the fragments has been improved, as well. In standard electrophoresis, as the voltage is applied across the gel, smaller segments have higher mobility and therefore travel further. However, segments larger than 50kb (1 kb = 1000 base pairs, a unit of measure of the length of DNA) cannot be resolved, as the mobility follows a power law by which the difference in size between two segments must be larger for long segments in order to achieve the same difference in mobility (23). Therefore, above 50 kb the mobility is dominated by conformational changes (13).

Fortunately, the speed of change in conformal states due to applied fields is dependent on segment size. By applying changing electric fields in varying directions, the conformational state of the DNA is altered in a manner dependent on its size. Using this process, segments up 2000 kb can be resolved (13). This technique, called pulsed field gel electrophoresis (PFGE), has proven to be useful in applications where long fragment sizes are desired, such as strain subtyping (9). However using PFGE to resolve differences in the sizes of DNA fragments is only an incremental change to the application of DNA fingerprinting. It requires trained operators, large amounts of material, and time (10)(18). The output bands are still difficult to resolve (17), and there is still a decreased resolution at longer segment length (23). Furthermore, it is difficult to create a truly repeatably quantifiable fingerprint due to inconsistencies in gel preparation between labs and even minute distortions in the gel, which will cause corresponding distortions in the spacing of the observed fingerprint(10). Then performing multiple independent

sample measurements, as required to construct a DNA fingerprint, these length errors accumulate, so more samples lead to more noise in the result (16).

In modern devices, capillary gel electrophoresis is commonly used, as it has improved heat dissipation (20) (allowing higher voltages to achieve greater mobility differences), and improved detection methods (21).

While techniques like PFGE and capillary gel electrophoresis have improved the ability to read the output of DNA fingerprinting processes, these techniques still have much room for improvement. Contamination of the sample, leading to mixtures of genetic material, can occur during or in between the process steps, leading to confusing results (1)(2). Even with a pure sample, fragments with different sequences may end up being the same size or a similar size, and these techniques will not be able to resolve them (12)(17). (This degeneracy of having the same size but different sequence is not as catastrophic to DNA fingerprinting as it may first seem. Actually, in capillary electrophoresis, two samples of the same size but with different sequences move at different speeds 56% of the time (17). So, while it is possible to differentiate two fragments with the same size, this effect still decreases the accuracy of a single run of these electrophoretic methods).

PCR based processes, which are necessary when dealing with a limited sample size, require trained personnel both to operate and interpret the results (7)(17) and reduce the amount of enzymes that can be used (16). Furthermore, because PCR methods typically copy the segments of several samples, the individual molecular sequence information is averaged, potentially missing important differences between strands (16) (8), and reducing the ability to build a comprehensive database (8). The process takes 10-50 hours per run (16) and because restriction enzyme digestion removes the ordering information of the segments, multiple restriction enzymes are required to construct a complete map (16). For *Staphylococcus aureus*, a frequent cause of infections in community and health care settings, it takes 21 hours to perform a single run, not counting over 24 hours of sample prep (22). Other work mentions that detection of hospital-acquired infections is still based on cell-culture methods, which require trained attention and time (over 48 hours) (19).

Single molecule DNA analysis

One way to fix several of the problems associated with the DNA fingerprinting methods mentioned above is to extract the information from a single piece of DNA. By using a single piece of DNA, it is possible to isolate specific differences between strands because the fragments from each sample are processed alone (16) (10)(24)(25). Also, by working with a complete DNA strand as opposed to fragments, it is easier to obtain an accurate genetic map or sequence when using a single DNA molecule because you can directly observe ordering information, instead of having to reconstruct the order of fragments via post processing (16) (10)(11). Single molecule methods are more robust to contamination, because it is easy to differentiate between different samples in the course of the procedure (14), some authors going so far to say that purification is not needed for single molecule studies (26).

While single molecule analysis has many application benefits, it also presents many engineering hurdles to its effective use. The detection of small signals from fluorescent tags, impedance measurements, mass, or other techniques is difficult. Specifically, when looking for such small signals background noise is significant. This noise usually comes from sources such as Raman and Rayleigh scattering from the medium (27) or impurities (26), fluorescence from impurities (26)(28)(29), or the dark current in the detector (26)(28). To enable single molecule detection, it is desired to have: small excitation volume (26)(28), high efficiency collection (26), highly efficient detectors (26), and careful elimination of background fluorescence (26)(28). Work in single molecule genetic analysis has provided many interesting results (19)(29)(30)(31)(32)(33). Two general methods of achieving these goals are point detection and wide-field detection (26).

Point detection methods reduce the volume of interest and couple with a highly sensitive point detector to detect individual events. The benefits of these methods are good signal-to-noise due to the low excitation volume and high temporal resolution. However, these processes are not parallel, and can only analyze one sample at a time. When initial point detection work in visualizing single virus cells was performed (28) (34), the authors realized the stringent requirements of single molecule detection and suggested the methods of making it possible were: reduced excitation volume, time-gated detection, and photobleaching of impurities to reduce the background signal (26) (28) (34). Accordingly, recent work at detecting single virus particles have worked with smaller channels and more sensitive detection techniques (25). After that first work in cell observation, researchers vision was narrowed and it was proposed that if one could couple single molecule detection of fluorescence with microfluidic flow, you could perform single-molecule DNA sequencing (35). In this process, a single strand of DNA is attached to a surface in a microfluidic flow. A complimentary strand is formed by attaching nucleotides that have base-specific fluorophores. The DNA is then digested with an exonuclease, sequentially cleaving the tagged base pairs one at a time, releasing them into the microfluidic flow. These cleaved, tagged base pairs are detected with a laser downstream (35). This process is a good initial step in identifying a single sample of DNA, but it is hindered by difficulties with contamination and background noise from fluorescent molecules (29). Also, isolating and immobilizing a single strand is a process step that would make this process time consuming and difficult to perform by untrained technicians.

Methods to improve sensitivity to fluorophores in microfluidic flows have been performed to work towards the benefits that come with single molecule detection. In the experiment above, it was required to process ~300 samples at once to achieve a detectable signal (29). Other, earlier, work on improved sensitivity was able to detect 67 fluorescent tags in a hydrodynamically focused stream (27). It was noted that the noise came mostly from Raman scattering of water from the excitation laser and there were suggested methods of improvement including: increased laser irradiance, increased photon collection efficiency, and decreased sample stream size(27). Another potential method of improving the detection efficiency would be to use metal nano-antennas to engineer the radiation pattern of the molecule to output light more efficiently to a detector (36). Different methods of detection are also possible in this area, such as detection the change of impedance as different molecules flow through a nanopore. This technique has been used to rapidly assess the binding affinity and location of drug elements along DNA molecules (30).

Wide-field detection methods generally work with immobilized particles, wide field illumination, and a CCD for detection. These methods can operate on many molecules in parallel, but suffer from low temporal resolution and low signal-to-noise (26). Some wide field methods can perform DNA sequence detection by observing the affinity of DNA to probe sequences by sensing the change in signal from a surface enhanced resonance Raman spectroscopy (SERS) measurement (19). Similar tests can be done with fluorescent tag detection, as well (31)(32). However, these are only binary tests that can indicate the presence of a given sequence. These tests do not have the capability to identify the sequence of an unknown sample. Also, they depend on a functionalized surface of probes, which reduce shelf life of a device (14).

Despite these drawbacks, wide-field detection methods have been found to be useful in several applications. Specifically, by multiplexing and using probes for many different organisms of interest, it is possible to use these methods to check what strands of virus are present in a hospital or patient (19) or to check for known biological warfare agents (1). Also, these methods can be cleverly multiplexed to provide a DNA fingerprint using SNPs (32).

An exciting recent method of detection combines wide-field and point detection components for single molecule DNA sequencing. In this method, a single strand of DNA is immobilized at the bottom of a small hole in a metal sheet, which is illuminated from behind. The hole is so small that light cannot propagate through, but there are strong evanescent fields inside of it. A complimentary strand is then produced from incorporating nucleotides with attached fluorophores. As each nucleotide is incorporated, it is brought into the ZMW, and therefore fluoresces brightly, as it is excited by the enhanced fields within the ZMW. As the next base is brought on, the link to the fluorescent molecule from the last nucleotide is cleaved, so only the signal from the most recently paired base is observed. When each nucleotide has a specific tag, it is possible to read out the exact sequence of the DNA as it is being paired (33). This process uses the point-detection idea of small excitation volume, but it can be performed in parallel, with many holes on the metal plate. However, this method also involves isolating and placing a single strand of DNA, a difficult and time consuming procedure. Also, as indicated before, for many applications, sequencing is not necessary, but a quick identifying “fingerprint” is what is needed in many applications.

Direct Linear Analysis

Direct Linear Analysis (DLA) is a high speed point detection technique for single molecule DNA fingerprinting based on fluorescent tags and microfluidic stretching (16). In DLA, double stranded DNA is fluorescently tagged at specific seven- or eight base pair sites using peptide nucleic acids (PNAs). The DNA is then also tagged with a non-specific intercalating dye, providing a fluorescent backbone along

the entire strand. This tagged sample is then run through a microfluidic device in which it is stretched via hydrodynamic forces into a linear configuration. While in this configuration, the DNA flows past three focused laser spots. Two of the spots are of one color, to excite fluorescence in the backbone dye, providing information on the start and end position of the sample, its velocity, and therefore its length. The third laser is coincident with one of the other two, and is used to detect the site-specific tags. With this information, the location of the target sequences on the DNA is determined, providing a fingerprint of the sample (16).

DLA enjoys all the advantages that go with a single molecule detection approach as well as additional benefits over other approaches that have been shown in the literature. Because there is no need to functionalize the surface or immobilize probe sequences or test sequences, the devices have no biological components, leading to a very long shelf life (14). Incorrect segmentation of DNA due to photolysis by the interrogation beam is not a concern, as the relaxation time of DNA in the channel is much greater than the interrogation time (14). Incorrect segmentation by restriction exonucleases is also not a concern, as they are not used in this process (14). Additionally, because isolation and immobilization of the sample is not needed, and single samples flow through the system very quickly, high throughput can be achieved (16). If a standard sample preparation process was followed, not using the site-specific PNAs, but instead digesting the DNA with a restriction enzyme (as in standard DNA fingerprinting methods), a DLA device can also be used to size individual fragments of DNA, providing a fast alternative to electrophoresis.

DLA is not without its limitations, however. The system currently employs three high power lasers and the associated precision optics that are required to focus those lasers to small, known locations. This equipment makes the system expensive, large, and dependent on alignment by a trained operator. The background noise is also a limiting factor (16). The resolution that is obtained is another limiting factor. The resolution is not as good as PFGE techniques for small (10,000 base-pair-long, or 10kb fragments), but it is better for long fragments (14). The resolution is important as it relates to the density of tags that can be resolved. If more closely-spaced tags can be resolved, more probe sequences can be used, and higher fidelity maps can be created, improving identification abilities with fewer sample pieces.

The resolution of a DLA device is dictated by several factors. The limiting factor of the current process is the speed at which the DNA is moving through the interrogation zone and the sampling frequency. The DNA is moving so quickly that one sample period of the detector accounts for a length in the DNA of 1.5 μm , or 5kb (16). This resolution limit could be lowered by simply reducing the velocity of the DNA or increasing the sample rate of the detector. However, a reduced velocity would reduce throughput and a faster sampling frequency would require brighter tags (16). If the excitation volume was reduced and background noise was lowered enough that similar accuracy could be achieved with fewer samples, throughput could be maintained while decreasing velocity. Additionally, reducing the excitation volume could reduce the background signal enough that a higher sampling frequency could be used.

Another limiting factor of the resolution is the reproducibility of the amount by which the DNA is stretched. This noise accounts for an uncertainty of $\pm 0.27 \mu\text{m}$ or $\pm 0.8\text{kb}$ in the location of tags (16). It is

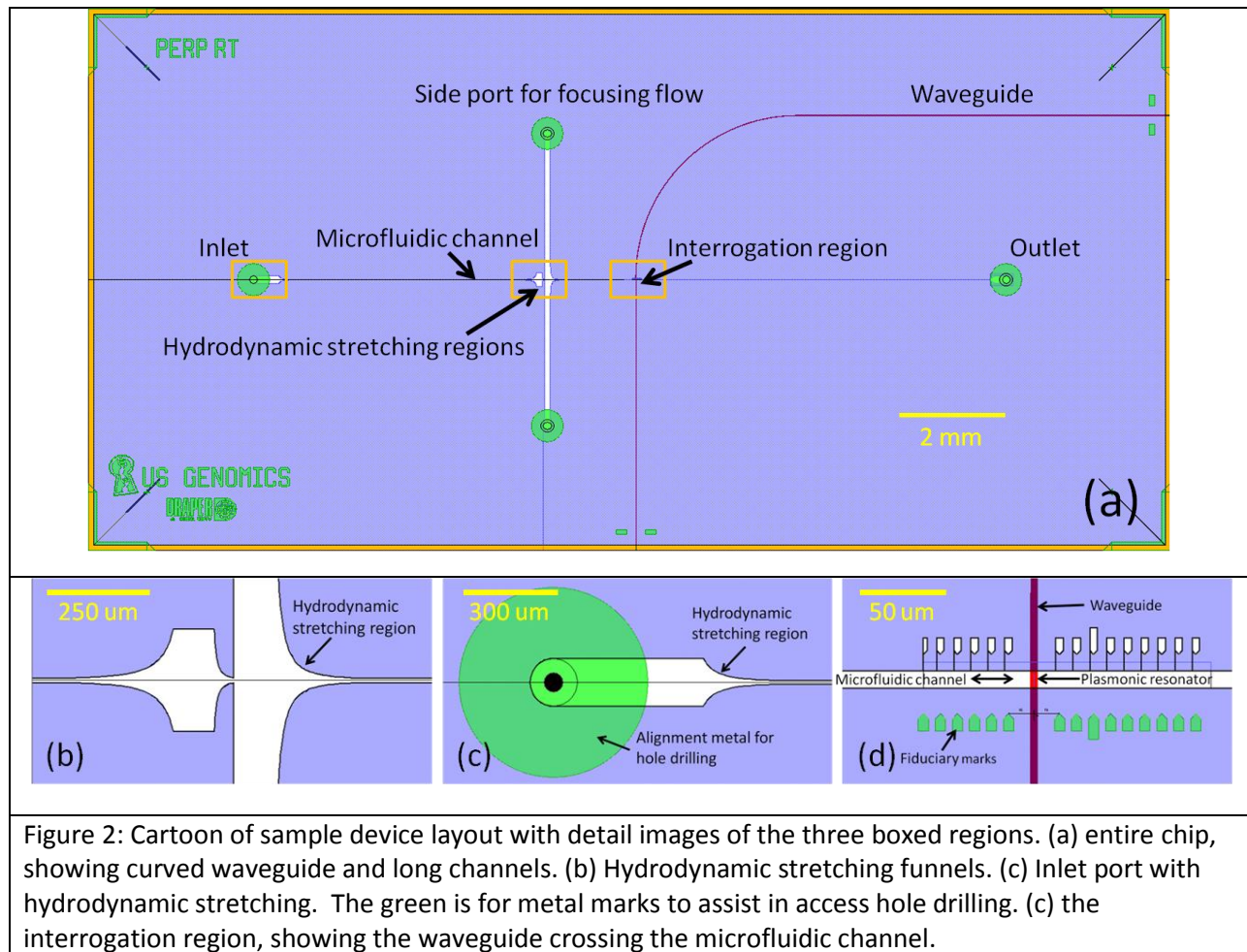
possible to improve on these numbers by further reducing the variation in DNA conformational states by reducing the volume of the microfluidic channel (37)(38).

The final limit of resolution is the diffraction limit of the laser light, which sets a minimum resolvable size at $\pm 0.23 \mu\text{m}$ or $\pm 0.68\text{kb}$ (16). We propose to concentrate the optical fields in the device, using a plasmonic resonator, to achieve a smaller excitation area, while reducing the interaction with the substrate of the device, improving this resolution and further suppressing background noise.

In this chapter, the components of DLA (reduced excitation volume and hydrodynamic stretching) are produced in an integrated optical and micro-/nanofluidic device utilizing the procedures developed in the preceding chapters. This work will improve on the DLA work done previously in several ways. Further reduction of channel volume will improve signal integrity and DNA localization. Reduction of the excitation volume will decrease the background fluorescence of the device and increase the sensitivity of the fluorescence detection (39). Integrating the optical excitation components will reduce the cost, size, and power requirements of this device, reduce the amount of background noise from stray light and fluorescence, and make it more robust and easier to operate. Additionally, integrating metal nanostructures to act as plasmonic resonators demonstrates the capability to drive confined, enhanced fields that will enable integrated high resolution readout that was not previously possible.

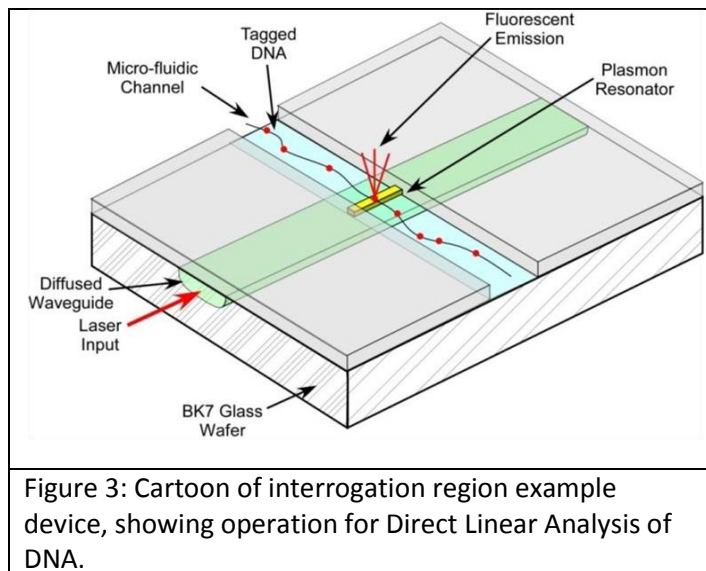
Device Design

To enable integrated DLA, this thesis strives to demonstrate an integrated architecture to detect submicron fluorescent particles. To accomplish this, the results from the previous chapters are utilized to fabricate an integrated optical detection fluidic device with reduced excitation volume, low noise, and improved resolution. The device is described along with considerations required in design and fluidic layout.



An example diagram of the device layout is shown in Figure 2, above. Unfortunately, the differences in scale between the length of the device and the size of the features make it difficult to see the features as well as the device shape at once on the printed page. Enlarged portions of the interesting areas are included as well. This device incorporates the features discussed in this thesis: waveguides, nanofluidics, and plasmonic resonators. The device also has some features that have not been discussed previously: hydrodynamic stretching funnels. These funnels and other fluidic considerations will be addressed after pointing out the components that have already been discussed.

This device incorporates the curved waveguides that were discussed in the optics chapter of this thesis. The curved waveguide and the index-matched polymer layer that defines the microfluidic channels are two advances from this thesis that reduce scattered noise, improving sensitivity. The region where the waveguide and the microfluidic channel overlap is called the interrogation region.



The diagram in Figure 3 demonstrates the structure of the interrogation region. The diffused waveguide runs beneath the microfluidic channel and the plasmonic resonator sits on the waveguide at that crossing point, placing it in the channel. The plasmonic resonator couples to evanescent fields from the waveguide as discussed in the plasmonic readout chapter. The resonance on the top surface of the plasmonic resonator then will excite fluorescence in the sample that flows above it, as described in that chapter, as well. This effect will be tested in this chapter.

Two aspects of this fluidic device that have not been covered previously in this thesis are the localization of the DNA in the depth of the channel and the hydrodynamic stretching of DNA. Those topics will be addressed here.

DNA Location

A cartoon of the cross-section of the interrogation area is shown below. This cartoon incorporates plasmonic fields from the FDTD simulations described in the plasmonic readout chapter. One question to the effectiveness of this device regards the proximity of a sample to the top surface of the plasmonic resonator. Because the confined plasmonic resonance decays exponentially into the fluid, proximity to the plasmonic resonator surface is important in order to achieve high magnitude excitation. How effectively will the DNA flow up over the plasmonic stripe, but stay in the high intensity field region? This concern is addressed with two solutions: channel dimensions and fluidic flow.

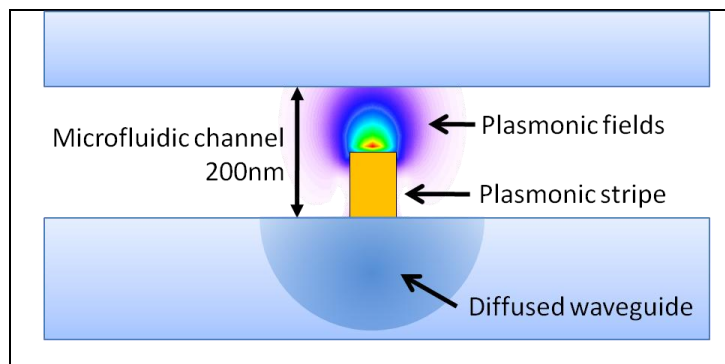


Figure 4: Cartoon cross-section of the interrogation region, showing the dimensions of the plasmonic resonator, plasmonic fields, and the channel thickness. The diffused waveguide is not to scale, but is included for demonstration.

The microfluidic channels in this device are very low aspect ratio: 10 μ m wide by 200nm deep. The chosen dimensions of the channels have two purposes. First, the low aspect ratio is useful in preventing clogging. As most contaminants are approximately spherical, any that arrive at the inlet to the channel will only block a small portion of the channel cross-section, allowing fluid and the small samples to still enter the channel. Even if contaminants were not spherical, it is very unlikely that a contaminant would have the proper shape and orientation to completely clog the

inlet. This prolongs the effective useful lifetime of the device.

A specific benefit of low aspect ratio channels in this device is the spatial confinement of the samples. By having very thin channels, we ensure that the samples flow within 100nm of the plasmonic resonator surface (when the resonator is 100nm tall). There is even a stronger likelihood that the samples are closer than 100nm, but that will be discussed in the fluidics discussion next. Regardless, the evanescent fields extend approximately 100nm into the fluid, ensuring excitation throughout the entire channel depth. A schematic diagram of the plasmonic stripe in the channel is shown by Figure 4. In this cartoon, while lateral dimensions are not to scale (the dimensions of the diffused waveguide are not accurate), the vertical dimension is, showing the extent of the evanescent fields into the channel.

Finally, as described above, the very small channel dimensions are also a benefit in improving optical sensitivity by reducing background noise from scattering and autofluorescence. Therefore the very low aspect ratio channels are a useful component of the system.

The second method to determine that the samples in the fluidic channel will pass near the plasmonic resonator is through analysis of the fluidic flow. This analysis was performed with information about the fluid behavior at nanoscale dimensions and qualitatively enforced with a finite element model of flow.

In microfluidic systems transporting particles of mass, the behavior of the particles is determined by two factors: advection and diffusion. Advection is the transport of something in the fluid due to the fluid's bulk motion. In other words, advection is the motion of particles due to fluid flow. Advective motion is described by a vector field and flow lines. Diffusion is the spread of particles due to random motion and is shaped by entropy considerations of the particles.

The ratio that determines which of these forces is dominant in a given situation is called the Péclet number. The Péclet number is the ratio of the rate of advection in a given system to the rate of diffusion in that same system. The Péclet number is generated by the simple equation:

$$Pe_L = \frac{LV}{D}$$

In the above equation, L is the characteristic length of the system, V is the velocity, and D is the diffusion constant. When the ratio is large, diffusion dominates, when it is small, advection dominates.

Now let us consider DNA flowing in our device. In the long segment of the channel before the interrogation volume, the location of DNA in the depth of the channel is regulated by diffusion and entropy. Because the characteristic length of the channel is very long compared to the velocity in this region, the Péclet number is large and diffusion dominates the transport phenomenon. Due to the conformal constraints induced by the walls of the channel, DNA will preferentially prefer to be in the center of the channel. The result of this is that the probability distribution of finding a piece of DNA at a given depth in the channel will follow a generally Gaussian distribution with the peak at the center of the channel. (38)

At the interrogation region, the plasmonic stripe constitutes a barrier to the fluid flow. Fluid must flow up and over the resonator, which fills approximately half the height of the channel. This region has a different Péclet number, as the characteristic length has changed. In this region, advection dominates (40). When advection dominates the probability distribution of the DNA location is no longer determined by the diffusion and entropic considerations, instead the entropic distribution that was present in the channel section will be altered by the fluidic flow. In this region, another flow parameter becomes important: the Reynolds number.

The Reynolds number is the ratio of inertial forces to viscous forces in a fluidic flow. It determines the quality of flow from laminar to turbulent. The Reynolds number is described by:

$$Re = \frac{\rho VL}{\mu}$$

The parameters for the Reynolds number are fluid velocity and characteristic length (V and L , as in the Péclet number), ρ is the fluid density and μ is the viscosity. A high Reynolds indicates that inertial forces or drag dominate, generating turbulent flow. A low Reynolds number indicates laminar flow. In our device near the interrogation region, the Reynolds number is very low, indicating that the flow is laminar. This means that the DNA will very closely follow the fluidic flow lines (41). Therefore, the probability distribution for the channel will be shifted by the fluidic flow lines above the plasmonic resonator.

Because of the low Reynolds number, these flow lines will minimize perturbation. This means that the flow lines that originated above the height of the plasmonic resonator are unlikely to change much. This means that the flow lines that must travel around the plasmonic resonator will compress into a much more tightly packed organization close to the surface of the resonator. This indicates that the distribution of DNA molecules will have its maximum near the surface of the plasmonic resonator.

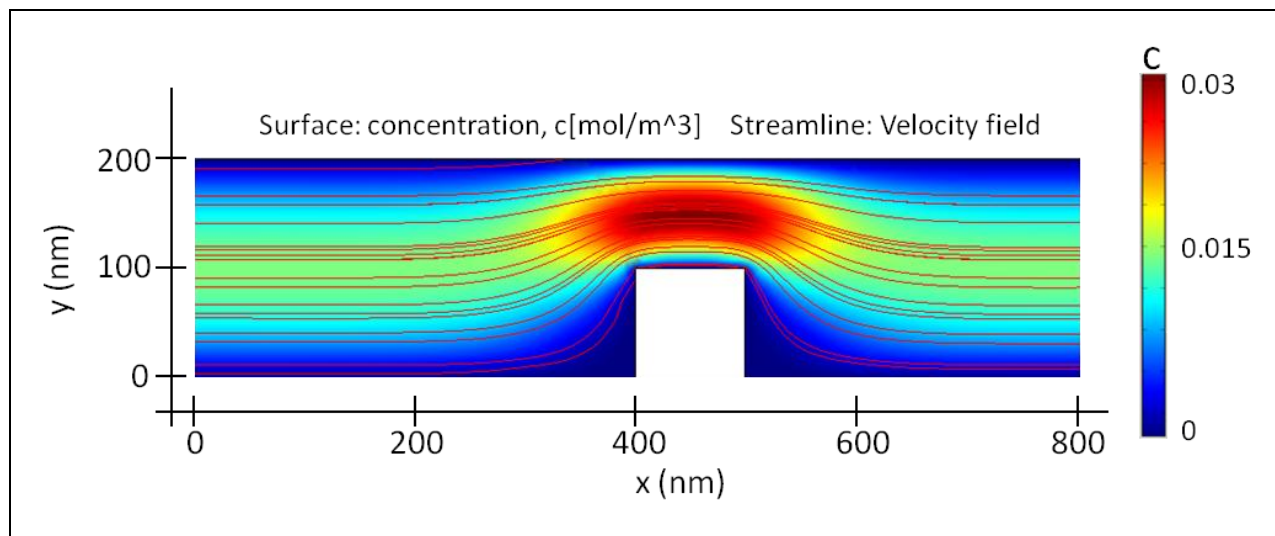


Figure 5: COMSOL model of flow in nanofluidic channel over plasmonic stripe. The color gradient indicates the concentration of a massless particle - indicative of DNA concentration. The flow lines are also shown, which DNA is expected to follow closely, due to the low Reynolds number of this flow.

A COMSOL finite element model was produced to indicate the change in portability distribution. This model is for massless concentration parameters, not actual DNA molecules. However, as the Reynolds number is very low, the DNA can be expected to follow a similar profile, indicating that the majority of DNA samples will pass close to the plasmonic resonator, as shown by the results from the simulation in Figure 5. More rigorous analysis could be performed with molecular simulations, but this was deemed unnecessary, as the arguments above were considered to be valid.(42)

DNA Stretching

An important factor in DLA is achieving reliable stretching of the DNA samples. The standard configuration of DNA is coiled up in a ball. For DLA, the strand must be stretched out in a regular, repeatable fashion. This stretching is important for several reasons: complete stretching is important in order to enable effective resolution of all base pairs. If the DNA is slightly bent, the observed length will be skewed. Complete stretching is important to provide space between tagged sections to enable their resolution. Finally, a repeatable stretching procedure is important to enable comparison of samples between different process runs. The DNA is stretched in this device via two methods: channel localization and hydrodynamic stretching(37). This work was not performed for this thesis, but is covered here for completeness.

The conformation of DNA is determined by entropic considerations. It has been shown that when placed in a channel with different crosssections, DNA conformal behavior will fall into two regimes. In larger channels, DNA is said to conform in the de Gennes regime, where DNA molecules tend to coil up into “blobs” of predictable shape (37)(23). In smaller channels (~100nm), there is a transition to the

Odijk regime(23), where the DNA tends to take on a generally linear orientation, whereupon the sample can be described by a model using balls and stiff connecting rods(43). This confined conformational regime has been shown to exist even in slit-like channels with large aspect ratio. (44). Therefore, by confining the dimensions of the channel, we are setting the DNA into a preferred, elongated state.

To stretch the DNA further and more reliably in a flow regime, hydrodynamic stretching is utilized(45)(46)(47). Other methods to stretch DNA include electrophoretic methods(48), or surface tension methods (47). In this device, hydrodynamic stretching is accomplished by integrating funnel designs into the fluidic layout. In these funnel regions, the fluid in the narrow region of the funnel travels faster than the fluid in the wide region. When an end of a DNA strand comes close to the faster-moving section of fluid, it is pulled along with the fluid, introducing a controlled strain along the DNA molecule. This strain will serve to stretch the DNA out, as it is pulled through the funnel (49)(46). Much work has been done to research the optimal funnel shape and the amount and repeatability of the stretching that can be achieved (45) (46) (49). A screen capture of a video courtesy of US Genomics in Figure 6 shows fluorescently tagged DNA being stretched via hydrodynamic forces in a funnel under pressure-driven flow.

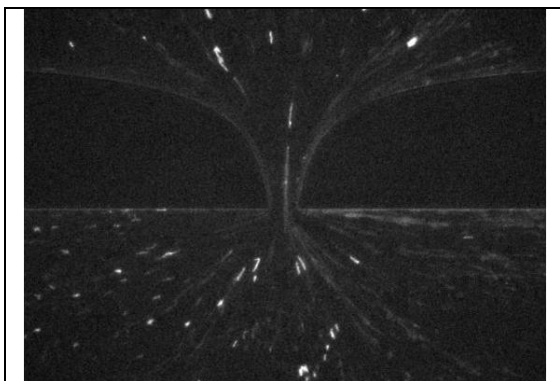


Figure 6: Fluorescently tagged DNA stretching in hydrodynamic funnel at 4.7atm pressure driven flow.

Therefore, by combining all these elements into one device, we are able to achieve a system that can provide beneficial DLA operation. Integrated, curved waveguides with an index-matched polymer layer achieve reduction of background noise. Plasmonic resonators provide localized, enhanced excitation fields. Nanofluidic channels and laminar flow ensure that the samples pass close to the plasmonic resonator. And fluidic considerations ensure that the DNA sample is stretched into a linear configuration, enabling linear readout.

Testing

The goal of this thesis is to provide a framework for creating useful devices. However, it is desired to demonstrate the capabilities enabled by this framework. Therefore, to demonstrate the capabilities of a device produced with this work, it was desired to test it and demonstrate the capability of achieving localized, high-sensitivity detection of fluorescent samples. Two types of test were carried out: bulk fluid tests and isolated particle tests. These tests demonstrate the successful accomplishment of high resolution, low noise optical detection. Typical spectra for filter set and a fluorophore used in these experiments is shown in Figure 7. The fluorophore absorbs at one wavelength, and emits at a slightly shifted wavelength. The combination of the dichroic mirror and emission filter filter out the excitation light and guide the emission light to the camera (as shown in Figure 8)

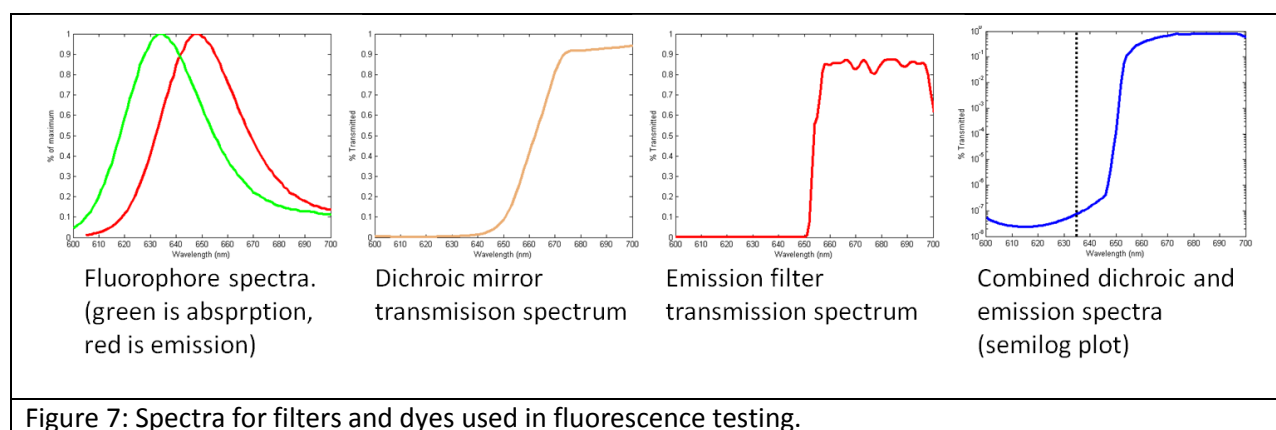


Figure 7: Spectra for filters and dyes used in fluorescence testing.

In bulk fluid tests, the entire channel was filled with a fluorescent fluid. By introducing laser light through the waveguide, it is possible to directly image the intensity of excited fields through the intensity of fluid. This test is capable of showing not only the shape, size and intensity of fields from the plasmonic resonance; it also provides a good indication of scattered light that may exist. Because the entire channel is filled with fluorescent fluid, any light from scattering sources would induce fluorescence, as well. Therefore, this test provides a great measure of not only the field concentration for the plasmonic resonator, but also is a test for reduction of background noise.

The discrete particle test provides the more directly analogous test to the applicability to DLA. By flowing discrete submicron fluorescent particles through the system, we are able to test the device capabilities in detecting discrete fluorescent signals.

The experimental test setup for both of these tests (bulk fluid and discrete particles) is the same – the only difference is the sample that is introduced. The experimental setup is shown in Figure 9, below. The tests take place in a standard inverted fluorescence microscope. The operation of general epifluorescence microscopy testing system is shown in Figure 8. In general fluorescence microscopy, illumination is achieved via a white light source that is sent through a filter and a dichroic mirror, providing a narrow wavelength range of illuminating light. This light excites fluorescence in the

fluorescent sample, which has absorption and emission curves as shown in Figure 7. The emitted light is slightly frequency shifted from the excitation light, enabling its isolation via filtering. This emitted light is collected via optics, and preferentially reflects off of the dichroic mirror, providing some filtering. The signal is further filtered by the emission filter. The combination of dichroic and emission filter provide approximately 10^7 reduction of excitation light while passing almost 100% of the emitted fluorescent light. This is shown by the transmission spectra in Figure 7.

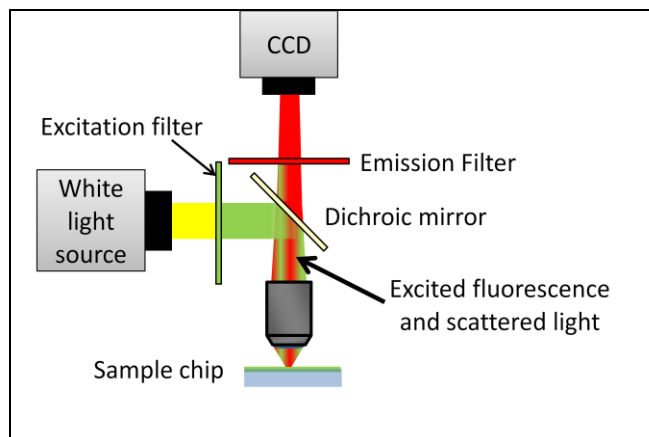


Figure 8: Experimental setup for standard fluorescence microscopy. White light is filtered and focused onto the sample. The fluorescent signal is collected along with scattered light, filtered and passed to the camera.

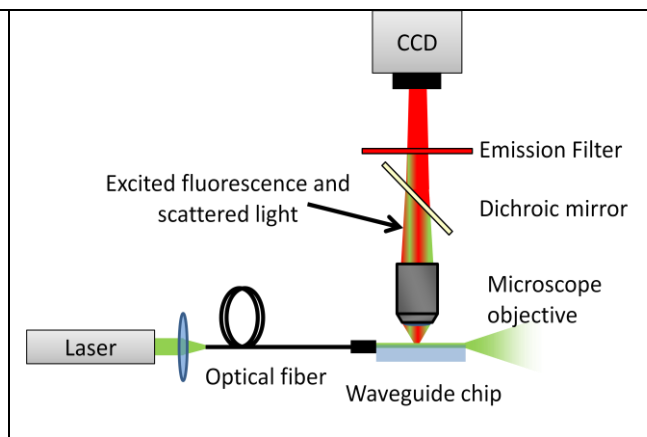


Figure 9: Experimental setup for laser-induced integrated system fluorescence testing. Laser light is introduced to the chip via an optical fiber and then routed on the chip via integrated waveguide. Excited fluorescence is collected and filtered as in standard fluorescence microscopy.

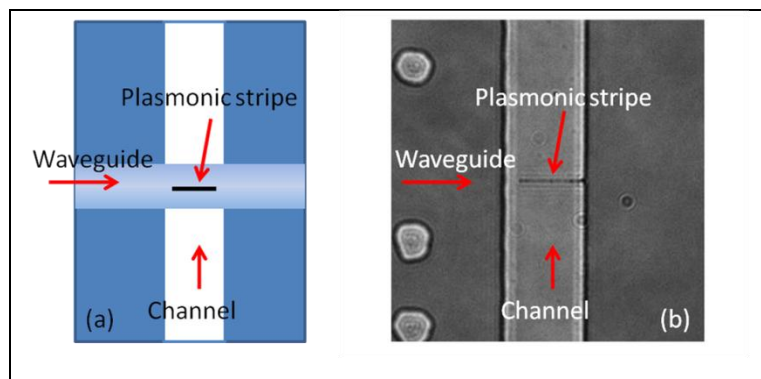


Figure 10: Interrogation region for fluorescence tests. (a) Cartoon showing how the waveguide crosses beneath the microfluidic channel and the plasmonic resonator sits at the intersection. (b) Optical microscope image at 100x magnification of the interrogation region of a tested device. The waveguide cannot be seen because the index contrast is very small.

To test the operation of our system, we remove the white light source and instead introduce excitation laser light via the diffused waveguide. This light propagates along the waveguide, exciting the plasmonic resonance which in turn excites the fluorescent sample. Other fluorescence may be excited by scattered light. The signal is then collected and filtered using the same filter setup as before. This test setup is shown in the diagram of Figure 9.

A cartoon of the interrogation region is provided in Figure 10. Also, a white-light image is shown for comparison.

The important characteristics to observe about this region are that the waveguide crosses underneath the fluidic channel at the middle, and the plasmonic resonator sits at that intersection.

The test results provided in Figure 11 show effective field localization and enhancement as well as noise suppression. Images are discussed below to illustrate these results.

The initial tests with fluorescent fluid in devices without the index-matched polymer layer showed a lot of scattered light in the interrogation region. This is indicated by the bright section in the middle of the image. This demonstrates the benefit of this test in visualizing scattered light.

When moving to the index-matched polymer layer, this scattered light was reduced to the level that we are able to observe the other interesting phenomena: evanescent fields and plasmonic resonator.

The next test took a long image to be able to observe the existence of evanescent fields above the waveguide, exciting the fluid in the field. This result is able to be separated from the scattered light as the fluorescence intensity is uniform across the width of the channel. This indicates that this is not scattering from one location, but a constant excitation along the waveguide. Additionally the sinusoidal profile demonstrates the shape expected from the waveguide mode. However, it is desired to achieve even further reduced excitation volume along with enhanced fields. This result provides a good result for microfluidic optical detection. We have demonstrated 5 μ m lateral resolution with little scattered light.

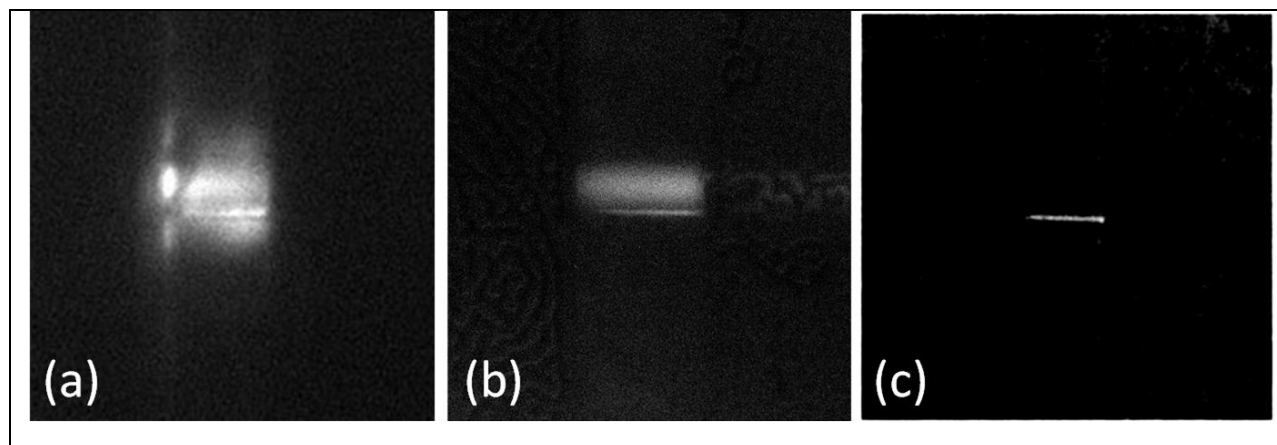
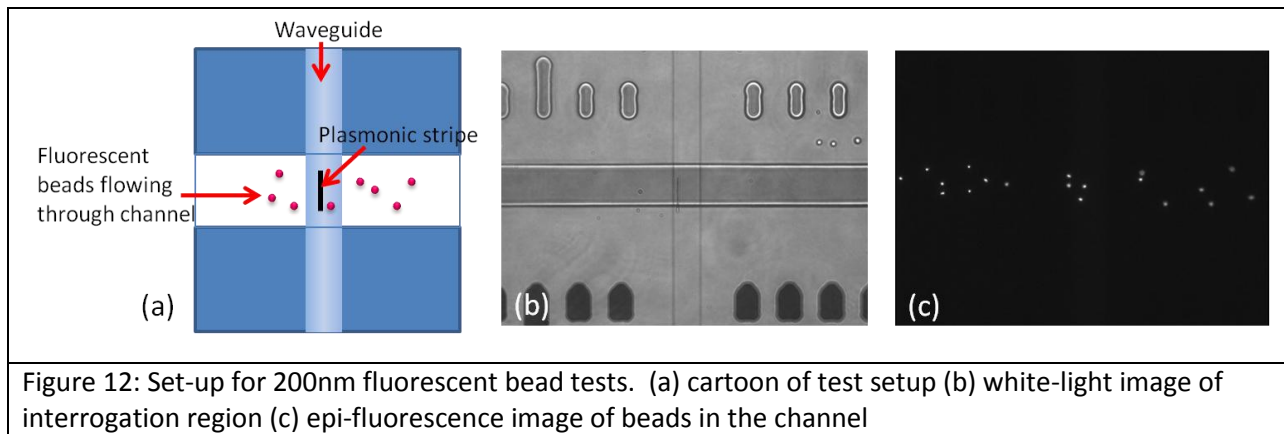


Figure 11: Results of bulk fluorescent fluid tests. (a) Device without index-matched polymer shows large amounts of scattered light in the channel. (b) With the index matched layer, scattering is reduced and evanescent fields are visible. (c) With shorter exposure times, only the enhanced fields from the plasmonic stripe are observed, demonstrating enhanced, localized fields.

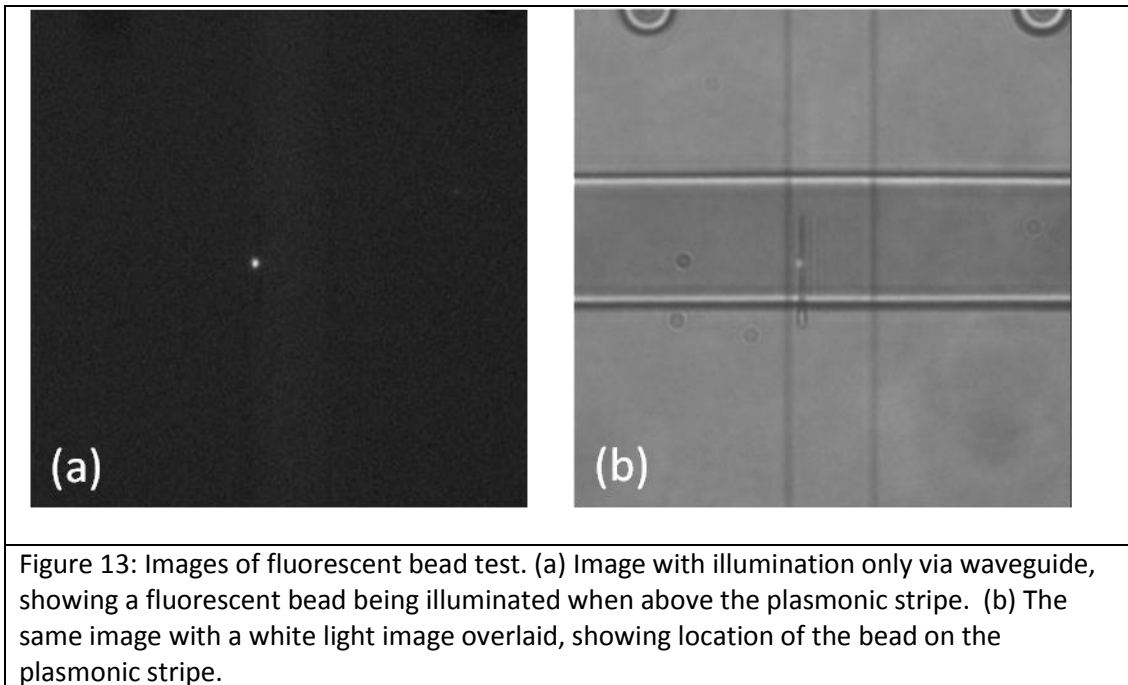
Finally, a short exposure shows only the most intense fluorescent areas. This is shown in Figure 11 (c). In this figure we are able to see the plasmonic stripe as the only source of fluorescent light. This image demonstrates both the spatial confinement as well as the field enhancement. Field confinement is verified by measuring the size of the observed fluorescent field, which corresponds to the size of the plasmonic stripe. This demonstrates 200nm lateral resolution – resolution that has not been achieved before in any integrated device. Additionally, because the plasmonic stripe is observed to have greater

brightness than the evanescent fields (which are not even observable in this image), field enhancement is demonstrated.

Further tests were performed to demonstrate the ability to detect submicron fluorescent particles. Molecular Probes' FluoSpheres from Invitrogen were used for this purpose. The particles are spheres of polystyrene embedded with fluorescent dye that can be chosen for a variety of excitation and emission spectra. Initial tests were performed with spheres with 200nm diameter. These spheres are implanted with "Yellow-green" fluorophore, which absorbs and emits light around 500nm. Figure 12 provides images describing the testing images. Figure 12 (a) provides a cartoon describing the interrogation area. This is very similar to the previous tests with fluorescent fluid. The only difference is that fluorescent fluid is replaced with discrete fluorescent beads suspended in a flowing solution. Figure 12 (b) provides a white-light image of that region, and section (c) shows an image under epi-fluorescence illumination. This image shows the fluorescent beads in the channel.



The tests were performed as the fluorescent fluid tests, above. The external illumination was turned off and the only electromagnetic excitation that was introduced was via the integrated waveguide. If operating properly, the plasmonic stripe will couple to those fields and produce confined, enhanced fields. Any image taken then should then only show beads as they flow over the plasmonic stripe, with the other beads throughout the channel not being illuminated. As shown in Figure 13, this is the case. The entire channel is filled with beads, as shown in Figure 12 (c), but the only one illuminated is directly over the channel. Figure 13 (b) shows the same image with a white-light image of the region superimposed over it, demonstrating that the fluorophore is indeed over the plasmonic stripe.



Further tests were performed to demonstrate excitation of smaller samples. The spheres used in this test were the Crimson color that is well matched to absorb at the 633nm wavelength. The size of the particles was measured with a Malvern Zetasizer 200 and found to average 16.5nm in diameter. The solution was mixed with IPA to improve wetting properties and allowed to flow into the channels. When the IPA solution evaporated, particles remained in the channel. The experiment was performed in this manner to keep the samples stationary. The images below demonstrate the results.

As shown in Figure 14, the particles were able to be observed via the integrated device. In section (b) the channel was filled with the fluorescent particles and illuminated with excitation light. All the particles are excited and observed. In part (c) only the laser illumination is used. This laser is guided via the diffused waveguide under the microfluidic channel. The plasmonic stripe couples light out of the waveguide and excites fluorescence in the particles that are directly above it. This is shown in that only the two particles above the stripe are visible. This test demonstrates the ability to excite and observe submicron particles.

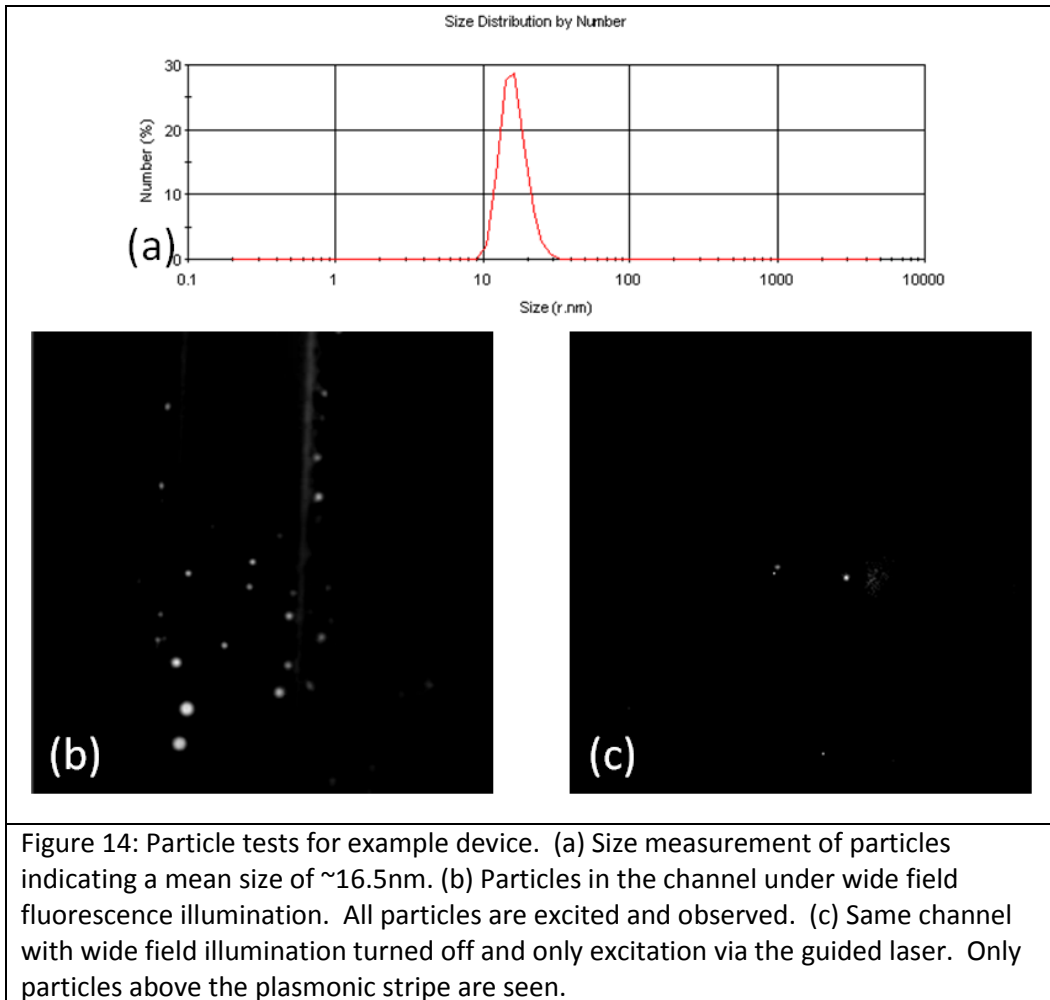


Figure 14: Particle tests for example device. (a) Size measurement of particles indicating a mean size of $\sim 16.5\text{nm}$. (b) Particles in the channel under wide field fluorescence illumination. All particles are excited and observed. (c) Same channel with wide field illumination turned off and only excitation via the guided laser. Only particles above the plasmonic stripe are seen.

Conclusion

A motivating factor for this work was the pursuit of an improved device for Direct Linear Analysis (DLA) of DNA. The merits of DLA were argued and the usefulness of an integrated device with reduced excitation volume was presented. It has been demonstrated that the process components developed in this thesis can be integrated to form a device capable of achieving the reduced excitation volume, reduced noise, and field enhancement necessary to enable improved, integrated DLA. We have demonstrated field enhancement and confinement to $<200\text{nm}$, achieving what we believe to be the smallest lateral excitation resolution ever demonstrated in this type of device. The resolution achievable by this system is therefore better than can be achieved with conventional optical tools at these wavelengths. Additionally, the ability to detect 200nm fluorescent particles in a flow condition and $\sim 16\text{nm}$ fluorescent particles at rest was demonstrated.

Works Cited

1. *Integrated microfluidic systems for high-performance genetic analysis*. **Liu, Peng and Mathies, Richard A.** 10, 2009, Trends in Biotechnology, Vol. 27, pp. 572-581.
2. *Encoded evidence: Dna in forensic analysis*. **Jobling, Mark A. and Gill, Peter.** 2004, Nature Reviews: Genetics, Vol. 5, pp. 739-751.
3. *Forensic application of DNA 'fingerprints'*. **Gill, Peter, Jeffreys, Alec J. and Werrett, David J.** 1985, Nature, Vol. 318, pp. 577-579.
4. *Editorial: Molecular advances in diseases*. **Koshland, Daniel E.** 1992, Science, Vol. 256, p. 717.
5. *Identification of the Cystic Fibrosis Gene: Chromosome walking and jumping*. **Rommens, Johanna M., et al.** 1989, Science, Vol. 245, pp. 1059-1065.
6. *Characterization of a yeast artificial chromosome contig spanning the Huntington's disease gene candidate region*. **Bates, G.P., et al.** 1992, Nature Genetics, Vol. 1, pp. 180-187.
7. *Nucleic acid approaches for detection and identification of biological warfare and infectious disease agents*. **Ivnitski, Dimitri, et al.** 2003, Biotechniques, Vol. 35, pp. 862-869.
8. *Principles and applications of methods for DNA-based typing of microbial organisms*. **Olive, Michael D. and Bean, Pamela.** 1999, Journal of Clinical Microbiology, Vol. 37, pp. 1661-1669.
9. *Rapid pulsed-field gel electrophoresis protocol for typing of Escherichia coli O157:H7 and other gram-negative organisms in 1 day*. **Gautom, Romesh K.** 1997, Journal of Clinical Microbiology, Vol. 35, pp. 2977-2980.
10. *Staphylococcus aureus strain typing by single-molecule DNA mapping in fluidic microchips with fluorescent tags*. **White, Eric J., et al.** 2009, Clinical Chemistry, Vol. 55, pp. 2121-2129.
11. *Rapid DNA mapping by fluorescent single molecule detection*. **Xiao, Ming, et al.** 2007, Nucleic Acids Research, Vol. 35, p. e16. published online 14 December 2006.
12. *Evaluation of pulsed field gel electrophoresis as a tool for determining the degree of genetic relatedness between strains of Escherichia coli*. **Davis, M.A., et al.** 2003, Journal of Clinical Microbiology, Vol. 41, pp. 1843-9.
13. *Separation of yeast chromosome-sized DNAs by pulsed field gradient gel electrophoresis*. **Schwartz, David C. and Cantor, Charles R.** 1984, Cell, Vol. 37, pp. 67-75.
14. *Application of single molecule technology to rapidly map long DNA and study the conformation of stretched DNA*. **Phillips, Kevin M., et al.** 2005, Nucleic Acids Research, Vol. 33, pp. 5829-5837.

15. *Individual specific 'fingerprints' of human DNA.* **Jeffreys, A. J., Wilson, v. and Thein, S. L.** 1985, Nature, Vol. 316, pp. 76-79.
16. *DNA mapping using microfluidic stretching and single-molecule detection of fluorescent site-specific tags.* **Chan, Eugene Y., et al.** 2004, Genome Research, Vol. 14, pp. 1137-1146.
17. *Whole-genome validation of high-information-content-fingerprinting.* **Nelson, William M., et al.** 2005, Plant Physiology, Vol. 139, pp. 27-38.
18. *An automated sample preparation system with mini-reactor to isolate and process submegabase fragments of bacterial DNA.* **Mollova, Emilia T., et al.** 2009, Analytical Biochemistry, Vol. 391, pp. 135-143.
19. *DNA Sequence detection using Surface Enhanced Resonance Raman Spectroscopy in a homogeneous multiplexed assay.* **MacAskill, Alexandra, et al.** 2009, Analytical Chemistry, Vol. 81, pp. 8134-8140.
20. **Camilleri, Patrick.** Capillary electrophoresis: theory and practice. 2. s.l. : CRC Press, 1998, Chapter 1, History and development of capillary electrophoresis.
21. **Guttman, Andras and Schwartz, Herbert.** Capillary electrophoresis: theory and practice. [ed.] Patrick Camilleri. 2. s.l. : CRC Press, 1998, Chapter 9, separation of DNA.
22. *Pulsed-field gel electrophoresis typing of oxacillin-resistant Staphylococcus aureus isolates from the Unites States: establishing a national database.* **McDougal, Linda K., et al.** 2003, Journal of Clinical Microbiology,, Vol. 41, pp. 5113-5120.
23. *The dynamics of genomic-length DNA molecules in 100-nm channels.* **Tegenfeldt, Jonas O., et al.** 2004, PNAS, Vol. 101, pp. 10979-10983.
24. *Direct molecular haplotyping of long-range genomic DNA with M1-PCR.* **Ding, Chunming and cantor, Charles R.** 2003, PNAS, Vol. 100, pp. 7449-7453.
25. *Nano-optofluidic detection of single viruses and nanoparticles.* **Mitra, Anirban, et al.** 2010, ACS Nano, Vol. 4, pp. 1305-1312.
26. *Fluorescence Spectroscopy of Single Biomolecules.* **Weiss, Shimon.** 1999, Science, Vol. 283, pp. 1676-1683.
27. *Laser-Induced fluorescence of flowing samples as an approach to single-molecule detection in liquids.* **Dovich, Norman J., et al.** 1984, Analytical chemistry, Vol. 56, pp. 348-354.
28. *Fluorescence background discrimination by prebleaching.* **Hirschfeld, Tomas.** 1979, The Journal of Histochemistry and Cytochemistry, Vol. 27, pp. 96-101.
29. *Towards a general procedure for sequencing single DNA molecules.* **Stephan, Jens, et al.** 2001, Journal of Biotechnology, Vol. 86, pp. 255-267.

30. *DNA Profiling using solid state nanopores: detection of DNA-binding molecules.* **Wanunu, Meni, Sutin, Jason and Meller, Amit.** 2009, Nano Letters, Vol. 9, pp. 3498-3502.
31. *Light-generated oligonucleotide arrays for rapid DNA sequence analysis.* **Pease, A. C., et al.** 1994, PNAS, Vol. 91, pp. 5022-5026.
32. *DNA probes for the highly sensitive identification of single nucleotide polymorphism using single-molecule spectroscopy.* **Friedrich, Achim, et al.** 2007, FEBS Letters, Vol. 581, pp. 1644-1648.
33. *Real time DNA sequencing from single polymerase molecules.* **Eid, John, et al.** 2009, Science, Vol. 323, pp. 133-138.
34. *Virometer - an optical instrument for visual observation, measurement, and classification of free viruses.* **Hirschfeld, Tomas, Block, Myron J. and Mueller, William.** 1977, The Journal of Histochemistry and Cytochemistry, Vol. 25, pp. 719-723.
35. *High speed DNA sequencing: an approach based upon fluorescence detection of single molecules*
High speed DNA sequencing: an approach based upon fluorescence detection of single molecules. **Jett, J. H., et al.** 1989, Journal of Biomolecular Structural Dynamics, Vol. 7, pp. 301-309.
36. *Efficient coupling of photons to a single molecule and the observation of its resonance fluorescence.* **Wrigge, G., et al.** 2008, Nature Physics, Vol. 4, pp. 60-66.
37. *Conformation and dynamics of DNA confined in slitlike nanofluidic channels.* **Bonthuis, Douwe Jan, et al.** 2008, Physical Review Letters, Vol. 101, p. 108303.
38. *Pressure driven transport of confined DNA polymers in fluidic channels.* **Stein, Derek, et al.** 2006, PNAS, Vol. 103, pp. 15853-15858.
39. *Rapid quantitative analysis using a single molecule counting approach.* **D'Antoni, Christina M.** 2006, Analytical Biochemistry, Vol. 352, pp. 97-109.
40. *Characterization of DNA hybridization kinetics in a microfluidic flow channel.* **Kim, Joshua Hyong-Seok, et al.** 2006, Sensors and Actuators B: Chemical, Vol. 113, pp. 281-289.
41. *Pressure driven transport of particles through a converging-diverging microchannel.* **Ai, Ye, et al.** 2009, Biomicrofluidics, Vol. 3, p. 022404.
42. **Doyle, Patrick S.** Private Meeting. *Private Meeting.* 2010.
43. *On the statistics and dynamics of confined or entangled stiff polymers.* **Odijk, Theo.** 1983, macromolecules, Vol. 16, pp. 1340-1344.
44. *Relaxation of stretched DNA in slitlike confinement.* **Balducci, A, Hsieh, C.C. and Doyle, P.S.** 2007, Physical Review Letters, Vol. 99, p. 238102.

45. *Conformational Preconditioning by Electrophoresis of DNA through a Finite Obstacle Array.* **Balducci, A. and Doyle, P.S.** 2008, *Macromolecules*, Vol. 41, pp. 5485-5492.
46. *Single DNA molecule stretching in sudden mixed shear and elongational microflows.* **Larson, Jonathan w., et al.** 2006, *Lab on a Chip*, Vol. 6, pp. 1187-1199.
47. *Stretching DNA with a receding meniscus: experiments and models.* **Bensimon, D., et al.** 1995, *Physical Review Letters*, Vol. 74, pp. 4754-4757.
48. *Methods to electrophoretically stretch DNA: microcontractions, gels, and hybrid gel-microcontraction devices.* **Randall, Greg C., Schultz, Kelly M. and Doyle, Patrick S.** 2006, *Lab on a Chip*, Vol. 6, pp. 516-525.
49. *Design and numerical simulation of a DNA electrophoretic stretching device.* **Kim, Ju Min and Doyle, Patrick S.** 2007, *Lab on a Chip*, Vol. 7, pp. 213-225.
50. *Coil-stretch transition of DNA molecules in slitlike confinement.* **Tang, Jiong, Thahan, daniel W. and Doyle, Patrick S.** 2010, *Macromolecules*, Vol. 43, pp. 3081-3089.
51. *Mechanisms of DNA separation in entropic trap arrays: a Brownian dynamics simulation.* **Streek, Martin, et al.** 2004, *Journal of Biotechnology*, Vol. 112, pp. 79-89.

Chapter 7: Conclusion

This thesis presented a fabrication procedure to create a new type of integrated optical / nanofluidic device that can accomplish low-noise, high resolution optical excitation of fluorescent samples. The creation of such a device required advances in several areas. It also presented opportunities for further work in the same areas as well as new ones.

This work

This work achieved the production of an integrated optical nanofluidic device with plasmonic readout in glass. To accomplish this, new fabrication procedures had to be developed and existing procedures had to be adjusted. Modeling and simulation of various components provided the necessary design optimization to ensure proper operation. An example device was fabricated and tested – demonstrating enhanced and confined electromagnetic fields excited via integrated waveguides. The decreased excitation volume and low noise are device characteristics that have been desired but unattainable before now. Furthermore, the lateral resolution achieved of 200nm is the best seen in this type of device until now. A summary of the achievements from each chapter are discussed below.

Optics

A model for the index profile of diffused waveguides was not agreed upon in the existing literature. This is probably due to difficulty of testing and differences due to slight differences in fabrication procedures. An accurate profile for fabricated waveguides was determined via simulation and test, enabling accurate simulations of the effects of waveguide modal properties on the plasmonic stripes. This model was not agreed upon in the existing literature. An index matched polymer layer architecture and device layout was developed in order to minimize scattered light in the interrogation region of the device, reducing background noise and improving sensitivity.

Fabrication

While most individual process steps used in this thesis were not new, their integration was. The specific considerations that must be taken into account and the proper method of integrating these fabrication procedures was developed and presented to enable production of these devices in the future.

Bonding

Several methods of bonding were explored to enable high-strength, robust, chemically compatible, optical quality bonding of glass that is compatible with the rest of the fabrication procedures. General considerations for bonding were presented and three bond procedures were explored. A glass-to-glass anodic type bond was explored and the effects of various materials and thicknesses were explored in a manner that made comparison possible between bond methods. The second type of bond explored was a polymer bond. Common methods to improve polymer bond strength were considered and tested. Finally, the voltage-assisted polymer bond procedure was developed. This bond procedure was tested

against the other two and found to produce the best combination of strength, robustness, and optical quality. The bond strength is far superior to standard polymer bonding in our tests. The effects of voltage magnitude and surface treatments were explored with two different polymers. The polymer Cytop was used to achieve an index of refraction match to water, reducing scattered light. This new bond procedure proved to be incredibly useful in optical microfluidic devices and we expect it can be used for other devices in the future.

Plasmonic Readout

The capabilities of a plasmonic resonator to enhance and confine excitation fields was presented. Resonators were designed and simulated using FDTD tools. An adjustment of the standard model for optical properties of metals was developed. Devices were fabricated to test the plasmonic behavior both in isolation and in an integrated system. The devices are shown to agree qualitatively with the simulations. Furthermore, the device was shown to effectively couple to the evanescent fields and achieve field enhancement and confinement.

Example application:

The theory and state of the art of Direct Linear Analysis (DLA) for DNA fingerprinting was presented. It was shown that an integrated device with reduced noise and reduced excitation volume is desired. A sample device was fabricated using the processes developed in this thesis and tested. The device is shown to perform effectively in reducing noise and excitation volume. The lateral excitation volume estimated to be around 200nm is the best that we have seen in this type of device. This demonstrates the ability of this type of device to achieve higher spatial resolution that is possible with conventional optics. The ability to detect submicron particles is also demonstrated – ensuring the usefulness of this type of device.

Future work

Future work can fall into two categories: improving on segments of this architecture, and applying this architecture to new applications.

There are a few areas of further improvement that present themselves immediately. The bond procedure that was developed is very useful, but the dynamics were not fully explored. Further study of the mechanisms of adhesion and the behavior of different polymers would be useful. Potential causes of the observed decreased bond strength at higher voltages were proposed in this thesis, but should be explored further.

The plasmonic component of this system could be a subject for further design and testing improvement. Different designs for the plasmonic device could incorporate a tapered structure to further confine and enhance the excitation fields. Alternatively, a plasmonic slot waveguide was shown in simulation to have broadband operation – these devices could be explored further. The tests in this thesis did not achieve rigorous results, as the sensitivity required to take accurate tests was difficult to obtain.

Standard test methods such as prism coupling and NSOM do not test the plasmonic operation of the completed integrated device. New test methods should be developed that can more thoroughly explore the plasmonic behavior in the integrated device.

Additional work needs to be performed to complete the integration of this system. Specifically, the fluidic handling and the optical signal gathering and processing can be improved and simplified to move from a research device to a device suited for general use. Fluidic handling could incorporate both filtering and flow control, potentially using integrated pumps.

Optical collection was presently performed with an inverted microscope. There are several ways that this functionality can be integrated into the system. Optics can be integrated via microfabricated lenses (1) (2) or zone plates (3) (4) to guide light to an integrated photodetector (5).

Another area of future work could apply this device architecture to other applications. Any application where there is a desire to detect small fluorescent particles will benefit from this type of device. DLA is an immediate application. By integrating our device into a high-speed photodetector with some signal processing, single molecule DNA fingerprinting should be possible.

In DNA fingerprinting, but without DLA, these devices could simply be used as a highly accurate DNA fragment sizing tool. Current microfluidic separation channels are limited by their background noise and lateral resolution. The improvements granted by this device could provide much improved DNA fingerprinting while enabling cheaper, faster analysis due to the integrated nature and small volumes presented by the system.

Another application that may benefit from this device is in the detection of microvesicles. Microvesicles can be important signaling mechanisms for many things in the body: including cancer or exposure to biological agents. Currently, it is not possible to detect these small particles. With a specific fluorescent tagging procedure, the devices presented in this thesis could be very useful in this application.

Works Cited

1. *Microfluidic measurement system for fluorescent particles with three-dimensional sheath flow and a self-aligned adjustable microlens.* **Bucheggera, Wolfgang, Rosenauera, Michael and Vellekoopa, Michiel J.** 2009, Proceedings of the Eurosensors XXIII conference. Procedia Chemistry, Vol. 1, pp. 1123-1126.
2. *Performance of an integrated microoptical system for fluorescence detection in microfluidic systems.* **Roulet, Jean-Cristophe, et al.** 2002, Analytical Chemistry, Vol. 74, pp. 3400-3407.
3. *High-throughput fluorescence detection using an integrated zone plate array.* **Schonbrun, Ethan, et al.** 2010, Lab on a Chip, Vol. 10, p. 852.
4. *A microfluidic fluorescence measurement system using an astigmatic diffractive microlens array.* **Schonbrun, Ethan, Steinvurzel, Paul E. and Crozier, Kenneth B.** 2011, Optics Express, Vol. 19, p. 1385.
5. *Fully integrated optical system for lab-on-a-chip applications.* **Balslev, S., et al.** 2004, Proceedings of the 17th IEEE MEMS (IEEE 2004), Vol. 1, pp. 89-92.

Appendix: Fabrication Procedures

Substrate fabrication process

Process Step	Operation	Details
Wafer prep and clean	Scribe Wafer ID	
	Top Gun Blow-off	
	Piranha Clean	20 min
	DI Rinse	10 min
	SRD	
	Dehydration Bake	1' @ 115 Hotplate
Ta ALMET	Spin on HMDS	HMDS Recipe
	Bake	1' @ 115 Hotplate
	Spin on S1805	1805 Recipe
	Bake	1' @ 115 Hotplate
	Clean Mask?	
	ALMET Expose	2.4 sec hard vac contact
	Develop	MF319 45 sec
	DI Rinse	5 min
	SRD	
	Photo Inspect	
	O2 Descum	55W 300 sec 30% O2
	200 Å Ta sputter	Mill Lane
	SVC-14 Lift-off	1 hour
	SCVC Ultrasound	5 minutes
	SVC-14 Lift-off	1 hour
	Solvent Bath	20 sec agitation in each: Acetone, Methanol, IPA

	DI Rinse	10 min
	SRD	
	O2 Descum	55W 300 sec 30% O2
	Photo Inspect	
Waveguides	Piranha Dip	1 minute
	DI Rinse	10 minutes
	SRD	
	400 Å Al front evap	Temescal 400Å - w ion mill
	400 Å Al back evap	Temescal 400Å - w ion mill
	Photo inspect	
	Dehydration bake	1' @ 115 °C Hotplate
	HMDS	HMDS Recipe
	Bake	1' @ 115 Hotplate
	Spin on 1822	-
	Bake	1' @ 115 C
	"Waveguide" Exposure	5.6 sec
	Backside protect	S1822 on back
	Bake	30 min 90 ° - Little oven under hotplates
	Develop	1 min MF-319
	DI Rinse	10 min
	SRD	
	Photo Inspect	
	O2 Descum	55W 300 sec 30% O2
	Photo Inspect	
	Al Etch	30sec (for 400 Å) in Al Etch @ 125° C hotplate for big beaker, 85° C hotplate for shallow - Could take longer, depending on freshness of etchant - let solution warm for 1 hour to get solution temp around 50° C - if using shallow beaker, check temp! Set to 85
	DI Rinse	10 min
	SRD	
	Photo Inspect	
	SVC-14 Resist Strip	20 minutes and 20 minutes
	Solvent Bath	20 sec agitation in each: Acetone, Methanol, IPA
	DI Rinse	10 min
	SRD	
	O2 Descum	55W 300 sec 30% O2
	Photo Inspect	

	Stress measurement	Use USG_glass.PRC process file
	Ion exchange	
	Info	
	Clean	DI bath 10 minutes
	Take full wafer pictures	
	Stress measurement	Use USG_glass.PRC process file
	Wet Al Mask Removal	Al Etch, @ 50°C solution, 125° C hotplate, as long as it takes - let solution warm for 1 hour to get solution temp around 50° C
	DI Rinse	10 min
	SRD	
	Photo Inspect	
Plasmonic Structures	Dehydration Bake	
	Spin on 950k PMMA A4 .2um	4500 rpm
	Oven Bake	180 C for 1 hour
	Hummer conductive coating	Mask over writing places - push cycle, need to wait 26 minutes to get down to pressure, push cycle again 2x to restart cycle
	The morning of the write - Spin on ESPACER	1500 RPM 30 sec
	Let sit 30 minutes	30 min
	Oven Bake	90 C for 10 minutes
	Ebeam Write	
	Rinse off ESPACER	In water 60 seconds, blow dry
	Develop	60 seconds 2:1 IPA:MIBK (in water bath @ 21 °C) constant agitation
	Stop Developing	IPA 30 seconds
	IPA spray	30 seconds
	Blow off	
	Photo inspect	
	Deposit Cr-Au (in Denton)	10nm Cr, 100nm Au (NO ROTATION! - rotation makes liftoff harder)
	SVC-14 Strip	1 Hour heated SVC-14 with stirrer
	SVC Rinse	Rinse with heated SVC to remove as much metal as you can. Be sure to not let dry!

	SVC Ultrasound	2 minutes
	SVC-14 Strip	1 Hour heated SVC-14 with stirrer (play musical hotplates)
	Acetone ultrasonics	2 minutes acetone ultrasonics
	Acetone Spray	30 sec vigorous Acetone spray off
	Solvent Bath (or Spray)	1 minute in each: A,M,I
	Di rinse	10 minute flowing DI rinse
	SRD	
	Photo Inspect	
Hole Drilling	Protect	1822 on front, bake, 1822 on back, oven bake
	Mount	
	Drill	
	Inspect	
	Clean	SVC 20 min, Acetone ultrasound 2 min, solvent baths, DI bath 10 min, blow dry
	Inspect	
Bond and dice	Prepare coverslip	
	Piranha dip	30seconds
	DI Rinse, SRD	
	Dehydration Bake	1' @115°C hotplate
	Spin on MEMO	
	Bake	1' @ 115°C hotplate
	O2 plasma coverslip	30s 55W
	Align	EVG 620 aligner
	Bond	Voltage assisted, ensure top and bottom heat at same rate
	Photo inspect	
	Dice	tape on both sides
	Remove from dicing tape	
	Clean	30 min hot SVC
		10 min acetone
	15 min Acetone:IPA 1:1	
	15 min Oven	
Optical Connections	Grind and Polish	30um grit, 9 um grit, 3um grit, 1um grit
	Fiber attach	

Coverslip Fabrication process

Clean	Piranha	
	DI Rinse	
	SRD	
If using Cytop A, use adhesion promoter	Dehydration Bake	1' @ 115 C
	Spin on adhesion promoter	
	Bake	1' @ 115 C
Spin, pattern and etch	Spin Cytop	4000 rpm for M, 1300 for A (to get 200nm)
	Bake	2' @ 90 deg C
	Spin Cytop	4000 rpm for M, 1300 for A (to get 200nm)
	Bake	2' @ 90 deg C
	O2 Plasma	55W 30s
	Spin 1822	3 kRPM - 1822 Recipe
	Bake	1' @ 115 C
	Expose	7s - Hard Contact
	Develop	1' in MF-319
	DI rinse	10 minutes
	SRD	
	Photo inspect	
	Etch	Oxford recipe JSV - Cytop etch
Clean	Acetone Spray	
	SVC Strip	20 min
	SVC Strip	20 min
	Solvent bath	2 minute in each Acetone, Methanol, IPA
	DI rinse	10 minutes
	SRD	
	Bond	